The University of Manchester

Fabrication and Characterisation of High-Speed Graphene Nanodevices for THz Detection

A Thesis submitted to the University of Manchester for the degree of Doctor of Philosophy in the Faculty of Science and Engineering

2021

Joseph A. Brownless

School of Engineering

Contents

LIST OF SYMBOLS **4**

LIST OF ACRONYMS **9**

ABSTRACT **11**

DECLARATION **12**

COPYRIGHT STATEMENT **13**

ACKNOWLEDGEMENTS **14**

PUBLICATIONS AND CONFERENCES **15**

1. INTRODUCTION **16**

2. THEORY **21**

2.1. GRAPHENE 21

2.1.1. Background and History 21

2.1.2. Crystal Structure 23

2.1.3. Electronic Properties 25

2.1.4. Dispersive Conductivity 31

2.1.5. Plasmonics 33

2.2. THZ RADIATION 36

2.2.1. Overview and Applications 36

2.2.2. Generation Techniques 37

2.2.3. Detection Techniques 39

2.3. RECTIFIERS AND RECTENNAS 41

2.4. GRAPHENE NANODEVICES 45

2.4.1. Ballistic Rectifiers 45

2.4.2. Self-Switching Diodes 48

2.5. ELECTRICAL NOISE 53

3. FABRICATION AND MEASUREMENT TECHNIQUES **55**

3.1. GRAPHENE FLAKE PREPARATION AND NANODEVICE FABRICATION 55

3.1.1. Graphene and Hexagonal Boron Nitride Exfoliation 55

3.1.2. Transfer and Encapsulation Methods 57

3.1.3. CVD Growth and Transfer of Graphene 62

3.1.4. Micro- and Nanofabrication 64

3.2. DC AND LOW-FREQUENCY AC MEASUREMENTS 73

3.3. NOISE MEASUREMENT 76

3.3.1. Two Channel Cross-correlation 76

3.3.2. Testing and Calibrating Setup 78

3.4. TIME-DOMAIN HIGH-FREQUENCY SIMULATIONS 80
4. GRAPHENE BALLISTIC RECTIFIERS 84
4.1. EXPANDED THEORY OF OPERATION 84
4.2. MODIFIED GBR DESIGNS 94
4.2.1. Designs 94
4.2.2. Measurements and Analysis 96
4.2.3. Low Temperature Measurement 101
4.2.4. Fitting Data with Developed Theory 104
4.3. PREDICTED OPTIMAL DEVICES 107
4.4. BALLISTIC RECTIFIER ARRAYS 109
4.5. GRAPHENE BALLISTIC RECTIFIERS USING CVD-GROWN GRAPHENE 115
4.6. NOISE MEASUREMENTS 119
4.7. SUMMARY 120
5. GRAPHENE SELF-SWITCHING DIODES 123
5.1. GSSD ARRAYS 124
5.2. GSSD BRIDGE RECTIFIER THEORY 128
5.3. ENCAPSULATED GSSD BRIDGE RECTIFIER MEASUREMENTS 131
5.4. CVD GSSD BRIDGE RECTIFIERS 138
5.5. NOISE MEASUREMENTS 144
5.6. SUMMARY 146
6. SIMULATION OF TERAHERTZ GRAPHENE ANTENNAS 149
6.1. DIPOLE ANTENNAS 151
6.1.1. Varying Length and Width 153
6.1.2. Calculating Plasmon Wavelengths 159
6.2. BOWTIE ANTENNAS 163
6.3. SUMMARY 167
7. CONCLUSIONS AND FUTURE WORK 169
7.1. CONCLUSIONS 169
7.2. FUTURE WORK 172
REFERENCES 173

Word count: 39,642

List of Symbols

Symbol	Meaning	Units (if applicable) and value (if constant)
a	Graphene bond length	1.42 Å
$\overrightarrow{\boldsymbol{a_1}}$ $\overrightarrow{\boldsymbol{a_2}}$	Graphene lattice vectors	Å
A	Frequency-independent constant in surface plasmon distribution	s
$A_{const.}$	Physical constant in GBR theory	$\mathrm{J\ s^2}/C^{3/2}m$
A_G	Gain of op-amp circuit	/
$\overrightarrow{\boldsymbol{b_1}}$ $\overrightarrow{\boldsymbol{b_2}}$	Graphene reciprocal lattice vectors	Å
B	Bandwidth	Hz
B_{geo}	Geometry factor in GBR theory	m^{-2}
C	Capacitance	F
C_G	Gate dielectric capacitance density	F cm^{-2}
C_t	GSSD side gate capacitance per unit length	F cm^{-1}
d	Separation between two graphene strips	nm
D	Antenna directivity	/
DFT	Discrete Fourier transform	/
D_t	Sub-determinant of 4-terminal conductance matrix	/
ε_0	Vacuum permittivity	$8.8542 \times 10^{-12}\mathrm{F/m}$
ϵ_A	Antenna efficiency	/
ε_r	Dielectric constant	/
ε_{r1} ε_{r2}	Dielectric constants on either side of graphene sheet	/
e	Electronic charge	1.6022×10^{-23} C
E	Energy	eV
$E_\pm$	Graphene band energy	eV
E_f	Fermi energy	eV
f	Frequency	Hz
f_c	Centre frequency	Hz
f_d	Fermi-Dirac distribution	/

g	Conductance	S
G_A	Antenna gain	/ (or dBi)
g_{SD}	Source-drain conductance	S
$g_{SD,arr}$	Input conductance of GBR array	S
$G_{\beta\alpha}$	Conductance between probes α and β	S
$\hbar$	Reduced Plank constant	1.0546×10^{-34} J s
h	Plank constant	6.6261×10^{-34} J s
$\mathrm{Im}(z)$	Imaginary component of complex number z	/
I_α	Current through probe α	A
$I_{asymm.}$	Current asymmetry through graphene self-switching diode	A
I_{GSSD}	Current through graphene self-switching diode	A
I_n	Electron current	A
I_p	Hole current	A
I_{SD}	Source-drain current	A
$I_{SD,arr}$	Input current to GBR array	A
$\vec{\mathbf{k}}$	Wavevector	cm^{-1}
$\overrightarrow{\boldsymbol{k_K}}$	Wavevector at graphene K point	cm^{-1}
Δk	Change in wavevector when current is applied	cm^{-1}
k_0	Free space wavenumber	cm^{-1}
k_B	Boltzmann constant	1.3807×10^{-23} J/K
k_f	Fermi wavevector	cm^{-1}
k_{SP}	Surface plasmon wavenumber	cm^{-1}
λ_0	Free space wavelength	μm
λ_{mfp}	Mean free path	μm
λ_{SP}	Surface plasmon wavelength	μm
L	Hall bar length	μm
L_c	GSSD channel length	μm
L_{bow}	Bowtie antenna length	μm
L_{dip}	Dipole antenna length	μm
$\{\mu\}$	Chemical potentials at all probes	eV
μ	Carrier mobility	cm^2/Vs
μ_α	Chemical potential at probe α	eV

μ_c	Chemical potential	eV
μ_e	Electron mobility	$\mathrm{cm^2/Vs}$
μ_h	Hole mobility	$\mathrm{cm^2/Vs}$
n	2D electron density	cm^{-2}
N	Number of samples	/
n^*	Spatial inhomogeneity carrier density	cm^{-2}
n_0	Neutrality point carrier density	cm^{-2}
n_{arr}	Number of GBRs in an array	/
n_c	Carrier density in GSSD channel	cm^{-2}
n_{cv}	Gate-induced carrier density	cm^{-2}
N_{LU}	Number of modes in ballistic rectifier output QPCs	/
N_{SD}	Number of modes in ballistic rectifier source, drain QPCs	/
n_{th}	Thermal carrier density	cm^{-2}
N_U	Number of modes in GBR upper QPC	/
p	2D hole density	cm^{-2}
$P(\theta)$	Angular distribution of carriers from quantum point contact	/
P_{SD}	Input power	W
$P_{SD,arr}$	Input power of GBR array	W
Q_{th}	Free charge density at neutrality point	C/cm^2
$\rho(E)$	Density of states per unit cell	eV^{-1}
$\mathcal{R}$	Voltage Responsivity	V/W
$\mathcal{R}_{50\Omega}$	Responsivity with impedance mismatch with $50\ \Omega$ source	V/W
$\mathcal{R}_{arr}$	Responsivity of GBR array	V/W
r	Electron/hole mobility ratio	/
R	Device resistance	Ω
$\mathrm{Re}(z)$	Real component of complex number z	/
R_{SD}	Source-drain resistance	Ω
$R_{SD,UL}$	Ballistic rectifier four-terminal resistance	Ω
$\sigma(\omega)$	Dispersive 2D conductivity	S
s	Graphene strip width	nm
s_1	Time-domain voltage noise signals measured by two channels	V
s_2	Time-domain voltage noise signals measured by two channels	V

S_{11}	Reflection parameter	/
S_V	Voltage noise spectral density	V^2/Hz
τ	Carrier relaxation time	ms
θ	Carrier trajectory from quantum point contact	rad
θ_0	Angle from source/drain normal to top corner of scattering centre	rad
θ_e	Angle of carriers with no applied current, at which they are at θ_0 with applied current	rad
T	Temperature	K
t	Graphene nearest-neighbour hopping energy	$\sim 2.8\ \mathrm{eV}$
t'	Graphene next-nearest-neighbour hopping energy	eV
t_c	GSSD channel thickness	nm
T_{samp}	Sampling time window	s
$T_{[\alpha\to\beta]}$	Transmission probability from probes α to β	/
$T_{[\beta,\alpha]}$	Transmission probability between α and β, with direction depending on relative chemical potentials	/
ΔV	Voltage difference between forward- and reverse-biased GSSDs	V
$v_1(f)$	Spectral noise voltage measured by two channels	V
$v_2(f)$	Spectral noise voltage measured by two channels	V
V_1	Voltage drops at forward- and reverse-biased GSSD arrays	V
V_2	Voltage drops at forward- and reverse-biased GSSD arrays	V
V_A	Gate voltage offset from neutrality point	V
v_d	Drift velocity	$\mathrm{m\ s^{-1}}$
V_D	Drain voltage	V
v_f	Fermi velocity in graphene	$\sim 1\times 10^6\ \mathrm{m\ s^{-1}}$
V_G	Gate voltage	V
v_n	Mean square noise voltage	V
V_{out}	GSSD bridge rectifier output voltage	V
$V_{out,asym}$	GSSD bridge rectifier output voltage asymmetry	V
V_{UL}	GBR output voltage (Upper-lower)	V
$V_{UL,arr}$	Output voltage of GBR array	V
$V(y)$	Voltage along GSSD channel	V
ω	Angular frequency	Hz
W	Hall bar width	$\mu\mathrm{m}$

W_{dip}	Dipole antenna width	μm
w_{SD}	Input (source, drain) quantum point contact width in GBR	nm
w_U	Output (upper) quantum point contact width in GBR	nm
W_c	GSSD channel width	nm
Z_0	Free space impedance	376.73 Ω
Z_A	Antenna impedance	Ω
Z_L	Load impedance	Ω
Z_S	Source impedance	Ω

List of Acronyms

1D	One-dimensional
2D	Two-dimensional
3D	Three-dimensional
ADC	Analogue-to-digital convertor
AFM	Atomic force microscopy
BR	Ballistic rectifier
BZ	Brillouin zone
CB	Conduction band
CVD	Chemical vapour deposition
D	Drain
DC	Direct current
DoS	Density of states
EBL	Electron beam lithography
EHT	Extra-high tension (SEM acceleration voltage)
FET	Field effect transistor
GBR	Graphene ballistic rectifier
GSSD	Graphene self-switching diode
hBN	Hexagonal boron nitride
ICP	Inductively coupled power
IPA	Isopropanol, 2-propanol
IR	Infra-red
L	Lower contact
NEP	Noise-equivalent power
NP	Neutrality point
Op-amp	Operational amplifier
PDMS	Polydimethylsiloxane
PMMA	Poly(methyl methacrylate)
PPC	Polypropylene carbonate
PVA	Poly(vinyl alcohol)
QCL	Quantum cascade laser
QPC	Quantum point contact

Rectenna	Rectifying antenna
RIE	Reactive ion etching
RF	Radio frequency
RPM	Rotations per minute
S	Source
SEM	Scanning electron microscope
SP	Surface plasmon
SPP	Surface plasmon polariton
SSD	Self-switching diode
THz	Terahertz
THz-TDS	Terahertz time-domain spectroscopy
TM	Transverse magnetic
U	Upper contact
VB	Valence band
WF	Write field
WP	Working point

Abstract

Despite graphene's excellent properties, there have been very few electronic devices which make full use of them due to the lack of bandgap. This research aims for the development of high-performance graphene THz detectors. Towards this goal, two nanodevices are investigated. Both do not require a bandgap, with each being capable of operating into the terahertz (THz) range. The graphene ballistic rectifier (GBR) uses the long mean free paths in graphene to achieve ballistic transport and redirect carriers preferentially towards a single output. Building on the extended Büttiker-Landauer formula for ballistic rectifiers in semiconductors, the operational theory of GBRs is derived and tested taking into account the coexistence of electrons and holes. The theory predicts large responsivities when there is a large disparity in carrier mobilities, while calculations using realistic device dimensions and parameters predict easily achievable responsivities of at least $50{,}800\ \mathrm{V/W}$ and noise-equivalent power (NEP) of $0.51\ \mathrm{pW/Hz^{1/2}}$. The second nanodevice is the graphene self-switching diode (GSSD), which uses electrostatic effects to cause asymmetric current flow through a conducting channel. By constructing a bridge rectifier from encapsulated GSSDs a modest peak responsivity of $4{,}400\ \mathrm{V/W}$ is found, with minimum NEP of $5.4\ \mathrm{pW/Hz^{1/2}}$ is found if thermal noise is assumed to dominate. Both nanodevices are then tested using graphene grown by chemical vapour deposition (CVD), an important step towards fabrication on a larger scale. A bridge rectifier constructed from CVD GSSDs demonstrates peak responsivity $> 100\ \mathrm{kV/W}$. However, poor noise performance puts the NEP at $11.7\ \mathrm{nW/Hz^{1/2}}$, worse than GBRs and many other room-temperature THz detectors. GBRs using CVD graphene show good results, with responsivity of $10{,}000\ \mathrm{V/W}$ and similar noise to encapsulated graphene ballistic rectifiers. However, combining graphene ballistic rectifiers into arrays gives mixed results. Finally, simulations of THz graphene bowtie antennas using parameters realistic for CVD graphene show that they can be operated with high-impedance detectors such as those investigated here. With a $1\ \mathrm{k\Omega}$ source they show reflection parameters under $-12\ \mathrm{dB}$ at THz frequencies, although improvement to CVD graphene quality would give significant improvement. While no THz results are presented here, the next step is combining these antennas with high-frequency graphene rectifiers such as the GBR or GSSD to form graphene THz detectors.

Declaration

I declare that no portion of the work referred to in this thesis has been submitted in support of an application for another degree or qualification of this or any other university or other institute of learning.

Joseph A. Brownless,

7st November 2021

Copyright Statement

I. The author of this thesis (including any appendices and/or schedules to this thesis) owns certain copyright or related rights in it (the "Copyright") and s/he has given The University of Manchester certain rights to use such Copyright, including for administrative purposes.

II. Copies of this thesis, either in full or in extracts and whether in hard or electronic copy, may be made only in accordance with the Copyright, Designs and Patents Act 1988 (as amended) and regulations issued under it or, where appropriate, in accordance with licensing agreements which the University has from time to time. This page must form part of any such copies made.

III. The ownership of certain Copyright, patents, designs, trademarks and other intellectual property (the "Intellectual Property") and any reproductions of copyright works in the thesis, for example graphs and tables ("Reproductions"), which may be described in this thesis, may not be owned by the author and may be owned by third parties. Such Intellectual Property and Reproductions cannot and must not be made available for use without the prior written permission of the owner(s) of the relevant Intellectual Property and/or Reproductions.

IV. Further information on the conditions under which disclosure, publication and commercialisation of this thesis, the Copyright and any Intellectual Property and/or Reproductions described in it may take place is available in the University IP Policy (see http://documents.manchester.ac.uk/DocuInfo.aspx?DocID=2442 0), in any relevant Thesis restriction declarations deposited in the University Library, The University Library's regulations (see http://www.library.manchester.ac.uk/about/regulations/) and in The University's policy on Presentation of Theses.

Acknowledgements

I would first like to thank my supervisor Professor Aimin Song for his supervision throughout, and all his guidance and advice. He has helped me keep my project on track throughout my time here, and I am especially grateful for his support in overcoming the disruptions caused by COVID-19.

I would also like to thank all of Prof. Song's current and former students and postdocs, especially Prof. Jiawei Zhang for all of his invaluable training, discussions, and advice throughout my time in Manchester. In addition, I am grateful to all members of my cohort at the Graphene NOWNANO CDT for their friendship and good times over these four years.

I would especially like to thank all the experimental officers for all their technical help and support, both inside and outside the clean room. This includes, but is not limited to, Mr Malachy McGowan, Dr Linqing Zhang, and Dr Ian Hawkins in the Sackville Street Building, and all of the National Graphene Institute cleanroom technicians and experimental officers.

A massive thank you to my parents for all of their support throughout all of my time at university, both undergrad and during my PhD. Finally thank you to my girlfriend Sinead, for putting up with my unsociable working hours especially during the write-up period, and for all of the love and support she's offered me.

Publications and Conferences

- *** J. Brownless**, J. Zhang, and A. Song, "Graphene ballistic rectifiers: Theory and geometry dependence," *Carbon*, vol. 168, pp. 201–208, Oct. 2020. DOI: 10.1016/j.carbon.2020.06.058.
- W. Cai, J. Zhang, J. Wilson, **J. Brownless**, S. Park, L. Majewski, and A. Song, "Significant Performance Improvement of Oxide Thin-Film Transistors by a Self-Assembled Monolayer Treatment," *Adv. Electron. Mater.*, vol. 6, no. 5, p. 1901421, May 2020. DOI: 10.1002/aelm.201901421.
- W. Cai, J. Wilson, J. Zhang, **J. Brownless**, X. Zhang, L. A. Majewski, and A. Song, "Significant Performance Enhancement of Very Thin InGaZnO Thin-Film Transistors by a Self-Assembled Monolayer Treatment," *ACS Appl. Electron. Mater.*, vol. 2, no. 1, pp. 301–308, Jan. 2020. DOI: 10.1021/acsaelm.9b00791.
- X. Zhang, W. Cai, J. Zhang, **J. Brownless**, J. Wilson, Y. Zhang, and A. Song, "Solution-Processed TiO_2 -Based Schottky Diodes With a Large Barrier Height," *IEEE Electron Device Lett.*, vol. 40, no. 9, pp. 1378–1381, Sep. 2019. DOI: 10.1109/LED.2019.2928007.
- W. Cai, **J. Brownless**, J. Zhang, H. Li, E. Tillotson, D. G. Hopkinson, S. J. Haigh, and A. Song, "Solution-Processed HfOx for Half-Volt Operation of InGaZnO Thin-Film Transistors," *ACS Appl. Electron. Mater.*, vol. 1, no. 8, pp. 1581–1589, Aug. 2019. DOI: 10.1021/acsaelm.9b00325.
- ***** J. Zhang, **J. Brownless**, and A. Song, "Graphene bridge rectifier based on self-switching diode arrays," *Nanotechnology*, vol. 30, no. 36, p. 364004, Sep. 2019. DOI: 10.1088/1361-6528/ab25fd.

***** J. Brownless and J. Zhang contributed equally to both of these publications

Conferences

IRMMW-THz 2019:

- **J. Brownless**, J. Zhang, and A. Song, "A Graphene Self-Switching Diode Bridge Rectifier," in *2019 44th International Conference on Infrared, Millimeter, and Terahertz Waves (IRMMW-THz)*, 2019, pp. 1–2. DOI: 10.1109/IRMMW-THz.2019.8873697.
- J. Zhang, **J. Brownless**, and A. Song, "High Performance Graphene Ballistic Rectifiers for THz detection," in *2019 44th International Conference on Infrared, Millimeter, and Terahertz Waves (IRMMW-THz)*, 2019, pp. 1–2. DOI: 10.1109/IRMMW-THz.2019.8874198.

1. Introduction

Since it was first isolated in 2004 [1], graphene has been subject to a huge quantity of research, in fields from electronics [2–7] to composites [8, 9] and biomedicine [10, 11]. For decades it had previously been studied theoretically as the monolayer form of graphite [12], but it was commonly regarded as purely an 'academic material' [1, 13] until the mechanical exfoliation with optical contrast method was developed. Since being isolated, it has been found to possess many excellent properties, for example its 2D Young's modulus of $340\ \mathrm{N/m}$ [14] or higher [15]. Combined with its flexibility, high surface area:mass ratio of $2630\ \mathrm{m^2/g}$ [16], and stability up to 2600 K [17], the development of liquid phase exfoliation has enabled graphene's use in many composites and other materials [8, 9], as well as for inkjet printed and flexible electronics [18]. Separately, graphene's excellent electronic properties, such as high carrier densities and ultra-high carrier mobilities [19, 20], have also led to a myriad of applications being studied.

Terahertz (THz) frequencies represent the region of the electromagnetic spectrum between infrared (IR) radiation and microwaves, and as such form the boundary between traditionally 'optic' frequencies and 'electronic' frequencies. Due to this, efficient generation and detection of THz radiation tends to be difficult, and for this reason the region is often referred to as the 'THz gap' [21]. The lower and upper bounds of this region are somewhat arbitrary, but are generally considered to be 0.1-0.3 THz and 10-30 THz respectively, spanning wavelengths from 10 µm to 3 mm [22]. Despite the difficulty in generation and detection, THz radiation has a huge array of potential applications, in security and medical imaging, as well as scientific and astronomical instruments and telecommunications [22–27]. Telecommunications in particular is an important area of applications, as the drive for ever-higher data transfer rates naturally pushes operational frequencies higher.

Due to THz radiation falling between these two regions, approaches to generation generally involve emitting ‘optical’ radiation of lower frequency by finding energy level transitions of lower energy, for example quantum cascade lasers [28–30], synchrotrons and gyrotrons [31, 32], and free electron lasers [33, 34]. While a large number of THz generation techniques and devices have been developed in recent years, state-of-the-art detection still mostly lies in technologies such as Golay cells, bolometers, and other devices which rely on heat generation by the incident radiation [35]. While these devices can detect a wide range of frequencies and give very high responsivities of well over $100{,}000\ \mathrm{V/W}$, due to their operational mechanisms they are limited to response times of the order of 10s of ms. In addition, many detectors, such as most bolometers, require cooling to cryogenic temperatures for sensitive detection [35]. An alternative approach is to increase the operational frequencies of traditional electronics-frequency detectors, such as rectennas, into the THz range. Such devices will naturally have a much faster response time, making their development highly desirable for applications which benefit from fast response, such as THz imaging or ultrafast spectroscopy [35]. Generation and detection methods for THz radiation will be discussed in more detail in Section 2.2.

Graphene’s high carrier mobilities make it naturally suitable for high frequency electronics, extending into the THz region. Coincidently, graphene’s unusual electronic properties make it suitable for hosting plasmonic oscillations in the THz region, enabling applications which use plasmonic resonance on graphene to couple to free space THz radiation [36, 37]. However, due to it being a ‘semi-metal’, graphene lacks a bandgap, severely hindering most potential electronics applications. For example, graphene transistors tend to have low on-off ratios, because the lack of a bandgap prevents a depletion region from forming, resulting in large off currents [38]. Many approaches have been developed to overcome this obstacle, for example tunnelling devices [39, 40] and graphene nanoribbon devices [38, 41], but both come with considerable disadvantages. Alternative device concepts that make use of graphene for high frequency applications while not suffering from the lack of a bandgap

are the ballistic rectifier (BR) and the self-switching diode (SSD). The BR is a planar four-terminal device which uses ballistic transport and an asymmetric structure to rectify input current into a DC output by redirecting carriers preferentially towards a single output, regardless of input current direction [42]. The SSD is a two-terminal planar device consisting of a conducting channel with insulating trenches on either side, similar to a side-gated transistor with two gates connected to the source or drain, which self-gates the channel when forward or reversed biased [43]. Due to the lack of bandgap both of these devices operate with zero threshold voltage, which is an advantage for high-frequency signals, which are often low in amplitude. Competing technologies include Schottky diodes, which are used at high frequencies and can also be operated without a threshold voltage. The main disadvantage of Schottky diodes compared to these graphene devices is the more limited frequency range, with the maximum possible operating frequency (assuming negligible parasitic capacitance) being limited by the plasma frequency of the semiconductor used [44]. Both the BR and the SSD have low parasitic capacitance due to their planar nature meaning contacts are arranged horizontally rather than vertically. Combined with input resistance, capacitance determines the cut-off frequency of a device and hence these devices have been shown to operate at or near THz frequencies [45–47]. However, it is important to note that in a real application the maximum operational frequency will also depend strongly on surrounding circuitry. For example, any transmission line or antenna will contribute to capacitance, reducing the cut-off frequency. However, compensation circuits containing inductive elements can be used to mitigate the effects of parasitic capacitance. These devices were first fabricated using III-V semiconductor 2D electron gasses [42, 43, 45, 48], but have since been fabricated using graphene [49–51], forming the graphene ballistic rectifier (GBR) and the graphene self-switching diode (GSSD). While these devices show good performance in III-V semiconductors, carrier mobilities in these materials depend strongly on temperature, limiting their use as uncooled detectors [42, 43]. In graphene, while

carrier mobilities are also extremely large, they are also mostly independent of temperature, meaning that graphene has the largest mobilities of any material at room temperature [19, 50, 52, 53].

The GBR has been shown to have excellent properties [50] and has been proven as a THz detector [47]. However, a large obstacle to further development has been the large input impedance of these devices. This causes large power losses when coupled to a low-impedance source, such as an antenna. There are several avenues to improving this, which will be investigated here. In addition, the majority of work on graphene ballistic rectifiers and self-switching diodes has been using exfoliated graphene, using the same sticky tape method by which was first discovered in 2004 [1]. While manual mechanical exfoliation and subsequent encapsulation in hexagonal boron nitride is capable of producing extremely high quality devices, it is extremely difficult to up-scale this method for industrial-scale production. Therefore, graphene produced by large-scale growth methods, such as chemical vapour deposition (CVD), must be investigated with these devices to test how their performance compares to using manually exfoliated and encapsulated graphene.

This work focuses on further development of GBRs and GSSDS, in particular moving towards larger-scale fabrication, followed by simulations of graphene-based THz antennas suitable to be integrated with these devices in rectennas. No THz results are contained in this thesis, however the work presented here allows for future research to combine these THz-capable rectifiers with graphene-based antennas to form THz detectors. All rectifier results measured here such as responsivity and noise-equivalent power are measured at low frequency. It is anticipated that these will become worse as frequency increases towards the THz region, as the cut-off frequency of devices is approached. Chapter 2 details graphene as a material, along with relevant electronic properties, followed by a summary of contemporary THz generation and detection techniques. Then, the structure and details of the GBR and GSSD are described, and finally relevant sources of electrical noise in these devices are outlined. Chapter 3 describes the various device fabrication and measurement techniques used, including the

low-frequency noise measurement setup and the electromagnetic simulation methods used. In Chapter 4, investigations of the GBR are presented. First, the theory of operation is extended to aid in the design of future devices, followed by predictions and calculations. Then, in the interest of larger-scale fabrication and reducing impedance mismatch, investigations are performed into how arrays of GBRs affect performance. Devices are then tested using commercial-scale CVD graphene and finally the noise performance of a large array of GBRs using CVD graphene is tested. Chapter 5 then shows tests of GSSDs and GSSD bridge rectifiers, fabricated using encapsulated graphene and CVD graphene, also in the interest of moving to large-scale fabrication. The noise performance of a CVD GSSD bridge rectifier is then tested. Chapter 6 contains simulations and analysis of THz graphene antennas, performed during the laboratory closures caused by COVID-19. These antennas make use of graphene's THz plasmonics to couple free space THz radiation to high-impedance devices such as the GSSD and the GBR. Dipole antennas are tested in terms of how size and graphene properties affect performance, and then bowtie antennas are tested. Finally, bowtie antennas with parameters realistic for CVD graphene are simulated and considered for use.

2. Theory

2.1. Graphene

2.1.1. Background and History

Graphene is a 2D allotrope of carbon, consisting of a single layer of carbon atoms arranged into a honeycomb structure. Because it is effectively a single layer of the 3D material graphite, which has been used for various purposes from pencils to lubricants due to its layered nature, it is certain that graphene has been produced accidently many times in the past. However, despite been studied theoretically for over 70 years [12], it was presumed to be unstable, preferring to roll up and rearrange into other allotropes such as carbon nanotubes or fullerenes [13]. Therefore, the discovery in 2004 of a simple method to fabricate monolayer graphene sheets by mechanical exfoliation using tape followed by identification using optical contrast on a SiO_2 substrate caused an explosion in research interest and lead to Andre Geim and Konstantin Novoselov winning the 2010 Nobel prise in physics.

A major breakthrough in graphene electronics occurred with the use of thin hexagonal boron nitride (hBN) crystals, first as a substrate for graphene [54], followed quickly by full encapsulation [53], alongside dry transfer techniques [55]. hBN is an ideal substrate, and encapsulation has allowed devices with carrier mobilities in excess of $100{,}000\ \mathrm{cm}^2/\mathrm{Vs}$ to be fabricated [50, 52]. In addition, the extremely large pressure exerted by these so-called 'Van-der-Waals heterostructures' causes any impurities present in between the layers to be squeezed into bubbles on the scale of 10s of µm. These bubbles are easily visible using a microscope, and can hence be avoided when fabricating devices. Alongside encapsulation and dry stamp transfer techniques, the development of one-dimensional (1D) contacts also offered reduced contact resistances and a much less capacitive structure than depositing metal directly onto graphene, while removing the need for any sort of resist or other polymer to ever come into contact with the graphene surface [52]. Carrier densities in graphene are typically in the range of

$10^{12}\mathrm{cm}^{-2}$ [56, 57], which is similar to that seen in GaAs/AlGaAs 2D electron gasses [58, 59]. While III-V semiconductor 2D electron gasses can have extremely high mobilities in excess of $10^{8}\mathrm{cm}^{2}/\mathrm{Vs}$ at cryogenic temperatures, the mobility drops off quickly with increasing temperature to around $10^{4}\mathrm{cm}^{2}/\mathrm{Vs}$ [43, 59]. In contrast, graphene's carrier mobility depends only weakly on temperature, with values greater than $10^{5}\ \mathrm{cm}^{2}/\mathrm{Vs}$ at room temperature being well documented [50, 52].

Early in the life of graphene as a newly discovered material, perhaps the most exciting area of potential applications was in electronics. It was hoped that graphene's ultra-high carrier mobilities, higher than any other material discovered at room temperature, would pave the way for a new era of ultra-fast electronics, with graphene replacing silicon at the heart of all electronics [13]. However, the majority of these electronics applications have yet to be realised, due in a large way to graphene's lack of a bandgap. Efforts to modify graphene to open up a bandgap invariably lead to a decrease in mobility, destroying the main benefit of using graphene at all. This means that electronic devices which rely on a bandgap to produce effects like depletion regions, such as field-effect transistors, operate very poorly in pure monolayer graphene. The lack of a depletion region means that reverse currents/off currents for these devices are extremely large [38]. A large drawback of graphene transistors at high frequencies is the low impedance of these devices. This means that they can support high currents but have extremely low gain and cannot drive high powers. In comparison, silicon MOSFETs can have extremely large current gain and voltage gain, and are widely used. This is widely considered the main obstacle preventing widespread use of graphene's otherwise excellent electronic properties in commercial devices. One approach to avoid this issue in graphene electronics has been to use devices which rely upon carriers tunnelling through some sort of thin potential barrier [39, 40]. The use of potential barriers allows for much reduced reverse current, however the nature of these structures, with conducting layers separated by thin insulators, is inherently capacitive. This causes large intrinsic device capacitance, massively reducing cut-off frequency. Another potential solution lies in the use of

graphene nanoribbons, which due to lateral quantum confinement do possess a bandgap, and hence boast far larger on/off ratios [38, 41, 60]. Graphene nanoribbons however have far lower carrier mobilities than graphene, eliminating one of the main advantages of the use of graphene [38, 41].

Due to graphene being a 2D material, it has an extremely large surface area – volume ratio. This allows graphene-containing batteries and supercapacitors to be lighter and more flexible, with much longer-term storage than traditional capacitors and extremely fast charge/discharge times [61–63]. As well as energy storage applications, the large surface area allows an extremely wide range of graphene-based sensors such as temperature or chemical sensors to achieve high sensitivities [11, 16, 64]. In addition, graphene has also been investigated for many applications in composite materials [8, 9].

2.1.2. Crystal Structure

The unit cell contains two carbon atoms, with unit cells being arranged in a hexagonal structure. This is shown in Figure 1.

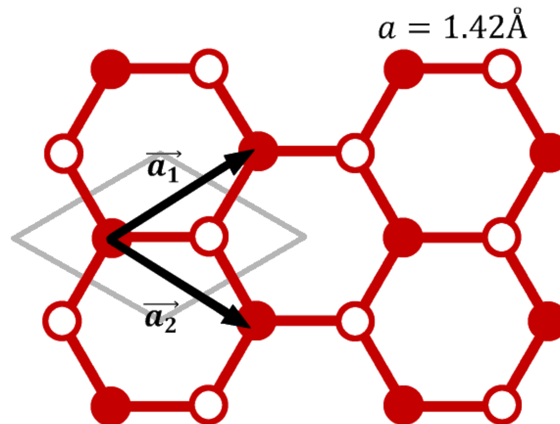

Figure 1: Lattice structure of graphene. The unit cell (grey diamond) is shown, as well as the lattice vectors $\overrightarrow{a_1}$ and $\overrightarrow{a_2}$ and the bond length a. The filled in and empty circles represent the two sub-lattices.

The atoms can be arranged into two distinct sub-lattices, corresponding to the two atoms in the unit cell. The lattice vectors are

$$\overrightarrow{\boldsymbol{a_1}} = \frac{a}{2}\binom{3}{\sqrt{3}}, \qquad \overrightarrow{\boldsymbol{a_2}} = \frac{a}{2}\binom{3}{-\sqrt{3}}, \qquad \text{Equation 1}$$

where $a = 1.42$ Å is the bond spacing. Atoms are bonded to the three nearest-neighbours by σ-bonds, with one π-bond extending in lobes perpendicular to the plane. This is due to sp2 hybridization, where one 2s two 2p orbitals are combined, as opposed to sp3 hybridisation, which is found in diamond and creates a 3D tetragonal shape. These half-filled π-bands contribute towards the vast majority of graphene's unique and unusual properties, because they leave electrons able to flow along the plane [20].

The reciprocal lattice vectors of graphene are

$$\overrightarrow{\boldsymbol{b_1}} = \frac{2\pi}{3a}\binom{1}{\sqrt{3}}, \qquad \overrightarrow{\boldsymbol{b_2}} = \frac{2\pi}{3a}\binom{1}{-\sqrt{3}}, \qquad \text{Equation 2}$$

as shown in Figure 2.

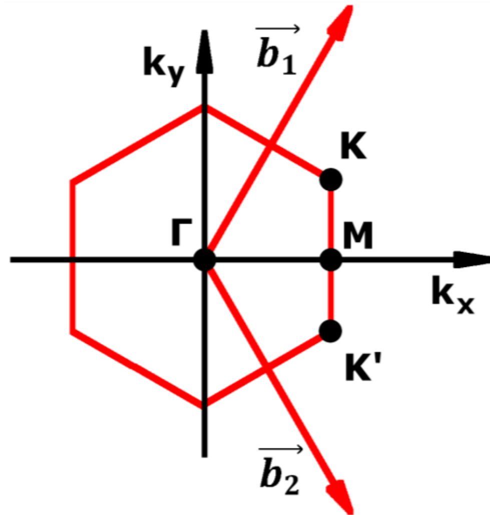

Figure 2: The first Brillouin zone of graphene (red hexagon). $\overrightarrow{\boldsymbol{b_1}}$ and $\overrightarrow{\boldsymbol{b_2}}$ are the reciprocal lattice vectors, with the symmetry points M, Γ, K, and K' also shown.

The first Brillouin zone (BZ), defined as the unit cell of the reciprocal lattice, is also shown. It has several unique points of symmetry, denoted as Γ, K, K', and M. Due to translation by whole number

combinations of the reciprocal lattice vectors, all 6 corners of the 1st BZ can be described by just K and K'. Their positions are

$$\vec{\boldsymbol{K}} = \frac{2\pi}{3a}\begin{pmatrix} 1 \\ \frac{1}{\sqrt{3}} \end{pmatrix}, \quad \vec{\boldsymbol{K}'} = \frac{2\pi}{3a}\begin{pmatrix} 1 \\ -\frac{1}{\sqrt{3}} \end{pmatrix}. \qquad \text{Equation 3}$$

2.1.3. Electronic Properties

Graphene is a semi-metal, alternatively known as a gap-less semiconductor, due to the fact that the conduction and valence band meet at a single point in k-space, known as the Dirac point [20]. This point has a density of states (DoS) of zero, and is 4-fold degenerate due to spin and K/K' degeneracy. In pristine graphene, the Fermi energy lies on the Dirac point.

The dispersion (energy-momentum) relation of graphene can be calculated using the tight-binding model, which models band structure using the electron wave functions of individual electrons with added terms for the interaction energies between adjacent lattice sites. In graphene, sp2 hybridization produces sp_z orbitals that are perpendicular to the plane and contain one electron per atom. The overlap between sp_z orbitals of neighbouring atoms creates π bonds, which account for graphene's electronic properties. The extent of this overlap is represented by the bond energy, also known as electron 'hopping' energy [20]. These orbitals are shown in Figure 3, with the π bond interaction energies between nearest-neighbours (t)_and next-nearest-neighbours (t') marked.

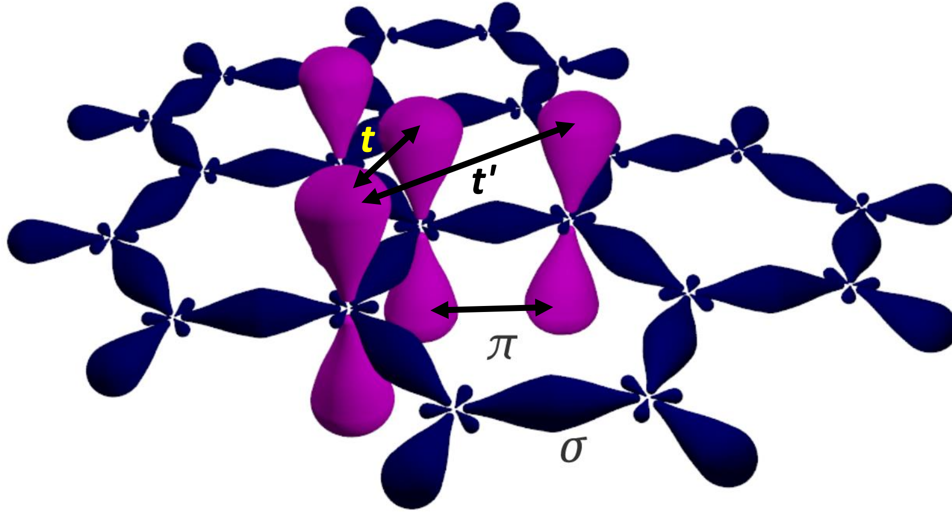

Figure 3: Bonds in graphene. σ bonds in the plane and π bonds out of the plane are shown, with the nearest- and next-nearest-neighbour overlaps corresponding to hopping energies t and t' shown. Adapted from [65].

Using the nearest and next-nearest neighbour interaction energies the dispersion relation is shown to be

$$E_{\pm}(\vec{\boldsymbol{k}}) = \pm t\sqrt{3 + f(\vec{\boldsymbol{k}})} - t' f(\vec{\boldsymbol{k}}),$$
$$f(\vec{\boldsymbol{k}}) = 2\cos(\sqrt{3}k_y a) + 4\cos\left(\frac{\sqrt{3}}{2}k_y a\right)\cos\left(\frac{3}{2}k_x a\right),$$ Equation 4

where $E_{\pm}$ is the band energy either above or below the Dirac point and $\vec{\boldsymbol{k}}$ is the wavevector. In the vicinity of the Dirac point, this dispersion can be simplified to give

$$E_{\pm}(\vec{\boldsymbol{k}}) = \pm v_f \hbar |\vec{\boldsymbol{k}} - \overrightarrow{\boldsymbol{k}_K}|,$$ Equation 5

where $\hbar$ is the reduced Planck constant, and $\overrightarrow{\boldsymbol{k}_K}$ is the wavevector at the K (or K') point. v_f denotes the Fermi velocity, defined as the velocity of carriers at the Fermi energy, which can depend on the graphene's condition and substrate, but is around $1 \times 10^6 \mathrm{m/s}$ [20]. This linear dispersion relation around these points can clearly be seen in Figure 4, adapted from [66], and holds true for energy scales even up to that of optical light [67].

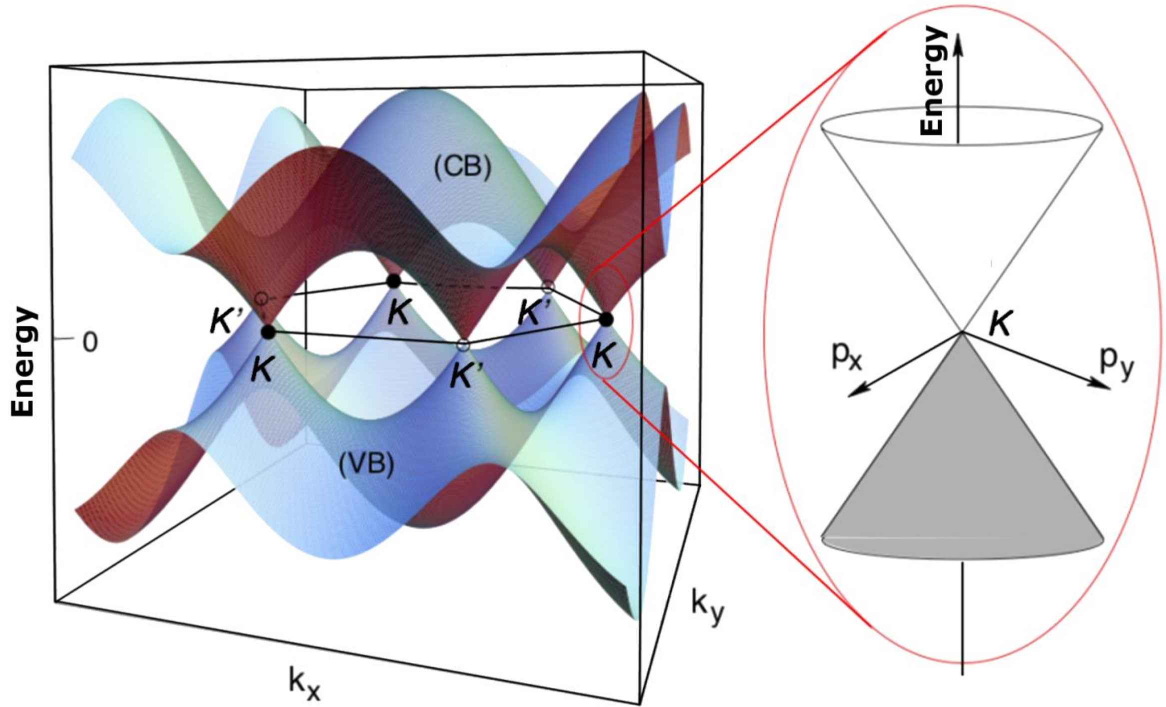

Figure 4: Energy-momentum dispersion relationship of graphene, with zoomed-in view showing its linear nature in the vicinity of the K and K' points, where the conduction band (CB) and valence band (VB) meet. Figure adapted from [66].

The dispersion relation given in Equation 5 has no dependence on electron effective mass in any way and there is no correlation between carrier momentum and velocity. It should be noted however that this is only true for an infinite graphene sheet, and finite device sizes and defects can cause localisation of carriers [20]. The approximation in the vicinity of the Dirac point giving this linear dispersion relation means electrons behave as massless particles, known as 'Dirac fermions'. This means that electrons in graphene act as relativistic particles with an effective 'speed of light' of v_f, and mimic many features of quantum electrodynamics [20, 56]. This extremely high Fermi velocity, roughly 1/300 of the speed of light, is nearly 10 times higher than that in 2D electron gasses formed in III-V semiconductor heterostructures at room temperature [68], allowing some types of device to operate much faster. As well as the lack of a bandgap, another consequence of graphene's linear dispersion is the small density of states at energies near the Dirac point,

$$\rho(E_\pm) = \frac{3\sqrt{3}a^2}{\hbar^2\pi}\frac{|E_\pm|}{v_f^2}, \qquad \text{Equation 6}$$

where $\rho(E_\pm)$ is the density of states per unit cell, which approaches 0 at the Dirac point [20]. An externally applied transverse electric field can tune the Fermi energy in graphene, resulting in an electrostatically tuneable carrier density. This is analogous to doping a semiconductor, and is hence known as electrostatic doping. Figure 5 shows how the carrier density varies with applied bias field (gate voltage). Due to graphene's nature as a bipolar material, it is possible to change the majority carrier between electrons and holes using the gate voltage. When graphene is biased such that the Fermi energy lies on the Dirac point, the density of electrons and holes is equal, as can be seen in Figure 5. This gate voltage will be referred to here as the neutrality point (NP), and for pristine graphene is $V_G = 0$ V.

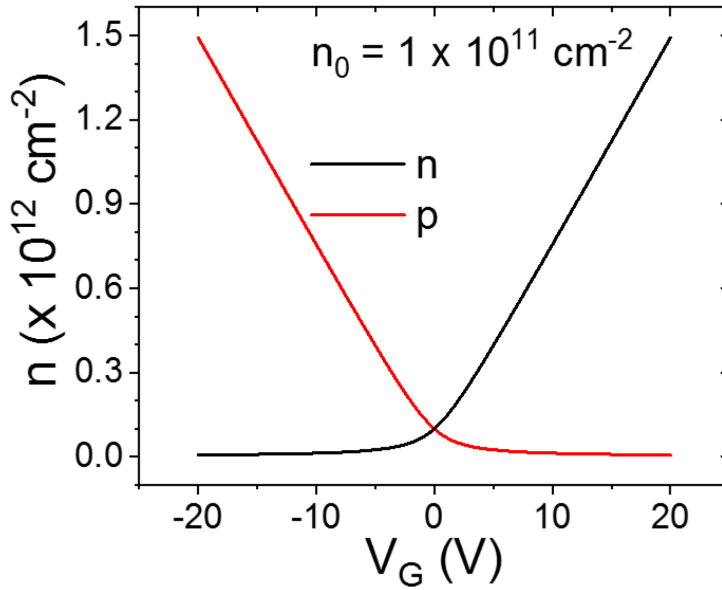

Figure 5: Calculated 2D carrier densities in graphene, for electrons (n) and holes (p), calculated from Equation 7 as a function of gate voltage. The gate capacitance is calculated assuming a Si/290 nm SiO_2 substrate, and the carrier neutrality point is assumed to be at $V_G = 0$ V. A typical value of $n_0 = 1 \times 10^{11} \text{cm}^{-2}$ is used, corresponding to the value of n and p at a gate voltage of $V_G = 0$ V. Reproduced from [69].

It has been shown [57] that the 2D carrier densities in graphene can be expressed as

$$n \approx \frac{1}{2}\left(-n_{cv} + \sqrt{n_{cv}^2 + 4n_0^2}\right),$$
$$p \approx \frac{1}{2}\left(n_{cv} + \sqrt{n_{cv}^2 + 4n_0^2}\right).$$
Equation 7

The value n_{cv} is the gate-induced carrier density, which depends on the back gate voltage V_G and gate dielectric properties, and n_0 is the carrier density at the NP. They are given by

$$n_{cv} = p - n = -\frac{C_G V_G}{e}, \qquad n_0 = \sqrt{\left(\frac{n^*}{2}\right)^2 + n_{th}^2},$$
Equation 8

where C_G is the gate dielectric capacitance density (also known as capacitance per unit area), $n_{th} = \frac{\pi}{6}\left(\frac{k_B T}{\hbar v_f}\right)^2$ is the thermal carrier density, and n^* is the carrier density caused by spatial inhomogeneities or 'charge puddles' over lengths in the order of 10s of nm [70]. Here, k_B is the Boltzmann constant and T is temperature. The values of n and p for an example piece of graphene are shown in Figure 5. At the NP we have $n_{cv} = 0$, so $n = p = n_0$. As gate voltage increases further away from the NP, one carrier density approaches becoming linear; the value of n_{cv}, while the other approaches 0.

One of graphene's most well-known and well-studied electronic properties is its carrier mobility, which is defined as the ratio between drift velocity and electric field. It has been demonstrated that mobilities far over $100{,}000\ \mathrm{cm^2/Vs}$ are easily achievable [50, 52], with values as high as $380{,}000\ \mathrm{cm^2/V}$ being demonstrated for suspended graphene [71]. The carrier mobility μ for a piece of graphene can be calculated from a transfer measurement on a Hall bar structure with low applied voltage, using

$$\mu = \frac{dg/dV_G}{C_G(W/L)},$$
Equation 9

where g is the conductance, and W, L are the hall bar width and length respectively. While 2D electron gasses formed by III-V semiconductor heterostructures can demonstrate even higher mobilities at low

temperatures [72], carrier mobilities in graphene are far less sensitive to increasing temperature, meaning that graphene has the highest room temperature mobilities of any material. This allows for the high current densities that are possible in graphene electronic devices [20], as well as meaning that devices which are limited by carrier transit time can operate at much higher frequencies. In electronics, the carrier mean free path λ_{mfp} is defined as the average distance travelled by a carrier in between collisions with the lattice, defects, or other carriers. In graphene, the elastic mean free path due to lattice and defect scattering (with the assumption of no carrier-carrier scattering) can be calculated from the carrier mobility:

$$\lambda_{mfp} = \frac{h}{2e}\mu\sqrt{\frac{n}{\pi}}, \qquad \text{Equation 10}$$

where h is the Planck constant, e is the electronic charge, and n is the 2D carrier density. The dependence on carrier density arises from the equation for Fermi wavevector, $k_f = \sqrt{\pi n}$. When λ_{mfp} is larger than the characteristic length scale of a device, then conduction in the device takes place in the ballistic regime. This means that in the absence of magnetic fields carriers move in straight lines, being only scattered by graphene edges or other boundaries, turning transport into a phenomenon which can be described as electron optics [73, 74].

When considering carrier transport in the ballistic regime in graphene, it is important to determine whether edge scattering is specular or diffuse. When graphene is etched, it is likely that the edge is comprised of both possible arrangements, armchair and zigzag. This causes the edge to be rough and makes edge scattering mostly diffusive, which has been confirmed by early experiments into ballistic transport in graphene [53, 75]. However, these edges also have dangling bonds, which when terminated cause strongly localised edge states [76, 77]. Under large applied fields, these states may trap carriers, causing Coulombic repulsion from the edges and allowing for specular scattering. This has

been confirmed by use of magnetic focusing of carriers [74] as well as by the successful operation of the ballistic rectifier in graphene [49].

2.1.4. Dispersive Conductivity

The electrical characteristics of graphene can be characterised by considering it as a 2D surface conductance, with a dispersive surface conductivity $\sigma(\omega)$, where $\omega = 2\pi f$ is angular frequency and f is frequency. With the assumption of an infinite pristine graphene sheet and non-interacting particles, using the Kubo formula this can be expressed [78] as

$$\sigma(\omega) = \frac{ie^2\left(\omega + \frac{i}{\tau}\right)}{\pi\hbar^2}\left[\frac{1}{\left(\omega + \frac{i}{\tau}\right)^2}\int_0^\infty E\left(\frac{\partial f_d(E)}{\partial E} - \frac{\partial f_d(-E)}{\partial E}\right)dE - \int_0^\infty \frac{f_d(-E) - f_d(E)}{\left(\omega + \frac{i}{\tau}\right)^2 - 4\left(\frac{E}{\hbar}\right)^2}\,dE\right], \qquad \text{Equation 11}$$

where τ is the time constant of carrier momentum relaxation and f_d is the Fermi-Dirac distribution, which itself depends on the chemical potential μ_c and temperature T. This is not the only method of modelling conduction in graphene; the Büttiker-Landauer formalism can also be used and leads to equivalent values in the limit of zero impurities or doping [20, 79]. The relaxation time can be calculated from the DC impurity-limited carrier mobility using Equation 12, and hence can be estimated from simple DC electrical measurements:

$$\tau \cong \frac{\mu_c \mu}{e\, v_f^2}, \qquad \text{Equation 12}$$

The Fermi energy E_f can be considered equivalent to the chemical potential under most conditions, and can be calculated by substituting the Fermi wavevector $k_f = \sqrt{\pi n}$ (relative to the Dirac point) into the approximate graphene dispersion relation shown in Equation 5, giving

$$E_f = \hbar v_f \sqrt{\pi n}. \qquad \text{Equation 13}$$

In Equation 11, the first term arises due to scattering within the energy band which contains the Fermi energy (the intraband term), whereas the second represents scattering between the two bands (the interband term). Throughout most of the THz range interband contributions can be ignored, because they are suppressed by Pauli exclusion for energies $\hbar\omega < 2|\mu_c|$ [36], which holds true into the 10s of THz for reasonable values of μ_c. Evaluating the first term of Equation 11, the dispersive 2D conductivity of an infinite graphene sheet can be approximated as [80]

$$\sigma(\omega) = \frac{2e^2 k_B T}{\pi\hbar^2} \frac{i}{\omega + {}^{i}/_{\tau}} \ln\left(2\cosh\left(\frac{\mu_c}{2k_B T}\right)\right). \qquad \text{Equation 14}$$

Two main material parameters affect the conductivity of a graphene sample, chemical potential and relaxation time. Figure 6 shows the real and imaginary components of graphene's sheet conductivity in the THz range as a function of frequency, taking only the intraband contribution as given in Equation 14. Realistic values of the relaxation time and chemical potential for graphene have been used, with $\tau = 0.5$ ps and $\mu_c = 0.2$ eV [78, 80, 81].

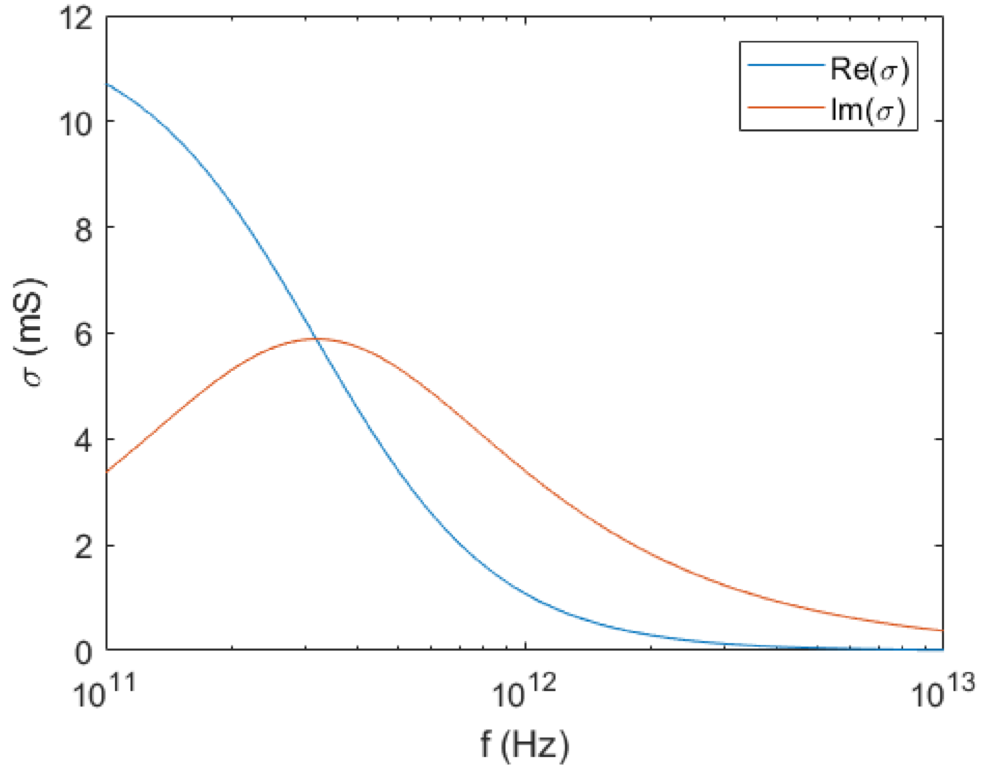

Figure 6: Dispersive conductivity of graphene, calculated using Equation 14 with $\tau = 0.5$ ps and $\mu_c = 0.2$ eV.

At low frequencies, the imaginary component of conductivity become negligible and the real component becomes constant, given by $e^2\mu_c\tau/(\pi\hbar^2)$. In the THz region however, the imaginary component rises as the real component falls, crossing when the product $\omega\tau = 1$ and each has half the value of the low frequency conductivity [80]. At higher frequencies, the conductivity decreases due to Ohmic loss, and at frequencies beyond the THz interband conductivity contributions start to play a role.

2.1.5. Plasmonics

Plasmonics deals with the collective motion of charge carriers in a gas (such as electrons in a metal). The quasiparticle that arises from this plasma oscillation is known as a plasmon, and plasmons play a large role in determining the optical properties of materials such as metals and semiconductors [82]. In particular, research has been focused on surface plasmon polaritons (SPPs), which are waves that travel along a conductor-dielectric boundary, for example a metal's surface in air. The manipulation of

these SPPs has drawn a lot of interest as a potential means to achieve, for example, subwavelength photonic systems and devices, as well as metamaterials for a wide range of applications [82].

A sheet of graphene behaves like a 2D gas of electrons, and as such is also capable of supporting SPPs. Unlike metals, the carrier density in graphene can be easily tuned by electrostatic or chemical doping, allowing for the properties of these SPPs to also be tuned. Because graphene's conductivity has a large imaginary component in the THz region [83], graphene's plasmonic properties have helped make it a promising material for the development of THz electronic and optoelectronic devices. While strictly speaking the quasiparticle under consideration here is the surface plasmon polariton, these seem to be commonly also referred to in the literature as 'surface plasmons' (SPs) or 'plasmons' [36, 37, 81]. On an infinite sheet of monolayer graphene embedded between two dielectrics (of relative permittivities ε_{r1} and ε_{r2}), SPs are transverse magnetic (TM) modes of electromagnetic wave, alongside charge-density oscillations on the graphene sheet [37]. Solving Maxwell's equations under these conditions [84] gives the following result for the plasmon dispersion relation.

$$\frac{\varepsilon_{r1}}{\sqrt{k_{SP}^2 - \varepsilon_{r1} k_0^2}} + \frac{\varepsilon_{r2}}{\sqrt{k_{SP}^2 - \varepsilon_{r2} k_0^2}} = -i \frac{\sigma(\omega)}{\omega \varepsilon_0}, \qquad \text{Equation 15}$$

where k_{SP} is the plasmon wavenumber, k_0 is the free space wavenumber (given by ω/c), and ε_0 is the vacuum permittivity. The most common case to consider is when the graphene lies on a dielectric substrate, with the other side being exposed to either air or vacuum, with dielectric constant of 1. Hence from here $\varepsilon_{r1} \equiv \varepsilon_r$ and $\varepsilon_{r2} = 1$ will be used. Hence, Equation 15 becomes

$$\frac{\varepsilon_r}{\sqrt{k_{SP}^2 - \varepsilon_r k_0^2}} + \frac{1}{\sqrt{k_{SP}^2 - k_0^2}} = -i \frac{\sigma(\omega)}{\omega \varepsilon_0}. \qquad \text{Equation 16}$$

In the region where $k_{SP} \gg k_0$, referred to in [84] as the 'nonretarded regime', a first order approximation means Equation 16 is greatly simplified [85] to

$$k_{SP} \cong i\varepsilon_0(\varepsilon_r + 1)\frac{\omega}{\sigma(\omega)}. \qquad \text{Equation 17}$$

Substituting in Equation 14, the dispersion relation in this regime becomes

$$k_{SP} \cong A\, k_0\left(\omega + \frac{i}{\tau}\right), \qquad \text{Equation 18}$$

where A is a frequency-independent constant given by $A = \frac{\pi\hbar^2(\varepsilon_r+1)}{2Z_0 e^2 k_B T \ln\left(2\, cosh\left(\frac{\mu_c}{2\, k_B T}\right)\right)}$ with Z_0 being the free space impedance, $Z_0 \equiv {}^{1}/_{\varepsilon_0 c} \cong 376.7\ \Omega$. Because $k_0 = \omega/c$, Equation 18 shows a quadratic relationship between plasmon wavenumber and frequency, as characteristic of 2D electron gasses [85, 86]. It is also noted that the plasmon wavenumber can be several orders of magnitude larger than k_0, meaning wavelengths much smaller than those of free space waves, and strong wave confinement [37]. Chapter 6 contains simulations of THz-frequency graphene antennas. Since graphene hosts plasmonic resonances in this frequency region, it will be useful to be able to compare antenna resonant frequencies to plasmon wavelengths. Therefore an equation for the plasmon wavelength as a function of frequency is needed. The SP wavelength is then given by

$$\lambda_{SP} \equiv \frac{2\pi}{Re(k_{SP})} \cong \frac{\lambda_0}{A\omega}, \qquad \text{Equation 19}$$

where λ_0 is the free space wavelength. Therefore, this first order approximation predicts that plasmon wavelength depends on the inverse square of frequency.

2.2. THz Radiation

2.2.1. Overview and Applications

Historically, the distinction between radiation of different frequency regions is due to differing methods of generation and detection. Electronic frequencies, i.e. GHz and below, are generated by movement of electrons in a wire or antenna, while higher frequencies are referred to as optical as they are typically generated by quantum energy level or bandgap transitions of electrons or by black body radiation. Between these two regions is radiation of frequencies within an order of magnitude of 1 THz. This region, generally considered to be between 0.1-0.3 THz and 10-30 THz, has often been called the 'THz gap' because technologies for detection and emission in this band tend to be far less efficient than on either side [21]. THz radiation has a huge array of potential applications over a range of fields. These range from sensing and scanning in medicine and in security [24] and medical imaging [26], to telecommunications as well as a wide range of scientific uses [22, 27].

In medicine, there is considerable interest towards using THz radiation for imaging. For example, it has been demonstrated effective at imaging of skin cancers [87].. Interest towards THz imaging in medicine was at first due to the strong absorption in water, which allows for changes in hydration of tissues to be detected [87, 88]. Since then, it has also been demonstrated applicable to imaging of tissue structure, independent of water content [89]. In security applications, THz radiation allows for detection of concealed weapons, as well as a wide range of explosives and biological substances. Because many fabrics and plastics are transparent to THz radiation, sensing systems are able to detect dangerous materials such as metal weapons [24, 90].

Aside from imaging, THz spectroscopy is also of considerable use in molecular analysis. Many biomolecules and pharmaceuticals exhibit intra- and intermolecular vibrations in the THz range, and as such THz radiation allows for identification of these molecules and their environment, both within

packaged pharmaceuticals and within cells [22]. In addition to this, the characteristic THz response observed for many organic molecules extends to many security-sensitive substances, for example illicit drugs or organic explosives [24, 27]. This means that THz radiation has applications in security scanning and imaging, with shoe scanners and full-body scanners already in use in airports [22].

Telecommunications applications of THz radiation are attractive due to the much higher data capacity such systems would support [22, 91]. THz frequencies suffer from high atmospheric attenuation although there are many frequency windows that exist, for example ~0.8-0.9 THz and ~1.5 THz [92]. However, communication ranges are typically limited to $< 100\ \mathrm{m}$ [91]. This makes THz frequencies more suitable for short-range, indoor, systems [22]. Regardless, there is still a huge potential market for communications at THz frequency. The main current challenges are the lack of compact sources with high output power at reasonable efficiency [91], as well as low-noise detectors with fast response times [22].

Aside from the applications outlined above, there is an ever-evolving range of scientific applications for THz detection and imaging. This includes astronomy [93], as well as many other spectroscopic applications [94–96]. Key to many applications is the development of terahertz time-domain spectroscopy (THz-TDS), which will be briefly explained in Section 2.2.3.

2.2.2. Generation Techniques

Many sources of THz radiation have been under investigation and development in recent years. The vast majority of contemporary THz sources are optics-based; i.e. they fundamentally involve creating and inducing low-energy electron transitions. This is often found to be difficult, as the photon energy is below the level of thermal fluctuations. The simplest form of THz emitter is black body radiation, of which typical sources include globars and mercury lamps [97]. Black body radiation is mainly comprised of IR and visible light, however extends into the THz region. Due to the nature of black body radiation,

increasing temperature increases the spectral intensity across the entire spectrum. Therefore, despite the massively increased intensity at higher frequencies it is beneficial for a THz source to use as high a source temperature as possible, with sufficient filtering.

Alternatively, coherent THz radiation can be created by photomixing, i.e. difference-frequency generation from two lasers of much higher frequency in a nonlinear medium. This can produce coherent THz radiation, continuous or pulsed, over a wide frequency range [98]. Using tuneable source lasers, this can also produce a freely tuneable THz beam. These systems can be relatively compact unlike many THz sources; however they tend to suffer from relatively low THz powers.

For many years gas lasers have been constructed in the far-infrared region, sometimes extending into the THz [97, 99], however constructing semiconductor lasers for the THz region is difficult because of the small bandgap required. A device structure that avoids this problem is the quantum cascade laser (QCL), which uses repeating patterns of quantum well heterostructures in order to create subband transitions of the desired energy. When a bias is then applied across the structure, a population inversion is created. Electrons undergo intersubband transitions in the quantum wells, then tunnel through narrow barriers into the next well to repeat the process [28]. This mode of operation allows the transition energy to be tuned by the quantum well width, meaning it can be far less than the bandgap and hence allows for THz emission. While QCLs can produce relatively intense coherent THz radiation, a major challenge to overcome is room-temperature operation of these devices [97, 100].

There are several types of vacuum-electric THz sources such as Synchrotrons, Gyrotrons, and free-electron lasers. While they have different modes of operation, they all use accelerated free electrons in magnetic fields to produce radiation in or around the THz region. While they can produce extremely high power coherent radiation, they are extremely bulky and consume large amounts of power [25, 101, 102].

In THz photoconductive antennas, a femtosecond optical pulse is incident onto the gap of a THz dipole antenna on a photoconductive substrate. Generated carriers are attracted into the antenna arms by a DC bias, where they drive the antenna and hence generate a THz pulse [103]. Photoconductive antennas are commonly used in THz-TDS, where the femtosecond optical laser pulse is also used to measure the time-domain signal at the detector. Other sources of THz radiation which rely on excitation by laser pulses include air plasma generation and relativistic laser-plasma generation. These use laser pulses ionise molecules and cause them to emit intense THz radiation. While these techniques can produce extremely high energy THz pulses, they require high power pump lasers and suffer from poor stability and low repetition rate [25].

2.2.3. Detection Techniques

There are several physical mechanisms which are used in THz detectors. In [35] these are sorted into 5 categories. Here will be given an outline of each, with some brief examples.

An important property of a detector system is coherency. Coherent radiation is formed of photons of the same frequency and direction in phase with each other, and coherent detectors are sensitive to the phase of incident photons. Some detectors are non-coherent, being sensitive only to the frequency (energy) and power of radiation. Some detection techniques require incident radiation to be coherent, however the sensitivity to phase allows more information regarding the incident radiation to be obtained [35].

The first category is detectors which rely on the ability of THz radiation to heat a surface or a substance. Detectors that use this sort of mechanism are usually common to detection of IR radiation, and it is a relatively mature category of detectors. It includes some of the most commonly used non-coherent detectors: Golay cells and bolometers. In a Golay cell, THz radiation heats a small amount of sealed gas. As it warms, the gas expands and deforms a membrane, which is then detected using

deflection of light or, for more precision, tunnelling current. They are generally capable of operating over wide frequency ranges with high sensitivity, with the main limiting factors being the extremely slow response time in the 10s of ms and the high sensitivity to vibration [35]. Bolometers detect the heat caused by incident radiation by measuring the change in resistance of, typically, a heavily doped semiconductor. They generally operate at low temperatures to increase sensitivity and reduce noise, where they can achieve extremely high responsivities of $10^7 \mathrm{V/W}$ and low noise equivalent powers of $10^{-14}\ \mathrm{W/Hz^{1/2}}$[35]. Room temperature bolometers have also been demonstrated, albeit with much worse performance [104]. Large arrays of room-temperature microbolometers are commercially available and marketed as THz cameras, with decent refresh rate of 20-30Hz but poor performance [105, 106]. The main downside, aside from the general need to cool to 4.2 K or below, is the slow response time, similar to that of Golay cells. Other detectors in this category include thermocouples and thermopiles, as well as pyroelectric detectors. However, they tend to offer similar or larger disadvantages than Golay cells and Bolometers, with the slow response times being perhaps the largest.

The third category is using the incident THz radiation to excite electrons to induce an electron transition between states or across a potential barrier. This includes diodes such as Schottky barrier diodes, as well as photodetectors. In diodes, incident photons excite electrons over the potential barrier, producing measureable current. They can operate at room temperature, and due to the electronic mode of operation they offer very fast response time [107], however they tend to have narrowband response. Photodetectors, in which the incident THz photon excites an electron to make an energy transition, are not very commonly used due to the typical need for cooling and narrowband response [35].

Fourth is detection via mixing with radiation of other frequencies. An incident continuous-wave THz signal is mixed with a reference signal in a nonlinear medium, creating components of the sum and

difference frequencies. These new frequencies are generally in much easier regions such as microwave, and are detected by a variety of methods. Due to the sensitivity to the reference signal these detectors tend to be narrow-band, however can be very sensitive for known frequencies.

The fifth category detailed in [35] is sampling of THz field with ultrashort optical pulses. This makes use of the fact that a THz field in an electro-optic material produces variations on the refractive index. Then, an ultrashort visible laser can be used to sample the instantaneous field. This is commonly used in THz-TDS. THz-TDS is a spectroscopic technique that uses time-domain measurements of a short THz pulse to measure the spectral THz response of a sample, in terms of changes to the pulse's amplitude and phase. An ultrashort optical laser pulse is split, with one beam being used to excite a THz emitter, such as a photoconductive antenna. The produced THz beam is guided and focused onto the sample and then onto the detector. At the detector, the same ultrafast laser, with known path difference, is sensitive to the instantaneous field of the THz pulse. With many repetitions the full time-domain THz signal is extracted, and the frequency domain response can be calculated using the Fourier transform of the sampled data [108]. THz-TDS is used for a wide range of applications, thanks to its ability to measure both the amplitude and phase of the signal. It allows for contact-free measurement of various chemicals, as well as the properties of materials and (opto-)electronic devices [108].

A method of THz detection not considered in [35] is the use of rectennas, by which free space THz radiation is transformed into THz field oscillation across a rectifier, which produces an output voltage. These are discussed in Section 2.3.

2.3. Rectifiers and Rectennas

A rectifier is an electrical device which converts a portion of an incoming AC signal into a DC voltage/current. The simplest form of rectifier is perhaps the diode detector, which consists of a single diode and some accompanying components for filtering and smoothing as shown in Figure 7(a) [109].

An AC signal is supplied on the left side of the diagram, with an output DC signal (with some rippling) being produced on the right. In the diagram shown here, the capacitor and load form a low-pass filter, ensuring that the input AC signal is not transferred to the load. They are commonly used in RF circuits as envelope detectors. There are several important parameters for a rectifier, including responsivity (sometimes known as sensitivity) and noise-equivalent power, which are described later in this section.

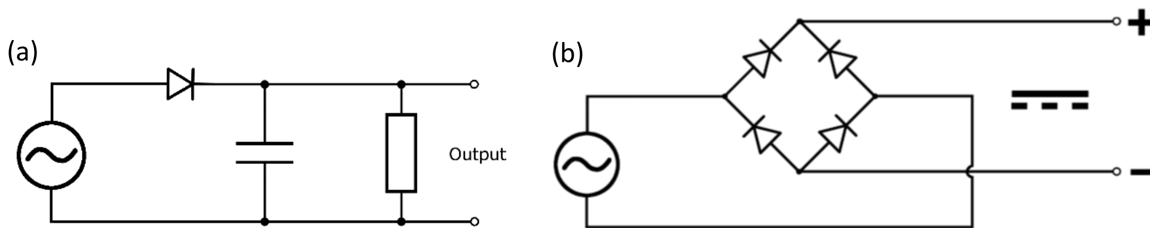

Figure 7: Electrical diagram of (a) a diode detector circuit and (b) a bridge rectifier.

While a single diode can be used as a ‘half-wave’ rectifier, with a maximum efficiency of 50%, using four diodes a bridge rectifier can be constructed as shown in Figure 7(b), which is capable of rectifying a full AC signal. In practice, the full signal is never converted, because the finite threshold voltage of conventional diodes means that the portion of the wave below the threshold is lost, and the output is also not a constant DC voltage, with ‘rippling’ amplitude. In the past, the diodes used have been mercury-arc valves or vacuum tubes, which were replaced by the advent of silicon electronics and semiconductor diodes. This allowed diodes and rectifiers to be greatly reduced in size, and now these devices benefit from the massive and extremely well-developed silicon-based electronics infrastructure [110]. However, these devices are limited in speed by the cut-off frequency of the diodes used, due to their parasitic capacitance, and as previously mentioned the finite threshold voltage results in a large loss in efficiency. The highest-frequency rectifier circuits currently available mostly use Schottky diodes.

A rectenna is, as the name would suggest, a rectifying antenna. These are typically constructed by coupling an antenna to a rectifier, such that radiation incident on the antenna is converted into an AC

signal of the same frequency, which is then converted into a DC output. Rectennas are commonly used for a wide array of technologies at frequencies from radio waves up to microwave, however at frequencies above the MHz and into the GHz, a larger portion of the power becomes reflected due to impedance mismatch as the cut-off frequency of the circuit is approached. This is taken into account by Equation 21. While it is straightforward to construct antennas for any frequency up to and beyond THz, this loss in efficiency is due to the limited operational speed of conventional rectifiers. Another important factor for the efficiency of a rectenna is impedance matching between the antenna and the rectifier. In order for maximum power to be transmitted to the rectifier,

$$Z_L = Z_S, \quad \text{Equation 20}$$

where Z_L and Z_S are the load (rectifier) and source (antenna) impedances, is required [111]. High frequency rectifiers, such as the ones discussed later on, tend to have large input resistance, making frequency matching with a (typically 50 Ω) antenna difficult. This means a large portion of the incident power is reflected by the rectifier, causing much reduced efficiency.

An important figure of merit for a detector is responsivity. Responsivity is defined as the output signal of a detector divided by the input power and has units of either V/W or A/W. Depending on the mode of operation and the specific application of a rectifier either a voltage signal or a current signal can be produced, meaning that the correct form of responsivity must be chosen Because the rectifiers considered here all produce a voltage output, voltage responsivity (open-circuit voltage responsivity) will be considered here, $\mathcal{R} = \frac{\text{output voltage}}{\text{input power}}$. When a rectifier with an *intrinsic* responsivity $\mathcal{R}$ is connected to a 50 Ω source, the *extrinsic* responsivity must be calculated, which takes into account power losses due to impedance mismatch and hence more closely represents the device's performance in most applications. In general, this is given by

$$\mathcal{R}_{50\Omega} = \mathcal{R}(1 - \mathrm{S}_{11}^2), \quad \text{Equation 21}$$

where $S_{11} = \frac{Z_L - Z_S}{Z_L + Z_S}$ is the reflection coefficient between the source and the load. When the load has impedance much larger than 50 Ω, and when measured at low frequencies, this can be simplified to give

$$\mathcal{R}_{50\Omega} = 4\mathcal{R}\frac{50\ \Omega}{Z_L}. \qquad \text{Equation 22}$$

Another figure of merit is the noise equivalent power (NEP), defined as

$$NEP = \frac{S_V^{1/2}}{\mathcal{R}}, \qquad \text{Equation 23}$$

where S_V is the voltage noise spectral density (for voltage-output detectors). It gives the minimum signal power which gives an output detectable above the detector's noise level, and as such is desired to be as small as possible.

For an antenna the factor S_{11} is important, because it signifies the fraction of power delivered to the antenna which is reflected. It is also sometimes known as the antenna return loss. There are several other important parameters to consider for an antenna. Input impedance is defined as electrical impedance as seen from the input feed. An antenna's radiation resistance represents the contribution to total impedance due to radiation from the antenna, and is calculated from the injected current and radiated current using $Radiation\ resistnace = \frac{Power\ radiated}{(Radiating\ current)^2}$. It must be differentiated from the antenna's loss resistance, which is calculated similarly using instead the power that is dissipated as heat and not radiated. Another antenna property is its radiation pattern, which describes the directional dependence of radiated field. Gain is another parameter, which is given by

$$G_A = \epsilon_A D, \qquad \text{Equation 24}$$

where G_A is antenna gain, ϵ_A is efficiency (calculated from input power and radiated power), and D is directivity. Directivity is calculated from the radiation pattern, as the ratio between highest radiation

intensity in any given direction to the average intensity over the sphere. Gain is usually expressed in decibels, with units referred to as decibels-isotropic (dBi).

2.4. Graphene Nanodevices

As described above, there is considerable interest in development of rectifiers and detectors devices that can operate at THz frequencies [112–116]. . For ultrafast electronic devices high carrier mobility is key for allowing fast response times and high frequency operation and therefore graphene, with its uniquely high room temperature mobilities, has been an extremely attractive material [117, 118]. Unfortunately the lack of a bandgap hinders most applications, in particular FETs, giving large reverse currents and low on/off ratios and gain [117, 118].

Unlike most graphene electronic devices, there exist several concepts for geometry-based devices which have no need of a bandgap to operate. These use effects that arise entirely from device geometry to produce the desired effect, usually some sort of carrier rectification. In fact, it has been shown that any device which uses ballistic transport in an asymmetric 2D channel will produce a non-zero rectified output [119]. There have been investigations into devices such as ‘geometric diodes’ [120, 121], 3-terminal junction rectifiers [122], as well as the ballistic rectifiers and self-switching diodes which are investigated here [49–51, 123, 124].

2.4.1. Ballistic Rectifiers

Structure and Theory of Operation

The ballistic rectifier is a four terminal planar electronic device which converts an input current, regardless of direction, into a DC bias. It does this by making use of quantum point contacts (QPCs), ballistic transport, and specular edge scattering in graphene structures, making carriers which pass through the source or drain QPC scatter preferentially towards the lower contact. This causes a DC bias

to build up between the upper and lower contacts. Due to relying on ballistic transport, the BR must be constructed in a material with an extremely high carrier mobility, giving a long mean free path of the same order of magnitude as or larger than the device geometry. Figure 8 shows two designs for ballistic rectifier which have previously been demonstrated in the literature [42, 49, 50, 125], with the typical carrier trajectories marked with arrows. The first design uses a triangular etched 'anti-dot' scattering centre to re-direct carriers, while the second instead uses angled QPCs with angled sidewalls. Because of this, it is expected that the source-drain (S-D) resistance is larger for the left design, because the scattering centre blocks direct transmission of carriers and increases the minimum possible S-D distance.

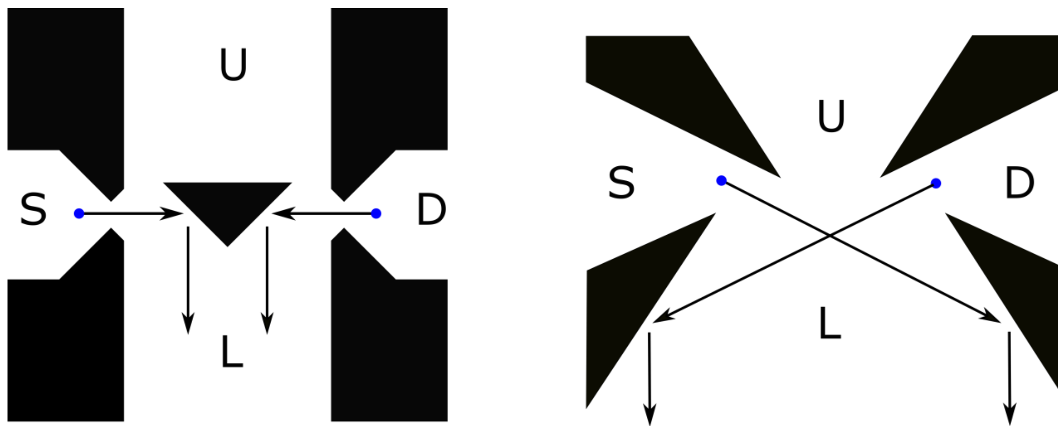

Figure 8: Two previously developed designs of ballistic rectifier. Black regions denote where the conducting material (semiconductor 2D electron gas or graphene) is etched away. Both use quantum point contacts with ballistic transport to redirect carriers, both electrons and holes, preferentially towards the lower (L) contact. Input contacts are labelled S and D for source and drain, and outputs are U and L for upper and lower. (Designs not to scale)

This model of ballistic transport with specular scattering is known as the 'billiard ball' model [77, 126] and is the basis for the BR's theory of operation. However, there are several complicating factors. Firstly, as discussed in Section 2.1.3, edge scattering in graphene is complicated and not fully specular. In addition, hydrodynamic effects further complicate ballistic transport in graphene. A more rigorous description of the ballistic rectifier's operational mechanism is detailed later in this section as

previously derived for semiconductor 2D electron gas BRs [127], and is derived here for the graphene ballistic rectifier in Section 4.1.

History

The ballistic rectifier was first proposed and tested by A. Song et al. in 1998 [42]. It was fabricated from a modulation-doped GaAs-AlGaAs heterostructure, which produced a 2D electron gas. Measured at 4.2 K, it produces an output voltage V_{LU} which has the same sign regardless of the direction of DC input current, and was demonstrated to work up to 77 K. Following this, they were demonstrated in a InGaAs/InP quantum well 2D electron gas, demonstrating room temperature operation and rectification at frequencies up to 50 GHz, with a rectification responsivity of roughly 3.5 mV/mW [45]. However, the mobility of 2D electron gasses like these depends strongly on temperature, in this example dropping from $450{,}000\ \mathrm{cm^2/Vs}$ at 0.3 K to $12{,}000\ \mathrm{cm^2/Vs}$ at room temperature. For this reason, graphene was considered as a natural choice for improvement of room-temperature performance, because graphene's mobility does not depend as strongly on temperature.

The first graphene ballistic rectifiers were demonstrated with graphene on bare SiO_2 [49]. It is here that the second of the two designs shown in Figure 8 is first tested. Due to graphene being a bipolar material, with electrostatically tuneable carrier densities, both positive and negative output voltages are observed depending on the gate voltage and hence on the majority carrier and carrier density. At an input frequency of 1 kHz, the device demonstrated a responsivity of 67 mV/mW, with a slightly higher value of 111 mV/mW obtained from DC measurements, and an NEP of $\sim 10^{-9}\ \mathrm{W/Hz^{1/2}}$. However, this device suffered from having SiO_2 as a substrate, which is known to greatly reduce mobility. Using hBN-encapsulated graphene, a device with a room temperature carrier mobility $\sim 200{,}000\ \mathrm{cm^2/Vs}$ was constructed, giving a mean free path of well over $1\ \mu\mathrm{m}$ [50]. This allowed the intrinsic responsivity to reach 23,000 V/W, with an extremely low NEP of $0.64\ \mathrm{pW/Hz^{1/2}}$. Using high-

mobility encapsulated graphene, a GBR was then demonstrated as a THz rectifier, shown to operate at 0.45 THz and then used to image an optically opaque object at 0.685 THz [47].

Büttiker-Landauer Theory

The Büttiker-Landauer formulisation describes conduction through a nanoscale device, by considering the transmission probabilities between probes for carriers at the Fermi level [79]. It is applicable when conduction is in the ballistic regime, i.e. where the carrier mean free path is longer than the characteristic device length [79, 128–130]. Considering a semiconductor 2D electron gas ballistic rectifier with a triangular scattering centre, in [127] A. Song uses the device geometry to derive the four-terminal resistance. This will not be reproduced here, however a similar derivation will be performed in Section 4.1, instead considering graphene devices. As part of this, this derivation will also consider the effect of the presence of both electrons and holes in the device.

2.4.2. Self-Switching Diodes

Structure and Theory of Operation

The self-switching diode (SSD) is a planar diode, consisting of a conducting channel with insulating trenches on either side. This allows forward and reverse bias to increase and decrease respectively the channel conductance. It is similar in design to a side-gated transistor, except with both side gates connected to the source (or drain), such that it switches itself on/off depending on the applied bias. It achieves switching without needing any doping junctions or barrier structures, instead relying purely on electrostatic effects arising from its geometry [43, 131]. The effective direction of the diode respective to its geometry depends on the majority carrier. When electrons are the majority carrier, forward bias causes the areas either side of the channel to become positively charged, increasing the channel's conductivity, while reverse bias causes electrons to build up on either side of the channel,

decreasing its conductivity. The opposite occurs when holes are the majority carrier. This is shown for both cases in Figure 9.

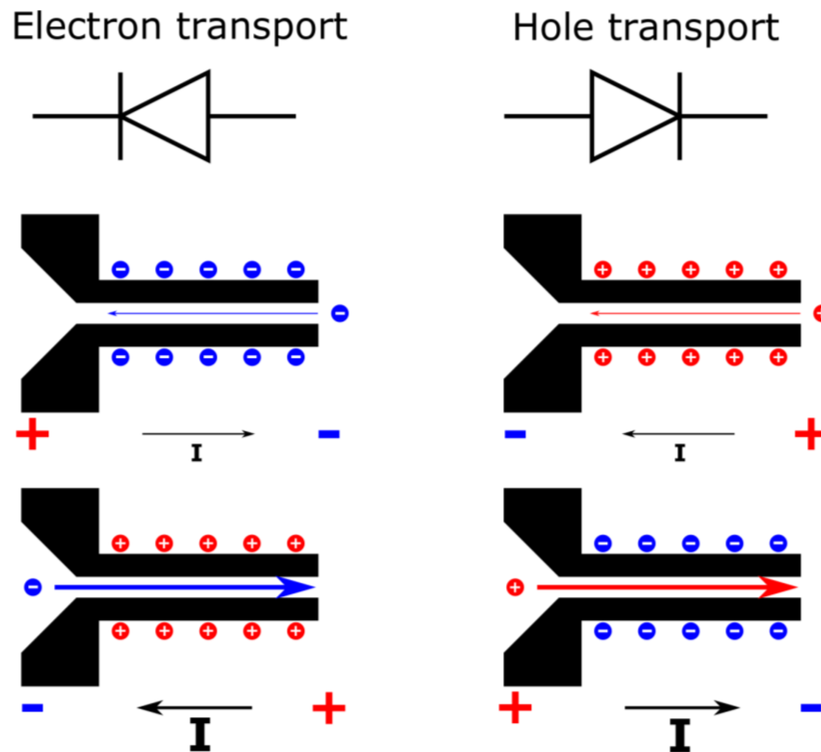

Figure 9: Structure and operational principle of a self-switching diode. Two cases are shown; in materials where electrons (left) or holes (right) are the majority carrier. The diode symbols at the top show the effective electrical direction of the diode in both cases. The device schematics below show the cases where the diode is forward (top) or reverse (bottom) biased.

In semiconductor SSDs, when the diode is reverse biased the charge buildup causes the depletion region around the trenches to grow, cutting off the channel. This means that reverse currents are extremely low. In graphene however, the lack of a bandgap means that no such depletion region exists, so it is not possible to fully switch off the channel. Because of graphene's minimum conductivity, reverse currents in graphene SSDs (GSSDs) are much larger than in semiconductor SSDs. However the presence of a threshold voltage in high frequency rectifiers is a major downside, as discussed in Section 2.3. Combined with its extremely high carrier velocities and naturally 2D nature, this makes graphene intrinsically suitable for fabrication of SSDs, as such device will have no threshold voltage [132].

The current passed by a GSSD can be found by considering the device to be a FET with the gate and drain connected, as mentioned above. This is shown schematically in Figure 10.

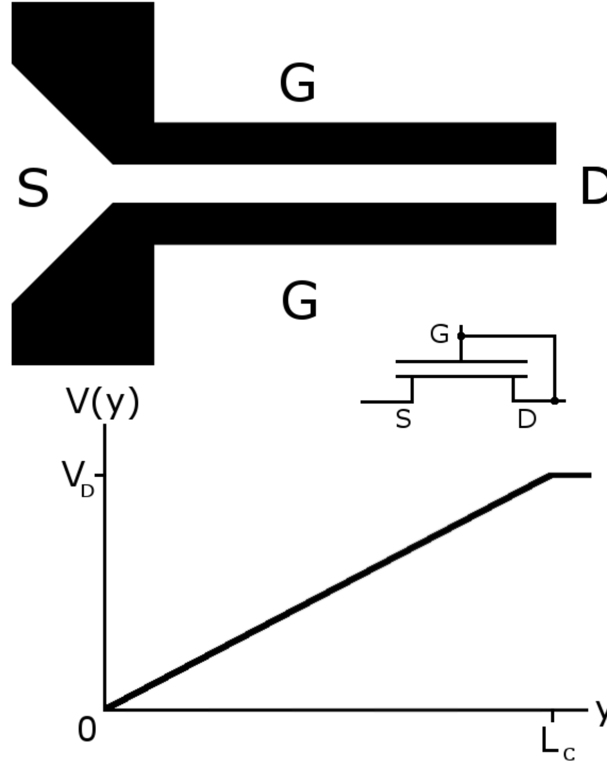

Figure 10: Schematic of a self-switching diode, showing how it can be considered a side-gated transistor with gate shorted to drain. The channel voltage as a function of distance is also shown.

Therefore, the current I_{GSSD} can be expressed using the Sichman-Hodges model [132, 133], and is given by

$$I_{GSSD} = W_c e n_c v_d, \qquad \text{Equation 25}$$

where W_c is the channel width, n_c is the 2D carrier density in the channel, and v_d is the carrier drift velocity. The 2D carrier density can be expressed as a function of back gate voltage, shown in Equation 26. It is important to distinguish between the effects of the back gate (usually the Si/SiO_2 substrate) and the side gate, which is the term usually denoted as V_G in this model but here is equal to V_D. Hence there is an additional term due to the capacitance of the back gate.

$$n_c = \frac{C_G V_A}{e} + \frac{C_t}{t_c e}\left(V_D - V(y)\right), \quad \text{Equation 26}$$

where C_G is back gate capacitance, C_t is the channel side gate capacitance per unit *length*, t_c is the channel thickness, V_A is the back gate voltage – neutrality point offset, V_D is the applied drain voltage, and $V(y)$ is the channel voltage as a function of distance along the channel as shown in Figure 10. In the low-field region, the drift velocity in the channel can be expressed as

$$v_d = \mu \frac{dV(y)}{dy}, \quad \text{Equation 27}$$

where μ is the carrier mobility. It must be noted that when the field becomes larger, velocity saturation can occur, destroying this simple relationship. This may manifest as variation of carrier mobility with field. Integrating along the channel, it is found that

$$I_{GSSD} = \mu \frac{W_c}{L_c}\left(C_G V_A V_D + \frac{C_t}{t_c}\frac{V_D^2}{2}\right), \quad \text{Equation 28}$$

Where W_c and L_c are the channel width and length. This equation appears similar to that derived for a typical FET using the Sichman-Hodges model, however except with no threshold voltage and the differing capacitance values. This predicts a quadratic relationship between applied voltage and current, with a large linear term that depends strongly on back gate voltage.

History

The SSD was first proposed and fabricated in 2003 using both InGaAs/InP and InGaAs/InAlAs 2D electron gasses, demonstrating its rectification ability both at low temperatures and at room temperature [43]. The weak dependence of output on temperature demonstrated that the device does not rely on carrier mobilities, unlike the ballistic rectifier which uses ballistic transport. Shortly afterwards, the SSD was simulated to operate at THz frequencies [134], which was confirmed in 2011 using a GaAs/AlGaAs 2D electron gas [135]. Operating a single SSD as a rectifier, it demonstrated a

responsivity of up to $300\ \mathrm{mV/mW}$ at room temperature at a frequency of $1.5\ \mathrm{THz}$, with a DC bias current of $0.1\ \mu\mathrm{A}$. As well as these, SSDs have also been demonstrated in a variety of other material systems, such as GaN [136], zinc-oxide thin films [137], and organic polymer [138]. The GSSD was first described in 2013 by Al-Dirini et al. [139, 140], who use quantum simulations of devices with channels only a few atoms wide. This makes the channel a graphene nanoribbon, which opens up a bandgap and hence in theory would allow for the channel to be fully switched off. However, the simulated reverse current was still of the same order of magnitude as the forward, and the bandgap caused a threshold voltage of around $0.4\ \mathrm{V}$. Another major downside is that fabrication of a device on this scale would be extremely difficult. Electron beam lithography is extremely difficult to perform at resolutions down to $1\ \mathrm{nm}$ [141], which is still too large for these devices [140]. The first GSSD was fabricated using graphene grown via hydrogen-intercalated epitaxial graphene on SiC, at far more reasonable sizes, with $\sim 1\ \mu\mathrm{m}$ long channels [51]. Measured electrically up to 67 GHz, they demonstrate a responsivity of $3.9\ \mathrm{V/W}$ and NEP of $2.2\ \mathrm{nW/Hz}^{1/2}$. Following on from this, it was shown using similar devices that performance depends strongly on the GSSD channel width, achieving a responsivity of $250\ \mathrm{V/W}$ at low frequency and $80\ \mathrm{V/W}$ at 49 GHz for a 30 nm wide channel. The NEPs achieved in these cases were $50\ \mathrm{pW/Hz}^{1/2}$ and $170\ \mathrm{pW/Hz}^{1/2}$ respectively, also far better than previously reported devices [142]. However, further improvements must be made for these to perform on par with conventional Schottky diode detectors, which typically show NEP $\sim 1\ \mathrm{pW/Hz}^{1/2}$ and responsivity of a few kV/W [35]. There has also been work published modelling the GSSD, in terms of parasitic capacitance, proving that suitably fabricated graphene devices are capable of operating at frequencies into the THz range [132]. In particular, it is desirable to fabricate GSSDs using exfoliated graphene, encapsulated using hBN, which is far higher quality than graphene epitaxial graphene grown on SiC [51, 142] or SiO_2 [132].

2.5. Electrical Noise

There are several sources of electrical noise which can appear in signals, and understanding and minimising all sources of noise is extremely important for maximising the performance of any detector. The most commonly expected sources of noise for devices such as those presented here will be outlined in this section, along with their frequency dependences.

Perhaps the most basic source of noise, thermal noise (also sometimes known as Nyquist or Johnson noise) arises from random fluctuations of carriers [143]. It is always present at finite temperature, and a device of resistance R gives rise to a mean square noise voltage, v_n, of

$$v_n = \sqrt{4R\left(\frac{hf_c}{e^{hf_c/k_BT} - 1}\right)B}, \quad \text{Equation 29}$$

where B is the system bandwidth and f_c is the central frequency. Even up to THz frequencies we typically have $hf \ll k_BT$, with $\frac{k_BT}{h} \cong 6\ \text{THz}$ at room temperature. Therefore Equation 29 is simplified to give $v_n = \sqrt{4k_BTRB}$. The spectral voltage noise S_v is given by

$$S_v^{1/2} = \sqrt{4k_BTR}. \quad \text{Equation 30}$$

Because of this, thermal noise is a form of 'white noise', because its spectral power does not change across the frequency spectrum.

Flicker noise is a form of '1/f' noise that arises from carriers passing over material interfaces/boundries. Although it is generally only relevant at low frequencies, 1/f noise may become important when, for example, using an optical chopper for detection measurements. There are several theories regarding the main cause of flicker noise in conductors, such as the Hooge model [144] and the McWhorter model [145], however to date the exact origin of this form of noise is yet to be fully understood. In general, flicker noise follows a $S_v = A/f$ relationship, where A is a constant, and in

everyday applications is often characterised by a corner frequency, above which flicker noise dips below flat-band noise sources such as thermal noise.

Shot noise arises from the discrete nature of charge carriers, and arises from random carrier fluctuations near some sort of potential barrier. It is commonly observed in p-n junctions and other semiconductor structures, however is not expected to be important here, due to the nature of the GBR and GSSD not relying on carrier transmission over potential barriers. It generally appears as a form of white (frequency-independent) noise up to a certain frequency, related to carrier transit time across the relevant structure.

Another common form of noise is carrier generation-recombination noise, which occurs due to random carrier transitions in a semiconductor, either over the bandgap or involving trap states or localised states.These random transitions cause fluctuations in the carrier density and hence fluctuations in resistance, which manifests as electrical noise. While no semiconductors are used in this work, noise of this form may appear in graphene devices due to the presence of trap states near graphene edges. Depending on the cleanliness of graphene and the dominance of edge states in conduction, this may become a significant source of noise. This form of noise is expected to follow a $1/f^n$ relationship [146].

3. Fabrication and Measurement Techniques

3.1. Graphene Flake Preparation and Nanodevice Fabrication

3.1.1. Graphene and Hexagonal Boron Nitride Exfoliation

Despite the considerable advancement made in graphene technologies since it was first isolated in 2004 [1], the technique which produces the highest quality individual flakes is fundamentally the same as that which was used by Geim and Novoselov [1]; mechanical exfoliation of a graphite crystal using adhesive tape. This process is shown in Figure 11.

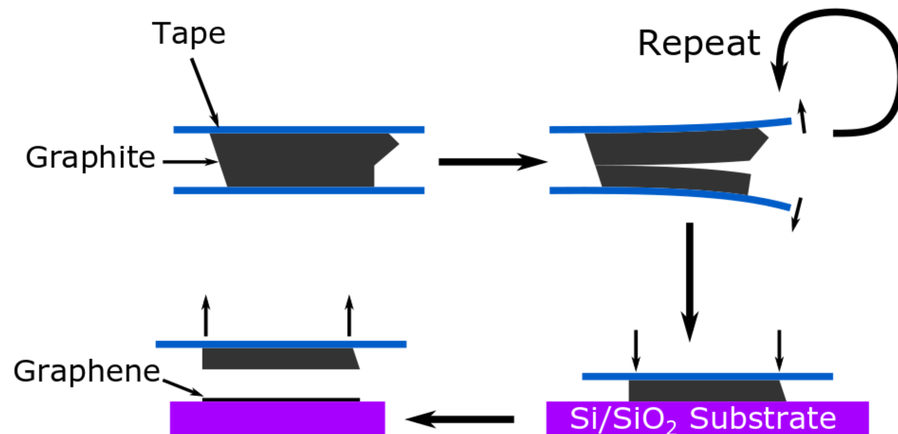

Figure 11: Graphene exfoliation process, whereby a graphite crystal is cleaved using tape and spread over an area of the tape, then pressed into a substrate and slowly peeled off to leave areas of monolayer graphene.

A piece of graphite is sandwiched between two pieces of tape, which are carefully peeled apart. This causes cleavage of layers in the graphite, exposing a clean atomically smooth edge. This process is repeated a few times in order to create a large number of clean crystalline surfaces on the tape, following which the tape is pressed firmly onto an atomically smooth SiO_2 surface. This substrate has previously been cleaned by sonication in acetone and rinsed in 2-propanol (also known as isopropanol, IPA), in order to avoid contaminating the graphene, and baked at 130°C to remove any water which had adsorbed onto the surface. Using oxygen plasma on the substrate for 10 minutes can drastically

increase yield of graphene flakes, however it increases adhesion and makes it more difficult to successfully lift flakes during transfer. After leaving the tape on the substrate for a short length of time, the tape is slowly peeled off. This causes a final cleaving of the graphite, leaving areas of monolayer graphene on the substrate. The substrate is important, because the colour contrast is used to identify monolayer graphene from bilayer and thicker flakes. Both 90 nm and 290 nm SiO_2 substrates give good contrast, however a 290 nm substrate is used for all work shown here due to the improved insulating properties. Figure 12 shows an image of a 290 nm SiO_2 substrate with different thicknesses of exfoliated graphite and graphene, showing the colour difference with different numbers of layers.

Figure 12: Optical image of a small exfoliated graphene flake on 290 nm SiO_2. For this picture, the camera white balance is set to make the substrate appear mostly grey. A ~15 µm wide monolayer graphene flake is labelled, alongside an area of bilayer graphene. The purple area is a thicker piece of exfoliated graphite, roughly 10 nm thick. Flake thickness can be determined from the apparent colour.

As can be seen, despite monolayer graphene only absorbing 2.3% of visible light [67], using this substrate areas of monolayer graphene can be easily found and distinguished from bilayer. This image

was taken while using a white balance setting which makes the substrate (which is usually purple in colour) appear mostly grey, however this is not at all necessary in order to identify graphene flakes.

As previously mentioned, hexagonal boron nitride makes an ideal substrate for graphene. Its high bandgap (5.2 eV) makes the barrier height with graphene large, and its atomically flat surface makes it ideal for high graphene quality in a hBN-graphene-hBN structure. The process for exfoliation of hexagonal boron nitride is very similar to that for graphene. Because hBN crystals are much smaller than graphite crystals, a single crystal must be cleaved many times and spread over a roughly 2x2 cm piece of tape before being pressed onto a substrate, in order to achieve decent yield. 290 nm SiO_2 substrates are again used, because the colour contrast allows the thickness of the hBN to be roughly determined. Because atomically flat substrates are desired, artificial colour contrast and dark-field imaging are used to detect the presence of any cracks, folds, or impurities on the surface. Flakes of thickness 20-70 nm are generally desired for graphene encapsulation, meaning a colour in the range of light blue – light green/yellow.

3.1.2. Transfer and Encapsulation Methods

Once suitable flakes of graphene and hBN have been found, they must be physically moved in order to encapsulate, and in order to move the resulting stack to the desired substrate. In the work shown here only dry transfer procedures were used, because they allow the graphene to not come into direct contact with any solvent or polymer, improving resultant graphene quality. In order to accomplish this a ‘stamp’ is used, which is capable of picking up thin hBN flakes intact, and of releasing them when desired. This process is shown in Figure 13.

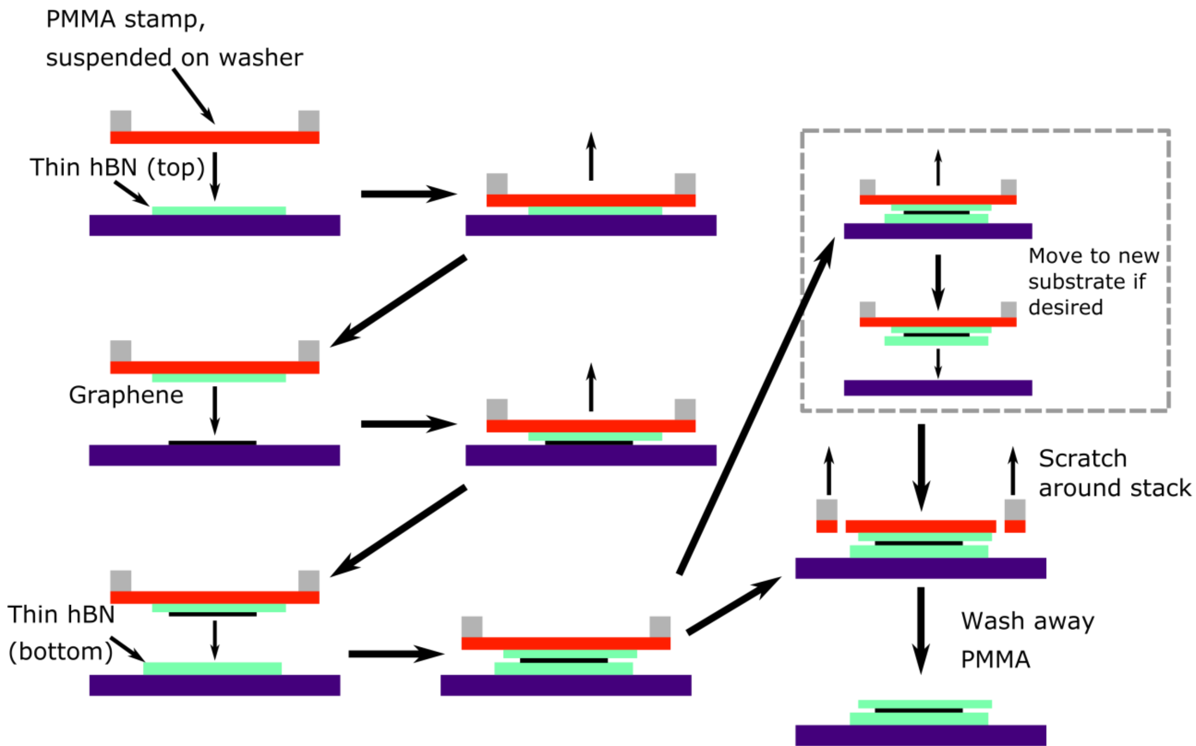

Figure 13: Diagram of the stamp transfer process for encapsulating graphene with hBN. The flakes are picked up in succession, optionally moved to the desired substrate, and then released. This is shown for a PMMA membrane stamp, with the process being almost identical for a PDMS/PPC stamp. With the PMMA stamp, the membrane is scratched to detach it from the washer, and then washed away in acetone. For a PDMS/PPC stamp, the substrate temperature can simply be increased to release the flakes. Note that although this is not indicated in the figure, the two hBN flakes seal around the graphene due to strong Van-der-Waals forces and do not leave the graphene exposed at the sides.

In this transfer process, the stamp is first used to pick up the piece of hBN which will form the top layer of the stack. This is possible if the adhesive force between the stamp and the flake is stronger than that between the flake and the substrate, meaning that oxygen plasma cannot be used on the substrate prior to exfoliation. This flake is then carefully positioned over the graphene flake to be used over the device and lowered. Positioning of the flake is achieved using an optical microscope (due to the transparency of both the stamp and the hBN flake) and an X-Y-Z-controllable micromanipulator arm. No effort is made to align the lattice structures of the hBN and graphene. Once fully in contact with the graphene, the hBN is quickly lifted. Due to strong Van Der Waal's interaction between hBN

and graphene, the graphene flake is easily picked up. Then, the hBN/graphene is positioned over the bottom hBN flake and lowered, bringing the graphene flake and top hBN flake fully into contact with the bottom hBN. It is at this point that any impurities present visibly form into bubbles due to the large pressures. Once the hBN/graphene/hBN stack has been assembled, it can be either left in place or moved to a different substrate. The method of removing the stack from the stamp depends on the type of stamp used so will be discussed later. This method of dry stamp transfer is very versatile and can be used to relatively quickly assemble Van Der Waals heterostructures from a variety of 2D materials [125, 147], but here has only been used to encapsulate graphene with hBN. Unlike other transfer methods which use sacrificial layers and wet chemistry, it allows the graphene to only ever come into contact with the initial cleaned SiO_2 substrate and the hBN used to encapsulate it, therefore reducing the risk and extent of contamination.

As mentioned in the caption of Figure 13, two types of stamp have been used in this work to prepare hBN/graphene/hBN stacks. The first is a stamp consisting of a poly(methyl methacrylate) PMMA membrane suspended over a small circular washer. The second is a layer of Polypropylene carbonate (PPC) on a Polydimethylsiloxane (PDMS) piece held by a glass slide. The preparation procedure for a PDMS membrane stamp is shown in Figure 14.

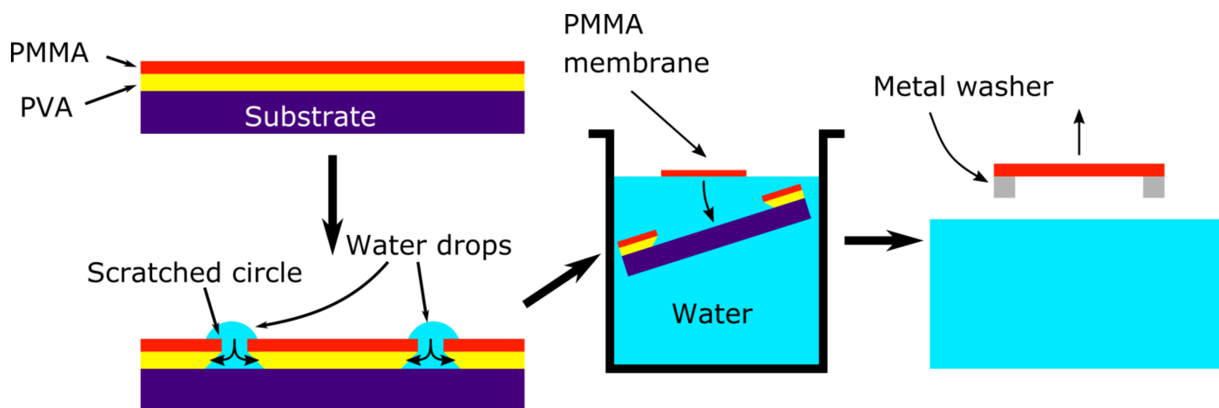

Figure 14: Preparation of a PMMA membrane to be used for stamp transfer. A bilayer of PVA and PMMA is spin-coated onto a substrate. A ~3 mm radius circle is scratched into the surface, and water is placed onto the scratch. Once the PVA under

the PMMA has dissolved and the membrane sits on a drop of water, it is then floated in a beaker of water. A metal washer, previously covered in PMMA to help adhesion, is then used to pick up the membrane.

First, a sacrificial layer of Poly(vinyl alcohol) (PVA) is spin-coated onto a SiO_2 substrate and baked. This is followed by spin-coating the PMMA layer which will form the membrane. A 3 mm radius circle is scratched through both layers near the substrate corner, and water droplets carefully placed on the scratch. Care must be taken to keep water from touching the middle of the circle, because this area of PMMA will be used for the transfer. Because PVA is soluble in water and PMMA is not, the water droplets dissolve the underlying PVA and allow the membrane to float on the formed droplet. More water may be carefully added during this process if necessary. Once the membrane is floating, the substrate is dipped into a beaker of water at an angle, such that the edge of the water droplet comes into contact with the water in the beaker and water tension then causes the membrane to move onto the beaker water surface. Meanwhile a 2 mm washer is cleaned, then coated in PMMA and baked at 130 °C for 5 minutes, in order to allow the membrane to adhere to the washer. The washer is then used to fish the membrane off the water surface, keeping the membrane taut and wrinkle-free, and is carefully placed on a paper towel on a hot plate at 130 °C for 5 minutes to remove any water traces. The washer is attached to the transfer arm using a vacuum, and the membrane is now ready to be used for the transfer as shown in Figure 13.

Due to the strong adhesion between PMMA and hBN, it is impossible to remove the finished stack from the membrane while keeping it intact. In order to remove the membrane, it is scratched on the inside of the washer, around the stack, detaching the membrane from the washer. The substrate is washed in water to remove any traces of PVA, then a small amount of PMMA is then spin-coated onto the substrate to soften and relax the membrane, following which the PMMA is removed by washing in acetone and IPA. The stack is then ready to be used for device fabrication.

An alternative to using a PMMA membrane stamp is to use a PDMS/PPC stamp. The preparation procedure for this is shown in Figure 15.

Figure 15: Preparation of a PDMS/PPC stamp. A piece of commercial PDMS is placed onto a substrate and cleaned using oxygen plasma. PPC is spin-coated on top and baked. The PDMS is cut into 2-5 mm squares and moved onto a clean glass slide using tweezers.

Firstly, a roughly 3 cm piece of PDMS is placed onto a clean flat substrate. It is then cleaned using 10 minutes of oxygen plasma in a Moorfield Nanoetch with 8 W of RF power in order to remove any contamination. PPC 15% by weight in anisole is then spin-coated at 2,000 RPM and baked at 110 °C for 5 minutes. Meanwhile, a glass slide is cleaned and placed in an oxygen plasma for 10 minutes. The PDMS/PPC is then cut into 4 mm squares using a sharp blade, and a square is transferred to the corner of the glass slide. Due to the relatively large thickness and robustness of the PDMS, this can be done using tweezers. Once on the slide, the stamp is carefully pressed down and then briefly placed into a vacuum in order to remove any bubbles and ensure good adhesion. After being baked at 150 °C for 5 minutes, the stamp is then ready to be used for transfer.

During transfer, the glass slide is attached to the transfer arm using a vacuum, and is held at a downwards angle of $1 - 2$ °. To pick up a flake, the stamp is positioned with its far corner just past the flake, and is lowered such that the corner of the stamp comes into contact with the flake. The reason for the use of PPC on the stamp is its adhesion to hBN, which can be changed using the substrate temperature. At a temperature of 53 °C, the adhesion is strong and the hBN flake can be picked up off a SiO_2 substrate. Heating to above 60 °C softens the PPC, allowing the flake/stack to be released and remain on the substrate. Flakes must be picked up by rapid movement of the arm, to avoid the flake

being shredded by differential forces across the stamp during slow movements. When releasing flakes, the arm must be lifted slowly.

The two types of stamps used offer different advantages and disadvantages. The PDMS/PPC stamp is easier to prepare than the PMMA membrane, and can generally be used multiple times. However, its performance for picking up flakes depends strongly on PPC quality and thickness, and care must be taken to not dry out the stamp. The adhesion between PPC and hBN is weaker than that between PMMA and hBN, meaning that picking up a flake using the PMMA membrane is generally relatively easy, while it often takes many attempts using the PDMS/PPC stamp. The PMMA membrane is rather fragile however, and can easily rip if dried out or used for too long. The PDMS/PPC stamp method also allows for finer control of the flake's position, and hence it can be used for fine alignment of flakes. This is useful when the target area of graphene and/or hBN is small. In general, it is found that the PDMS/PPC stamp is easier to use, and has been used for the majority of encapsulated graphene devices shown here.

3.1.3. CVD Growth and Transfer of Graphene

Almost all cutting-edge graphene electronics research uses manually exfoliated and encapsulated graphene, using a method similar to that described above. While this is capable of producing very clean and high quality graphene flakes, and has been used to explore many of graphene's more interesting and unusual properties, it is not possible to scale these methods up to the kind of mass production which is necessary for industrial/commercial applications. For large-scale fabrication of graphene electronics it is necessary to use large-scale growth of graphene.

By far, the most well developed and successful method for growth of monolayer graphene is chemical vapour deposition. The growth of graphene using CVD is a complex topic, which is out of the scope of this work, but current commercial-scale graphene production involves growth on copper foil.

All work using CVD-grown graphene shown here used graphene supplied by Graphenea [148], with a quoted grain size of $20\ \mu m$ and electron mobility of $\sim 1500\ cm^2/Vs$, however electrical measurements generally showed a higher mobility within a single grain. The vast majority of CVD-based devices fabricated used graphene as supplied already on the desired substrate (SiO_2 or fused quartz). However, transfer of CVD graphene from the copper foil to a target substrate was sometimes performed, and this process will be outlined here.

As mentioned, currently the best methods for CVD growth of graphene use copper foil as a growth substrate. Copper is unsuitable for use as a device substrate however, so the grown graphene must be detached from the copper and transferred to another substrate. First, a 1x1 cm piece of foil with graphene is coated with PMMA by spin-coating PMMA in anisole, 8%, at 3,000 rpm followed by baking at $130\ °C$ for 5 minutes. This serves to support the graphene after the copper has been etched away. Because the CVD process produces graphene on both sides of the film, the foil is then placed PMMA-side-down in an oxygen plasma (Moorfield Nanoetch, 60s at 8 W) to remove graphene from the underside. Meanwhile, a dish is filled with 0.2 M aqueous ammonium persulfate ($(NH_4)_2S_2O_8$) to a depth of 2cm. The copper foil is floated in the dish, PMMA/graphene side up. After 2-4 hours, the copper has fully dissolved. In order to clean the graphene underside, a small Si/SiO_2 wafer is then used to scoop up and move the graphene/PMMA film to be floated on three successive dishes of DI water. The film is then picked up from the final water bath using the target substrate, and baked at $130°$ to remove water from the graphene/substrate interface and enhance adhesion to the substrate. Finally, the substrate is placed in acetone to remove the PMMA layer and rinsed in IPA, followed by careful drying with a nitrogen jet.

3.1.4. Micro- and Nanofabrication

In order to construct a device from an encapsulated graphene flake, electrical contacts must be made to the graphene, and the stack must be etched into the desired structure. All graphene device fabrication here used electron-beam lithography (EBL), with a PMMA positive resist. This allowed features as small as 100 nm to be defined, with maximum pattern sized of over 1 mm. Photolithography was avoided as the majority of commonly used photo-resists are known to severely contaminate graphene, causing doping and reduced mobility [149]. The use of PMMA as electron-beam resist simplifies device fabrication; because it can be developed in an IPA/water mixture, it resists commonly used hBN etches, and it can be washed away using acetone without substantially contaminating graphene and leaving little residue.

A typical fabrication procedure for an encapsulated graphene device would be to first pattern and expose crosses and large-scale contacts, as shown in Figure 16.

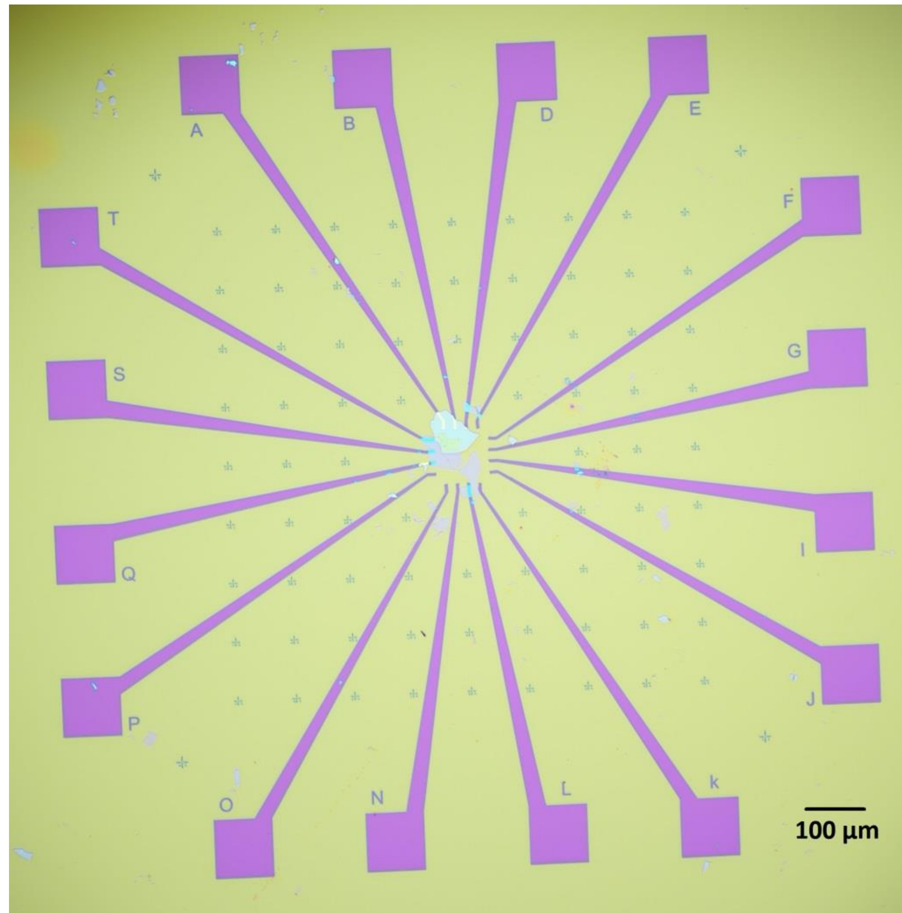

Figure 16: Example image of an hBN/graphene/hBN stack with bilayer PMMA resist on Si/290 nm SiO_2, after alignment crosses and large-scale contacts have been patterned and developed.

An image is then taken of the device, with the crosses used to align the image to the coordinate system. Using the image as a guide, the positions of the graphene flake, hBN, and any impurities or other areas to be avoided are marked and the design is created around the flake geometry. After the design is complete, device fabrication can continue. The small contacts are patterned and developed using the same bilayer PMMA, followed by etching and deposition of one-dimensional (1D) contacts. 1D contacts will be described in more detail later in this section. Another set of 4 crosses was typically included in the small contacts layer, allowing the following layer to be directly aligned to the contacts. Then, the etch mask is spin-coated, and the etch layer is patterned, exposed, and etched. Figure 17(left)

shows an exposed etch mask, with all unnecessary areas of graphene and hBN exposed, and Figure 17 (right) shows the etched device, etch mask removed.

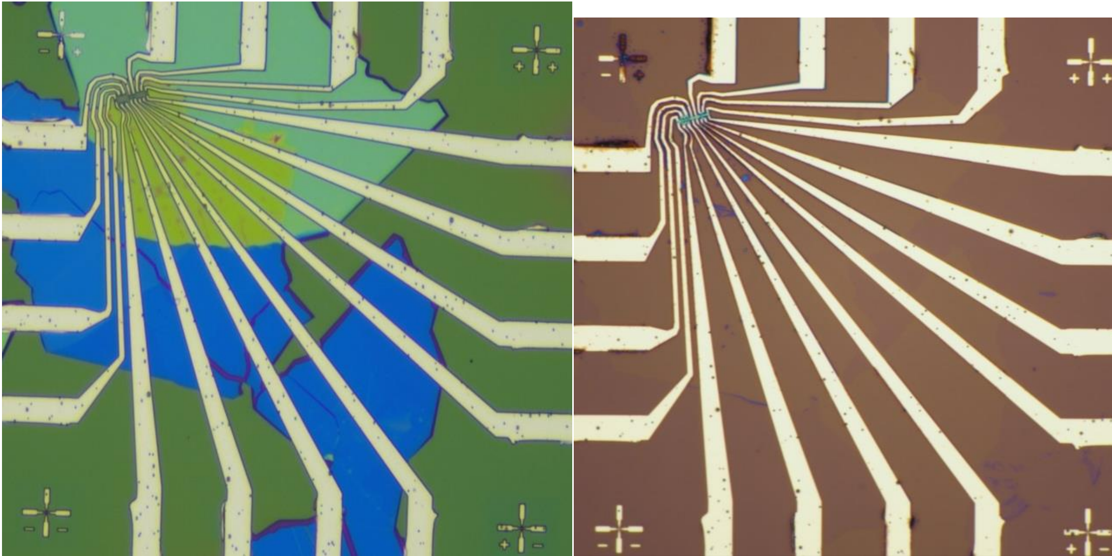

Figure 17: (Left) An example encapsulated graphene device on Si/290 nm SiO_2, with contacts deposited and etch mask developed. (Right) the same device after etching and removing etch mask. In both images, the scale is $100\ \mu\mathrm{m}$ between the crosses shown in the corners.

Etch masks were created by first spin-coating PMMA with a molecular weight of 950k, 3% in anisole, at 5,000 rpm, followed by baking at $150\ °\mathrm{C}$ for 5 minutes. The desired pattern was then exposed with a dose of $145\ \mu\mathrm{C}/\mathrm{cm}^2$, using an acceleration voltage of 10 kV. Often, for the smallest features of size ~100 nm, a higher dose is required to fully expose the shape. In those cases, the relative dose for those features was increased somewhat, for example to 1.5x the dose used elsewhere. For contact deposition, a bilayer of PMMA resist was used. A layer of PMMA 495k, 3% in anisole was spin-coated at 5,000 rpm and baked at $150\ °\mathrm{C}$ for 5 minutes, followed by PMMA 950k as described above. The exposure for the bilayer also uses a dose of $145\ \mu\mathrm{C}/\mathrm{cm}^2$. During development, the softer underlying PMMA 495k is developed more readily than the 950k, resulting in an undercut, hence giving good lift-off quality. When patterning on a non-conductive substrate, for example fused quartz, a conductive polymer must be added to the surface to avoid charge buildup during patterning. The conductive

polymer is spin-coated at 2,000 rpm and baked at $120°C$ for 2 minutes. Prior to first patterning, scratches are made at the bottom corners of the substrate, relative to which the sample coordinates are recorded using an optical microscope with motorised stage. If necessary, a scratch was also made ~1 mm from the sample location, for focusing.

EBL was performed using a Zeiss EVO 100 scanning electron microscope (SEM) with a LaB_6 tip, using ELPHY Quantum for patterning control. After the sample was loaded and the system returned to vacuum, the acceleration voltage (EHT) was switched on to 10 kV, and the beam was aligned. A Faraday cup was then positioned such that the entire beam area was recorded, and the total beam current was measured. During a single stage of patterning, sometimes two different write fields (WFs) were used, corresponding to different maximum and minimum feature sizes. Typical WF sizes used were $125\ \mu m$ or $250\ \mu m$ for smaller features and $1500\ \mu m$ for large features, however write fields as large as $2000\ \mu m$ have been used. Before use, all needed WFs were calibrated using a nested chequered pattern with known feature sizes. This pattern was also used to perform any necessary astigmatism correction and aperture alignment.

After beam alignment and initial current measurement, the sample substrate was located, with the corner marks used to set up the global coordinate system. The sample position was then found, taking care not to expose the sample using the electron beam. The sample was brought into focus using a nearby flake or focussing scratch. The first exposure for a device was almost always to pattern an array of crosses, to be used for alignment of other features. Subsequent patterning then used these crosses to set up a local coordinate system, around which the device design was created. If very fine focus was required, for very close alignment between layers or small features, burning spots allowed for high focus precision. For this, the beam was moved to a position which was close to the sample but not required for the pattern, the magnification set to 50,000x, and the beam kept in one position for a few minutes. This resulted in a small high-contrast circle of carbon, with its size dependent on the beam

focus and its shape dependent on the astigmatism. These controls could then be adjusted to improve the image of the spot, followed by burning another spot $\sim 1\ \mu m$ away, and repeating until the focus was satisfactory. Ideally, a spot size of below $50\ nm$ was achieved to give a good level of focus for the smallest features.

Meanwhile, the design, if needed, had been loaded into ELPHY quantum. The working area was set to match the used WF, which should enclose the layer(s) set to be patterned. Once the local coordinate system had been set up, the beam current was again measured at the Faraday cup. From this measurement, the patterning parameters were set to ensure the correct patterning dose. If no further alignment was required, for example if just writing crosses and large-scale contacts, the patterning could now be started. Otherwise, the crosses were then used to perform a fine alignment of the WF, immediately followed by initiating the patterning. After patterning had finished, if a second WF was to be patterned the stage was moved back to the Faraday cup position, the WF changed, and the process repeated. For large WFs/large pattern areas, the small spot size used for smaller features and for imaging gives too small beam currents, leading to very long patterning times. In this case, a larger spot size was set after alignment. This can massively speed up patterning, but also reduces resolution and hence is not suitable for any portions of the pattern where high resolution or fine alignment is necessary.

Once patterning had finished, the SEM chamber was vented and the sample removed. If a conductive polymer was used, it was first removed by washing in DI water and blow drying. The sample was developed in an IPA:water 3:1 mixture at $5\ °C$ for one minute, followed by rinsing in IPA and blow drying. Encapsulated graphene samples were etched using an Oxford Instruments System 100 reactive ion etch (RIE). This system uses inductively coupled plasma (ICP), where an additional radio frequency power source is used allowing the plasma density to be modulated without affecting DC bias on the lower electrode . A mixture of CHF_3 and O_2 was used, with flow rates of 17.5 ccm and 8 ccm respectively.

An RF power of 5 W was used, with an ICP power of 50W, at a pressure of 10 mTorr and temperature of 10 °C. The etch rate for hBN was typically around 3 nm/s, with monolayer graphene taking 10 s to etch. A 20 minute long oxygen clean process is used before loading the sample and after removing it, using 45 ccm of O_2, an RF power of 100 W and an ICP of 300 W. Any thicker graphene or graphite present on the substrate or in the stack could not be etched by this method, so an oxygen/argon etch in a Moorfield Nanoetch was sometimes also used. Typically, etches were for less than two minutes, because longer etches can cause the PMMA resist to become too thin. Longer etch time also increases the risk of some of the PMMA becoming cross-linked. Cross-linked PMMA cannot be easily removed using acetone, therefore making subsequent lift-off difficult as well as leaving substantial residue on the sample.

Contacts to encapsulated graphene were made using 1D contacts, where the deposited metal bonds with the narrow (effectively one-dimensional) exposed graphene edge, resulting in a high quality contact [52]. This is achievable because of the etch rate of the monolayer graphene being much less than that of hBN, resulting in a step in the edge profile of the etched stack. A schematic of the process of forming a 1D contact is shown in Figure 18.

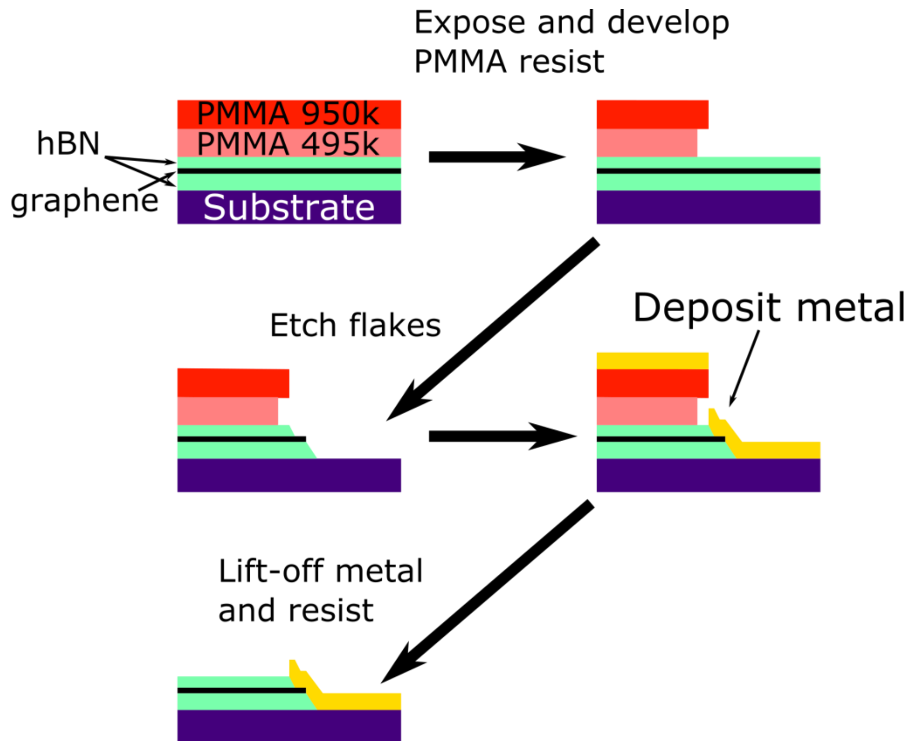

Figure 18: Formation of a 1D contact. First, a bilayer PMMA resist is spin-coated, followed by exposing and developing the contact pattern. The hBN/graphene/hBN stack is then etched, leaving a step with graphene exposed. Metal is then immediately deposited, forming the contact. Finally, the resist and excess metal is removed by lift-off.

After etching the contact area using RIE as described above, the sample was immediately placed under vacuum in an electron-beam evaporator system, minimising time in air in order to minimise contamination by water and hydrocarbons. Around 3 nm of Cr was first deposited, because the adhesion of gold directly on SiO_2 is generally poor. Following this gold was immediately deposited, with a typical thickness of 70 nm. It was found that this contact thickness ensures that the graphene is contacted, because it is larger than the bottom hBN thickness, but is thinner than the PMMA 495k thickness ensuring a good lift-off quality.

Lift-off is the process by which the un-exposed resist on a substrate is removed, taking any metal which does not lie on the patterned area with it. Because PMMA is soluble in acetone, it was performed by placing the sample in a beaker of acetone. The sample in acetone was first placed in a sonication bath at low power for a few seconds, to loosen the PMMA resist, followed by placing in a fume hood

on a hot plate at $65\,°C$, covered with a glass dish. After around 20 minutes, a pipette was used to agitate the acetone around the sample. If all of the metal-covered resist could be seen to flake off, then the lift-off was complete. If however the resist came off only partially or not at all, then the beaker was re-covered and placed back on the hot plate. The acetone was changed if there was a considerable amount of flakes floating in the beaker. As mentioned previously, the presence of cross-linking in the PMMA resist can make the lift-off more difficult, and impossible in some cases. If after over an hour on the hot plate the resist still was not removed by agitating the acetone, then further sonication at low power was used to loosen the PMMA. Using sonication on an encapsulated graphene or CVD graphene sample is dangerous, because it can cause the stack/graphene to become detached from the substrate, destroying the device. Once all areas of metal-covered resist could be seen to have been removed from the substrate, the sample was washed several times in acetone to remove any PMMA residue, followed by rinsing in IPA and blow-drying with a nitrogen jet.

When using CVD graphene instead of an hBN/graphene/hBN stack, some changes to the nanofabrication processes were used. Firstly, when recording coordinates prior to the first EBL session, instead of locating a particular flake it is necessary simply to locate a large enough clean area of the substrate. Etching was simpler, requiring only 30 seconds in an oxygen/argon plasma at 8 W to completely etch through the graphene. However, because the graphene is present all over the sample, it is necessary to etch a large pattern around the contacts, to ensure that they are electrically isolated from each other. An example image of the etching pattern used to accomplish this is shown in Figure 19.

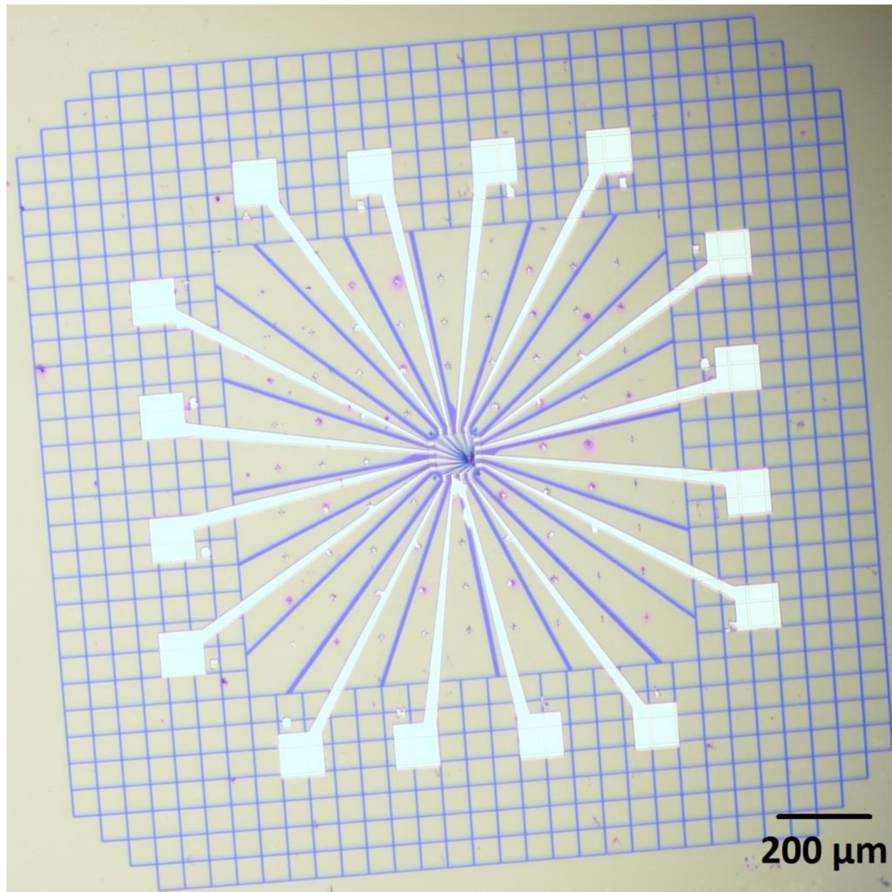

Figure 19: PMMA etch mask for a CVD graphene device, as an example of the etch pattern used to isolate contacts from each other on a substrate covered in CVD-grown graphene

At smaller scales, a line was etched between each pair of contacts. However, a large chequered pattern was etched around the contact pads. This was to ensure that even if individual bonded wires were in contact with the substrate outside the bounds of the contact pad, they would not be shorted through graphene on the substrate.

Due to the lack of encapsulation, 1D contacts were not necessary to contact the CVD graphene. Electrical contact was instead made by depositing metal directly onto the graphene. When depositing contacts on top of graphene however, large areas tended to cause the underlying graphene to peel off of the substrate, taking the contact with it. To resolve this, unlike for encapsulated graphene samples, contacts were deposited in two steps. The first step consisted of the large contacts, contact pads, and

alignment crosses. Prior to Cr/Au deposition underlying graphene was etched, allowing the large-scale contacts to lie directly on the substrate and hence have good adhesion. After lift-off, a second bilayer resist was applied, and the small contacts patterned. These contacts were then deposited directly onto the graphene. The large overlap with the large contacts, as well as the small area, allowed the graphene and contacts to remain on the substrate.

3.2. DC and Low-Frequency AC Measurements

In order to perform electrical measurements of a sample, contact must be made between the Cr/Au contacts that lie on the substrate, as shown above, and the electrical measurement equipment. The simplest way to do this is using a probe station, where thin metal probes are carefully pressed down onto the contact pads.

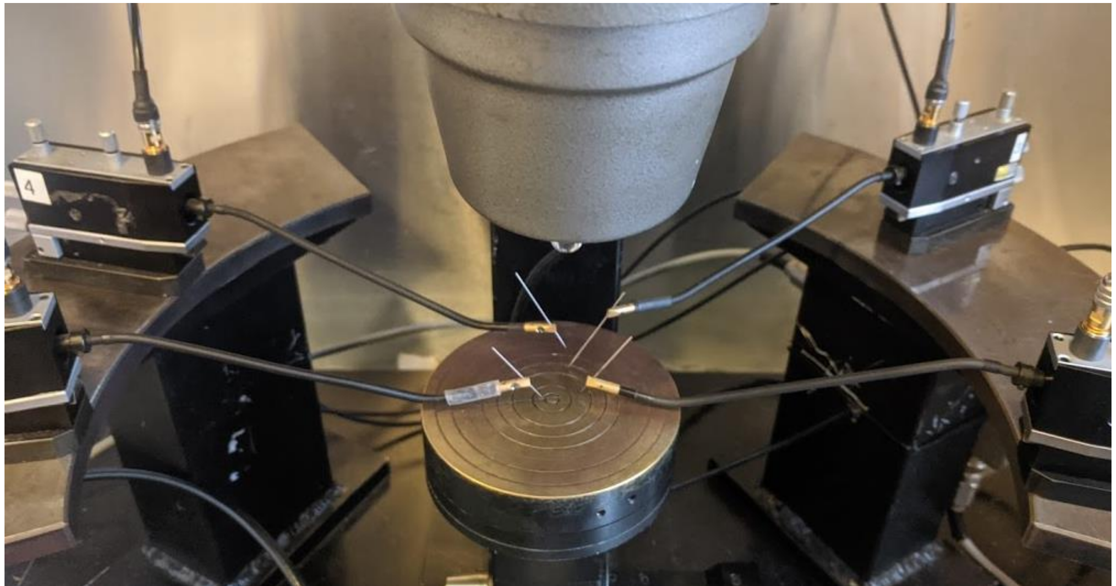

Figure 20: One of the probe stations used for electrical measurements. Four probes are visible.

A probe station allows for measurements of a newly fabricated device relatively quickly, and without leaving the clean room used for fabrication, however has several drawbacks. Firstly, the physical contact between a probe head and the contact pad is relatively fragile, and prone to be disrupted by

any movement or vibration of the surroundings. This can cause errors in the measured data, or in a worst-case scenario can lead to a build-up of voltage between the probe head and the device, leading to a static discharge and damaging the device. Secondly, using a probe station for measurements generally means that the measurements are limited to being performed at room temperature, in atmosphere. Vacuum/low temperature probe stations do exist, but were unavailable for this project. Thirdly, using a probe station limits the potential complexity of measurements that can be performed, due to the limited number of probes available. The probe stations available were limited to five probes, some of which were often faulty. For these reasons, most measurements were performed by bonding the finished device onto a chip carrier. By semi-permanently bonding gold wires to the device's contact pads, the instability of measurement using probes is avoided. Loading the device onto a standard chip carrier also allows for far more complex measurements, because it can be much more easily integrated into circuitry, such as in a vacuum system and/or cryostat.

Before bonding onto a chip carrier, the device substrate generally must be cleaved down to a $2-4\ \mu\mathrm{m}$ square size. This is done by first spin-coating a protective layer of PMMA onto the substrate, following by scoring the desired cleave line with a diamond scribe and breaking over the edge of a glass slide. Silicon dust can then be blown away by nitrogen jet, and the PMMA removed in acetone. The substrate is secured to the chip carrier using a conductive silver paint, which also allows electrical contact to the substrate Si bulk for purposes of gating the device. Once secured onto the chip carrier gold wires are wedge-bonded to the device contact pads. This is a particularly dangerous part of device fabrication, because care must be taken to avoid using too much force and breaking through the SiO_2 under the bond area. Figure 21 shows an example image of a device on Si/SiO_2 substrate, with gold wires bonding it to the connectors on a chip carrier.

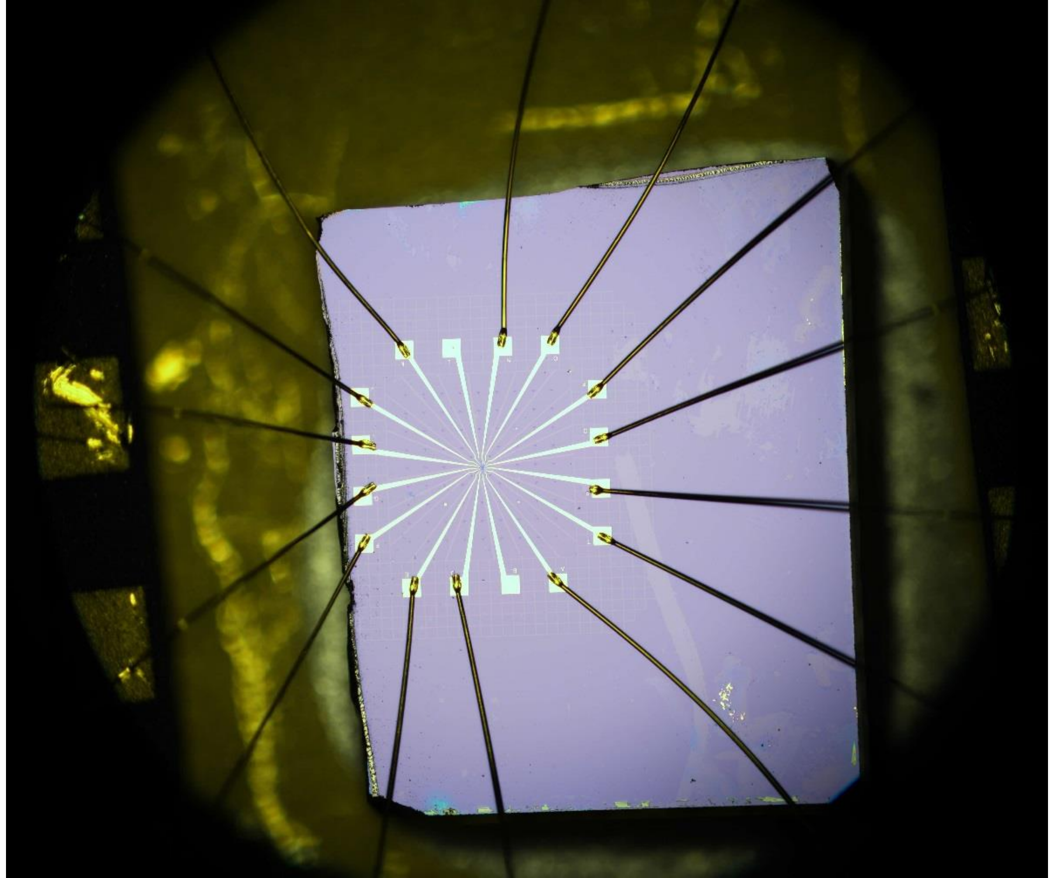

Figure 21: 5x zoom image of a device on Si/SiO_2 (290 nm) substrate, mounted and bonded to a chip carrier. All but 2 contacts on the device are bonded to the carrier using gold wire. Contacts on the chip carrier are barely visible on the left and right.

As well as wires connecting the chip carrier contacts to contact pads on the device, usually a wire is also bonded to the chip carrier floor, which is electrically contacted to the substrate bulk, to act as the gate contact. Once the substrate is secured and all desired contacts are bonded, the device was loaded into the chip holder built into the cryostat.

Once mounted into the cryostat, measurements can be taken using BNC coaxial cables. Typical DC measurements involved using a pair of voltage sources/ammeters, one to apply current to the device through a large resistor and the other to apply the gate voltage, and a pair of voltmeters to measure input and output voltage. 4-contact methods were used in order to eliminate contact resistance and accurately measure input voltage. The low-frequency AC measurements were performed using a lock-

in amplifier. The lock-in internal oscillator was used to drive the measurements, with the output being passed through a large resistor. Input voltage was measured using the A and B lock-in input terminals, and recording the in-phase component of A - B. LabVIEW [150] was used to control all instrumentation programmatically, as well as to record values and perform some basic initial analysis. Origin [151] was used to perform subsequent analysis and plotting of data, with Matlab [152] also being used for more complex calculations.

3.3. Noise Measurement

3.3.1. Two Channel Cross-correlation

In order for electrical noise to be measured accurately and precisely, it must be amplified to a suitable level. However for commercially available amplifiers, for example the SR 560 voltage amplifier, the equipment noise can be of comparable magnitude to the device under test. A solution to this is the cross-correlation technique [153], in which the device noise is independently amplified and measured by two channels. By then performing a correlation calculation on the data recorded by each channel, any components that appear in only one channel are eliminated leaving only the true noise of the device. This removed any noise signals which arise during the amplification, because they are uncorrelated between the two channels. Using the derivation shown in [153], it can be shown that an estimate of the spectral device noise can be obtained using

$$S_v(f) = \frac{Re\left(V_1(f)V_2^*(f)\right)}{N}, \qquad \text{Equation 31}$$

where N is the number of samples, $V_{1,2}$ are the (complex) spectral noise voltage measured by the two channels, and the * superscript represents the complex conjugate.

The measurement setup is similar to that shown in the supporting information of [50]. The measurement setup uses two TL081 operational amplifiers (op-amps) on each channel, each in a

closed-loop non-inverting setup such that the gain of each is defined by the surrounding resistances. The voltage sources used are 9 V batteries, in order to not introduce excessive amounts of outside noise to the setup, however low-pass filters are also present to decouple any input noise from the circuit. A simplified diagram of the setup used for measuring the noise of four-terminal rectifiers is shown in Figure 22.

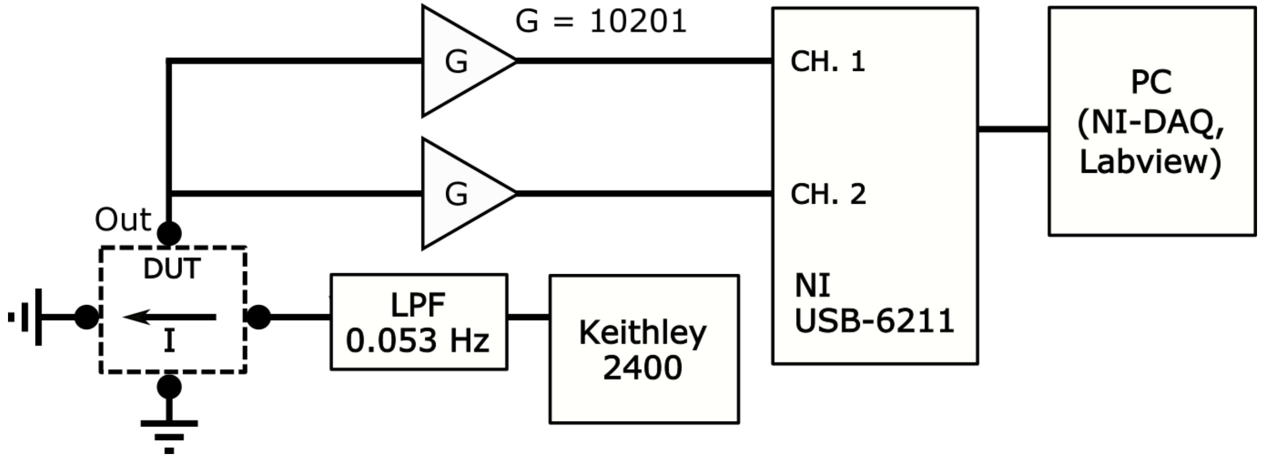

Figure 22: Schematic diagram of the two channel cross-correlation noise measurement setup. Also shown is a DC current source setup for use when measuring a ballistic rectifier or similar device. Current is passed through the device as shown, with the upper and lower contacts shown being the output contacts. The amplifiers shown each consisted of two op-amps.

After amplification to measurable levels, the noise signal of each channel is sampled at 125000 s^{-1} using an NI USB 6211 analogue-to-digital convertor (ADC) to give two time-domain noise signals. From these time-domain signals, Equation 31 is implemented by the LabVIEW program, calculating the voltage noise spectral density $S_v^{1/2}(f)$ using

$$S_v^{1/2}(f) = \frac{1}{A_G}\sqrt{\frac{2|Re(DFT(s_1)DFT(s_2)^*)|}{N^2}T_{samp.}}, \qquad \text{Equation 32}$$

where $DFT(s)$ represents the discrete Fourier transform of a time domain signal s, A_G is the total gain of the two stages, and $s_{1,2}$ are the time-domain voltage signals measured by the two channels. The sampling time window $T_{samp.}$ is included as a correcting factor, and the factor of 2 is to correct for the

two-sidedness of the Fast Fourier Transform algorithm used. For the Fourier transform a rectangular window was used. The measurement is repeated many times with new incoming data, for example 100x or 1000x, and averaged in order to increase measurement accuracy.

To drive the rectifier, a Keithley 2400 source meter is used for a constant DC power source, which is passed through a 0.053 Hz low-pass filter (with $R = 1\ \mathrm{M\Omega}$). Devices were contacted using coaxial cables connected to probes on a probe station as shown in Figure 20, and the entire measurement setup (aside from PC running LabVIEW) is placed in a metal box to shield from radiation and interference from external sources.

3.3.2. Testing and Calibrating Setup

In order to test and calibrate the setup, the voltage noise across a range of resistors was measured and compared to the theoretical value. In the absence of current flow, the noise across a pure resistance is independent of frequency, with magnitude given by the thermal noise as shown in Equation 30. Shown in Figure 23(a) are the raw measured noise spectra, measured by simply connecting an un-biased resistor between the channel inputs and ground.

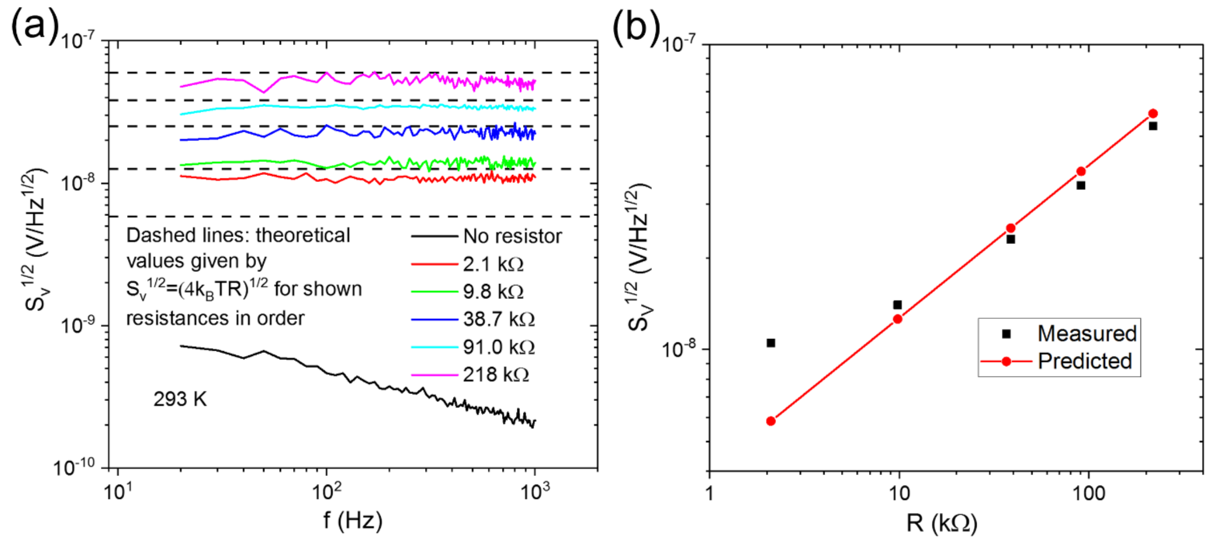

Figure 23: (a) Measured voltage noise spectra across various resistors, without any corrections. The black dashed lines show, with increasing resistance from bottom to top, the theoretical thermal noise generated by the five resistances tested. (b) shows the flat-band noise of each resistance, directly comparing the measured value to the theoretical value.

As expected for thermal noise, the voltage noise spectra are mostly flat. However, the values do not match those predicted by Equation 30. Figure 23(b) shows the difference between predicted and measured noise more clearly. At high resistances, the measured noise is lower than the theoretical noise by a constant ratio. This is a very strong indication that the assumed gain of the system is slightly incorrect. This may be due to a number of factors. For example, some drift in the resistances of the resistors which surround each op-amp and define its amplification factor. As well as this, it can also be observed that for smaller resistances the noise is larger than predicted by a constant amount. It was found that this excess noise is equivalent to each resistance being $\sim 6.5\ \mathrm{k\Omega}$ larger than expected. This may be due to loose connections in the noise circuit's input, or the input resistance of the op-amps themselves. With both of these factors accounted for, a calibration of the setup has been performed using the measured thermal noise voltages. Figure 24 shows the same data again, with these calibrations now taken into account.

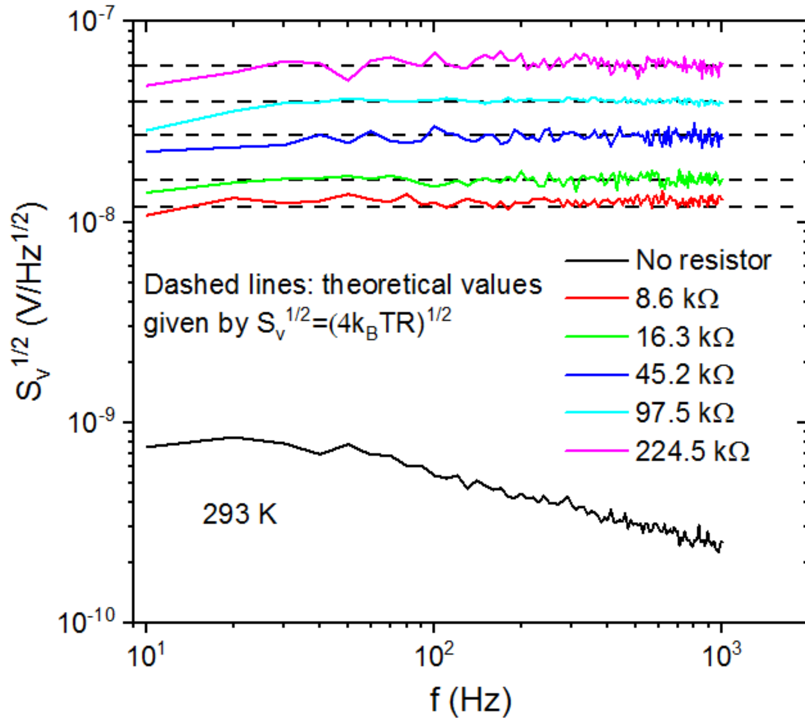

Figure 24: Voltage noise spectra across various resistors, measured using the two channel cross-correlation method, with calibration of the gain and input resistance. Dashed lines show the theoretical thermal noise. All measurements were taken at room temperature inside a metal box

With these corrections, the measured thermal noise voltages now match what is expected well. All future measurements using this noise setup will use these calibrations. The rapid decrease in measured noise voltage at higher frequencies is due to the limited bandwidth of the op-amps used. Therefore, the setup is best used for measuring spectral noise up to the $\sim 1 - 10$ kHz range. The black curve shows data taken with no resistor connected across the input, and therefore represents the noise floor of the setup. This is far below the expected thermal noise generated by even low-resistance devices.

3.4. Time-domain High-frequency Simulations

There are many different ways to perform electromagnetic simulations. All involve solving Maxwell's equations over a structure, with the structure being defined in terms of material parameters such as permittivity, permeability, and conductivity, to obtain the electric and magnetic fields across

the structure under certain conditions. In general, these are divided into differential solvers and integral solvers, depending on which formulation of Maxwell's equations they solve. They can also be divided into time-domain and frequency-domain. Frequency domain simulations are sometimes preferable when the simulated structure is far smaller than the smallest wavelength of interest, or when only a narrow range of frequencies need be considered [154]. All simulations shown here however used a time domain method as it allows broadband frequency behaviour to be extracted from a single run of the simulation.

Simulations were performed using *CST Studio Suite* [155]. The time domain method used is the finite integration technique, which uses the integral form of Maxwell's equations. Firstly, the simulated structure is broken down into a 3D mesh (the 'primary' mesh). A secondary mesh is also created, with the edges of each cell being normal to the faces of each cell in the primary mesh. When performing simulation, the electric field and magnetic flux are defined on the primary mesh while the magnetic field and electric flux are defined on the secondary grid [154, 155]. The simulation is performed by repeatedly stepping through a small time interval. At each step, the flux and fields are calculated from the previous values, using discrete forms of integral Maxwell's equations. These use discretized forms of the curl and divergence operators, describing how change in flux corresponds to total field around the cell face perimeter, and charge corresponds to the divergence in field. In [155] the derivation of these from the integral forms of Maxwell's equations is outlined. Material properties such as permittivity and permeability are defined per cell in the simulation model, and can be set programmatically. This allows for materials with dispersive properties to be simulated accurately.

C*ST Studio Suite*'s High Frequency Module [155] provides a graphical interface to construct and configure a solid structure and to set up the simulation using desired settings. Structures are meshed automatically using a hexahedral mesh, with mesh cells being conformed to structure edges. The hexahedral mesh consists of parallel lines of varying separation in each dimension, creating array of

rectangular cells. To aid the mesh generation, some simulation areas were defined to have a higher mesh density than the rest of the simulation. This includes the areas around the graphene sheets boundaries, and the antenna feed gap. Because higher mesh density generally gives a more accurate simulation, this allows for the smallest feature sizes and more critical areas to be meshed with a higher density and therefore improve accuracy without drastically increasing total the number of mesh cells. The total number of mesh cells was managed carefully, in order to allow simulations to be performed over a reasonable timescale while not sacrificing accuracy.

In order to have reasonable simulation accuracy, a number of mesh cells must span every object's thickness in each direction. Due to graphene's extremely low thickness, at roughly 0.34 Å, modelling a sheet of monolayer graphene as a 3D object with permittivity and permeability would cause the minimum cell size to be extremely small, sub-10^{-11} m. The Courant–Friedrichs–Lewy criterion for simulation stability [156] means that the simulation time step depends on the smallest dimension of any single mesh cell. Therefore the presence of a thin sheet such as this massively shortens the time step, which significantly increases the computational cost of the simulation. An alternative approach is instead to model the graphene sheet as a 2D sheet with frequency-dependent resistance. By using Equation 14, the conductivity of graphene, modelled as a 2D sheet with negligible thickness, can be calculated as a function of frequency taking chemical potential, relaxation time, and temperature as parameters. Then, the dispersive sheet resistance is obtained by taking the inverse. This allows the simulation to be performed much faster than by considering the graphene as a thin but 3D object. CST studio contains macros to define the 'tabulated surface impedance' of a graphene material, and uses both interband and intraband contributions [155], as derived from Equation 11. However, as described in section 2.1.4 in the frequency range of interest only the intraband contribution need be considered, which is given by Equation 14. Within CST, surface impedances are modelled with zero thickness and

as opaque in the normal direction. Calculations are performed using a multi-pole model fitted to the tabulated impedance data [155].

4. Graphene Ballistic Rectifiers

As detailed in Section 2.4.1, the GBR is a planar four-terminal rectifier which uses the high carrier mobilities, and hence long mean-free paths, in graphene. Weakly nonlinear ballistic transport [127] alongside a vertically asymmetric structure causes DC bias to build up at a particular output terminal, regardless of input current direction. While the theory of operation for the semiconductor 2D electron gas ballistic rectifier has been derived, no such theory exists for the graphene ballistic rectifier, where the lack of bandgap means that both carriers contribute simultaneously to output. In this chapter the theory is re-derived for graphene and extended to account for both carriers. Following this, the theory is verified by comparison to real devices of various structures, and then used to predict the performance of more optimised devices. Arrays of GBRs are then tested and compared to individual devices, with the aim of reducing impedance mismatch losses, and finally the performance and noise of GBRs fabricated from CVD graphene is tested.

4.1. Expanded Theory of Operation

The theory of operation for BRs previously derived by A. Song [127] deals with the case of a 2D electron gas formed using semiconductor heterostructures, with only one type of carrier present. Due to graphene's nature as a semi-metal however, both electrons and holes are simultaneously present in the channel unless a large gate bias is applied. This must be taken into account, because carriers of different charge have opposite effects on the BR's output voltage. One key advantage of graphene is that the carrier density is tuneable by an external electric field (known as electrostatic doping), allowing device performance to me modified. For this reason, it is highly desirable to know the full dependence of the GBR output on gate voltage. In the theory derived here, the first half is similar to that in [127], but with some key differences. The new contributions here are the addition and modification of some graphene-relevent terms in the derivation of the output voltage due to a single character, as well as

the combination of both carriers' contributions. This derivation is as published in my article, reference [69].

The Büttiker-Landauer formula for current I_α through probe α is

$$I_\alpha = \frac{2e}{h}\sum_\beta \left(T_{[\alpha\to\beta]}\mu_\alpha - T_{[\beta\to\alpha]}\mu_\beta\right), \quad \text{Equation 33}$$

where $T_{[\alpha\to\beta]}$ is the transmission probability from probe α to probe β and μ_α is the chemical potential at probe α. Noting that within each pair of probes, only carriers from the one with greater chemical potential contribute to conduction, the equation becomes

$$I_\alpha \approx \frac{2e}{h}\sum_{\beta\neq\alpha} T_{[\beta,\alpha]}(\{\mu\})\left(\mu_\alpha - \mu_\beta\right), \quad \text{Equation 34}$$

where $T_{[\beta,\alpha]}$ is given by $\int_{\mu_\beta}^{\mu_\alpha} T_{[\alpha\to\beta]}(E,\{\mu\})\, dE/(\mu_\alpha - \mu_\beta)$ when $\mu_\alpha > \mu_\beta$ and by $\int_{\mu_\alpha}^{\mu_\beta} T_{[\beta\to\alpha]}(E,\{\mu\})\, dE/(\mu_\beta - \mu_\alpha)$ when $\mu_\alpha < \mu_\beta$, and represents the transmission coefficient for carriers at the chemical potential. Here, E is carrier energy, and $\{\mu\}$ is the chemical potentials at all probes. In the absence of high fields, $|\mu_\alpha - \mu_\beta|$ is small, so the dependence of $T_{[\beta,\alpha]}$ on energy within this range can be ignored, massively simplifying $T_{[\beta,\alpha]}$ to be simply a function of $\{\mu\}$.

In the ballistic rectifier, the transmission probabilities depend on the angular distribution of carriers emitted from the QPCs. According to Landauer's theory, this depends on the self-consistent field $U(\boldsymbol{x},\{\mu\})$. However, this can be closely approximated by considering the effect of the applied current on the angular distribution. Therefore, Equation 34 reduces to give

$$I_\alpha \approx \frac{2e}{h}\sum_{\beta\neq\alpha} T_{[\beta,\alpha]}\left(I_{[\beta,\alpha]}\right)\left(\mu_\alpha - \mu_\beta\right). \quad \text{Equation 35}$$

The above is true for any form of ballistic rectifier, but the derivation from this point is specific to a graphene ballistic rectifier. It uses the design of a GBR with triangular scattering centre, but can be applied to other designs as described in Section 4.2.1.

When the source-drain current in a graphene ballistic rectifier is $I_{SD} = 0\ \mathrm{A}$, the angular distribution of carriers emitted by a QPC is given by

$$P(\theta) = \frac{1}{2}\cos(\theta), \qquad \text{Equation 36}$$

where θ is the carrier trajectory away from the QPC normal, and is in the range $-\pi/2 < \theta < \pi/2$ [126]. This is shown in Figure 25.

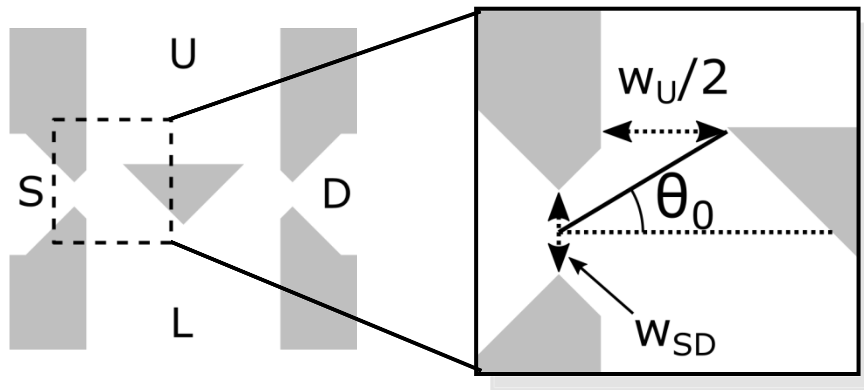

Figure 25: Schematic of a ballistic rectifier with a triangular scattering centre. The zoomed-in view shows the area around the source quantum point contact. The definition of θ_0 is from the QPC normal to the top edge of the scattering centre. w_{SD} is the source (and drain) QPC width, and w_U is the *total* width of the upper contact QPCs. Adapted from [69].

In graphene, the angle of a carrier can be stated as a function of its momentum components in the plane, because $\theta = \arctan(k_y/k_x)$. If θ_0 is the top edge of the scattering centre as shown in Figure 25, then any carriers directed towards θ_0 or below are redirected towards the lower contact (L), while others are redirected towards U. Therefore, the transmission probabilities from S and from D to U and to L can be described by

$$T_{S\to L}(0) = T_{D\to L}(0) = \int_{-\frac{\pi}{2}}^{\theta_0} \frac{N_{SD}}{2}\cos(\theta)\,d\theta = \frac{N_{SD}}{2}[1+\sin(\theta_0)]$$

and

Equation 37

$$T_{S\to U}(0) = T_{D\to U}(0) = \int_{\theta_0}^{\frac{\pi}{2}} \frac{N_{SD}}{2}\cos(\theta)\,d\theta = \frac{N_{SD}}{2}[1-\sin(\theta_0)],$$

where N_{SD} and N_{LU} represent the numbers of modes in the source/drain and upper/lower QPCs respectively. In graphene's dispersion relation, as shown in Figure 4, there is an extra source of degeneracy between the K and K' valleys (known as valley degeneracy [20]. Taking this into account, the number of modes in the source and drain QPCs is given by $N_{SD} = {}^{2}/_{\pi}\, k_f w_{SD} = 2w_{SD}\sqrt{n/\pi}$. When a small current is applied to the device, the angular distributions of carriers emitted from S and D change. (In this portion of the derivation, electrons are assumed as the majority carrier, therefore carriers are being emitted by the source). The angle of ejection of a given carrier changes from $\arctan\left(\frac{k_y}{k_x}\right)$ to $\arctan\left(\frac{k_y}{k_x+\Delta k}\right)$. Because of this, the transmission probabilities from S to U and to L change to

$$T_{S\to L}(I_{SD}) = \frac{N_{SD}}{2}[1+\sin(\theta_e)],$$
$$T_{S\to U}(I_{SD}) = \frac{N_{SD}}{2}[1-\sin(\theta_e)].$$

Equation 38

This angle θ_e ($> \theta_0$) is defined as the angle with which a carrier could be travelling when $I_{SD} = 0$, at which it will be travelling at θ_0 after a current is applied, and therefore is redirected to L instead of U. It is given by $\theta_e = \theta_0 + \arcsin\left[\left(\frac{\Delta k}{k_F}\right)\sin\theta_0\right]$.

From Equation 35, the conductance between two probes is given by

$$G_{\beta\alpha} = \frac{2e^2}{h} T_{[\beta,\alpha]}\big(I_{[\beta,\alpha]}\big).$$

Equation 39

Using this, a four-terminal system such as the GBR produces a 4D conductivity matrix:

$$\begin{pmatrix} I_S \\ I_D \\ I_U \\ I_L \end{pmatrix} = \frac{2e^2}{h} \begin{pmatrix} T_{SS} & -T_{SD} & -T_{SU} & -T_{SL} \\ -T_{DS} & T_{DD} & -T_{DU} & -T_{DL} \\ -T_{US} & -T_{UD} & T_{UU} & -T_{UL} \\ -T_{LS} & -T_{LD} & -T_{LU} & T_{LL} \end{pmatrix} \begin{pmatrix} V_S \\ V_D \\ V_U \\ V_L \end{pmatrix}. \qquad \text{Equation 40}$$

This matrix can be simplified using several facts about the GBR geometry and operation. Firstly, no current flows through the U and L probes, meaning that $I_L = I_U = 0$. In addition, $I_{DS} = -I_{SD} = I_S$, so one row and column can be eliminated. Due to the scattering centre it is also assumed that $T_{SD} = T_{DS} = 0$ and $T_{UL} = T_{LU} = 0$, giving

$$\begin{pmatrix} I_S \\ I_U \\ I_L \end{pmatrix} = \frac{2e^2}{h} \begin{pmatrix} T_{LS} + T_{US} & -T_{US} & -T_{LS} \\ -T_{US} & T_{UU} & -T_{UU} + T_{US} + T_{DU} \\ -T_{LS} & -T_{UU} + T_{US} + T_{DU} & T_{LS} + T_{DL} + T_{UU} - T_{US} - T_{DU} \end{pmatrix} \begin{pmatrix} V_S \\ V_U \\ V_L \end{pmatrix}, \qquad \text{Equation 41}$$

where $T_{UU} = N_U = 2k_F w_U/\pi$, and w_U is the width of the U terminal as shown in Figure 25. The inverse of this matrix is the resistance matrix, from which we can determine $R_{SD,UL}$, which is the objective. Thankfully, not all terms of the resistance matrix are necessary for this:

$$R = G^{-1} = \frac{h}{2e^2}\frac{1}{D_T} \begin{pmatrix} \cdots & \cdots & \cdots \\ T_{DL}T_{US} - T_{LS}T_{UD} + T_{LS}T_{UU} - T_{UL}T_{US} + T_{US}T_{UU} - T_{US}^2 & \cdots & \cdots \\ T_{LS}T_{UU} - T_{UL}T_{US} + T_{US}T_{UU} - T_{US}^2 & \cdots & \cdots \end{pmatrix}, \qquad \text{Equation 42}$$

with these two terms being the only necessary ones. The value D_T is the determinant of the reduced conductance matrix. Then, we use $R_{SD,UL} = V_U - V_L/(-I_S) = -R_{US} + R_{LS}$ and simplify to give

$$R_{SD,UL} = \left(\frac{2e^2}{h}\right)^2 \frac{1}{D_T}(T_{LS}T_{DU} - T_{DL}T_{US}). \qquad \text{Equation 43}$$

Then, using Equation 38 to express these transmission probabilities in terms of device geometry, this becomes

$$R_{SD,UL} = \left(\frac{2e^2}{h}\right)^2 \frac{N_{SD}^2}{2D_T}[\sin(\theta_e) - \sin(\theta_0)]. \qquad \text{Equation 44}$$

The value of D_T, the determinant of the reduced conductance matrix, can then be found using $D_T = G_{SS}(G_{UU}G_{LL} - G_{UL}G_{LU}) - G_{SU}(G_{US}G_{LL} - G_{UL}G_{LS}) + G_{SL}(G_{US}G_{LU} - G_{UU}G_{LS})$, which simplifies to give

$$D_T = \left(\frac{2e^2}{h}\right)^3 N_{SD}^2 \left[N_U - \frac{1}{2}N_{SD}(1 - \sin\theta)^2\right]. \quad \text{Equation 45}$$

Therefore, the four terminal resistance can be expressed as

$$R_{SD,UL}(I_{SD}) = \frac{h}{2e^2}\frac{\sin\theta_e - \sin\theta_0}{2N_U - N_{SD}(1 - \sin\theta_0)^2}. \quad \text{Equation 46}$$

When $\Delta k \ll k_f$, it can be easily shown that $(\sin\theta_e - \sin\theta_0) \approx \frac{\Delta k}{2k_f}\sin(2\theta_0)$. Using this alongside $\frac{\Delta k}{k_f} = \frac{I_{SD}}{w_{SD}nev_f}$, the output voltage due to a single carrier is given by

$$V_{UL} = \frac{h\sqrt{\pi}}{4e^3 v_f w_{SD}}\frac{\sin(2\theta_0)}{2w_U - w_{SD}(1 - \sin(\theta_0))^2}\frac{I_{SD}^2}{n^{3/2}}, \quad \text{Equation 47}$$

where n is the carrier density. This equation is similar to the one derived for BRs in semiconductor 2D electron gasses [127], but with differences due to the nature of graphene. It predicts a quadratic relationship between input current and output voltage, matching reported results [49, 50]. This only considers the existence of a single carrier however, so must now be modified to account for both carriers.

As previously discussed, graphene's lack of a bandgap means that spatial charge inhomogeneities and thermally generated carriers cause electrons and holes to coexist in the device when the graphene is biased to be within the vicinity of the Dirac point. Due to the assumptions of the Büttiker-Landauer formalism that carriers are non-interacting (which can be assumed true for graphene [70]), it is sufficient to consider the effects of electrons and holes on the output voltage separately. As explained in Section 2.1.3, the carrier densities in graphene can be expressed as $n, p \approx \frac{1}{2}\left(\pm n_{cv} + \sqrt{n_{cv}^2 + 4n_0^2}\right)$,

with the electron density n taking the negative sign and the hole density p taking the positive sign. The relative contribution of each carrier to conductivity in the device depends on the number of carriers injected from the reservoirs at the S and D contacts (where conduction is assumed to not be ballistic due to the larger length scales). Therefore, the current can be split into electron and hole contributions depending on their relative densities and mobilities:

$$I_{SD} = I_n + I_p = I_{SD}\frac{\mu_e n}{\mu_e n + \mu_h p} + I_{SD}\frac{\mu_h p}{\mu_e n + \mu_h p}, \quad \text{Equation 48}$$

where μ_e and μ_h are the electron and hole mobilities respectively. Therefore, with constant applied current I_{SD}, the composition varies as a function of the relative carrier densities and hence as a function of gate voltage, as shown in Figure 26.

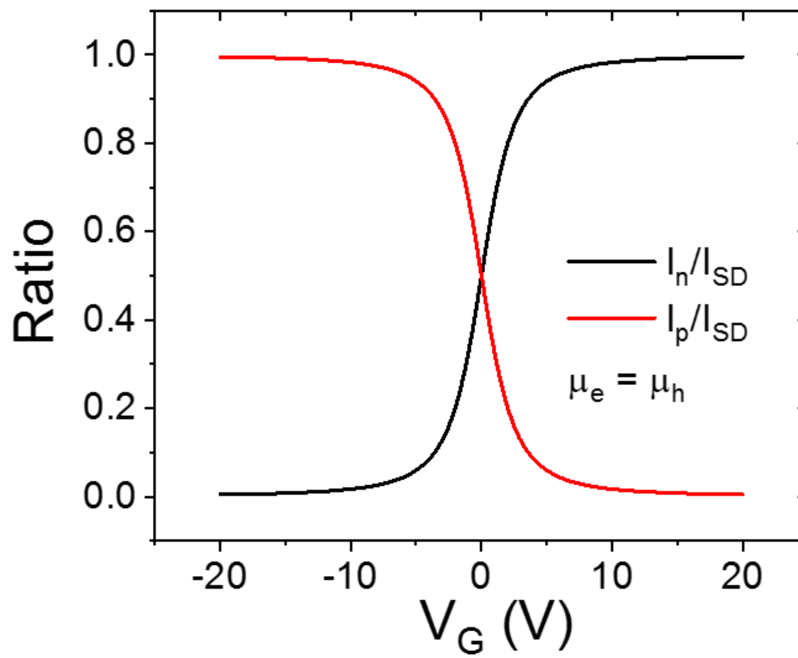

Figure 26: Composition of source-drain current in terms of electron current I_n and hole current I_p, as a function of gate voltage, assuming the electron and hole mobilities are equal and the graphene's NP is at 0 V. Reproduced from [69].

Therefore, taking into account the contributions from both types of carriers, the GBR output voltage can be written as

$$V_{UL} = \frac{h\sqrt{\pi}}{4e^3 v_f w_{SD}} \frac{sin(2\theta_0)}{2w_U - w_{SD}(1 - sin(\theta_0))^2} \left(\frac{\boldsymbol{I_n^2}}{\boldsymbol{n^{3/2}}} - \frac{\boldsymbol{I_p^2}}{\boldsymbol{p^{3/2}}}\right). \qquad \text{Equation 49}$$

In this equation, only the bold section depends on applied gate voltage. The preceding terms are constants, depending only on material properties and device geometry. From here, we can compare the electron and hole contributions, and see the predicted resultant output for an example GBR, shown in Figure 27. The output has two peaks as a function of gate voltage, one positive and one negative, which will be referred to as the electron peak $(V_G > 0)$ and the hole peak $(V_G < 0)$, showing how the output direction depends on the majority carrier in the device.

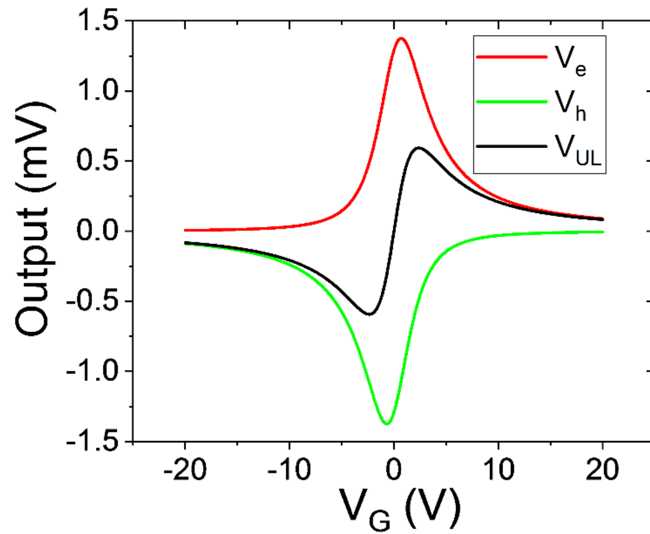

Figure 27: Calculated output components due to electrons, holes, and the total output for an example GBR, as a function of gate voltage using Equation 49. For this calculation equal electron and hole mobilities were used, with $n_0 = 1 \times 10^{11} \text{cm}^{-2}$, a 290 nm SiO_2 substrate, and with the graphene's NP being at $V_G = 0$ V. Reproduced from [69].

This dependency can be seen in real GBR output data, shown later for several devices in Figure 33. Substituting in Equation 7 and Equation 48, we obtain the full output voltage dependency on gate voltage:

$$V_{UL} = A_{const} B_{geo} \frac{I_{SD}^2}{C_G^{3/2}} \frac{r^2 \sqrt{V_A + \sqrt{{V_A}^2 + \frac{Q_{th}^2}{C_G^2}}} - \sqrt{-V_A + \sqrt{{V_A}^2 + \frac{Q_{th}^2}{C_G^2}}}}{\left((r-1)V_A + (r+1)\sqrt{{V_A}^2 + \frac{Q_{th}^2}{C_G^2}} \right)^2}, \qquad \text{Equation 50}$$

where $A_{const} = \frac{h\sqrt{\pi}}{\sqrt{2}e^{\frac{3}{2}}v_f}$ is a physical constant, $B_{geo} = \frac{\sin(2\theta_0)}{w_{SD}(2w_U - w_{SD}(1-\sin(\theta_0))^2)}$ depends purely on the device geometry, $V_A = V_G - V_{G0}$ is the gate voltage offset from the NP, $r = \mu_e/\mu_h$ describes the ratio of the electron and hole mobilities, and $Q_{th} = 2n_0 e$ represents the total free charge density at the NP. Because the GBR is affected by carrier mixing, the output depends strongly on the value of n_0, the neutrality point carrier density which is given in Equation 8. Figure 28 shows calculated GBR output curves using the same conditions as for Figure 27, but with three different values of n_0.

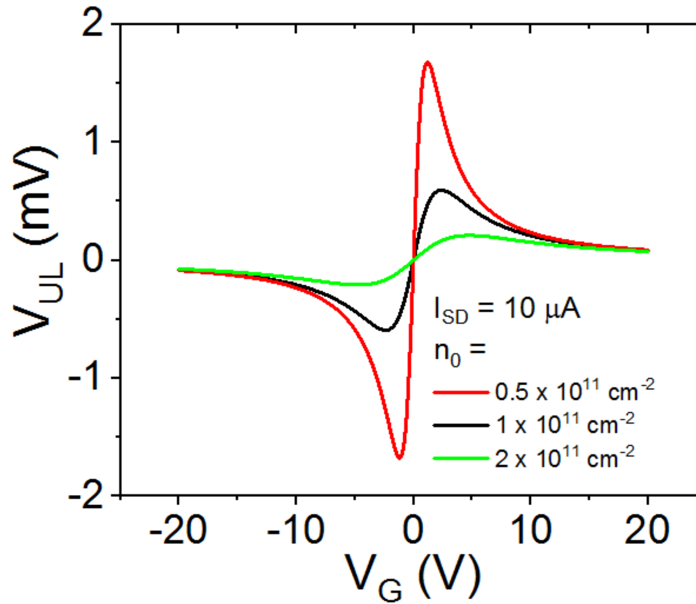

Figure 28: Calculated GBR outputs as a function of gate voltage, with a NP of 0 V. Three different values of n_0 are used for the calculations, which all use $r = 1$ and a 290 nm SiO_2 substrate.

As can be seen from Equation 8, n_0 depends both on spatial charge inhomogeneities and on temperature. Variation in the output due to different n_0 can be due to either of these factors, with for

example lower temperature corresponding to a lower value of n_0, decreasing carrier mixing. This causes both output peaks to increase in magnitude, with their positions moving towards the NP. The value of r determines the symmetry of the GBR output. When r is close to 1, the electron and hole components are of roughly equal magnitude. When $r > 1$, the electron component is greater, increasing the magnitude of the electron peak and moving its position towards lower (and possible negative, if r is large enough) V_A. Conversely, when $r < 1$, the hole component is greater, moving the hole peak and increasing its magnitude. This can be seen from calculations in Figure 29(a), and in example data obtained from real devices in (b).

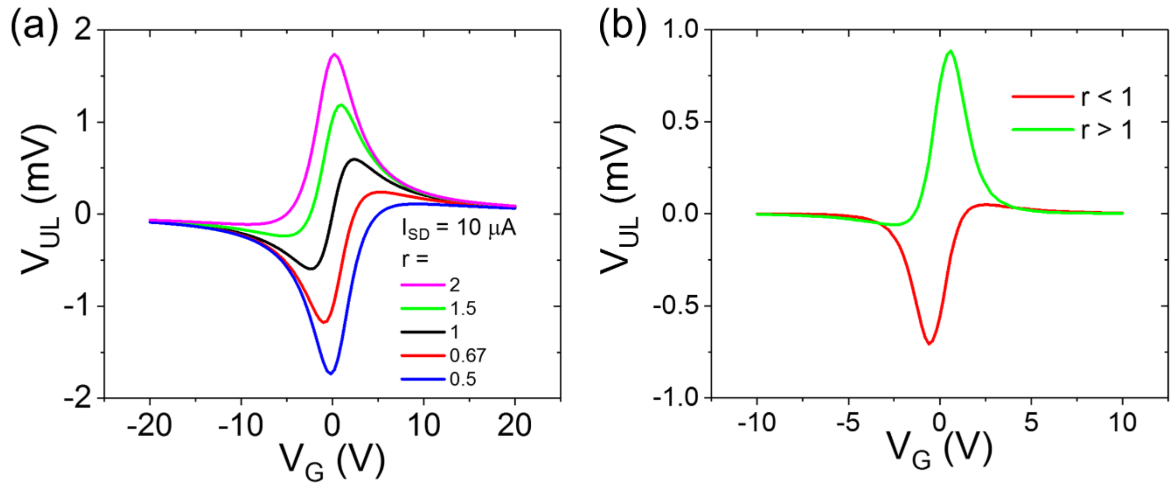

Figure 29: The effect of relative carrier mobility on GBR output. (a) Calculated GBR output voltage as a function of gate voltage, with different values of r, the electron/hole mobility ratio. For this calculation, $n_0 = 1 \times 10^{11} \mathrm{cm}^{-2}$ and a 290 nm SiO_2 substrate was used, with the graphene's NP being at $V_G = 0$ V. (a) is adapted from [69], supplementary materials. (b) shows example data from real GBRs, with large and with small mobility ratios ($r = \mu_e/\mu_h$).

Therefore in order for the peak output voltage and hence the responsivity to be maximised, a large disparity in electron and hole mobilities is desirable. Another parameter with a large effect on the output magnitude is B_{geo}, which depends on device geometry. From this, it is easy to see that smaller values of w_{SD} and w_U are desirable, and that values of θ_0 around $45°$ give maximum output. These

device parameters offer guidance to future development of GBRs; responsivity can be improved by constructing devices with smaller quantum point contacts and a large difference in carrier mobilities.

4.2. Modified GBR designs

The theory of GBR operation given in the previous section was derived using the geometry of a GBR with a triangular scattering centre. However, this is not the only GBR design to have been investigated [49]. By manipulating the position and orientation of the two input QPCs, along with the two sides of the triangular scattering centre, different GBR designs can be produced. If the assumptions made during the derivation of the above theory still hold for the newly produced designs, they should give roughly similar output characteristics to the GBR with triangular scattering centre.

4.2.1. Designs

Four designs of GBR have been produced, labelled A-D in Figure 30. Device A is the GBR design with triangular scattering centre, as shown in Figure 25. In this GBR design the most important features for operation are the width and design of the source and drain QPCs, and the scattering centre. However, only the bottom two edges of the triangle are relevant for scattering carriers, meaning that if the triangle were reduced to two etched lines at the positions of these edges the scattering behaviour should be maintained. This is shown in Figure 30 as device B. The design can be simplified further by rotating each QPC by $45°$, along with its corresponding scattering edge, such that the scattering edges lie on top of each other, meaning that only a single etched line is needed. This is denoted as device C. Alternatively, by rotating each QPC and scattering edge by $22.5°$ they can be positioned such that each scattering edge overlaps with the opposite sidewall. This means that the scattering centre can be eliminated completely, resulting in device D.

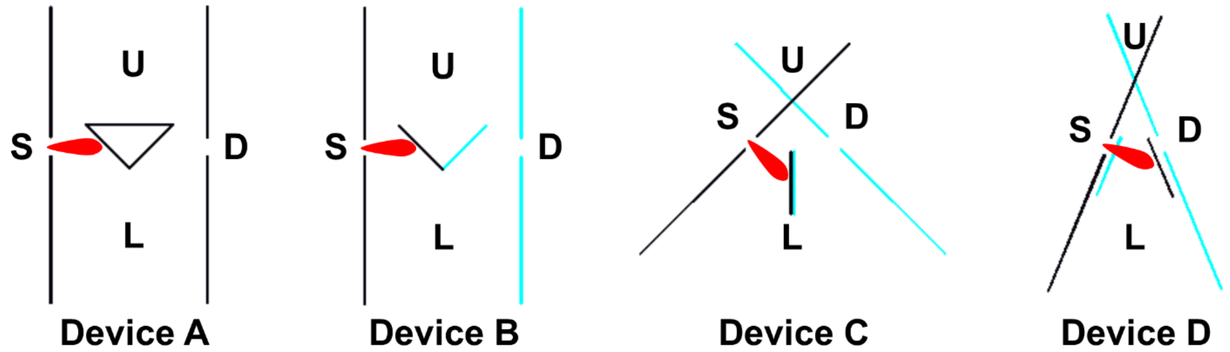

Figure 30: Four GBR schematics, showing how the positions of the input source and drain QPCs, along with the scattering edges, can be manipulated while maintaining the angle between them. A representation of the electron momentum angular distribution is also shown from the source QPC. Reproduced from [69].

Using the schematics shown in Figure 30, four GBR designs have been produced, and used to fabricate devices using hBN-encapsulated graphene using the methods shown in Section 3.1. Figure 31(a) shows the designs used, with grey areas representing where the hBN/graphene/hBN stack has been etched.

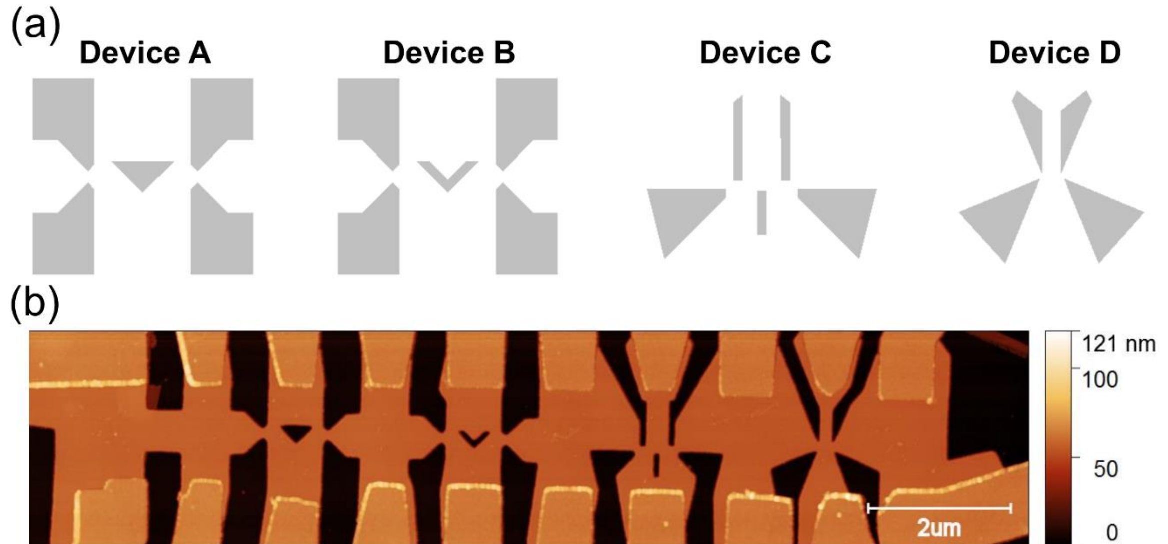

Figure 31: (a) Designs of four GBRs fabricated, using the schematics shown in Figure 30. (b) An AFM image of the fabricated GBRs, which are constructed using an etched hBN/graphene/hBN stack. A Hall bar was fabricated in the far left of the sample, followed by devices A-D from left to right. Reproduced from [69].

Figure 31(b) is an atomic force microscopy (AFM) image of the devices fabricated using the above designs. The four devices are denoted as devices A-D, corresponding to designs A-D, and are visible from left – right in the AFM image. To the left of device A is a Hall bar, which has been used to calculate the carrier mobilities on the sample (see Figure 32). The source, drain and upper contact QPC widths are important for the device characteristics. Because the feature sizes of these devices is near the resolution limit of the electron-beam lithography system used, there is some variation in contact width between devices. Table 1 shows the quantum point contact widths for each device, measured using the AFM image shown in Figure 31(b).

Table 1: Quantum point contact widths of the devices shown in Figure 31, measured from the AFM image. Reproduced from [69], supplementary materials.

Device	w_{SD} (nm)	w_U (nm)
A	140 ± 5	395 ± 5
B	150 ± 5	395 ± 5
C	135 ± 5	330 ± 5
D	165 ± 5	180 ± 5

4.2.2. Measurements and Analysis

All measurements shown here were taken in a vacuum. Using the Hall bar visible in Figure 31(b) with four contacts, the encapsulated graphene's conductance was measured as a function of gate voltage. The sheet conductance is shown in Figure 32. Equation 9 was used to calculate the carrier mobilities, using the gradients at low carrier densities, giving values of $86{,}700\ \mathrm{cm^2/Vs}$ for electrons and $57{,}500\ \mathrm{cm^2/Vs}$ for holes.

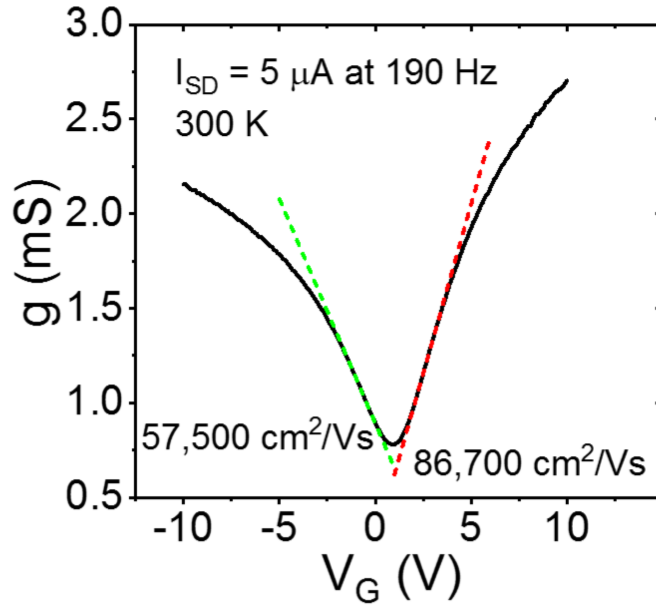

Figure 32: Sheet conductance of the encapsulated graphene sample used to fabricate different GBR designs, measured using four probe AC measurements at room temperature in a vacuum. The carrier mobilities have been calculated using gradients taken at low carrier densities, as shown. Reproduced from [69], supplementary materials.

By using Equation 10, the mean free path of carriers was calculated to be up to 0.64 μm at room temperature.

A constant AC current was applied between the source and drain contacts of each device, with the DC output measured between the U and L contacts. At S and D, two additional probes were used with a lock-in amplifier in order to measure the voltage drop across the device and hence its input conductance. The measured output voltage V_{UL} as a function of back gate voltage is shown for devices A-D in Figure 33(a). It can be clearly seen that each device's output shows two peaks, one negative in the hole transport region and one positive in the electron transport region. This is in agreement with the GBR theory of operation.

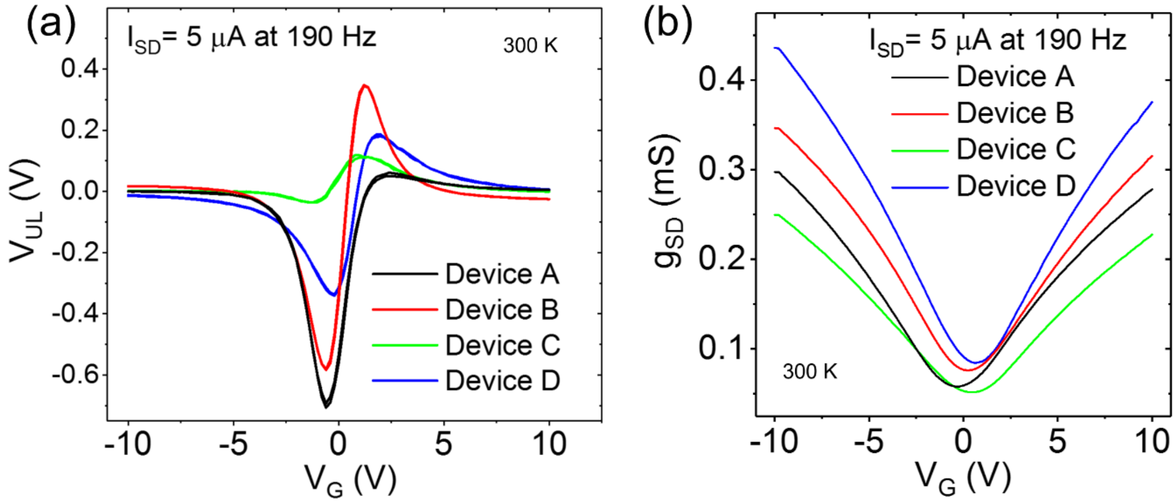

Figure 33: (a) Output characteristics of GBRs fabricated using designs A-D, measured using a constant input AC signal at room temperature in a vacuum. (b) Source-drain conductance of each device, using the same conditions as in (a). Adapted from [69].

For each device, V_{UL} crosses 0 at a slightly different gate voltage. This is due to slight variation in the NP position across the sample, and hence between each device. It is also partially due to different values of r, the electron/hole mobility ratio, as shown by Figure 29. Each device has a different ratio between electron and hole peak magnitude, again indicating differing values of r across the device. The source-drain conductance of the four devices is shown in Figure 33(b). The input resistance is due to the resistance of the source and drain QPCs, as well as the resistance between the S and D. Device D has the narrowest S-D gap, with no etched scattering centre directly between them. This means it is expected to have the lowest input resistance, matching measurements in Figure 33(b). Using Figure 33(a) and (b), the NP is found to be at around $V_G = +1$ V, although with some variation between devices.

The responsivity of devices A-D has been calculated by

$$\mathcal{R} = \frac{V_{UL}}{P_{SD}} = \frac{V_{UL}}{I_{SD}^2 R_{SD}}, \qquad \text{Equation 51}$$

where P_{SD} is the power received by the device, and using the RMS value of the input current.

Figure 34(a) shows the responsivity of all four devices, calculated using the data in Figure 33. Devices A, B, and D have similar peak responsivities, B having the largest with 2,010 V/W in the hole transport region.

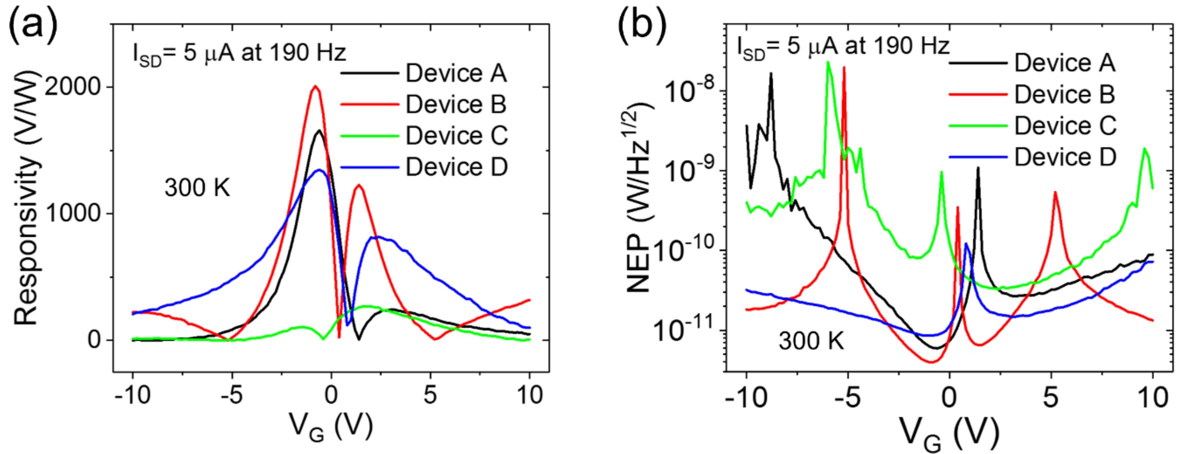

Figure 34: (a) Responsivities of devices A-D as a function of back gate voltage, calculated using the data in Figure 33, which was measured at room temperature at a frequency of 190 Hz. (b) Noise equivalent power of all devices, calculated using the same data. Reproduced from [69].

The GBR's structure has the direction of output (U and L) orthogonal to that of input (S and D), and does not require a DC bias to be applied to either input or output. This means that flicker and shot noise from the input signal will not affect the output. Because no current flows through the output terminals, output noise is only due to thermal noise generated by the U-L resistance [50], which can be calculated using

$$\mathrm{NEP} = \sqrt{4\mathrm{kTR_{UL}}}/\mathcal{R}. \qquad \text{Equation 52}$$

Figure 34(b) shows the NEP of each device as a function of gate voltage. Devices A, B, and D all show a minimum NEP of below 10 $\mathrm{pW/Hz^{1/2}}$, corresponding to the gate voltages which give maximum responsivity.

Devices fabricated with the four designs show similar characteristics, with all differences attributable to imperfections in device fabrication and spatial variation in parameters like carrier

mobility and NP. While device B has a slightly higher peak responsivity than the others, device D has only a slightly lower responsivity while boasting the smallest input resistance. Input resistance is a key factor for high frequency rectifiers, which must be minimised in order to reduce efficiency losses due to impedance mismatch with antennas. For this reason, design D has been investigated in more detail in the rest of this section and in the following section.

In Figure 35(a) the output voltage of device D is shown as a function of back gate voltage at room temperature in a vacuum, with 190 Hz input currents of varying magnitude. As expected, the output voltage increases with increasing input current amplitude, with the V_G position of each output peak remaining constant. This is in agreement with Equation 50, in which I_{SD}^2 is simply a multiplier to the output voltage. The point where the output crosses zero also remains constant.

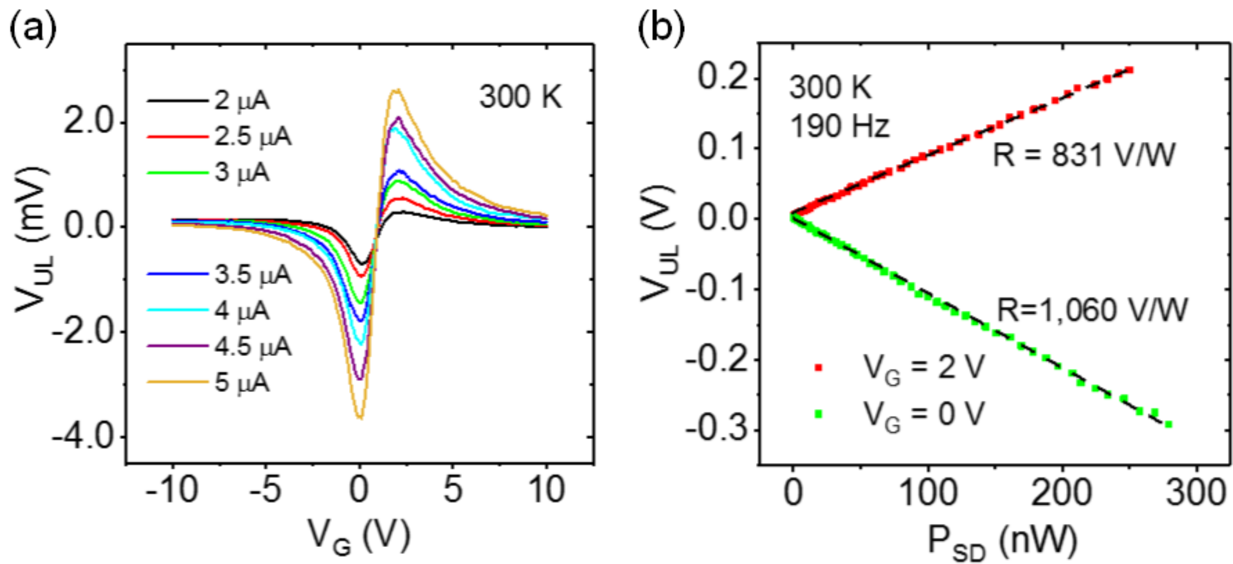

Figure 35: Room temperature output characteristics of device D. (a) Output voltage as a function of gate voltage, at different input current amplitudes at 190 Hz. (b) Output voltage as a function of input power with a 190 Hz input, in the electron and the hole conduction regions, showing the responsivities. Reproduced from [69].

Figure 35(b) shows the output voltage of device D as a function of input AC power P_{SD}, measured at room temperature and 190 Hz. Two gate voltages are shown, roughly corresponding to the output peaks in the electron and hole regions. There is a strong linear relationship between V_{UL} and P_{SD} at

both gate voltages, giving constant responsivities of 1060 V/W in the hole transport regime and 831 V/W in the electron transport regime, in agreement with the values from Figure 34(a) at these gate voltages. It is likely that this performance will be somewhat worse at higher frequencies, however the planar nature of the GBR means that it is likely to have a high cut-off frequency compared to devices such as Schottky diodes and therefore the device is still expected to perform well into the THz region.

4.2.3. Low Temperature Measurement

At lower temperature, the output voltage of a GBR is expected to increase. This is because lower temperature decreases the value of n_{th}, and hence causes lower n_0 as can be seen in Equation 8. This decreases carrier mixing near the NP and hence increases the peak output value, as well as moving the peak's position in V_G closer to the NP. This can be seen directly as a function of n_0 in Figure 28, which is calculated using Equation 50.

Figure 36 shows the output voltage of a device fabricated using design D in Figure 31(a) at different temperatures, with varying gate voltage at a constant input of $2\ \mu A$ at 190 Hz. The peak output magnitude can be seen to increase dramatically with decreasing temperature, as expected.

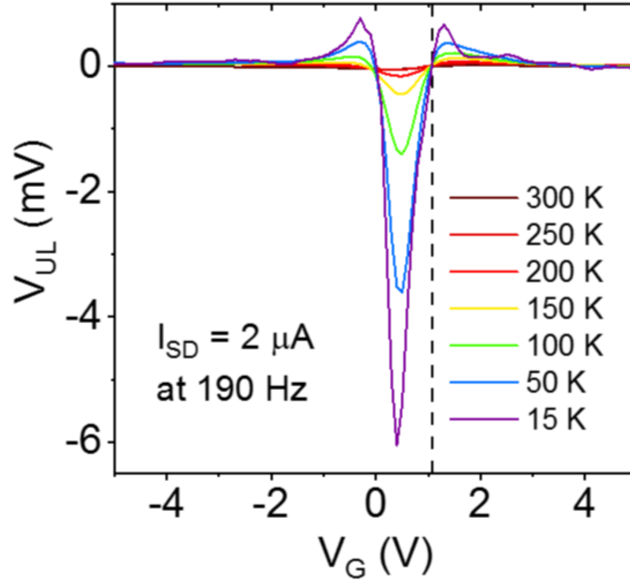

Figure 36: Output voltage of device D at different temperatures as a function of gate voltage, with a constant AC input of $2\ \mu\text{A}$ at 190 Hz. The dotted line shows the position of the carrier neutrality point. Reproduced from [69].

However, the two output peaks do not increase in equal amounts, with the hole peak increasing far more than the electron peak. This discrepancy in peak magnitude may indicate a value of r far less than one, as in Figure 29. However, there is little reason for such a drastic change from room temperature, where the similar peak magnitudes indicates a value of r close to 1. Instead, the reason may lie in the explanation for another unusual feature in Figure 36, which is the appearance of a positive peak in the hole conduction region at around $V_G = -0.3\ \text{V}$ for temperatures below 150 K. It is thought that both of these features in the low temperature output are due to the Seebeck effect, which produces a voltage output in a GBR which is opposite in sign to the rectified output [50]. The input current of $2\ \mu\text{A}$ causes localised heating of the graphene, creating a temperature gradient across the device and hence producing an output voltage. The peaks of this effect do not necessarily lie at the same V_G positions as the peaks in rectified output. In the hole conduction region, the Seebeck effect causes the output voltage to become positive for a small range of gate voltage, before the rectified carriers overcome this effect and dominate the output at around $V_G = 0\ \text{V}$. However, in the electron conduction region the peaks of the rectified output and the Seebeck effect lie at roughly the same value of V_G. Therefore they

subtract, meaning that the Seebeck effect peak is not seen and the rectified output peak is much reduced in magnitude compared to the hole peak. Investigation of this is expected to be somewhat difficult, as both effects are likely to be proportional to the square of input current.

When measured at low temperature with an extremely low input current, the output voltage oscillates as a function of gate voltage. This is shown at a temperature of 15 K in Figure 37(a). The low input current of 1 nA means that (unlike in Figure 36) any carrier heating is negligible, avoiding any contribution to output voltage from the Seebeck effect. While it can be seen that under these conditions the output voltage can be substantially larger than the input voltage, the power available from the output is still substantially lower than the power supplied to the input. As has been previously found for the GBR, these oscillations are likely to be due to changing numbers of lateral quantum confinement modes in the input S and D QPCs [50]. Figure 37(b) shows the first derivative of the output voltage as a function of the graphene's Fermi energy relative to the Dirac point. This shows that the output voltage oscillates periodically with Fermi energy, indicating that these oscillations are not due to traps, and are indeed due to lateral quantum confinement modes in the QPCs.

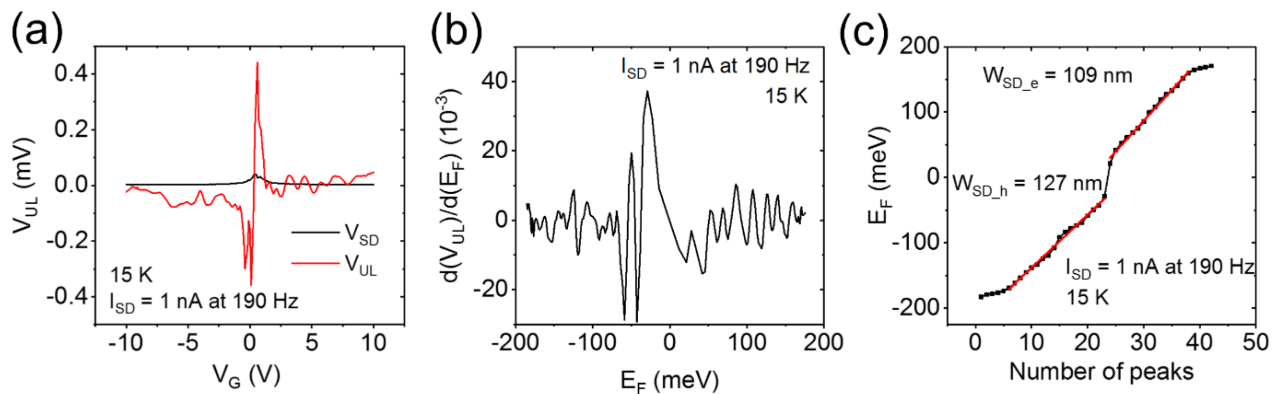

Figure 37: Characteristics and analysis of device D at 15 K, with a low input current of 1 nA at 190 Hz. (a) Output voltage V_{UL} as a function of gate voltage, with the input voltage V_{SD} also shown for comparison. (b) First derivative of the output voltage data shown in (a), as a function of graphene Fermi energy. It has been confirmed by repeated measurements that these oscillations are real characteristics of the device and not noise. Due to this and the high-resolution low-noise data, the use of

a numerical derivative is justified. (c) Increase of Fermi energy with cumulative number of peaks in the data shown in (b), with linear dependence marked. Reproduced from [69].

This periodicity of oscillation is shown in Figure 37(c), which clearly shows that the cumulative number of peaks has a linear relationship with Fermi energy. Because the oscillations are due to lateral quantum confinement modes in the QPCs, their Fermi energy spacing is given by $\Delta E_F = \hbar v_F \pi / w_{SD}$. Using this, the effective width of the input QPCs for device four is calculated to be 127 nm for holes and 109 nm for electrons at a temperature of 15 K. These widths are less than that measured using an AFM image of this device, as shown in Figure 31(b) and Table 1. The ballistic rectifier operates in the non-linear conduction regime, with high applied fields, especially within the QPCs. These high fields can cause carriers to become trapped by strongly localised edge states which are known to appear at graphene edges [74, 157]. Trapped charges at the graphene edges cause coulomb repulsion, slightly narrowing the effective QPC widths. This effect also enhances the specular edge scattering in etched graphene, as mentioned in Section 2.1.3. The effective QPC widths are narrower for electrons than for holes. This indicates that there are more electron-trapping localised states at the QPC edges than hole-trapping states, causing a slightly larger magnitude of trapped negative charge when in the electron conduction regime than the positive charge in the hole conduction regime. This lowers the effective QPC widths more for electrons than for holes [157].

4.2.4. Fitting Data with Developed Theory

In Section 4.1, the theory of operation of the graphene ballistic rectifier was derived from the Büttiker-Landauer formulisation of coherent transport, taking into account the opposite contributions of electrons and holes. This produced Equation 50, which expresses output voltage V_{UL} as a function of input current I_{SD} and gate voltage – NP offset V_A, with fitting parameters of the electron/hole mobility ratio r, a device geometry factor $B_{geo} = \frac{\sin(2\theta_0)}{w_{SD}(2w_U - w_{SD}(1-\sin(\theta_0))^2)}$, and total free charge density around

the NP $Q_{th} = 2n_0 e$. It also contains a constant A_{const} and the gate capacitance density C_G, which are known. Although B_{geo} is in theory a known parameter, because it depends only on the device geometry, it is included as a fitting parameter because the effective geometry of the device is likely to be different from that of the design, or from measurements from an AFM image. Figure 38 shows fittings using Equation 50 to the output data of devices A-D, all at room temperature, with a constant amplitude input of 5 μA at 190 Hz.

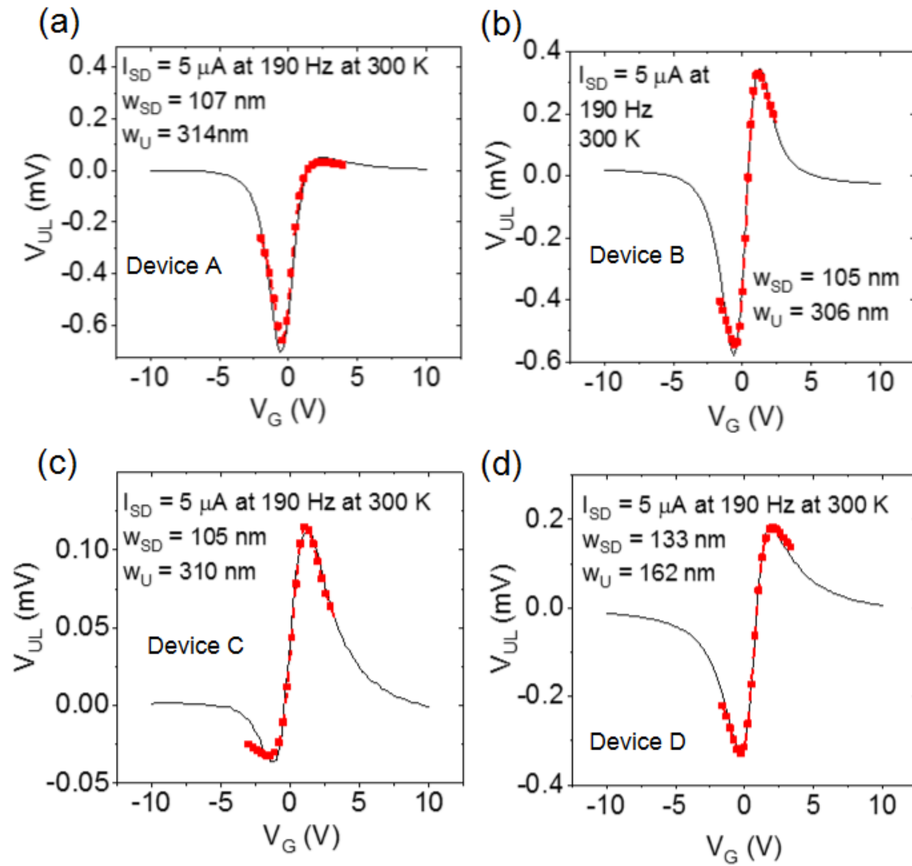

Figure 38: Output voltages of GBRs as a function of gate voltage, with constant current input. (a)-(d) shows devices A-D respectively, with the device designs visible in Figure 31. The red dashed-dotted lines show the fitting to each curve, which have been generated using Equation 50. Reproduced from [69].

Despite the large variation in shape, Equation 50 gives a good fit to each output curve, indicating that the GBR theory derivation given in Section 4.1 is a good description of the characteristics of real GBRs. A slight deviation between the fitting and data for device C appears to be present at just below

$V_G = 5\text{V}$. This small difference is due to being slightly further away from the NP, as well as the lower output of this device making a small deviation look more significant than it really is. Based on measurements of these four devices, each of the modified GBR designs is described well by the developed theory. This indicates that the design modification arguments given in Section 4.2.1 do produce devices with similar output characteristics, with the differences in output voltage shape between devices being due to different values of r, as well as slight variation in n_0 and in NP position. From the fitting parameters obtained, the source/drain and upper QPC widths can be obtained, and the calculated values are shown on the output graphs for each device in Figure 38(a)-(d). These values are consistently narrower than the values measured from the AFM image of the devices, which are given in Table 1. For device D, the value of w_{SD} obtained in the fitting is in relatively good agreement with the values obtained from lateral quantum confinement mode oscillations, as shown in Figure 37(c), which are 109 nm for electrons and 127 nm for holes. This indicates that the fitting parameters can also be used to calculate the effective QPC widths, instead of using AFM images which tend to overestimate the values. One slight complication to the GBR operation that is not considered by the above theory is that the effective contact widths at the S, D, and U QPCs may be slightly different for electrons and holes. This may cause slight discrepancies between the fits and the real device data. From the fitting of device D (Figure 38(d)) the carrier mobility ratio is found to be $r = \mu_e/\mu_h = 0.86 \pm 0.04$. This value is below one, which is why the peak output magnitude is larger in the hole conduction region than the electron region. This is an extremely different value from that obtained from carrier mobilities measured on the Hall bar at the other side of the device, shown in Figure 32, which is 1.51. This indicates that the relative value of the electron and hole mobilities varies substantially across the device, and therefore that the absolute value of each likely varies substantially also. The variation in mobility ratio can also be seen in the different shapes of Figure 38(a)-(d). From the value of Q_{th} obtained from the device 4 fit, the value of n_0 is found to be $(4.0 \pm 0.1) \times 10^{10}$ cm^{-2}. As explained in Section 2.1.3, n_0

depends on the carrier density caused by spatial inhomogeneities, as well as the thermal carrier density n_{th}. At room temperature, the thermal carrier density is $n_{th} = \frac{\pi}{6}\left(\frac{k_B T}{\hbar v_f}\right)^2 = 3.59 \times 10^{10}$ cm^{-2}, meaning that the value of n_0 obtained is close to the minimum possible at room temperature, indicating that the carrier density due to spatial inhomogeneities or 'charge puddles' is low. This is to be expected, because hBN-encapsulated graphene is known to result in far lower charge inhomogeneities than graphene on bare SiO_2 [54, 57].

4.3. Predicted Optimal Devices

Section 4.1 gave a derivation of the operational theory of a graphene ballistic rectifier. This resulted in Equation 50, which gives the expected output voltage of a GBR as a function of input current and gate voltage, with several parameters which arise from device characteristics. As has been shown in Section 4.2.4, this equation can be used to fit the characteristics of real devices with a range of structures, and agrees well with the output characteristics. As well as fitting real device characteristics, Equation 50 can also be used to predict the output voltage of a GBR with a given set of conditions and parameters. This allows predictions to be made of device characteristics, including output voltage, responsivity, and NEP, under optimal conditions. Three sets of device conditions have been considered, with differing values of input QPC width w_{SD}, upper QPC width w_U, and electron/hole mobility ratio r. Each case uses $\theta_0 = 45°$ and assumes a 290 nm SiO_2 gate insulator, with $n_0 = 4.0 \times 10^9 \text{ cm}^{-2}$ as was calculated for device D from the fit in Figure 38, and assumes an NP of $V_G = 0$ V. The predicted output voltage, responsivity, and NEP are shown for each of the three cases in Figure 39(a), (b), and (c) respectively. V_{UL} is obtained directly from the Equation 50, responsivity is calculated using Equation 51 with input resistance calculated from w_{SD}, and NEP is calculated using Equation 50 with output resistance calculated from w_U.

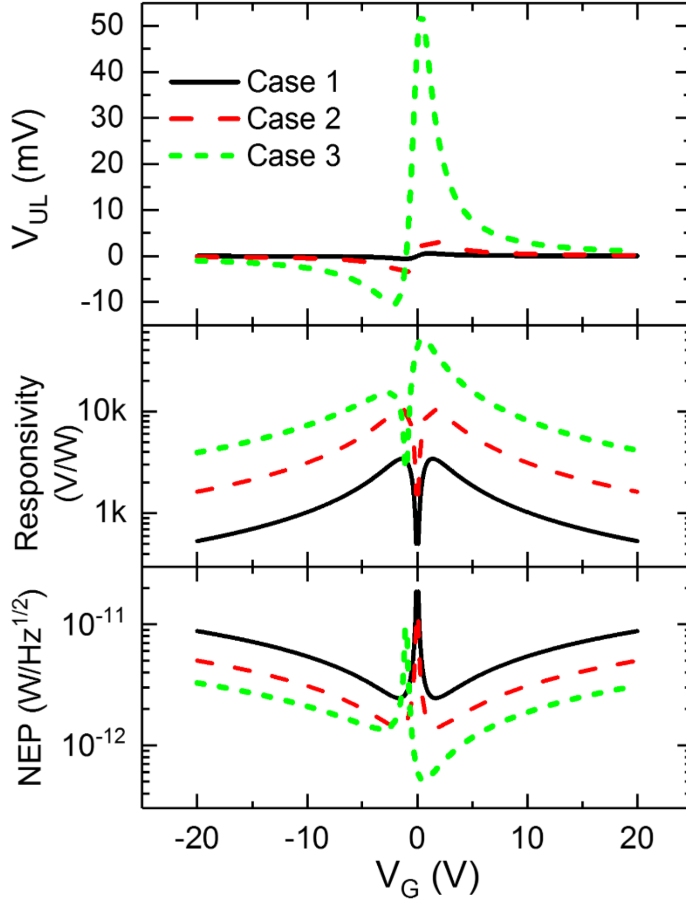

Figure 39: Predicted output characteristics of GBRs using Equation 50, for three different cases of device parameters. Output voltage V_{UL}, responsivity, and NEP are shown as functions of gate voltage V_G. Reproduced from [69].

Case one uses parameters only slightly improved from those of the devices examined in Section 4.2, with $w_U = 150$ nm, $w_{SD} = 100$ nm, and $r = 1$. It gives peak output voltage magnitude of 0.59 mV, symmetrical for both electrons and holes due to having $r = 1$. The maximum calculated responsivity is 3,430 V/W and minimum NEP is 2.46 pW/Hz$^{1/2}$. The second case uses improved geometry with narrower QPCs; both w_{SD} and w_U being 50 nm, and again $r = 1$. Under these conditions, the maximum output voltage increases to 3.6 mV, again symmetrically for both electrons and holes. Peak responsivity increases to 10,400 V/W and minimum NEP decreases to 1.40 pW/Hz$^{1/2}$. The third case uses very narrow QPCs, while still being within the rage of achievable feature sizes, with $w_{SD} = w_U = 20$ nm. In addition, a value of $r = 1.5$ is used. These parameters vastly increase the theoretical output voltage,

reaching a maximum of 52 mV in the electron-dominated region. The value of r being above 1 increases the magnitude of the electron peak, while decreasing that of the hole peak. The maximum responsivity was calculated to be $50{,}800$ V/W with these conditions, with NEP as low as 0.51 pW/Hz$^{1/2}$.

The calculated performance is a considerable improvement on the previously reported best GBR, which was itself one of the best reported room-temperature rectifiers with a peak responsivity $23{,}000\ \mathrm{V/W}$ and NEP of 0.64 pW/Hz$^{1/2}$ [50]. These calculations show how, with device feature size reasonable achievable using the resolution of electron-beam lithography, extremely high responsivities and low NEPs are easily achievable with the graphene ballistic rectifier.

4.4. Ballistic Rectifier Arrays

As well as increasing the performance of individual graphene ballistic rectifiers, an alternative strategy to increasing rectenna performance is to construct arrays of GBRs. These arrays are arranged such that the GBRs are in parallel with each other with respect to the AC input, but in series with respect to the DC output. This offers the major advantage of reducing the total input resistance, therefore reducing power loss due to impedance mismatch when coupled to an antenna.

When the GBRs are arranged with their DC outputs in series, it would at first be expected that the total output voltage would simply be the sum of that of each individual device. This would certainly be the case if they were separate devices, however when GBRs are constructed close together on a graphene flake there may be complications due to, for example, ballistic transport effects.

In an array of n_{arr} identical GBRs, the current passed through each device will be $I_{SD} = {I_{SD,arr}}/{n_{arr}}$. For an individual GBR, as can be seen in Equation 50, the output voltage depends on current as $V_{UL} \propto I_{SD}^2$. Assuming that the total output voltage is simply the sum of each device, the output will be $V_{UL,arr} = n_{arr}\, V_{UL} \propto n_{arr} \times \left({I_{SD,arr}}/{n_{arr}}\right)^2$, giving $V_{UL,arr} \propto {I_{SD,arr}^2}/{n_{arr}}$. Because

the output of a single GBR *with input current equal to* $I_{SD,arr}$ would be $V_{UL} \propto I_{SD,arr}^2$, this means that for the same current input amplitude, the output of an array of n_{arr} devices is expected to decrease by a factor of $1/n_{arr}$. In fact, if the array output is the sum of each device the lowest possible output voltage occurs when current is split equally between each device, which is what is assumed here. Any change from uniform current distribution will cause the total output voltage to be larger.

The responsivity of the array is given by $\mathcal{R}_{\mathrm{arr}} = \frac{V_{UL,arr}}{P_{SD,arr}} = \frac{V_{UL,arr}\, g_{SD,arr}}{I_{SD,arr}^2}$. The array's input conductance is simply given by $g_{SD,arr} = n_{arr} g_{SD}$, meaning that the array's responsivity is $\mathcal{R}_{\mathrm{arr}} = \frac{\frac{V_{UL}}{n_{arr}} \cdot n_{arr} \cdot g_{SD}}{I_{SD,arr}^2} = \frac{V_{UL} \cdot g_{SD}}{I_{SD,arr}^2}$. This is the same as the responsivity of a single device with input current of $I_{SD,arr}$, meaning that in theory the responsivity should be unchanged when constructing an array of GBRs, assuming constant current input.

In order to test this several arrays of 3 GBRs as described above has been fabricated, along with single GBRs of the same design on the same samples. The devices were fabricated using hBN-encapsulated graphene, on a Si/290 nm SiO_2 substrate using techniques shown in Section 3.1. Figure 40 shows an AFM image of a fabricated device.

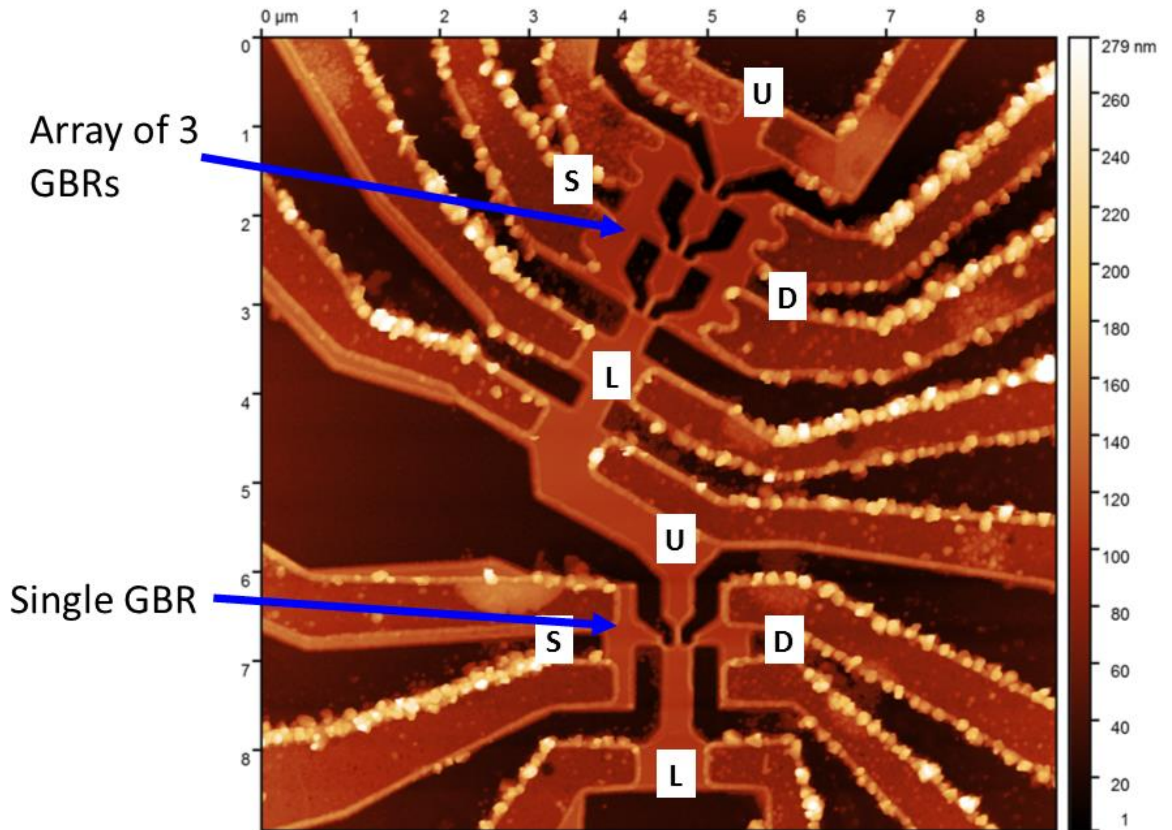

Figure 40: AFM image of an encapsulated graphene GBR sample, consisting of an array of 3 GBRs, a single GBR of the same design, and a Hall bar to be used to calculated the carrier mobilities. Sample is fabricated on a Si/290 nm SiO_2 substrate. Many white circular features are visible on the image, likely due to dirt on the AFM tip. The source (S), drain (D), upper (U), and lower (L) contacts are labelled for the array and for the single GBR.

In the array the GBRs were positioned with a distance of $0.75\ \mu m$ between adjacent devices. The GBR design used was a slight variation of those shown in Section 4.2.1, with QPCs at $45°$ to the device axis and vertical opposite sidewalls scattering carriers towards the L contact. In Figure 40 the source, drain, upper, and lower contacts are marked for the single GBR and for the GBR array, with each having two 1D contact metal probes for elimination of contact resistance.

Figure 41 shows the S-D conductance of a single device and of an array on the same sample, measured at room temperature in a vacuum as a function of input AC amplitude at 190 Hz. The

conductances are both found to be mostly independent of input amplitude; however a slight rise of conductance can be seen for the single GBR.

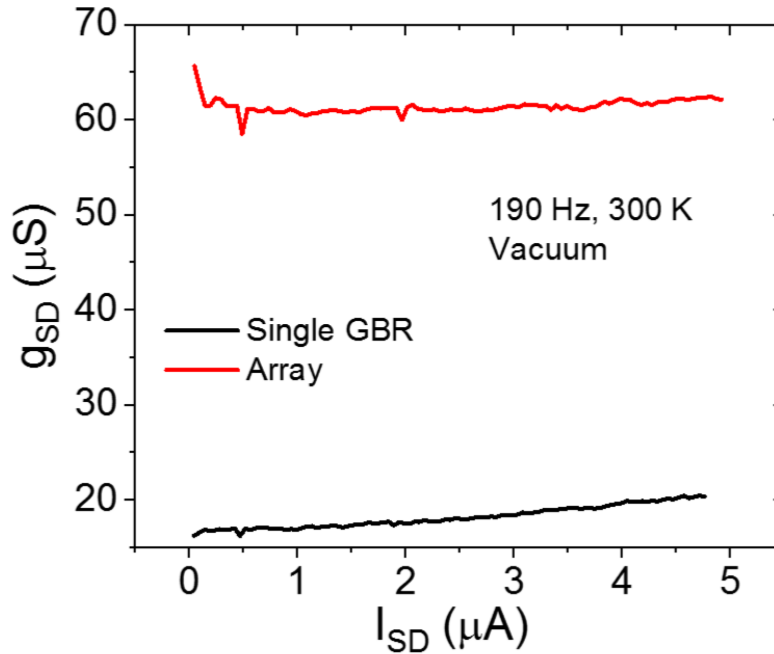

Figure 41: Source-drain conductance of a single encapsulated GBR, and of an array of 3 GBRs, as shown in Figure 40. Shown as a function of 190 Hz input current amplitude, at room temperature in vacuum. Measured with no gate voltage applied to the sample.

The S-D conductance of the single GBR was measured to be $21\ \mu\mathrm{S}$ at the maximum input current amplitude, just below $5\ \mu\mathrm{A}$. At the same input amplitude, the array's conductance was measured to be $63\ \mu\mathrm{S}$. This is three times the conductance of the single GBR, in agreement with the expected conductance of $g_{SD,arr} = n_{arr} g_{SD}$ with $n_{arr} = 3$. Figure 42 shows the measured output voltages as a function of input current for one sample. As expected, the array gives a much lower output magnitude than the single GBR at all input currents. The array/single output voltage ratio at the maximum input current is 0.19, with all measured combinations of single GBR/array giving a ratio in the range of 0.19 – 2.4. This ratio is somewhat lower than that expected, which was $V_{UL,arr} = V_{UL}/n_{arr}$. The explanation for this may be, as mentioned above, the presence of ballistic effects in the graphene between adjacent

GBRs causing additional carrier reflection, meaning that the total output voltage of the array is slightly less than the sum of that of each device.

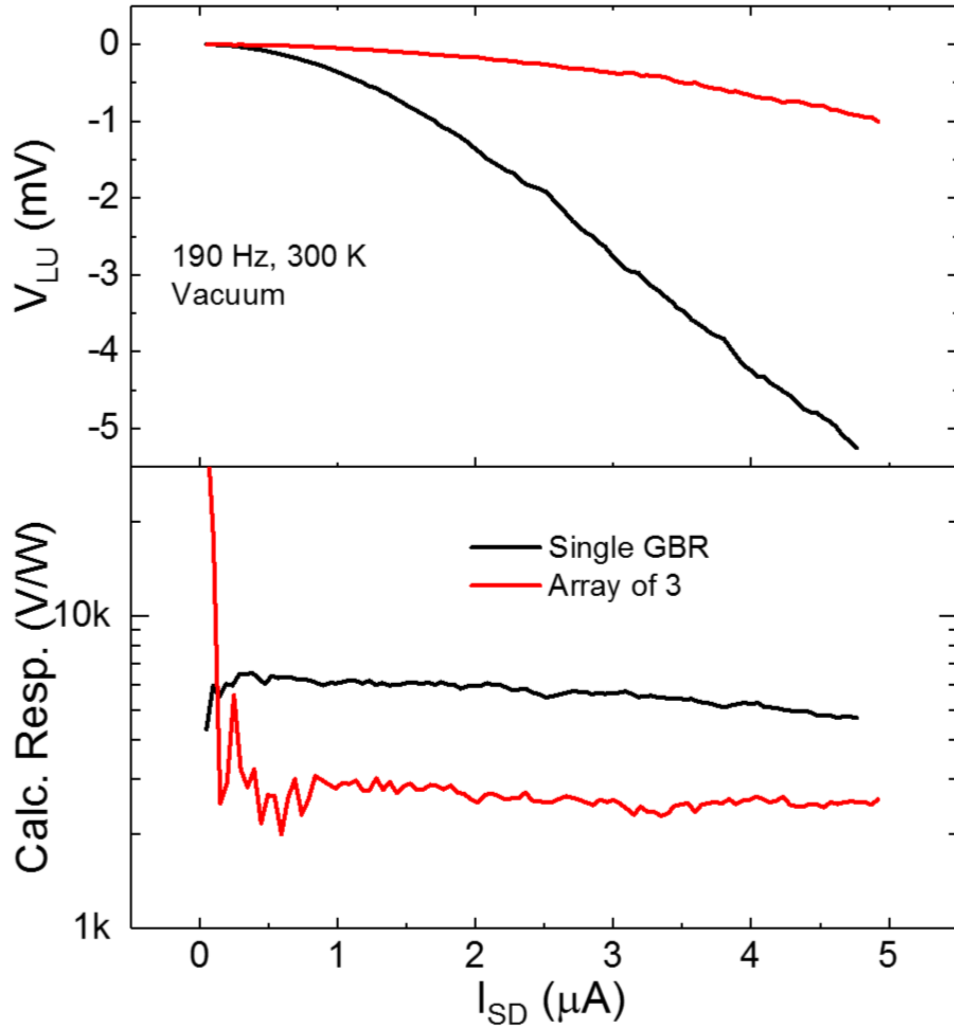

Figure 42: Comparison between output of single GBR and array of three GBRs. Output voltage and responsivity are given as a function of input current amplitude, at 190 Hz at room temperature in a vacuum. Measured with no gate voltage applied to the sample.

Also shown in Figure 42 is a comparison of the responsivities of the single GBR and array; measured on the same sample as the output voltage above. The responsivities were found to both be roughly constant with input amplitude, as is expected due to the quadratic relationship between output voltage and input current. The responsivities are found to be 2,580 V/W for the array and 4,700 V/W for the

single GBR. This is unexpected, as explained earlier the responsivity is expected to be unchanged for GBRs arranged into arrays in this way. The ratio between intrinsic responsivities is found to be around 0.55-0.6 for all samples. The lower responsivity of the array may indicate, as mentioned above, that multiple GBRs in close proximity have slightly worse performance than an isolated GBR. This may be due to unwanted ballistic effects such as reverse scattering of carriers from L to U by the adjacent device. An alternative potential cause of this reduced output involves the way that the GBRs are arranged in the arrays. Within an array, the sources of each GBR are shorted together and hence lie at the same chemical potential (and similarly for the drains). The effect of these shorts needs to be considered in more detail, possibly involving re-derivation of the GBR output formula shown in section 4.1. This may cause the difference in potential between the U and L contact of the array to be equal to only that of a single GBR, instead of the sum of V_{UL} for each individual device. This could also potentially be investigated experimentally in the future, by incorporating high-capacitance structures into the S/D contacts of each GBR separately to avoid this shorting.

For use of GBRs in real applications, it is likely that they will be directly coupled to a $50\ \Omega$ antenna. As discussed in Section 2.3, the mismatch between the impedance of the rectifier and of the antenna causes a large amount of input power to be reflected, lowering the extrinsic responsivity. When the rectifier resistance is far greater than the antenna resistance, the extrinsic responsivity can be calculated using Equation 22. This gives values of 32.5 V/W for the array and 19.7 V/W for the single GBR. The much lower input resistance of the GBR array means that despite having a lower intrinsic responsivity, the extrinsic responsivity with a $50\ \Omega$ antenna is larger than for a single GBR. Therefore, combining GBRs into arrays of this structure is a potentially useful strategy for increasing effectiveness of these devices in real applications.

Perhaps the simplest way to integrate an array of GBRs into a rectenna is to fabricate the array directly in the centre of the antenna, such a large electrical field across the array is generated. In this

geometry, the upper limit to the number of devices in the array is determined by the antenna gap. In a bowtie or log-periodic antenna, the central antenna gap size is determined of the wavelength of the maximum antenna frequency, which for an example of 10 THz gives $L_{gap} = c/(2f) = 15\ \mu\mathrm{m}$. An array of 15 GBRs as shown above would likely be able to fit into this gap, giving an input resistance of $1/(15 \times 21\ \mu\mathrm{S}) \cong 3.2\ \mathrm{k}\Omega$. If it is assumed that the array of 15 has the same intrinsic responsivity as a single GBR, as is predicted earlier in this section, the extrinsic responsivity when coupled to a $50\ \Omega$ antenna is predicted to be 296 V/W. This is a drastic improvement from a single GBR, showing the large benefit of using arrays of GBRs in rectennas. This does assume, however, that the problem of lower-than-expected output voltage in these arrays is solved.

4.5. Graphene Ballistic Rectifiers using CVD-grown Graphene

The previous best examples of GBRs in the literature have all used graphene encapsulated with hexagonal boron nitride, due to its flat surface and absence of dangling bonds allowing for extremely high carrier mobilities [47, 50]. However, fabrication of such devices requires manual exfoliation, selection, and alignment of high quality flakes. In the future, if graphene electronic devices such as these are to be used in large-scale applications, they must be tested with large-scale graphene manufacturing techniques such as CVD growth. Use of graphene on a wafer-scale may also allow devices such as these to be integrated with THz antennas, such as those discussed in Chapter 6.

Using CVD-grown graphene supplied by Graphenea [148] on SiO_2, arrays of 5 GBRs were fabricated alongside single GBRs of the same design. Figure 43(a) shows the final etch mask of such a device; the etch mask is shown in order to clearly show the structure, because the finished device consists of graphene on SiO_2 and hence is both difficult to see and easy to damage using AFM. Figure 43(b) shows the input conductance of a typical device, measured using 4-contact techniques to eliminate contact resistance, showing both the single GBR and the array of 5 GBRs. The array has significantly higher

conductance than the single device, at $2.8\ \mathrm{mS}$ compared to $0.80\ \mathrm{mS}$ respectively. This is an increase of a factor of 3.5, somewhat lower than the 5-fold increase expected. Both devices show no significant change in conductance over the range of inputs shown.

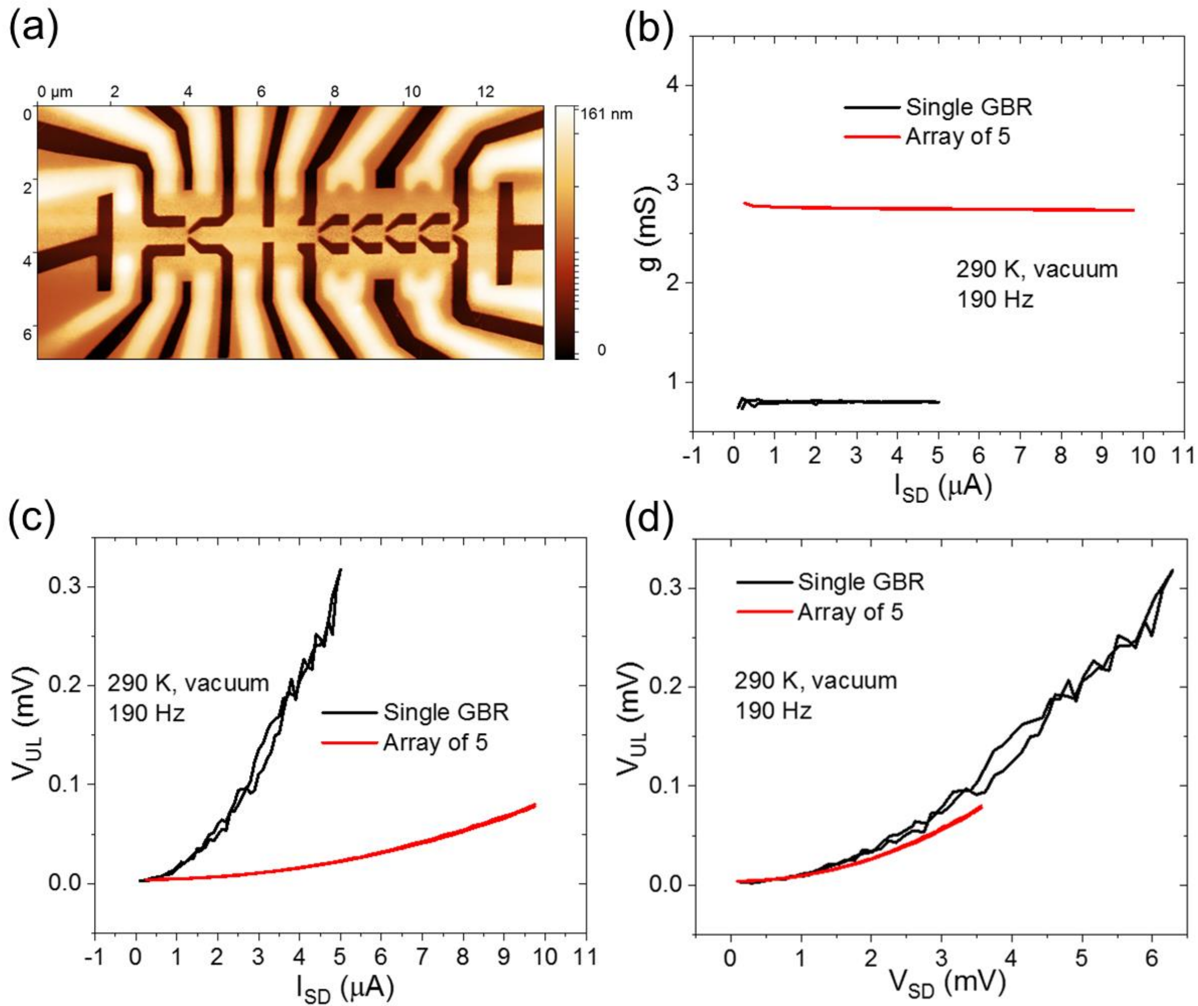

Figure 43: (a) AFM image of the *etch mask* of a CVD graphene device on SiO_2 (no encapsulation), with an array of 5 GBRs and a single GBR of the same design. (b) Input conductance of the single GBR and the array of 5. (c) and (d) show the output voltages, as functions of input current and input voltage respectively. All measurements were taken with no applied gate voltage, at room temperature in a vacuum.

Figure 43(c) shows the output voltage for the singe GBR and the array, as a function of input current. The output voltage of the array is significantly lower than the single GBR, at less than $1/13^{th}$ for the

same input currents. It is expected for output to be reduced for the array, because for each GBR the output voltage depends on the square of input current (see Equation 47 and Equation 50), and the current is split between each device in the array. However, when plotted against input *voltage*, as shown in Figure 43(d), the array only has slightly lower output. Under both conditions, constant input current and constant input voltage, the array has lower output voltage than expected. The simple consideration of the combination of GBRs in an array like this predicts that compared to a single device, the array is expected to have output reduced to $1/n$ for equal current, or increased by $\times n$ for equal voltage. This indicates that the output voltages of GBRs this close together in the array is somewhat supressed, and the total output of the array is not simply the sum of each device as if they were isolated. This was also observed for the encapsulated array of 3 GBRs in the previous section. From this data, the responsivities are shown in Figure 44, with (a) as a function of input current and (b) of input voltage.

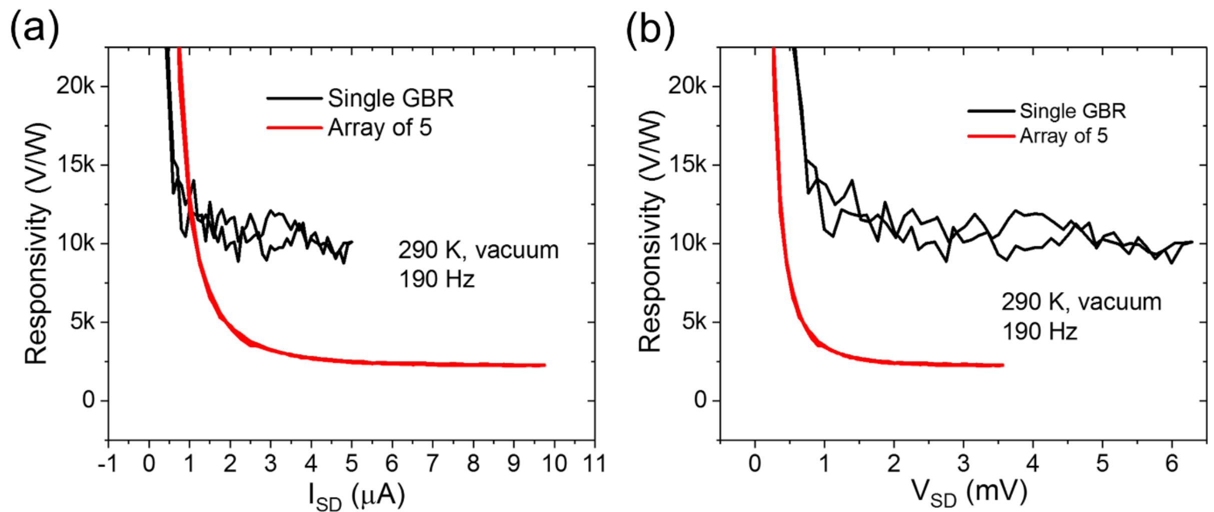

Figure 44: Responsivities of a single GBR and an array of 5 GBRs, both constructed from the same piece of CVD graphene. Shown as a function of input current (a) and voltage (b). All measurements were taken with no applied gate voltage, at room temperature in a vacuum.

The responsivity of the single GBR reaches an equilibrium value of $10.0\ \mathrm{kV/W}$. Unexpectedly, this value is better than the encapsulated GBRs reported here in earlier sections [69], and is just under half

that of the best reported encapsulated GBR in the literature [50]. The reason for this high responsivity lies in the conductance (Figure 43(b)), which is higher than typically reported for encapsulated GBRs [50, 69]. It is thought that this is partially due to the design of GBR used here, which maintains a short S-D distance and contains no scattering centre, as well as the potential presence of chemical dopants on the CVD graphene surface, giving the graphene a high conductivity. The output voltage is also of decent size, although far below that typically observed in the best encapsulated devices [50].

The responsivity of the array plateaus at $2.3\ \mathrm{kV/W}$, which is considerably lower than the single GBR as would be expected from the considerably lower output voltage. From the simplistic reasoning shown in the previous section and earlier in this section, the responsivity of a GBR array would be expected to be the same as for a single device, so the fact that it is less than a quarter is a strong indicator that GBR output voltages do not simply 'add up' when combined into arrays. A brief discussion on potential causes for this is given in the previous section.

As with the encapsulated GBR array measured in Section 4.4, it is useful to consider the power losses when these devices are coupled to a $50\ \Omega$ source, because these devices have input resistances of $1250\ \Omega$ and $360\ \Omega$ for the single GBR and the array respectively. Using Equation 21, the extrinsic responsivities are calculated as $1500\ \mathrm{V/W}$ for the single GBR and $990\ \mathrm{V/W}$ for the array. The gap between the two has been significantly closed, but unlike the encapsulated device shown in Section 4.4, for these devices the single GBR outperforms the array even when impedance mismatch losses are taken into account. This is partially due to the surprisingly low input resistance of the single GBRs, as well as the poor output voltage of the arrays. More testing with variations on the array structure would shed light on ways to improve its output voltage, as well as further testing the reproducibility of these results.

4.6. *Noise Measurements*

It has previously been demonstrated [48, 50] that ballistic rectifiers have low output noise, since the output is only rectified DC voltage with no bias or current flow. Based on this, the same low output noise should also be observed for GBR arrays. To test the extremes of this, an array of 15 GBRs has been fabricated from CVD graphene and output noise measured with a range of input currents. A two-channel cross-correlated noise measurement method is used; the measurement setup is described and calibrated in Section 3.3. Figure 45(a) shows the design of the array used. The output contacts are shown in green on the top right and bottom left, with the input contacts being in green on the right and left with an interdigital structure. Each individual GBR in the array is of identical design to those in Sections 4.4 and 4.5.

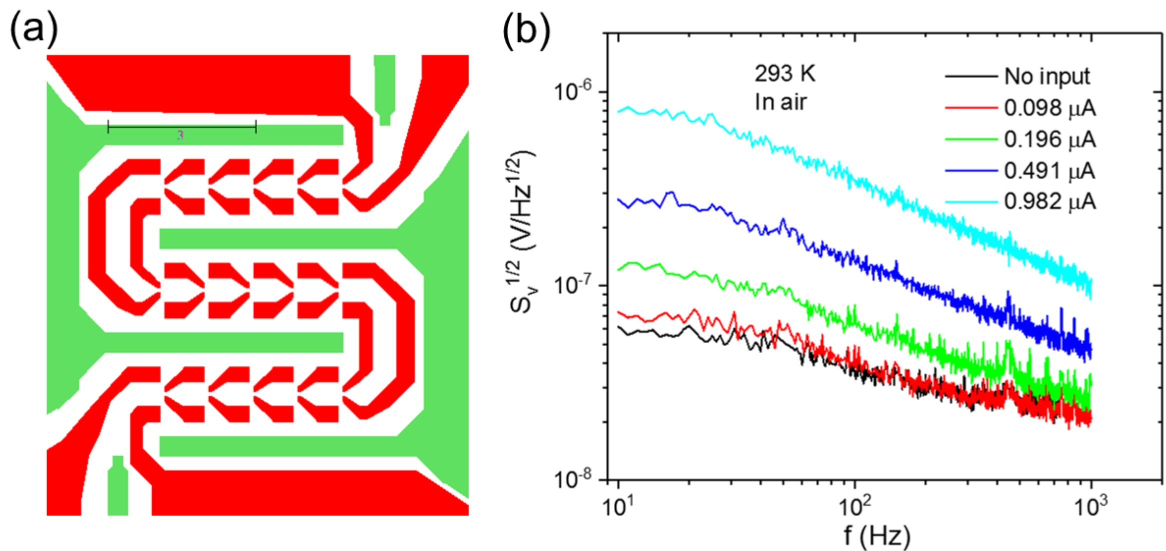

Figure 45: (a) design of the GBR array used in the noise measurements. Red areas represent where the CVD graphene is etched away, and green represents Cr/Au (2 nm/40 nm) contacts deposited on top of the graphene. The black scale bar is 3 μm. (b) shows the measured spectral voltage noise of the device, measured in air at room temperature, with a range of input currents.

With current input, the noise spectrum is as expected. Based on the strong 1/f relationship seen especially for the largest currents, flicker noise is dominating. However, unlike previously observed for

a single encapsulated GBR [50] the thermal noise floor of the output is not visible for no input current. This device has an output resistance of $\sim 10\ \mathrm{k\Omega}$, so we would expect thermal noise $\sim 1.3 \times 10^{-8}\ \mathrm{V/Hz^{1/2}}$. This noise being above thermal noise at these frequencies is thought to be due to the charging/discharging of edge states in the CVD graphene, which is expected to be much more significant in this device due to the larger size and the lower-quality graphene. This is discussed in more detail in comparison to the GSSD noise measurements in Section 5.5. However, the level of noise measured is only slightly larger than a single encapsulated GBR [50], indicating that neither the combination of many GBRs into arrays nor the fabrication of GBRs from CVD-grown graphene cause significantly worse performance in terms of noise.

4.7. Summary

The graphene ballistic rectifier is a nanodevice with extremely exciting potential, and has had excellent properties as a detector up to THz frequencies demonstrated in the past [47, 50]. However, despite this the theory of operation of these devices had not been analytically explored. Here, a derivation for such a theory has been presented, followed by investigations of devices based on the theory. Starting with the Büttiker-Landauer formula-derived model for operation of a ballistic rectifier constructed from a semiconductor heterostructure 2D electron gas, the theory has been re-derived considering the nature of graphene and then combined with expressions describing the densities of both electrons and holes. Resulting from this is an equation that expresses GBR output voltage in terms of input current, gate voltage, and device geometry, which predicts the output voltage to depend strongly on carrier mixing and relative mobilities.

The newly derived theory was then used to fit measured data from four different GBR designs made using hBN-encapsulated graphene. All measurements fit the equation well, demonstrating the applicability to this range of GBR designs. As well as fitting real measurements, Equation 50 was also

used to predict the performance of devices with 3 sets of parameters. The most optimal device considered, which has QPC widths of 20 nm and a mobility ratio of 1.5, has peak responsivity of 50,800 V/W and NEP as low as $0.51\ \mathrm{pW/Hz^{1/2}}$. This NEP is calculated assuming that, due to the GBR's orthogonal layout isolating output noise from the input and the lack of bias or current flow through the output, output noise is dominated by thermal noise. These predictions are considerably better than the best reported GBR in literature, and use geometry that, while beyond the range of fabrication equipment used here, is fully achievable using current technology.

The benefits gained by combining GBRs into arrays were then investigated, including in devices constructed from CVD graphene. For encapsulated GBRs, it was found that as a function of input current arrays produce a much lower output voltage and hence a somewhat lower responsivity. However, when taking into account impedance mismatch from a $50\ \Omega$ source the much reduced input impedance of an array means the extrinsic responsivity is improved from an individual GBR. For encapsulated GBRs, an array of 3 GBRs demonstrates an extrinsic responsivity of 32.5 V/W compared to 19.7 V/W for an individual device. This however does not take into account the contact resistance between graphene and a metal antenna. GBRs fabricated using CVD-grown graphene on SiO_2 were also demonstrated, with intrinsic responsivity of $10{,}000\ \mathrm{V/W}$ for a single GBR and $2{,}300\ \mathrm{V/W}$ for an array of five. The corresponding extrinsic responsivities with a $50\ \Omega$ source are $1500\ \mathrm{V/W}$ for the single CVD GBR and $990\ \mathrm{V/W}$ for the array. Unlike for the encapsulated GBRs, the single CVD device still outperforms the array with impedance mismatch taken into account. This may be due to random variation between devices; the GBR array measured for this comparison being particularly poor quality. Alternatively, it may be an indication of the degradation in GBR output voltage caused by combining them into an array in this manner. If the latter is the case, alternative array geometries may improve device performance. Finally, measurements of output noise in an array of 15 GBRs fabricated from CVD graphene show a similar noise level to single high-quality GBRs [50]. These measurements confirm that

the combination of GBRs into arrays such as these does not have significant detrimental effects on the noise performance, and neither does fabrication of devices from CVD graphene.

5. Graphene Self-Switching Diodes

The graphene self-switching diode (GSSD) is a planar two-terminal device which uses electrostatic effects to cause asymmetric current through a conducting channel. The operational mechanism is explained in Section 2.4.2. By using graphene, they are capable of operating at THz frequencies, with no threshold voltage. In this section, arrays of GSSDs are fabricated using high-quality graphene encapsulated with hBN, as shown in Figure 46.

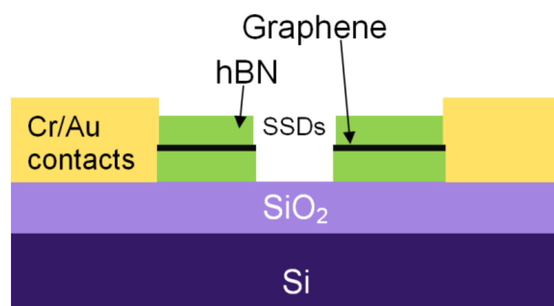

Figure 46: Cross-sectional diagram of an SSD formed by etching encapsulated graphene, with the graphene contacted at the side using Cr/Au 1D contacts. Diagram does not represent the lateral structure or scale of a real GSSD sample; it serves only to give an example view of the relevant aspects of the structure.

This shows the stack having been etched all the way through, leaving an insulating trench between the two areas of graphene. These areas could for example represent the channel and the side gate. Figure 47 is an example AFM image of an array of 3 GSSDs showing the insulating trenches having been etched into the hBN/graphene/hBN stack, and the 100 nm wide and 1 μm long channels.

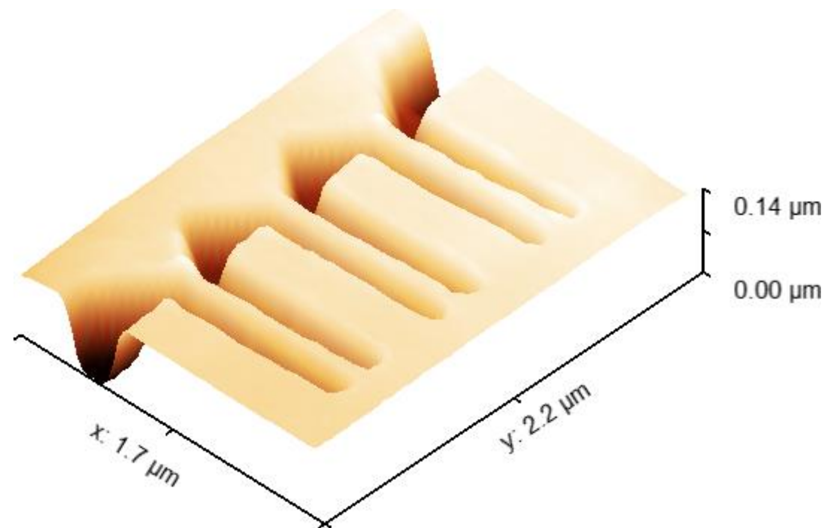

Figure 47: 3D AFM image of an array of 3 GSSDs, fabricated from a hBN/graphene/hBN stack. Insulating trenches have been etched through the stack.

Despite the work previously done on GSSDs [51, 132, 138], there had been no reported attempt to combine 4 of these diodes (or arrays) together to construct a bridge rectifier. This would offer considerable advantages over operating a single GSSD as a rectifier, because a bridge rectifier acts as a full-wave rectifier (see Section 2.3). In this chapter, the operational theory of a GSSD bridge rectifier is derived in Section 5.2, followed by the fabrication, measurements, and analysis of a GSSD bridge rectifier constructed from encapsulated graphene in Section 5.3 and CVD graphene on SiO_2 in Section 5.4. These are therefore fully-graphene bridge rectifiers, with each 'arm' of the rectifier consisting of an array of 3 GSSDs.

5.1. GSSD Arrays

As described in Section 2.4.2, GSSDs use electrostatic effects to achieve asymmetry in channel conductivity. This diode-like behaviour can be seen by measuring current asymmetry through a single GSSD or an array. The direction of current asymmetry depends on the majority carrier, and hence in graphene depends on the applied gate voltage.

Using the techniques shown in Section 3.1.2, hBN-encapsulated graphene was used to construct arrays of 3 GSSDs and a bridge rectifier alongside a Hall bar. 1D contacts were used to measure the device, and all measurements were taken at room temperature in a vacuum unless stated otherwise. Figure 48(a) shows the conductivity of the Hall bar, which was fabricated with the same piece of graphene as the GSSD arrays and bridge rectifier. This shows the minimum sheet conductivity to be at a gate voltage of around -8 V, indicating that this is the position of the NP. From this, using Equation 9, the room temperature carrier mobility is calculated from Equation 9, and is shown in Figure 48(b) as a function of gate voltage.

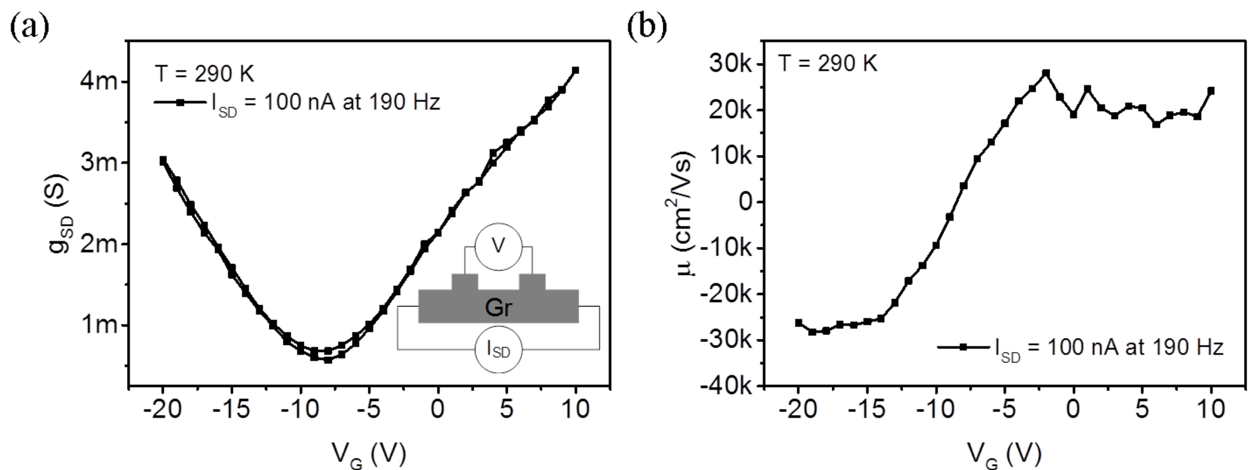

Figure 48: (a) Conductance of the encapsulated graphene used to fabricate the GSSDs as a function of gate voltage. (b) The carrier mobilities, calculated from (a). Positive values represent electron mobility, while negative represent hole. Reproduced from [123].

Here, positive values of mobility are for electrons and negative are for holes. The peaks are $28{,}200\ \mathrm{cm}^2/\mathrm{Vs}$ for electrons and $26{,}600\ \mathrm{cm}^2/\mathrm{Vs}$ for holes. The NP is some distance away from 0 V, the expected value for pristine graphene, which indicates the presence of some amount of impurity present on the graphene. This also causes the carrier mobilities to be somewhat lower than has been previously reported possible for encapsulated graphene [50].

Due to the lack of a depletion region, current through a GSSD has a large linear component. Because of this, I-V data obtained from a GSSD array appears very symmetrical, as shown in Figure 49.

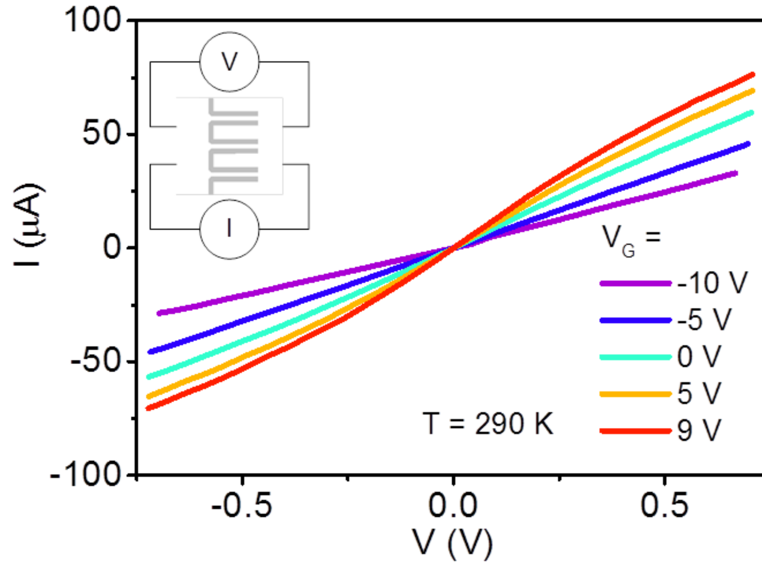

Figure 49: Four-probe I-V characteristics for an array of three GSSDs, with measurement setup shown in the inset. Measured in vacuum at room temperature, at a range of gate voltages as shown. Reproduced from [123].

In order to identify the asymmetry in the conduction, and hence the diode-like behaviour, the current asymmetry must be measured:

$$I_{Asymm.} = \frac{I_{SD}(V_D) + I_{SD}(-V_D)}{2}. \qquad \text{Equation 53}$$

This is shown for the same array as above in Figure 50.

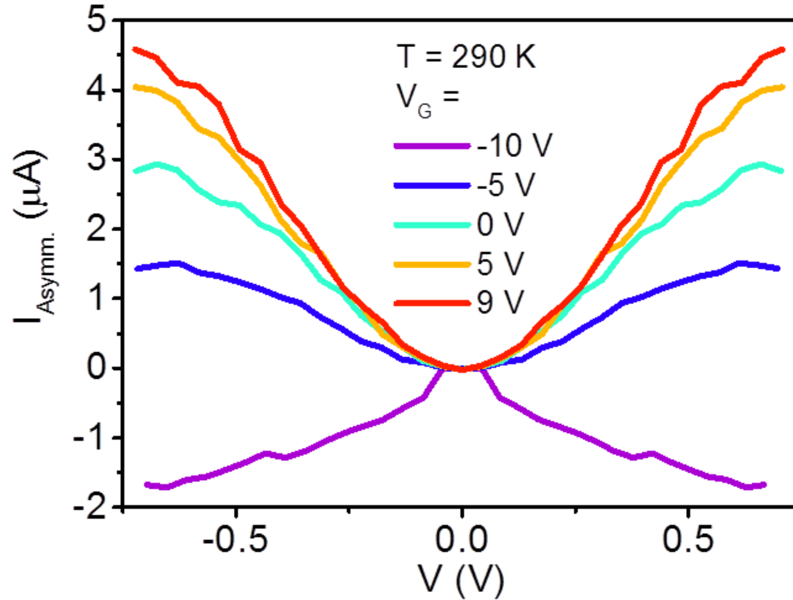

Figure 50: Current asymmetry for an array of three GSSDs, calculated using Equation 53 for the data shown in Figure 49. This shows the rectification behaviour of the GSSD, with output direction dependent on the gate voltage. Reproduced from [123].

Looking at the current asymmetry, the rectification capabilities of the GSSD can now be seen. The direction of asymmetry depends on the applied back gate voltage V_G. Figure 48 shows the NP to be at $V_G = -8\,\mathrm{V}$, which means that gate voltages close to this value produce the lowest output, due to similar numbers of electrons and holes coexisting in the GSSD channels. When V_G moves from below the NP to above it, the majority carrier switches from holes to electrons, causing the expected change in rectification direction. At low biases, it also shows a quadratic dependence, matching what is predicted by Equation 28. Higher voltage, however, causes the breakdown of this dependence, with the dependence becoming linear and the asymmetry even starting to decrease at voltages approaching ± 0.7 V. This region of high field is not covered by the theory shown in 2.4.2, and this deviation may be caused by several factors; for example velocity saturation, carrier-carrier interactions or impurities in the channel.

At zero applied bias and zero gate voltage, the resistance of the array is measured as $13.2\ \mathrm{k\Omega}$. Using the method described in [132], the capacitance per unit length for coplanar graphene strips of width s and separation d can be calculated using

$$C_l = \frac{\varepsilon_0 \varepsilon_r}{\pi} \ln\left(8\frac{s}{d}\right). \qquad \text{Equation 54}$$

Because the surrounding dielectric medium for the encapsulated GSSDs is somewhat complicated, consisting of air, hBN, and SiO_2, an approximate value of $\varepsilon_r \sim 2.5$ is used, giving a total extrinsic capacitance for the array of 3.1×10^{-17} F. Combined with the zero-bias resistance of $13.2\ \mathrm{k\Omega}$, this gives a cut-off frequency of $1/_{2\ \pi RC} = 0.39\ \mathrm{THz}$. This puts the operational frequency of this GSSD array well into the THz range, although perhaps not as high as graphene ballistic rectifiers. However, in a real application the ultimate performance will depend on surrounding circuitry. Structures such as transmission lines and antennas can add substantial capacitance, reducing the maximum operational frequency to well below this value. This value is presented only as a theoretical limit; the cut-off frequency of the diode array assuming no contribution from surrounding structures.

5.2. GSSD Bridge Rectifier Theory

The below derivation is as presented in my publication, reference [123]. As shown in Section 2.4.2, the current passed through a single GSSD is given by $I_{GSSD} = \mu \frac{W_c}{L_c}\left(C_G V_A V_D + \frac{C_t}{t_c}\frac{V_D^2}{2}\right)$. Figure 51 shows the structure of a GSSD bridge rectifier. In the bridge rectifier structure there are two routes for current to pass through the device. Because the arrangement of diodes in a bridge rectifier is symmetric, the GSSD arrays are arranged such that no matter what the majority carrier is, each route has one forward biased and one reverse biased array of diodes.

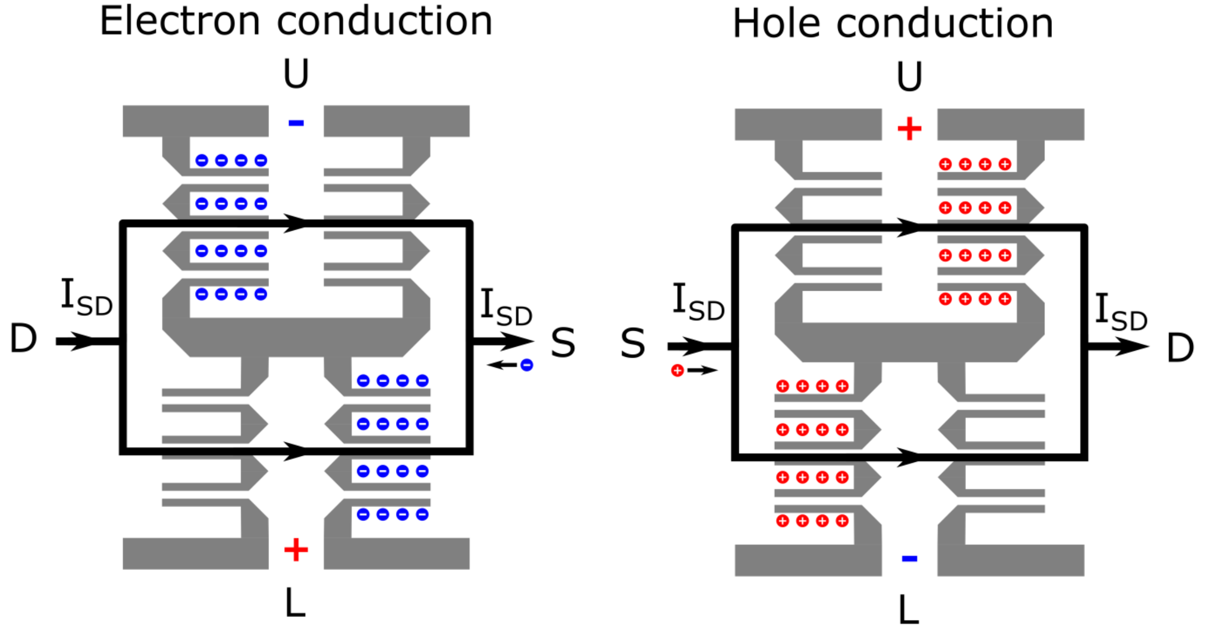

Figure 51: Operational mechanism of a GSSD bridge rectifier, consisting of four arrays of GSSDs. The cases of either electrons or holes being the majority charge carrier are shown. Current is applied between S and D, showing how charge buildup on either side of the GSSD channels causes a DC bias buildup, the direction of which depends on the majority carrier.

Due to similarities between the operation of this device and the graphene ballistic rectifier, the same naming convention for contacts is used. The input AC signal is applied between the source S and drain D contacts, and the DC output voltage is measured between the upper U and lower L contacts. The device's symmetry means that, assuming that each GSSD array is identical, the resistance between S and D is equal along each side of the rectifier. Because no current is allowed to pass through the U or L contacts, it can therefore be deduced that the current through each GSSD array is equal under all conditions. Using Equation 28 for the GSSD current it can be said that

$$C_G V_A V_1 + \frac{C_t}{t_c}\frac{V_1^2}{2} = C_G V_A V_2 - \frac{C_t}{t_c}\frac{V_2^2}{2}, \qquad \text{Equation 55}$$

where V_1 and V_2 are the voltage drop at the forward biased and the reverse biased GSSD array respectively. These can be expressed in terms of their difference, ΔV, and their sum, which is equal to the input voltage V_{SD}:

$$V_1 = \frac{V_{SD} - \Delta V}{2} \quad \text{and} \quad V_2 = \frac{V_{SD} + \Delta V}{2}. \qquad \text{Equation 56}$$

Substituting this into Equation 55, we obtain

$$\Delta V = 2\frac{C_t}{C_G t_c} V_F \pm \sqrt{4\left(\frac{C_t}{C_G t_c} V_A\right)^2 - V_{SD}^2}. \qquad \text{Equation 57}$$

This expression is only valid for $V_{SD} \ll |V_A|$, i.e. the back gate voltage is much larger than the input voltage. The positive solution is non-physical, as it gives $\Delta V \gg |V_{SD}|$. Taking the negative solution, a series expansion with $V_{SD} \ll |V_A|$ gives

$$\Delta V = \frac{C_G t_c}{4C_t}\frac{V_{SD}^2}{V_A} + \frac{C_G^3 t_c^3}{64 C_t^3}\frac{V_{SD}^4}{V_A^3} + O\left(V_{SD}^6\right). \qquad \text{Equation 58}$$

The higher order terms drop off in magnitude extremely quickly, meaning that the first term gives a good approximation. The output voltage V_{out} is simply given by twice of this difference voltage, meaning that

$$V_{out} \approx \frac{C_G t_c}{2C_t}\frac{V_{SD}^2}{V_A}. \qquad \text{Equation 59}$$

However, when operating the rectifier with input current of constant amplitude, it is desirable to instead express the output voltage in terms of input current. In a GSSD, the linear component of Equation 28 dominates, therefore this relationship is

$$V_{out} \propto \frac{I_{SD}^2}{V_A^3}. \qquad \text{Equation 60}$$

This predicts that output voltage depends on the square of the input current, with no linear term, and that it decreases with the inverse cube of the gate voltage – local NP offset. However, this gate voltage dependence breaks down in the vicinity of the NP ($V_A = 0$), defined as the value of V_G at which

a bulk piece of graphene has an equal density of electrons and holes, with no locally applied drain voltage. Here, carrier mixing due to graphene's lack of a bandgap distorts the dependence on V_G.

5.3. Encapsulated GSSD Bridge Rectifier Measurements

By combining four GSSD arrays as shown in Figure 7, a bridge rectifier can be constructed. A bridge rectifier is constructed by etching the design shown in Figure 52(a) into a hBN/graphene/hBN stack, which was assembled from exfoliated hBN and graphene using the techniques detailed in Section 3.1.2. Each GSSD is identical in design, with a channel of width 100 nm and length 1 μm, and insulating trenches designed to be 100 nm in width. However, due to 100 nm being close to the resolution limit of the EBL system used for patterning, and due to slight impurities being present during etching of the hBN/graphene/hBN stack, some amount of roughness and variation in this is seen. A diagram showing the structure and measurement setup is shown in Figure 52(a), while an AFM image of the finished rectifier is shown in Figure 52(b).

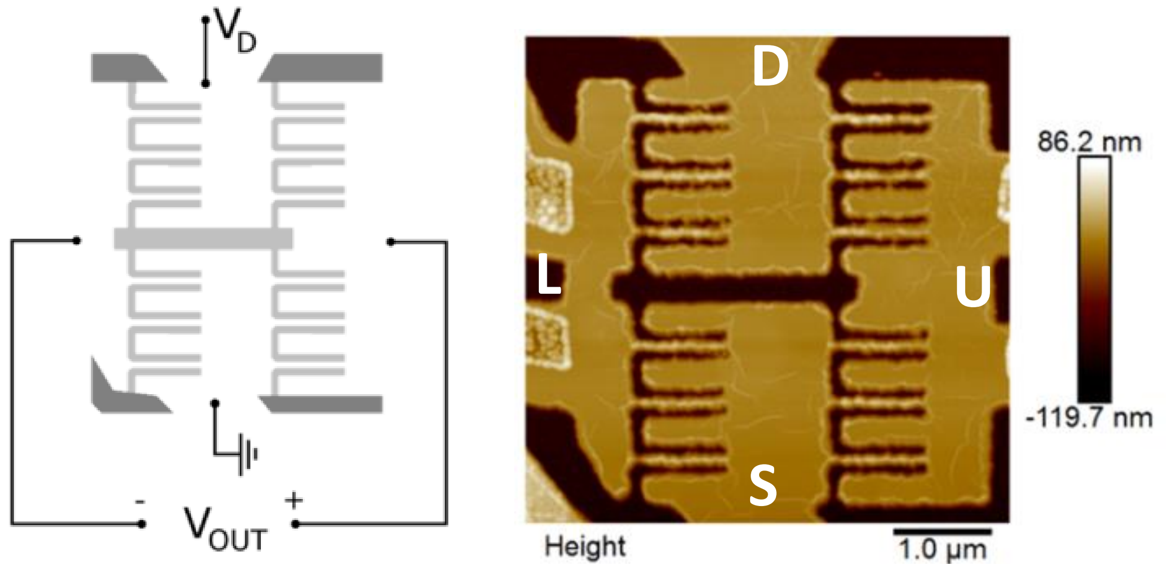

Figure 52: Left: Structure of the fabricated encapsulated GSSD bridge rectifier, with input current applied and output voltage measured as shown. Right: AFM image of the fabricated rectifier. Reproduced from [123].

This device has two probes each at the S and D, in order to use four-probe measurements to bypass the contact resistance and measure the true conductivity of the device. By passing DC current between S and D, the output voltage can be measured as a function of input current. This is shown in Figure 53.

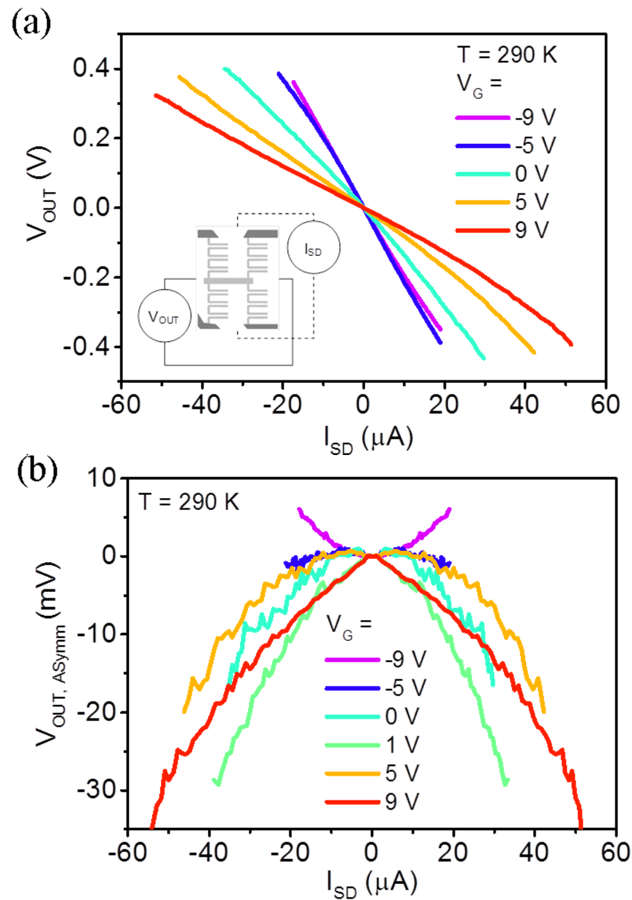

Figure 53: (a) Room temperature output voltage of the encapsulated GSSD bridge rectifier shown in Figure 52 as a function of DC input current, shown with different applied back gate voltages. The inset shows the measurements setup. (b) Output voltage asymmetry, as a function of input current and for different gate voltages. Reproduced from [123].

Similar to the I-V for a single GSSD array, this data shows only small amounts of curvature, with a mostly symmetrical shape. Again similarly, the output voltage asymmetry (calculated by Equation 61) must be calculated to show the rectification behaviour.

$$V_{OUT,Asymm.} = \frac{V_{OUT}(I_{SD}) + V_{OUT}(-I_{SD})}{2}, \qquad \text{Equation 61}$$

This is calculated using the data from Figure 53(a) and is shown in Figure 53(b). The output voltage asymmetry shows a quadratic dependence on input current, as expected from Equation 60. Again, it can be seen that the output direction depends on the majority carrier, switching from positive to negative at between $V_G = -9\ \mathrm{V}$ and $-5\ \mathrm{V}$. This is in agreement with the independently measured neutrality point at $-8\ \mathrm{V}$ (Figure 48), however the extremely low output for $V_G = -5\ \mathrm{V}$ indicates that the NP is closer to this than to $-9\ \mathrm{V}$, implying that there is variation in the NP across the graphene sample. In Figure 53, the input current range varies depending on the applied gate voltage. This is because during measurement, the input voltage V_{SD} was swept, meaning that as the device conductance varied with gate voltage, different ranges of I_{SD} were produced. From this DC data, it is possible to calculate the responsivity of the device using $\mathcal{R} = \frac{\text{output voltage}}{\text{input power absorbed}}$. Taking the gate voltages from Figure 53(b) which give the largest output, Figure 54 shows the calculated responsivity in the electron and hole conduction regions.

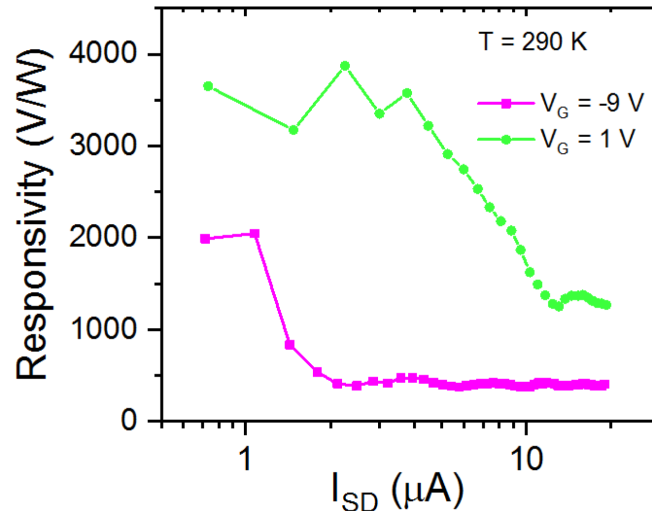

Figure 54: Responsivity of the GSSD bridge rectifier, calculated from the DC output data shown in Figure 53(b), for gate voltages of $V_G = -9$ V and $V_G = 1$ V, when holes and electrons respectively are the majority carrier. Adapted from [123].

At these gate voltages, with an input current of $I_{SD} = 5\ \mu\mathrm{A}$ the electron and hole responsivities are $3{,}000\ \mathrm{V/W}$ and $400\ \mathrm{V/W}$ respectively.

While DC measurements can give an indication of a rectifier's performance, measurements with an AC input are necessary to evaluate performance, because it avoids the need to calculate output asymmetry, instead showing the true output voltage of the rectifier. Due to this device having been fabricated on a n-Si/SiO_2 substrate, the parasitic capacitance is very large, meaning that the cut-off frequency is low and hence this device cannot be measured at high frequencies. All AC measurements shown below were performed at a frequency of 190 Hz. At room temperature, the output voltage as a function of gate voltage and input current is shown in Figure 55.

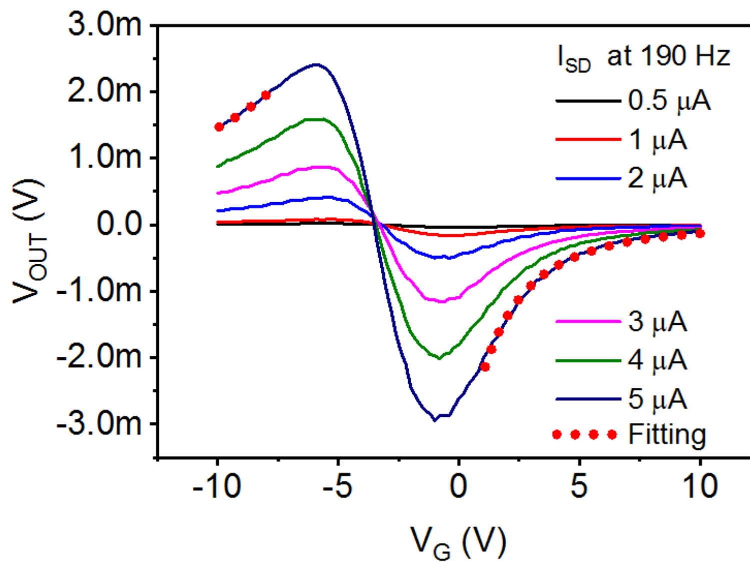

Figure 55: DC output voltage from the GSSD bridge rectifier, with a 190 Hz constant amplitude AC input, as a function of gate voltage and input amplitude. The dotted line shows a $\propto V_G^{-3}$ fitting for the $I_{SD} = 5\ \mu\text{A}$ data, at gate voltages far from the NP. Reproduced from [123].

Here it is found that this measurement setup shows the relationship between output voltage and both input current and gate voltage much more clearly. It is observed that for all input current magnitudes, the output voltages switches from positive to negative at $V_G = -3.5\ \text{V}$, indicating that this is the position of the NP in and around the device. This has a large difference in position from the value measured on a hall bar structure, as shown in Figure 48, indicating variation in graphene doping across the device. The fitting in Figure 55 shows that at gate voltages far from the observed NP, the output

voltage follows a $\propto V_A^{-3}$ dependence, with V_A being the gate voltage – NP offset. This was observed for all values of I_{SD}, but only plotted for $I_{SD} = 5\ \mu\text{A}$ for clarity. This confirms the other expected dependence for the GSSD bridge rectifier as shown in Equation 60, which is that $V_{out} \propto V_A^{-3}$. As is also expected, near the bulk carrier neutrality point the mixing of both types of carrier distorts this dependence.

Figure 56 shows how the rectifier output varies with temperature. It can be seen that as temperature decreases, the magnitude of output increases. This cannot be explained by the GSSD theory derived in Section 2.4.2, or by the bridge rectifier theory above. The reason for this increase is that with decreasing temperature, the mixing of carriers in the device decreases according to the Fermi distribution. Because oppositely charged carriers produce opposite output, this causes the output to increase. As well as this, with decreasing temperature the gate voltages which give maximum output move closer to the NP. This is also due to a reduction in carrier mixing, allowing conduction to be dominated by a single carrier at gate voltages closer to the NP.

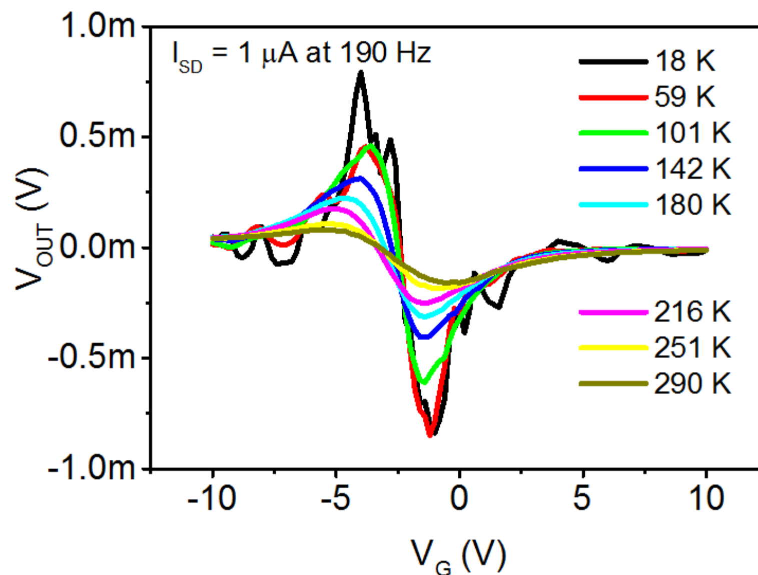

Figure 56: GSSD bridge rectifier output voltage at different temperatures, as a function of gate voltage and with a constant AC input current. Reproduced from [123].

At temperatures of 142 K and below, the output voltage starts to fluctuate as a function of gate voltage. This is especially prominent at 18 K. This is likely to be caused by edge states in the etched GSSD channels, and surface traps. While at higher temperatures these are all thermally activated and their contribution to conduction is constant, at low temperatures they become activated at different gate voltages, causing these observed conductance changes as a function of gate voltage.

At room temperature, the values of V_G which produce maximum output are around 0 V for electrons and -5 V for holes. Shown in Figure 57 is the output voltage as a function of input current, at gate voltages close to these.

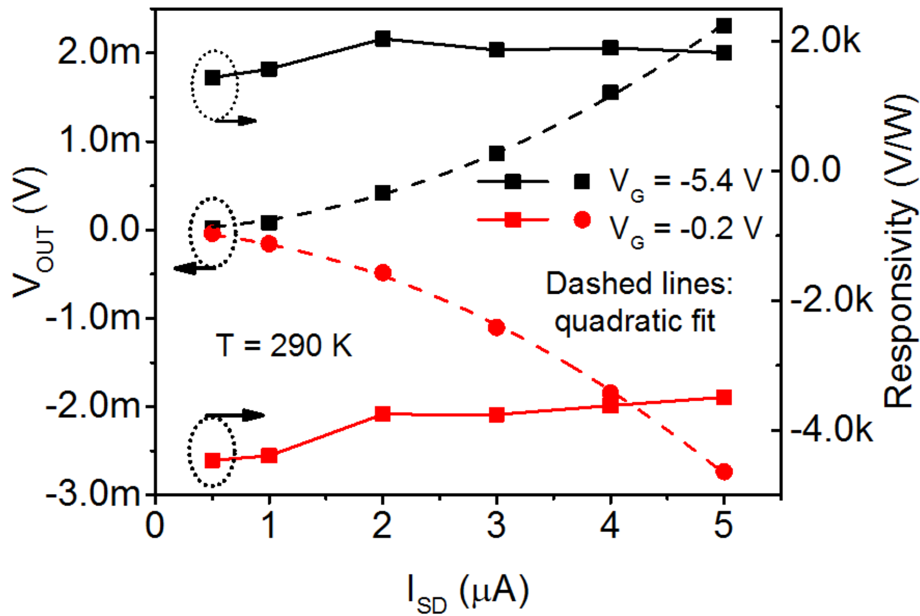

Figure 57: Output voltage and responsivity of the GSSD bridge rectifier at room temperature as a function of AC input current amplitude. It is shown for gate voltages of -5.4 V and -0.2 V, close to the maximal point for the output in the hole- and electron-dominated regions of conduction respectively. The dashed lines show quadratic fits to the output data. Reproduced from [123].

Fitting shows that the output voltage increases with the square of the input current, confirming Equation 60. The power supplied to the device is calculated from the RMS current and the voltage drop across the device, and the responsivity is calculated from this data using $\mathcal{R} = \frac{\text{output voltage}}{\text{input power absorbed}}$, and

is also shown in Figure 57. The responsivity remains mostly constant with input current, as expected due to both input power and output voltage increasing with the square of input current. At these gate voltages, the responsivities are found to be $4{,}400\ \mathrm{V/W}$ for electrons and $1{,}570\ \mathrm{V/W}$ for holes at $I_{SD} = 1\ \mu\mathrm{A}$. If it is assumed that, because there is zero bias applied to the input or output, the output voltage noise spectral density is dominated by thermal noise as is seen for the GBR, the voltage noise is hence is given by $S_V^{1/2} = \sqrt{4k_BTR_{SD}}$. The corresponding NEPs, defined by Equation 23, are calculated to be $5.4\ \mathrm{pW/Hz^{1/2}}$ for electrons and $18.2\ \mathrm{pW/Hz^{1/2}}$ for holes.

At the gate voltages considered, the input resistance of the GSSD bridge rectifier is $35.5\ \mathrm{k\Omega}$. Because this devices has an input impedance much greater than 50 Ω, the extrinsic responsivity with a 50 Ω source can be calculated using Equation 22, giving $\mathcal{R}_{50\Omega} = 24.8\ \mathrm{V/W}$ for electrons and $6.2\ \mathrm{V/W}$ for holes. If this extrinsic responsivity is then used to calculate NEP, the obtained values are increased to $0.96\ \mathrm{nW/Hz^{1/2}}$ and $4.61\ \mathrm{nW/Hz^{1/2}}$ respectively. Due to the structure of the bridge rectifier, the total extrinsic capacitance is the same as that of a single array, 3.1×10^{-17} F. Using this, the cut-off frequency is calculated to be ${}^{1}/{}_{2\pi R_{SD}C} = 0.15\ \mathrm{THz}$, with the device on a non-conductive substrate. While this places the device in the THz range of operation, its theoretical operation frequency is lower than other THz rectifiers, for example the ballistic rectifier [47]. Fortunately, it is in theory possible to significantly improve the theoretical operational frequency using some modest changes to the GSSD bridge rectifier design which is shown in Figure 52. The following section begins with a discussion of improvements that can be made, in order to reduce both extrinsic capacitance and input resistance, and hence improve the operational frequency.

5.4. CVD GSSD Bridge Rectifiers

In order for graphene-based devices such as the GSSD bridge rectifier to move towards larger-scale fabrication, and potentially towards industrial use and commercial availability, it will be necessary to move away from fabrication of devices using manually exfoliated and encapsulated flakes, using techniques such as those described in Section 3.1.1. Instead, use of graphene produced by some sort of scalable method, such as CVD growth, is essential. Unlike the graphene ballistic rectifier, which relies on the ballistic transport caused by high carrier mobilities in order to function, GSSDs are less dependent on having large carrier mobilities. Therefore, the reduction in performance when moving from encapsulated graphene to CVD-grown graphene on SiO_2 is expected to be much lower for the GSSD bridge rectifier. Towards this end, GSSD bridge rectifiers have been fabricated using CVD-grown graphene on SiO_2, in order to evaluate their performance and compare it to devices using encapsulated graphene.

As well as using CVD graphene instead of hBN-encapsulated exfoliated graphene, these devices also use a modified bridge rectifier design. In order to increase the operational frequency of the GSSD bridge rectifier, the design used for measurements shown in Section 5.3 must be modified in order to increase its cut-off frequency. This means decreasing its extrinsic capacitance, and decreasing its input (S-D) resistance. To this end, Figure 58 shows the old device design (used in Section 5.3) alongside the newly modified design. Each design uses arrays of 3 GSSDs for each arm, with the GSSDs themselves being identical; it is only the arrangement of these GSSDs which is improved. The reasoning behind these changes are given here.

As shown in Figure 58(a), the path from S to D is blocked by the central etched region, meaning that the conduction path is much longer than is necessary. Carriers passing from S to D or vice versa must travel a considerable distance between the GSSD arrays, with a $180°$ turn in trajectories that may also cause problems when in or near the ballistic transport regime. This causes the input resistance to be

increased. By rotating all four GSSD arrays and the central etch by $90°$, the conduction path from S to D is made much more direct. As well as this, it is now easily possible to decrease the spacing between adjacent arrays, further decreasing the S-D distance and hence decreasing the input resistance.

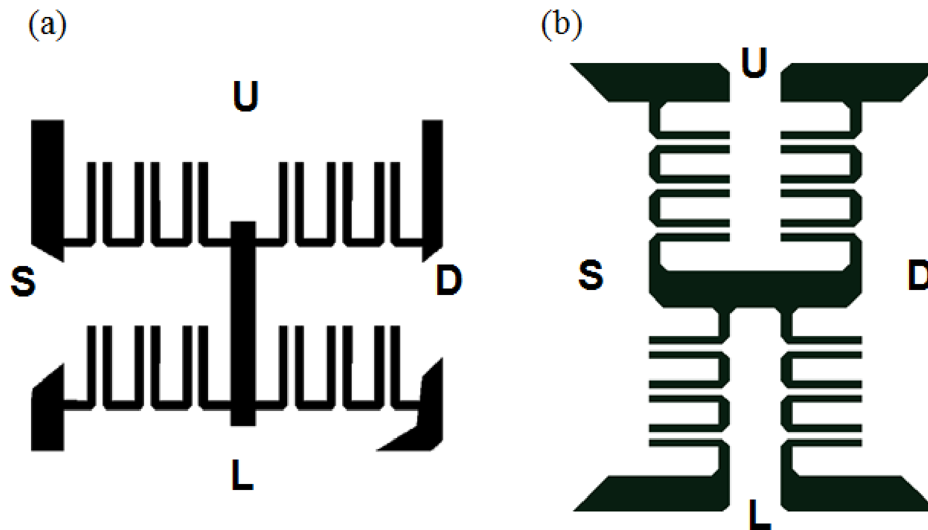

Figure 58: Comparison of old (a) and new (b) GSSD bridge rectifier designs. The new design has thicker perpendicular trenches between individual GSSDs, and a shorter S-D path. Black regions show where the graphene is etched. The design in (a) is identical to that shown in Figure 52, but rotated $90°$ to the left for direct comparison to (b). In both designs, the channel length is $1\ \mu m$.

The extrinsic capacitance is mostly due to the insulating trenches between GSSDs, which run parallel to the device channels. In general, capacitance can be reduced by either lowering the dielectric constant or by increasing the spacing between the two conductors. However, because reducing the dielectric constant within the trenches is not practical, the only way to reduce capacitance is to increase the separation, i.e. the trench width. While this does also mean a very slight increase to the S-D separation, the increase is insignificant compared to the possible decreases in separation, as well as the achieved decrease in capacitance. Figure 58 shows a comparison between the design used for the encapsulated GSSD bridge rectifier above and the newly obtained design, with the above modifications.

Figure 59 shows the source-drain AC conductance of a CVD graphene GSSD bridge rectifier, in comparison to that of the encapsulated device shown in Section 5.3.

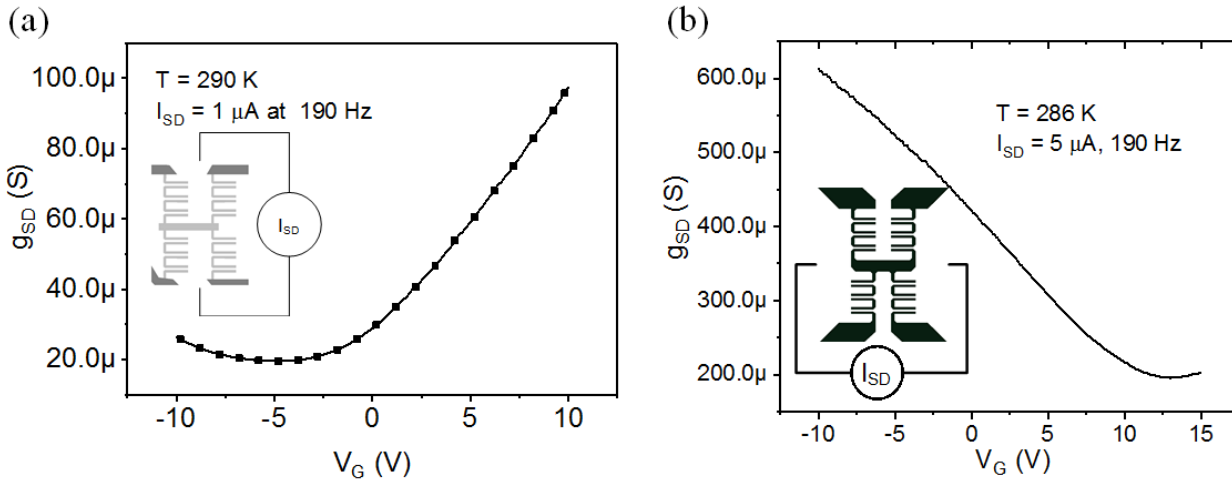

Figure 59: Comparison between the source-drain conductance of (a) the encapsulated GSSD bridge rectifier shown in Section 5.3 and (b) a CVD graphene GSSD bridge rectifier, using the modified design. Insets to both graphs show schematics of the designs, with the current measurement direction shown. Both are measured at or near room temperature, with an AC frequency of 190 Hz.

The conductance of the CVD rectifier is far larger than that of the encapsulated rectifier, even at the NP for both devices. This indicates that the modified design is successful, in that reducing the S-D path length substantially reduces resistance. The higher minimum conductance of the CVD device also indicates a higher value of n_0, the NP carrier density, indicating a much larger carrier density due to spatial doping inhomogeneities. This is expected due to the SiO_2 substrate [54, 57]. The CVD GSSD bridge rectifier also shows a NP of almost $+15$ V. This indicates a relatively high degree of doping for the graphene.

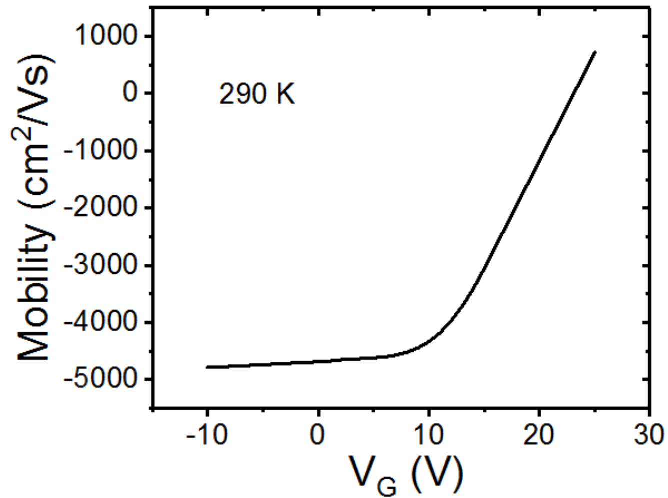

Figure 60: Carrier mobility for the CVD graphene used to fabricate the GSSD bridge rectifier, measured on a Hall bar. Negative values represent hole mobility and positive represent electron mobility. Note the different position of the neutrality point in this figure compared to Figure 59(b).

Figure 60 shows the carrier mobility for the CVD graphene used, calculated from measurements on a Hall bar structure next to the bridge rectifier. As can be seen, the position of the neutrality point is almost $+25\ \mathrm{V}$, very different from that measured at the GSSD bridge rectifier (Figure 59(b)). This indicates a large degree of variation in doping across the graphene. Due to the extremely positive position of the NP, the mobility can only be calculated for holes. The value reaches a peak of $4{,}800\ \mathrm{cm}^2/\mathrm{Vs}$.

Figure 61 shows the output voltage for a CVD GSSD bridge rectifier, as a function of gate voltage and at temperatures from room temperature down to 23 K.

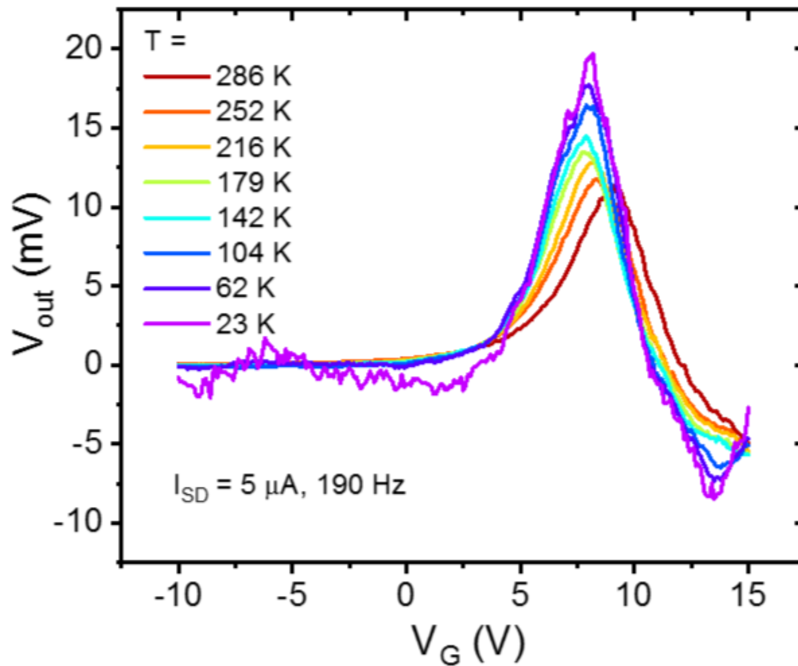

Figure 61: Output voltage of the CVD graphene GSSD bridge rectifier as a function of gate voltage, for an AC input of 5 μA at 190 Hz. Shown for a range of temperatures from room temperature down to 23 K.

This shows that unlike for the encapsulated GSSD bridge rectifier as shown in Figure 56, there is only a small increase in output voltage with decreasing temperature. The exact reason for this is unclear, but the fact that spatial charge inhomogeneity is much larger, as shown by the large minimum conductivity, may mean that thermally generated carriers play less of a role in conduction at room temperature. Therefore, the mixing of carriers cannot be reduced with decreasing temperature to the extent that it is for the encapsulated device. Despite this, however, the output voltage is very large in magnitude, greater than the encapsulated device by almost a factor of 5 at room temperature (see Figure 55 for comparison). The cause of this large difference is unknown. One possible explanation is the presence of a large amount of doping (due to, for example, PMMA residue) in certain parts of the device, creating effective P-N junctions to appear. If these were present in a fortunate arrangement on GSSD channels, they could massively increase the output at low frequencies.

Because of the large S-D conductance and the high output voltage, it is clear that the CVD GSSD bridge rectifier boasts an extremely large responsivity. This is calculated at room temperature, shown in Figure 62.

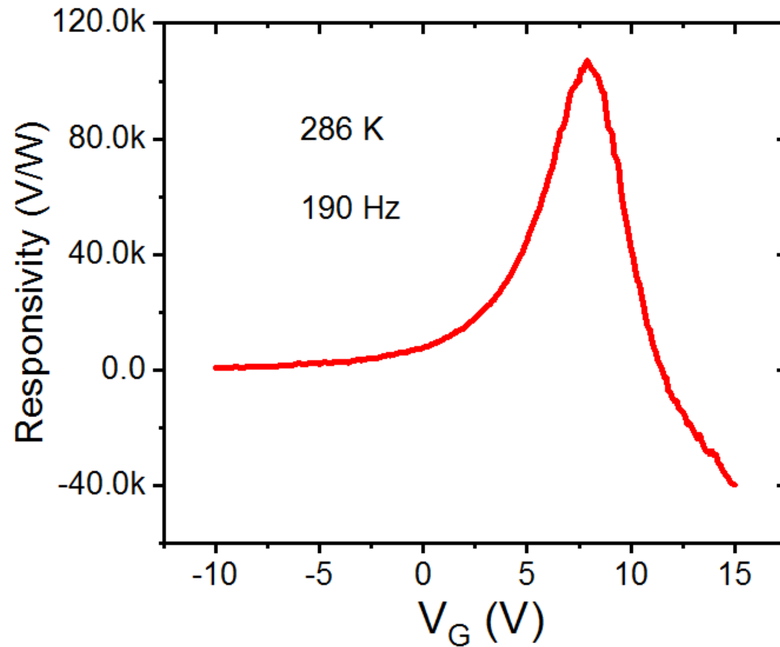

Figure 62: Calculated responsivity for a CVD graphene GSSD bridge rectifier, as a function of gate voltage. Data was measured near room temperature, at a frequency of 190 Hz. Here, positive values represent the hole conduction region, which forms the vast majority of the gate voltage range shown here, while negative values represent the electron conduction region.

This shows that the responsivity is indeed far larger than that calculated for the encapsulated GSSD bridge rectifier, which is shown in Figure 57. The low-frequency room-temperature responsivity exceeds 100,000 V/W, with a peak of 101,500 V/W, making it far higher than that measured for any ballistic rectifier [50]. However, it is expected that responsivity will decrease as frequency increases.

Using Equation 54, the extrinsic capacitance of this design is calculated to be 2.3×10^{-17} F, due to the thicker trenches perpendicular to the GSSD channels. At the gate voltage which gives maximum responsivity, +8.8 V, the input resistance is $4{,}290\ \Omega$. Therefore, this device has a cut-off frequency of

1.6 THz. This is much higher than for the encapsulated rectifier, meaning that this device is capable of operating over a much larger portion of the THz frequency range.

5.5. *Noise Measurements*

One of the benefits of the ballistic rectifier is its low noise, because its output consists entirely of the rectified voltage with no current flow or DC bias, meaning that output noise is dominated by thermal noise between the U and L contacts [50]. While the GSSD does not have the same benefits, the GSSD bridge rectifier designs shown above have the same general layout as a ballistic rectifier, with the U and L output terminals orthogonal to the input S and D. Therefore, it might be expected to observe a similar trend as the ballistic rectifier. To test this, a CVD GSSD bridge rectifier of the design shown in Figure 58(b) was connected to the 2 channel cross-correlation noise measurement circuit shown in Section 3.3.1. Voltage noise in the output was measured with no input bias, then with increasing input current until the detector saturated. The measured noise spectra are shown in Figure 63.

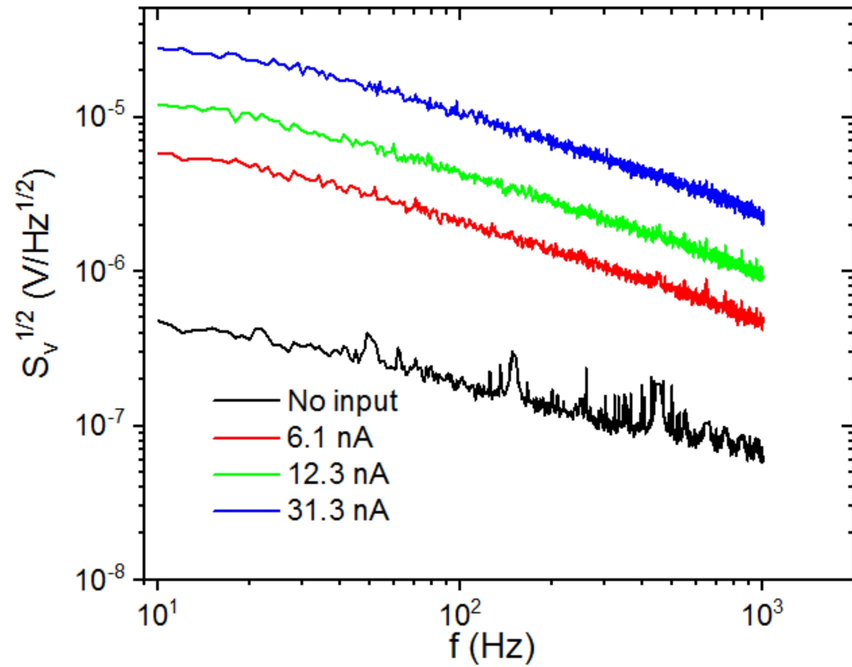

Figure 63: Spectral noise voltage from the output of a CVD GSSD bridge rectifier, with different input currents. Input currents were kept small, as larger currents caused enough noise to saturate the detector.

The spectral noise voltage measured for this device is extremely large, even when no input current is applied. Even for extremely small input currents, the output noise increases in magnitude extremely quickly, to the point where the detector was in danger of saturating for any input currents larger than shown in Figure 63.

These noise measurements can be used to give a rough estimation of the NEP of the device shown in Section 5.4. However, because these measurements only deal with input currents in the nA range and those responsivity measurements used input currents of $5\ \mu\mathrm{A}$, some estimation must be performed. Hooge's model for flicker noise predicts that S_V/V_{SD}^2 is constant at a given frequency [144]. If it is assumed that the device's input resistance stays constant with input current, then S_V/I_{SD}^2 would also hold constant. Using the values shown in Figure 63, this relationship predicts a noise level of $S_V^{1/2} \sim 1.2 \times 10^{-3}\ \mathrm{V/Hz^{1/2}}$ for an input current of 5 μA at 190 Hz, which is extremely large. However,

with the also extremely large peak responsivity of 101,500 V/W this gives a minimum NEP of $11.7\ \mathrm{nW/Hz^{1/2}}$. This indicates that although the GSSD bridge rectifier and the GBR have somewhat similar layouts, with output orthogonal to the input direction and no current flow through the output, the GSSD bridge rectifier does not benefit from the same isolation of output noise from the input. This has considerable detrimental effect on the noise equivalent power for these devices. CVD-grown graphene is expected to have large low-frequency noise [158]. It is commonly expressed that this is due to trap states at the graphene:substrate interface [158, 159]. However, an explanation for the much larger noise in this case lies in the long, narrow channels that all current must pass through in a GSSD bridge rectifier. It is expected that the large amount of etched edges cause large densities of trap states in these channels. If charging/discharging of trap states contributes significantly to noise in CVD graphene [158, 159], it follows that these edge traps are responsible for much of this measured noise. This is confirmed by comparison to noise measurements of a GBR array in Section 4.6, which does not pass current through micron-long narrow channels and hence is less susceptible to noise originating from edge traps. In addition, any noise arising from temperature fluctuations in these extremely narrow channels may also contribute to this large noise.

5.6. Summary

In this chapter, graphene self-switching diodes made using both hBN-encapsulated manually exfoliated graphene and CVD-grown graphene on bare SiO_2, and arrays of GSSDs were combined into bridge rectifiers.

A GSSD bridge rectifier constructed from hBN-encapsulated graphene was demonstrated, showing peak responsivities of $4{,}400\ \mathrm{V/W}$ and $1{,}570\ \mathrm{V/W}$ in the electron and hole conduction regimes respectively. Much like the ballistic rectifier, the GSSD bridge rectifier has output consisting purely of rectified voltage and is orthogonal to the input. If, therefore, it is assumed that only thermal noise

dominates the output, the minimum NEPs are calculated to be $5.4\ \mathrm{pW/Hz^{1/2}}$ for electrons and $18.2\ \mathrm{pW/Hz^{1/2}}$ for holes. The cut-off frequency for this device was calculated to be 0.15 THz, putting this graphene SSD bridge rectifier only just into the THz region with an operational speed considerably lower than a graphene ballistic rectifier.

In the interest of moving towards up-scaling production of these devices, the next step was to test a GSSD bridge rectifier constructed from CVD-grown graphene. This device was fabricated using a modified bridge rectifier design which allowed for reduced extrinsic capacitance and much reduced input resistance. At low frequency, the device demonstrated far larger output voltage than the previous encapsulated device, with a peak output of over 10 mV at room temperature. The increased conductance gives the device a peak responsivity of 101,500 V/W. Not only is this far larger than the encapsulated GSSD bridge rectifier, it also exceeds any measured ballistic rectifier and even the predicted optimal GBR shown in Section 4.3. The reason for this large output is unknown, however it was theorised that local doping (due to for example PMMA residue on the graphene) variations may create effective P-N junctions at fortunate positions on the device, increasing current asymmetry on the GSSDs. Unfortunately, if this is the true cause, these high outputs are unlikely to be maintained at high frequencies. The low input resistance and capacitance puts the cut-off frequency at 1.6 THz. However, further testing must be done to test the reproducibility of these results, and measure the response at higher frequencies and into the THz region.

The fabricated CVD GSSD bridge rectifiers show relatively large levels of noise even for extremely low input currents, which is likely due to charging/discharging of edge states. For example, if the CVD GSSD bridge rectifier with high responsivity shown in Figure 62 is assumed to have similar noise performance as the device measured in Figure 63, the minimum NEP is estimated as $11.7\ \mathrm{nW/Hz^{1/2}}$, far worse than a ballistic rectifier [50]. While the extraordinarily large measured responsivity means this value is somewhat reasonable, it is considerably worse than most THz detectors [35]. By

comparison to the GBR array noise measurements in Section 4.6, it is theorised that this large noise is due to charging/discharging of edge trap states in the long narrow GSSD channels. Further testing must be performed to determine whether this noise is a result of the CVD graphene used to fabricate the device, or whether it also extends to the encapsulated graphene-based GSSD bridge rectifiers presented earlier in the section and shown in [123].

6. Simulation of Terahertz Graphene Antennas

A major obstacle to the implementation of THz rectennas using rectifiers such as GBRs and GSSDs is the typically high impedance of these devices. When coupled to a metal antenna, which generally would have an impedance of around $50\ \Omega$, the impedance mismatch causes large power losses, greatly degrading the performance of the resulting device. This is discussed in Section 2.3, with Sections 4.4 and 4.5 giving calculations for the reduced responsivities of GBRs when impedance matching losses are taken into account. Graphene antennas are desirable for combining with graphene rectifiers such as the GBR and the GSSD, as this eliminates the metal:graphene contact as a source of loss, and also allows for simpler fabrication. As explained in Section 2.1.4, graphene's electronic properties cause it to be capable of hosting plasmonic resonances at THz frequencies. Because of this, plasmonic graphene THz antennas can be constructed, using the plasmon resonance to couple free-space THz waves to emitters, detectors, or other THz circuitry. These graphene-based antennas have been shown by simulation to have much higher impedances than metal antennas, up to and potentially beyond $1\ \mathrm{k}\Omega$ [36, 160–162], which massively reduces losses due to impedance mismatch when coupled to a high-impedance device. Graphene antennas with lengths in the 10s of $\mu\mathrm{m}$ have been demonstrated to have resonance peaks in the THz region, and in addition due to the nature of graphene the resonant frequency as well as other properties can be tuned by various doping methods [36, 80, 161, 163]. Due to the higher impedance of these antennas, they offer much better matching to high-impedance rectennas such as the GBR and GSSD. During the 2020 laboratory closures caused by COVID-19, it was decided that simulations of THz graphene antennas would be extremely beneficial, in order to test their performance when coupled to high-impedance rectifiers such as these and hence pave the way for future fabrication of all-graphene THz rectennas.

It was first demonstrated using simulation in 2010 that that graphene patches can resonate in THz region, with subwavelength size of the order of micrometers [81, 164]. Shortly afterwards,

subwavelength THz graphene antennas were first simulated, demonstrating how SPPs can be excited on a graphene sheet in order to couple to far field radiation [161]. In both cases, tunability was demonstrated by means of modifying the graphene's chemical potential, which practically can be achieved simply by using an electric field. In addition, simulations of graphene microstrip patch antennas have been reported in the literature [80, 165]. These also operate with deeply subwavelength sizes, showing for example that a circular patch with radius $18\ \mu m$ can resonate at around 2 – 4 THz depending on substrate, with reflection parameter S_{11} in the range of -20 dB to -40 dB [80]. As one example of the interesting potential applications made possible by graphene's tunability, a proposal has been made to construct an antenna with several areas which can be effectively switched on or off purely by electrostatic field, allowing for the antenna polarisation to be modified [166]. Another possibility that has been considered is using graphene as a reconfigurable element in a larger metal antenna [162].

Despite the wide range of interesting graphene-based THz antennas which have been investigated in the literature, there has been surprisingly little thorough testing of simple dipole and bowtie antenna structures. This chapter contains parametric studies of two simple 2D antenna structures, the dipole antenna and the bowtie antenna, with varying antenna sizes and with different graphene material parameters. These structures are capable of being easily integrated with a graphene-based rectifier such as a GBR array or GSSD bridge rectifier, because the rectifiers are of suitable size to be located directly in the antenna's central feed. In addition, having both the antenna and the rectifier be comprised of monolayer graphene makes device fabrication potentially simpler, and would eliminate graphene:metal contact resistance, which even advanced 1D contact fabrication techniques can only reduce to the 100s of Ω [52].

The simulations in this section all use the method described in section 3.4. The accuracy of simulations was confirmed in several ways. THz-frequency metal dipole antennas were simulated, with

the resonance peaks found to vary with antenna length as expected. To verify the accuracy and validity of the simulation of graphene, simulations were performed replicating the structures of graphene antenna simulations found in the literature. In all cases the simulated results were a close match.

6.1. Dipole Antennas

A dipole antenna is an extremely simple antenna structure, generally consisting of two identical conducting arms with a central feed. A sinusoidal varying current is applied between the arms, producing an oscillating electric field that is the antenna's radiation. The first resonance peak of a typical dipole antenna is for a wavelength double that of its total length. At this frequency the antenna impedance as seen at the central feed has no imaginary component and the antenna is said to be resonant. The typical radiation pattern of a dipole antenna is symmetrical around the axis of the antenna's orientation (the x axis in the following simulations), with almost no power radiated in the x direction. Metal dipole antennas are extremely commonly used for a wide range of telecommunications applications. In this section, 2D dipole antennas consisting of monolayer graphene on a dielectric substrate ($\varepsilon_r = 3.8$) have been simulated in CST studio suite [155]. All simulations have been using a fixed-impedance discrete port as an emitting source, because due to antenna reciprocity the antenna properties in transmission are identical to those in reception.

The simulated structure consists of two identical rectangular 2D graphene sheets for the antenna arms, connected by a central feed, as shown in Figure 64(a). The total antenna length L_{dip}, which includes both arms and the central feed, and width W_{dip} are defaulted to $24\ \mu\text{m}$ and 3 μm respectively, but can be set parametrically as desired for simulations. The central feed is implemented in the simulations as a discrete port, connecting between the two antenna arms, with a length of $3\ \mu\text{m}$ and width equal to W_{dip}. The default feed impedance is set to $1\ \text{k}\Omega$, as this acts as a suitable target value for reducing the input impedance of the rectifiers in previous setions. The substrate is modelled

as a simple dielectric with $\varepsilon_r = 3.8$. The substrate dimensions are held constant in all simulations of this structure, with thickness $10\ \mu\mathrm{m}$, width $20\ \mu\mathrm{m}$, and length $40\ \mu\mathrm{m}$ as shown in Figure 64. The substrate, with antenna on top, is surrounded by free space, $\varepsilon_r = 1$.

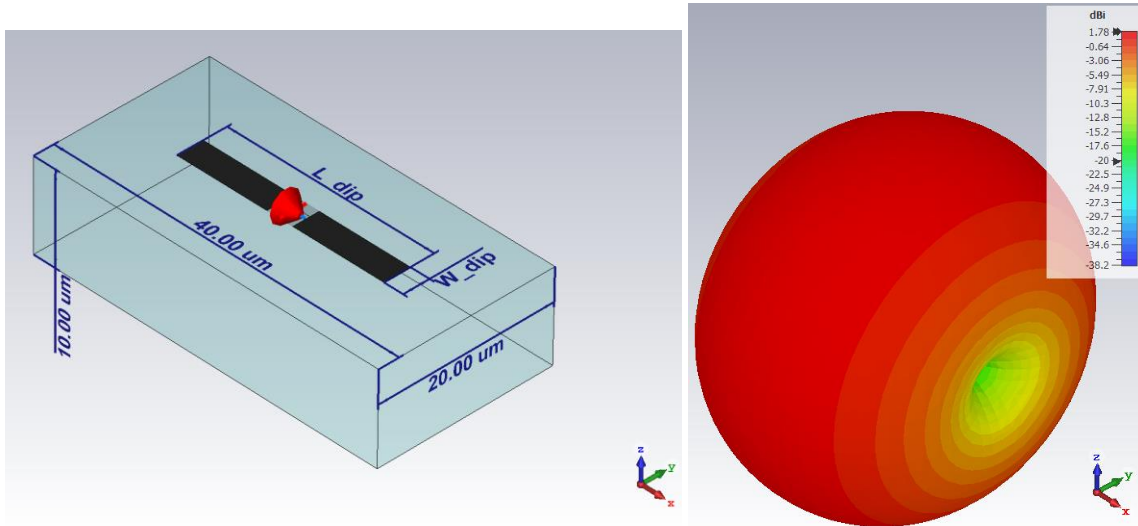

Figure 64: (a) Simulation structure for graphene dipole antennas. The substrate dimensions are shown, as well as the antenna width and total length W_{dip} and L_{dip} respectively. The central feed is $3\ \mu\mathrm{m}$ in length, with the excitation directed between the antenna arms in the direction indicated by the red arrow. (b) Radiation pattern for this antenna, with scale showing the directivity in dBi. Simulated with antenna width and length of $3\ \mu\mathrm{m}$ and $24\ \mu\mathrm{m}$ respectively and graphene properties of $\mu_c = 0.2\ \mathrm{eV}$ and $\tau = 0.5\ \mathrm{ps}$, at a frequency of 1 THz.

The graphene material is created in the simulation using CST studio's built-in macros for graphene, which generate the dispersive 2D conductivity for given values of chemical potential, relaxation time, and temperature. The intraband contribution is calculated using Equation 14, and the interband contribution is negligible at these frequencies. For all simulations, a temperature of 293 K is used. This macro produces values identical to those calculated using Equation 14 over the frequency range of interest. In order to achieve accurate simulation, in every direction the simulation must include some free space in between the device structure and the simulation boundaries. In all directions, a distance equal to $\frac{\lambda_0}{4}$ at the central simulation frequency is added. All boundaries are defined as a perfectly matched layer with minimum width of 5 mesh cells, which eliminates all reflections and gives a good approximation to effectively infinite free space. An ultrashort THz pulse is used as the excitation signal,

with Fourier transform giving the desired range of frequencies to be simulated. The simulation mesh is created automatically by CST, as described in section 3.4.

6.1.1. *Varying Length and Width*

Shown in Figure 65(a) is the reflection parameter S_{11} for the dipole antenna structure described above (and visible in Figure 64), as a function of frequency and for different antenna lengths. From the graph, it can be seen that the vast majority of peaks shift to lower frequency with increasing length, as expected. Reflection parameter peaks reach below -10 dB for all values of L_{dip}, with the peak heights for each resonance number increasing in magnitude (i.e. becoming more negative) with length. This indicates that with a source impedance of $1\ \mathrm{k\Omega}$, the majority of emitted power is coupled from source to free space via the antenna. This performance is much improved from what would be expected of a metal antenna of similar resonant frequency, because reflection losses between the $1\ \mathrm{k\Omega}$ source and $\sim 50\ \Omega$ antenna would be large, over 90%. Each value of L_{dip} produces several peaks in S_{11}, indicating the presence of several resonant frequencies. However there are some peaks, visible between 3 and 4 THz, which do not appear to move with antenna length and are almost identical for all except $L_{dip} = 8\ \mathrm{\mu m}$. Therefore, these peaks may arise from resonance across the antenna width, which is held constant for all simulations. This agrees with the much higher frequency of these peaks than the first resonance peaks for all values of L_{dip}.

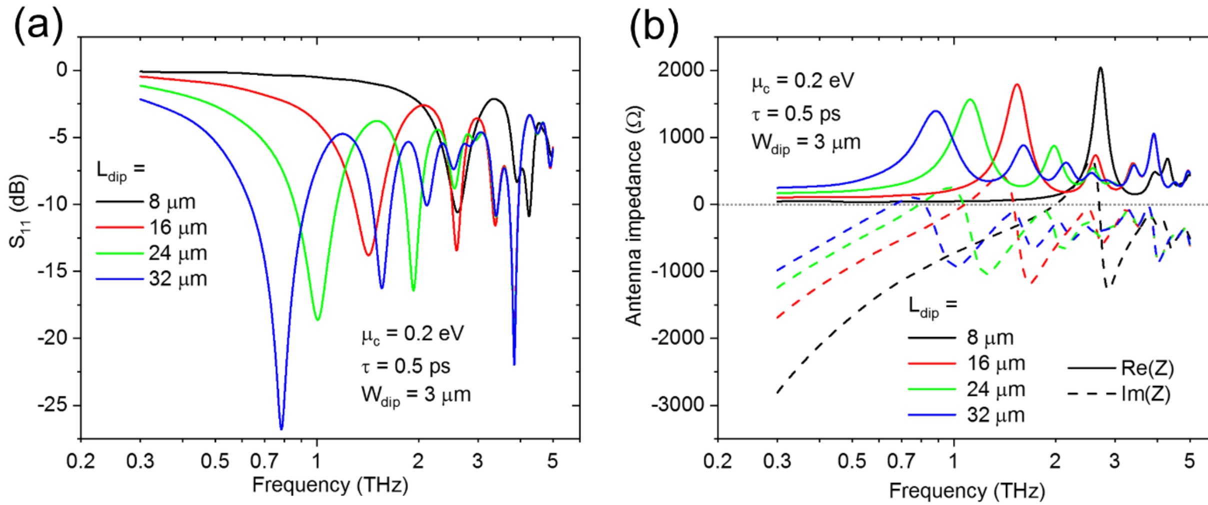

Figure 65: (a) Reflection parameter and (b) antenna impedance calculated from simulations of graphene dipole antennas with varying lengths, as a function of excitation frequency. Calculated using a source impedance of $1\ \mathrm{k\Omega}$. For all simulations graphene parameters of $\mu_c = 0.2\ \mathrm{eV}$ and $\tau = 0.5\ \mathrm{ps}$ have been used, with constant antenna width of $3\ \mu\mathrm{m}$.

The antenna reflection parameter depends on the impedance of the load or source it is operated with, which for the data shown in Figure 65(a) is $1\ \mathrm{k\Omega}$. As such, although plotting the calculated S_{11} as a function of frequency easily allows the resonance peaks to be seen when coupled to a given impedance load, the antenna's dispersive impedance is what directly determines the properties. The antenna's complex dispersive impedance is shown in Figure 65(b), for the same simulations as the S_{11} values shown in Figure 65(a).

By comparing Figure 65(a) and (b), one can see that S_{11} peaks coincide with frequencies where $\mathrm{Im}(Z_A) \approx 0$, and $\mathrm{Re}(Z_A) \approx \mathrm{Z_S}\ (= 1\mathrm{k\Omega})$. For the lower-frequency resonances for each value of L_{dip}, this occurs when $\mathrm{Im}(Z_A)$ crosses $0\ \Omega$, however higher-frequency S_{11} peaks tend to correspond to frequencies where $\mathrm{Im}(Z_A)$ approaches $0\ \Omega$, but reaches a maximum before crossing it. Instead of analysing the positions of the various S_{11} minima, which depend on the load impedance, it is preferable to look at the antenna 'working points', which are frequencies where $\mathrm{Im}(Z_A) = 0$ [161]. These represent positions where signal reflection between the antenna and the load (rectifier, or source for

the case of the simulations) are minimum, and hence roughly correspond to S_{11} minima. It is worth noting, however, that this does not mean that all power is received/transmitted by the antenna. It is likely that a sizable portion of the power is absorbed by the graphene itself. The positions of the first two resonant points (working points) are shown for an example antenna impedance curve in Figure 66.

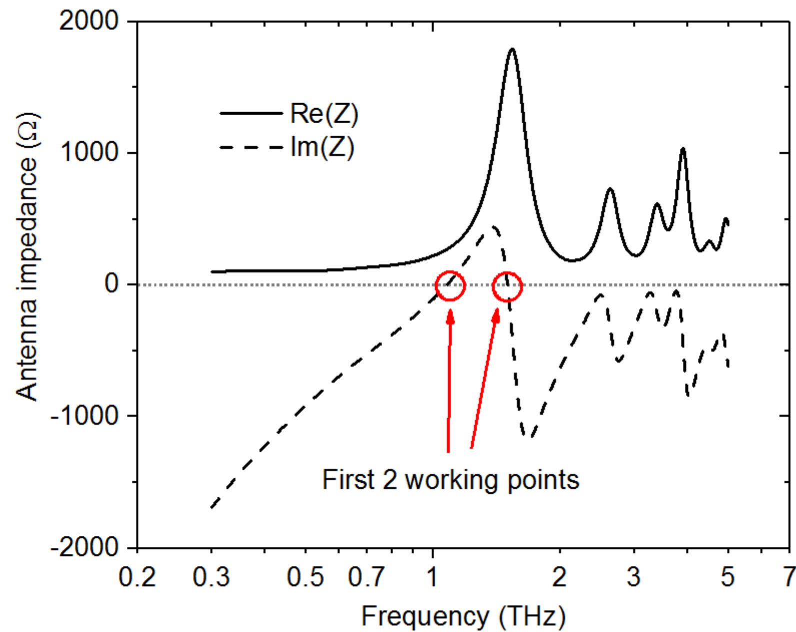

Figure 66: Positions of the first two resonant point frequencies for an example graphene dipole antenna.

This shows the structure of the dispersive antenna impedance. At the frequencies corresponding to the first two resonant points, the antenna resistance has very different values. For the example data shown here, the first has a resistance of around $270\ \Omega$ while the second has a much large resistance of $1700\ \Omega$.

Figure 67 shows how the positions of the first 2 of these resonant points vary with antenna length, as well as the (wholly real) antenna impedance at those points.

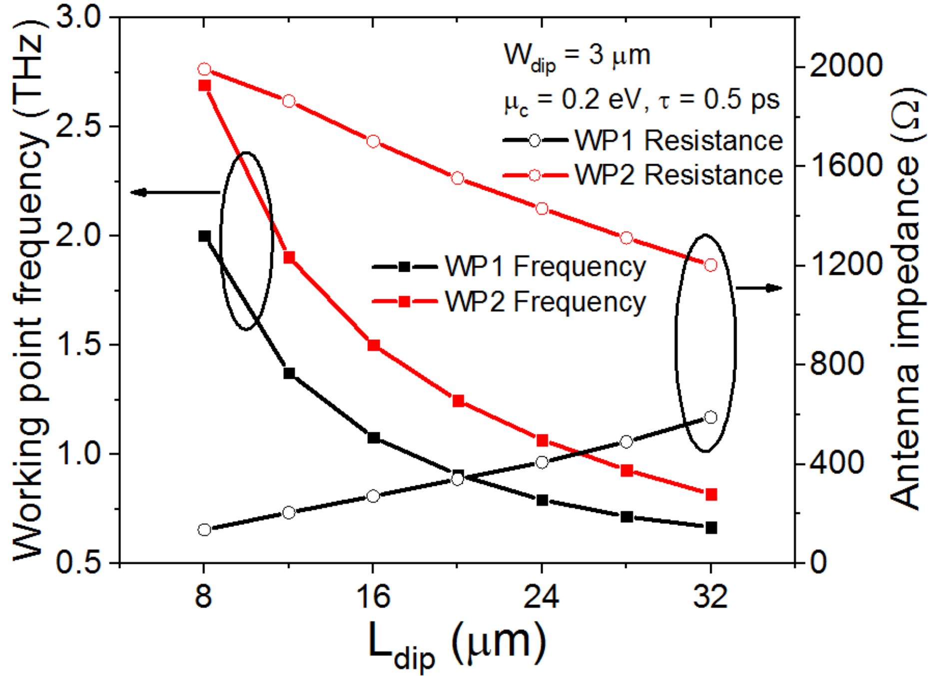

Figure 67: Resonant point (or working point, WP) frequencies of graphene dipole antennas as shown in Figure 64, as well as the antennas' real resistance at those frequencies, with varying total antenna length. Simulated using graphene chemical potential of 0.2 eV and relaxation time of 0.5 ps. For all cases, the antenna width is constant at $3\ \mu\mathrm{m}$.

As Figure 65(b) also shows, the frequency of each resonant point decreases with increasing antenna length. This *trend* is to be expected when considering the simple resonance condition, because shorter antennas lead to increased mode confinement and hence higher resonance frequencies. For each value of L_{dip}, of the two resonant points (P2) one has high impedance of the order of $1\ \mathrm{k\Omega}$ and the other (P1) has much lower impedance. In [36] it is stated that these correspond to the resonance conditions of $L_{dip} \approx \frac{1}{2}\lambda_{SP}$ and $L_{dip} \approx \lambda_{SP}$ respectively, however the frequencies in question for the referenced data are nowhere near a factor of 2 apart. This gives a strong indication of the non-linear relationship between frequency and plasmon wavelength. This can also be seen in the frequencies shown in Figure 67, which *do not show* the perfectly inverse relationship between resonant frequency and antenna length that is expected from Fabry-Perot resonance.

For simple resonance on a dipole antenna with large aspect ratio (i.e. $L_{dip} \gg W_{dip}$) one would expect the positions of resonance peaks to be independent of width, and depend only on length. Figure 68 shows the S_{11} and impedance of the dipole antenna, with varying W_{dip} and constant $L_{dip} = 24$ μm. Graphene parameters used are the same as for the previously shown data.

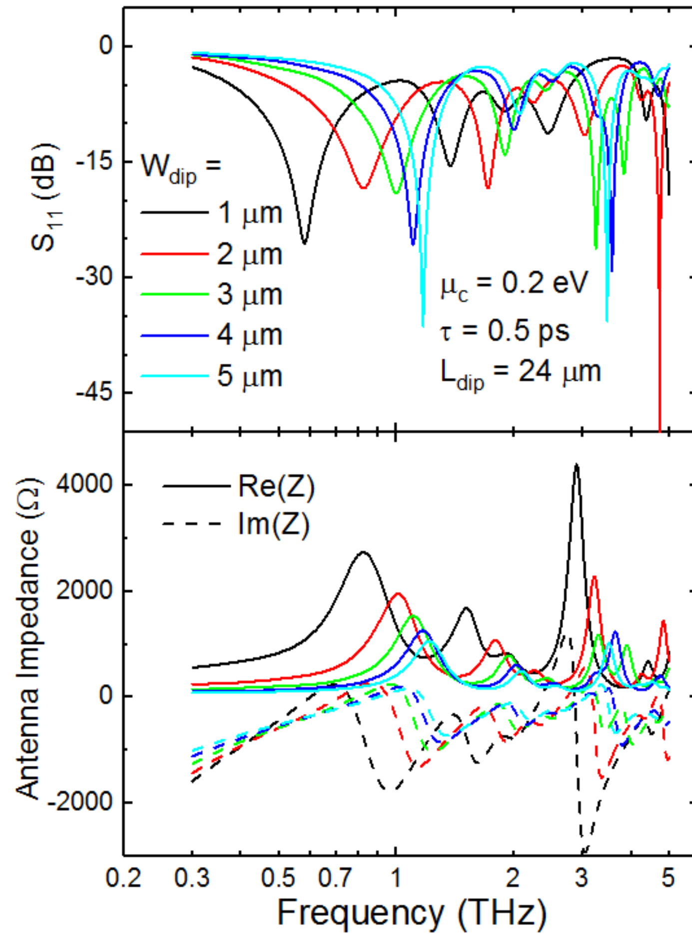

Figure 68: Reflection parameter (top) and antenna impedance (bottom) as a function of frequency, obtained from simulations of the graphene dipole antenna structure depicted in Figure 64. Data is shown with varying values of the dipole antenna width, W_{dip}, with constant total dipole length $L_{dip} = 24$ μm. Graphene parameters of $\mu_c = 0.2$ eV and $\tau = 0.5$ ps have been used for all simulations. S_{11} values calculated using a source impedance of 1 kΩ.

As can be seen, there is a strong dependence of the antenna properties on W_{dip}. This again indicates that the resonances seen in the simulation are not adequately described as simple Fabry-Perot resonance. In fact, the resonant frequencies seem to increase with increasing width, which is opposite

to the length dependence observed earlier. All values of width give resonances of at least -10 dB, indicating that there is still strong power transference from a 1 kΩ source to the antenna. This can also be seen by the real components of antenna impedance in areas where imaginary components are near 0, which are in the order of 1 kΩ. This is shown more clearly in Figure 69, which shows frequency positions and antenna resistances at the first two resonant points, as a function of antenna width.

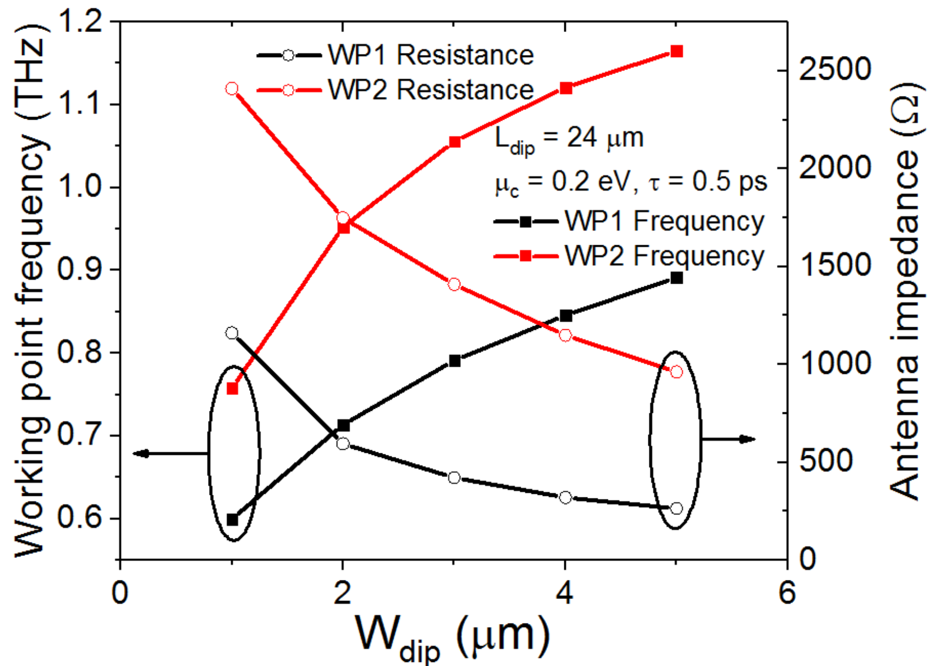

Figure 69: Resonant point (or working point, WP) frequencies and resistances of the graphene dipole antenna, with constant length but varying antenna width. Simulated using graphene chemical potential of 0.2 eV and relaxation time of 0.5 ps, and length $L_{dip} = 24$ μm.

Here, the increase in resonant point frequencies with width can be clearly seen. This trend is matched by results in literature which also observe strong dependence of resonant frequency on antenna width [81, 164]. This has been attributed to the reduced width causing increased confinement of surface plasmons, increasing the effective permittivity of the graphene in the length direction, and hence lowering the resonance frequency [81]. As well as increasing resonant point frequency, higher width also decreases antenna impedance. This is expected, due to the increased resonating area and source width.

6.1.2. Calculating Plasmon Wavelengths

In Section 2.1.4, a first order approximation is used to simplify the graphene plasmon dispersion relation in order to give Equation 19, which predicts that plasmon wavelength depends on the inverse square of frequency. However this equation, which approximates $\frac{\varepsilon_r}{\sqrt{k_{SP}^2-\varepsilon_r k_0^2}}+\frac{1}{\sqrt{k_{SP}^2-k_0^2}}$ as $\frac{\varepsilon_r+1}{k_{SP}}$, eliminates any dependence of plasmon wavelength on the graphene's carrier relaxation time τ, and can easily be shown to not fit the dependences shown in the previous section. An alternative approximation is to instead approximate as $\frac{\varepsilon_r+1}{\sqrt{k_{SP}^2-\varepsilon_r k_0^2}}$, which retains more information without drastically more complexity, and is applicable over a wider frequency range. This gives

$$k_{SP} \cong k_0 \sqrt{\varepsilon_r - \left(\frac{\varepsilon_r + 1}{Z_0 \sigma}\right)^2}, \qquad \text{Equation 62}$$

which after substituting in the conductivity becomes

$$k_{SP} \cong k_0 \sqrt{\varepsilon_r + A^2 \left(\omega + \frac{i}{\tau}\right)^2}. \qquad \text{Equation 63}$$

However, the wavelength $\lambda_{sp} \equiv \left(\frac{2\pi}{Re(k_{SP})}\right)$ now has no analytical solution using Equation 63, meaning that a second approximation must be taken. A first order expansion of Equation 62 leads back to Equation 17, so a second order expansion is taken. Rearranging, this gives an analytical approximation for the plasmon wavelength:

$$\lambda_{SP} \cong \frac{\lambda_0}{A\omega + \frac{\varepsilon_r}{2A} \cdot \frac{\omega}{\omega^2 + \frac{1}{\tau^2}}}. \qquad \text{Equation 64}$$

These different formulas for graphene plasmon wavelength are shown for example graphene parameters in Figure 70.

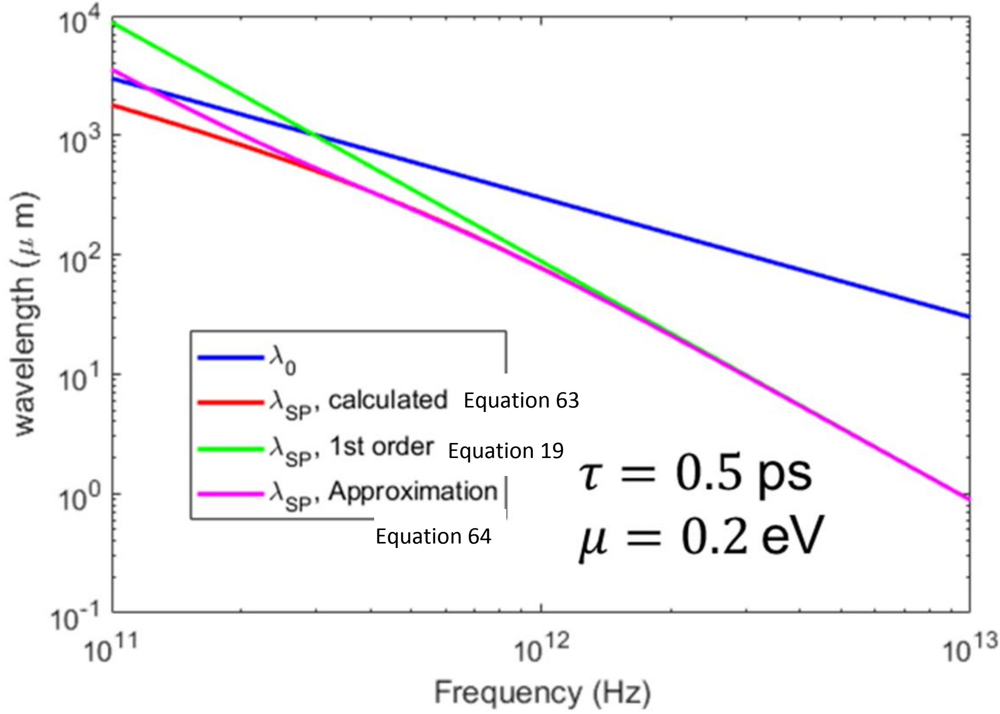

Figure 70: Different approximations for the plasmon wavelength, alongside the free space wavelength λ_0 shown in blue. Of the three values for λ_{SP} shown here, 'calculated' denotes calculated *numerically* from the real component of Equation 63, '1st order' is calculated from Equation 19, and 'Approximation' is the formula derived just above, Equation 64.

From this comparison, it can be seen that the simple formula shown in Section 2.1.4 is only accurate at high frequencies, above 1 THz, and is obviously unphysical at lower frequencies when it becomes larger than λ_0. The 2nd order expansion of Equation 62 is a good approximation down to a much lower frequency range, but also diverges at the bottom end of the THz region. It must be noted however that even Equation 63 uses an approximation of Equation 16. Hence the 'calculated' values in Figure 70, which are calculated numerically from $\lambda_{sp} \equiv \left(\frac{2\pi}{Re(k_{SP})}\right)$, differ slightly from the true plasmon wavelength over this range.

Here it can be clearly seen that plasmons in graphene are expected to have wavelengths far below the free space wavelengths, showing the theoretical founding for subwavelength graphene THz

antennas. However, it is also worth noting that all equations shown here assume an infinite uniform graphene sheet, which is an important limit to their applicability for small graphene patches.

Using this approximate formula for plasmon wavelength in terms of frequency and graphene properties, the theoretical wavelength at simulated antenna resonant points can be compared to the antenna length. Simulations have been performed with varying antenna length, for a range of antennas with different graphene properties. Figure 71 shows the frequency and calculated plasmon wavelength of the first resonant point, as a function of total antenna length L_{dip}, with varying graphene chemical potential. Note that some points are missing. Under these conditions no resonant points exist; the antenna impedance always has a negative imaginary component which never crosses $0\ \Omega$ and hence the antenna impedance is never real.

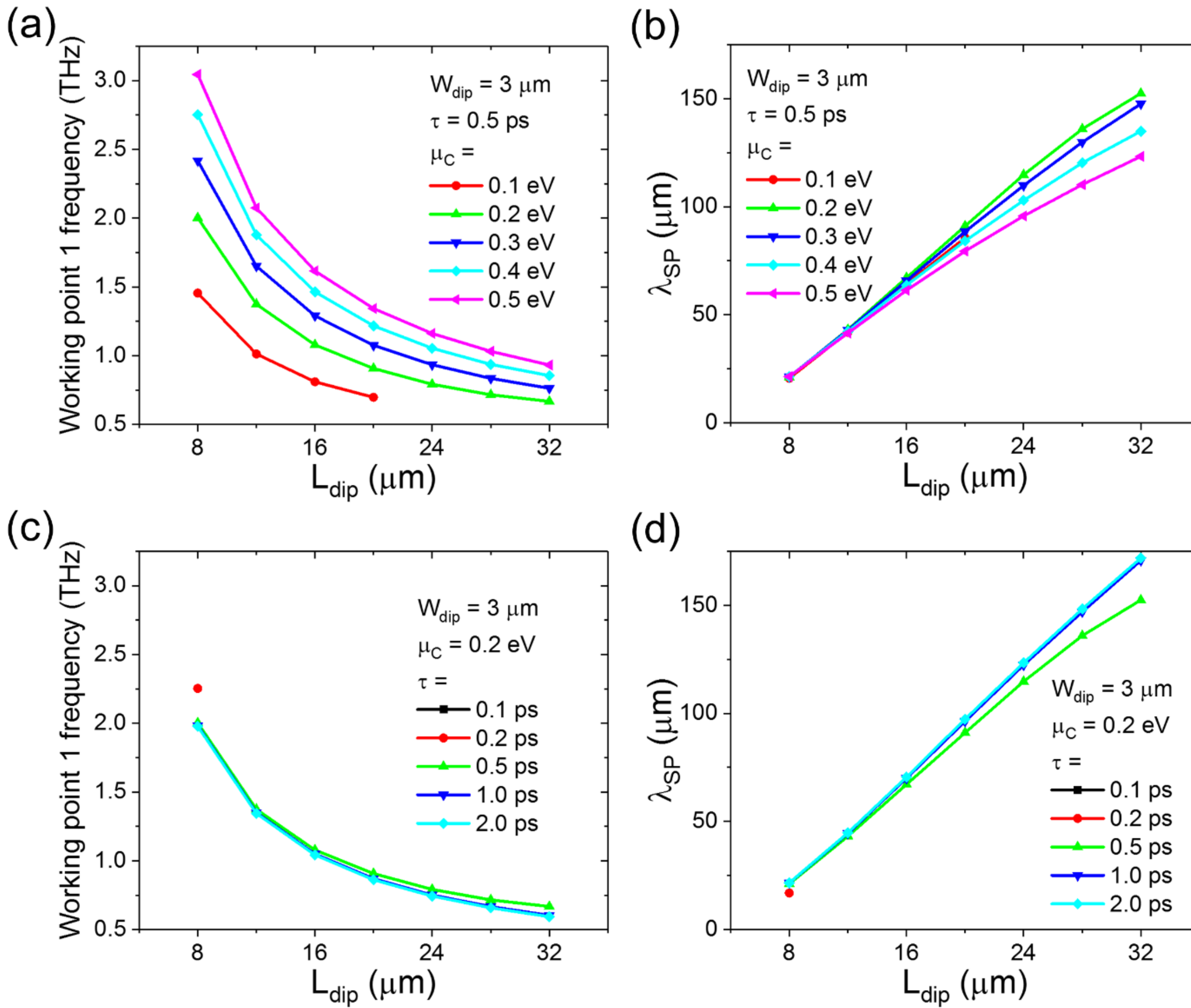

Figure 71: (a) First resonant point frequency of a graphene dipole antenna, as a function of antenna length and with increasing graphene chemical potential. (b) Theoretical plasmon wavelengths at the frequencies shown in (a), calculated using Equation 64 with the given graphene parameters. (c) and (d) show the same with varying carrier relaxation time. The data shown in green is duplicated between (a) and (c), and between (b) and (d). Missing data points indicate that no resonant points exist under these conditions. All simulations and calculations assume a temperature of 293 K.

In Figure 71(a) it can be seen that as in Figure 67 (from which the $\mu_C = 0.2$ eV, $\tau = 0.5$ ps data is duplicated here), resonant point frequency decreases with increasing antenna length for all chemical potentials. There is also a strong link between graphene chemical potential and resonant point frequency, with increasing μ_c causing higher frequency. This is expected, because increasing chemical potential increases conductivity and hence decreases plasmon wavenumber, meaning that for given

antenna length a higher frequency resonance is observed [37]. Figure 71(b) shows plasmon wavelengths calculated with Equation 64 for the frequencies and graphene properties shown in (a). Here it can be seen that despite the large variation in resonant point frequency caused by different values of μ_c, all calculated wavelengths are similar. At lover values of L_{dip}, the calculated values are almost identical and seem to follow a linear relationship, however with increasing L_{dip} the calculated wavelengths fall off for the largest values of μ_c. It must be noted however that despite the mostly linear relationship with antenna length, the calculated plasmon wavelengths at these frequencies are far larger than the antenna length and do not lie on a whole number multiple. This is due to Equation 64 being derived assuming an infinite graphene sheet. The confinement caused by the narrow graphene patches causes them to resonate at higher frequencies than an equivalent area of an infinite sheet [81]. Figure 71(c) shows how the first resonant point moves with graphene carrier relaxation time. It can be seen that over the range of values there is little change in frequency. In the plasmon wavelength calculations shown in (d), a consistent straight line dependence is observed with some deviation for $\tau = 0.5$ ps. However, for lower values of τ there is in fact no resonant point at all. When $\tau = 0.2$ ps a resonant point only appears for the shortest antenna, and for $\tau = 0.1$ ps there are no resonant points. This indicates that lower quality graphene, which is expected to have lower carrier mobilities and shorter relaxation times, is less suitable for use in THz antennas than graphene of higher quality.

6.2. Bowtie Antennas

A bowtie antenna is another simple planar antenna structure, with two arms being triangles or circle sectors. Metal bowtie antennas are generally much more wideband than dipole antennas, with the maximum and minimum frequencies depending on the minimum and maximum radii. The antenna simulated here uses circle sector arms, with all angles being $90°$ such that the antenna is self-

complimentary. Other than the antenna design and substrate dimensions, the simulation setup is identical to the dipole antenna simulations shown in Section 6.1.

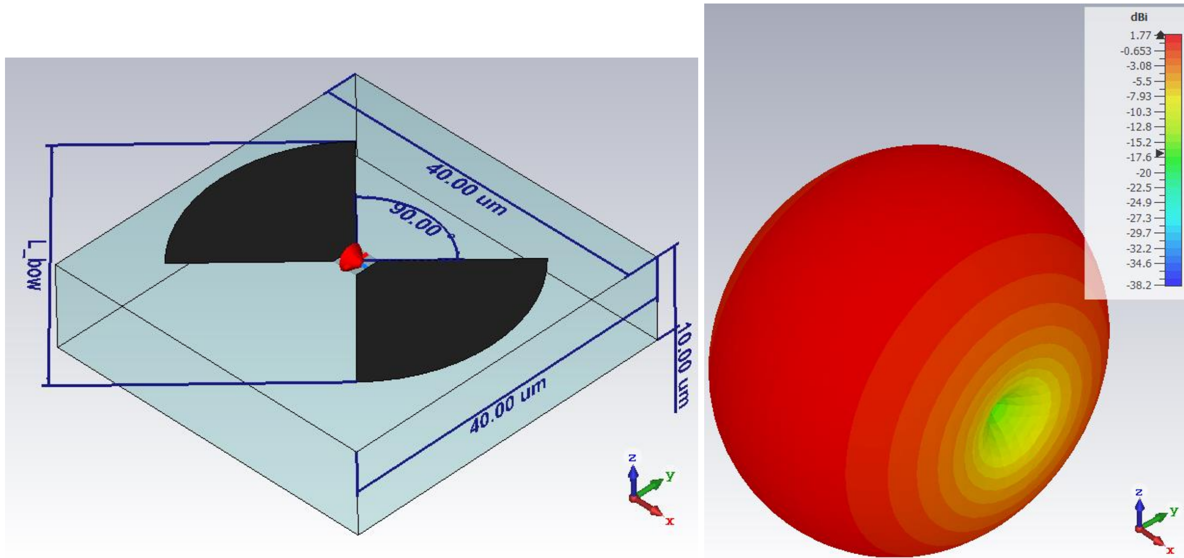

Figure 72: (a) Simulation structure for graphene bowtie antennas. The substrate dimensions are shown, as well as the antenna length L_{bow}. The central feed is 3 μm in length, with the excitation directed between the antenna arms in the direction indicated by the red arrow. Each arm covers an angle of 90°, with 90° between the arms. (b) Radiation pattern for this antenna, with scale showing the directivity in dBi. Simulated with antenna length of 24 μm with graphene properties of $\mu_c = 0.2$ eV and $\tau = 0.5$ ps, at a frequency of 1.4 THz.

Figure 73(a) shows the reflection parameters of this antenna when simulated with $\mu_c = 0.2$ eV and $\tau = 0.5$ ps. The first S_{11} peak is slightly broader than that shown for the dipole antenna shown in Figure 65(a), as is expected for a bowtie antenna, although the difference is less stark than would be expected for metal antennas. This antenna structure shows a strong, much narrower second resonant peak for all antenna sizes however. The expected trend of all resonance peaks moving to lower frequencies with increasing antenna size is observed, as expected.

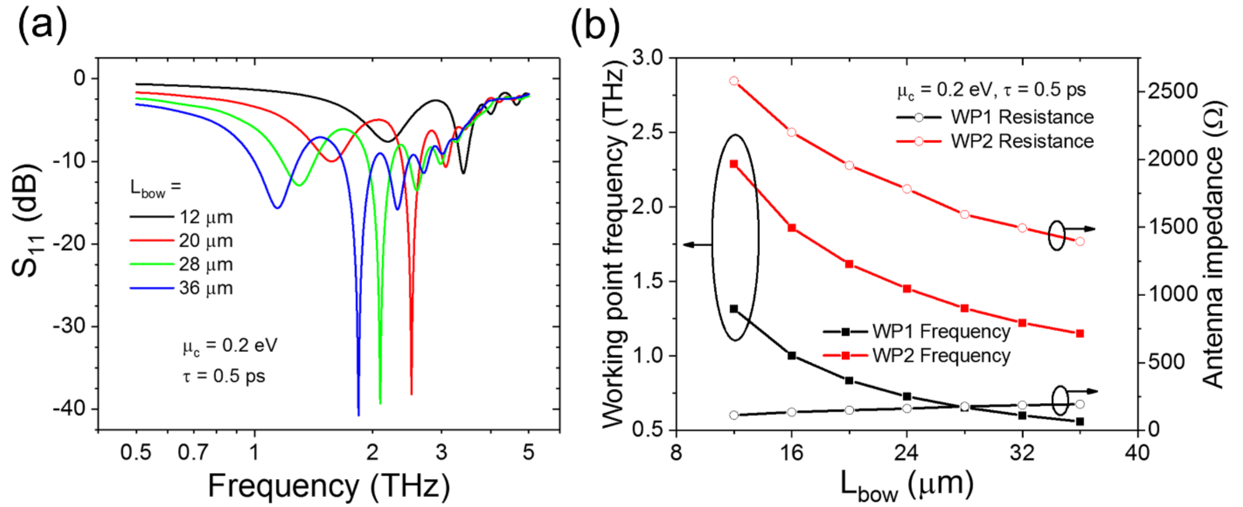

Figure 73: Characteristics of a simulated graphene bowtie antenna with structure shown in Figure 72, with parameters $\mu_c = 0.2$ eV and $\tau = 0.5$ ps. (a) shows the reflection parameter with varying antenna length, with a source impedance of $1\ \text{k}\Omega$. (b) shows the frequency and resistance of the first two resonant (working) points of the antenna.

The frequency and antenna resistance at the first two resonant points is shown in Figure 73(b). A similar trend in both results is observed to that of the dipole antenna seen in Figure 67. Both resonant points decrease in frequency with increasing length, with the first resonant point resistance increasing while the second decreases. A large difference in resonant point resistances is observed for this antenna structure. For the application of antennas such as these with high-impedance graphene rectennas such GSSDs and GBRs, an antenna impedance in the $\text{k}\Omega$ range is preferable in order to avoid high power losses to impedance mismatch. This can been seen in Figure 73(a), where the reflection parameter is calculated with a $1\ \text{k}\Omega$ source, meaning that the first peak frequency lies close to the second resonant point in frequency. For this reason resonant point two is preferable for these devices, which also means a higher minimum operating frequency.

Graphene produced by CVD growth is well known to be of lower quality than mechanically exfoliated and hBN-encapsulated graphene. Graphene is typically characterised by its carrier mobility, which is related to chemical potential and relaxation time by Equation 12. If we assume a high quality sample

of CVD graphene on bare SiO_2 with a mobility value of $5{,}000\ \mathrm{cm^2/Vs}$ [167, 168], a modest chemical potential of $0.2\ \mathrm{eV}$ gives $\tau \cong 0.1\ \mathrm{ps}$. Figure 74 shows impedance and reflection parameter of an antenna with these parameters, with larger size in the range $32 - 56\ \mathrm{\mu m}$.

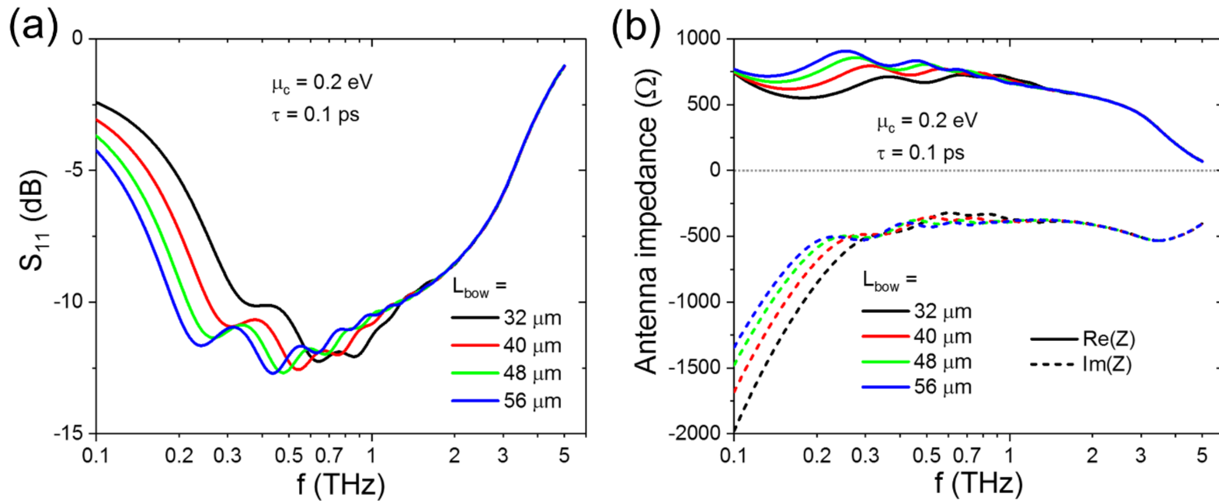

Figure 74: Simulated performance of a larger graphene bowtie antenna using parameters applicable to CVD-grown graphene. (a) shows reflection parameter S_{11} as calculated with a $1\ \mathrm{k\Omega}$ source, and (b) shows the complex antenna impedance. Both are shown over a range of antenna lengths.

Under these conditions, these larger antenna sizes give an extremely broad response, with S_{11} in the range of $-10\ \mathrm{dB}$ over an extremely broad range of frequencies and each size having a peak return loss of just over $-12\ \mathrm{dB}$. No sharp peaks are observed for any antenna size, which is due to the lack of antenna resonant points as shown in Figure 74(b). As is observed for dipole antennas in Figure 71, this lack of resonant points is due to the short carrier relaxation time considered in these simulations. This lack of strong peaks in S_{11} means that maximum power transfer to/from the antenna is somewhat limited, although a return loss of $-12\ \mathrm{dB}$ corresponds to a 94% power transfer from source to antenna, or from antenna to detector (e.g. rectifier).

6.3. Summary

It has been shown extensively that due to graphene's plasmonic properties, graphene antennas resonate in the THz range [36]. Simulations in this section show that due to the high impedance of simple graphene antennas, low reflection parameters, under $-20\ \mathrm{dB}$ from a $1\ \mathrm{k\Omega}$ source, and hence high levels of power transfer are observed, meaning that graphene antennas are also suited for high impedance detectors such as GSSDs and GBRs. Unlike metal dipole antennas, it was found that graphene dipole width has a strong effect on resonant frequency, as well as antenna length. This is likely due to narrow antenna widths causing additional confinement to plasmon modes, increasing the effective permittivity [81].

An alternative approximation to the graphene SP dispersion relation, which gives an analytical equation for plasmon wavelength, has been described here. It was shown that this approximation is applicable over a wider frequency range than the equation typically used in literature [37], and hence is applicable to frequencies $< 1\ \mathrm{THz}$. However, a large mismatch was found between antenna lengths and calculated plasmon wavelengths at resonant points. This is due to the confinement of the small antennas, meaning that the infinite sheet plasmon wavelength is not directly applicable to antennas in the 10s of $\mu\mathrm{m}$. Despite this, the resonant point frequencies do give plasmon wavelengths using this equation which change linearly with antenna length.

It was found that antenna resonant frequencies depend strongly on chemical potential, but less so on carrier relaxation time. However, for short relaxation times (or for very low chemical potentials) no resonant points exist for these antenna designs. In general, graphene antennas show many resonance peaks, many of which are broad. This is bad for frequency-specific THz detection without use of grating or resonating cavity, but good for broadband detection. Simulations using parameters realistic for CVD-grown graphene show that these antennas lack resonant points, so have no sharp resonance peaks for any size. CVD graphene can be used for antennas in these size ranges, giving extremely broad response

but peak power transfer of between $-12\ \mathrm{dB}$ and $-13\ \mathrm{dB}$ at just below 1 THz, depending on length. However, improved graphene quality, in terms of carrier mobility and hence relaxation time, has a lot of potential, because the presence of antenna resonant points will improve impedance matching and drastically increase the size of S_{11} peaks.

7. Conclusions and Future Work

7.1. Conclusions

This work has demonstrated several developments towards the use of graphene's excellent electronic properties for nanoelectronic devices. While unfortunately no THz results are presented here, this work paves the way towards combination of graphene THz antennas with high-frequency graphene nanodevices.

One such device is the GBR, which has previously had extremely good performance demonstrated, such as a room-temperature low-frequency responsivity of $23{,}000\ \mathrm{V/W}$ and NEP of $0.64\ \mathrm{pW/Hz^{1/2}}$, and THz detection up to and potentially beyond $0.685\ \mathrm{THz}$ [47, 50]. The newly developed theory in Section 4.1 shows a range of applicability over GBRs with different designs, and makes several predictions which will aid in the design and optimisation of GBRs. In particular, it highlights how the output voltage increases with narrower QPCs and is strongly improved by a large difference in carrier mobilities. Using optimistic, but fully achievable, device parameters, the theory predicts room temperature responsivity and NEP greatly improved from those previously demonstrated, at $50{,}800\ \mathrm{V/W}$ and $0.51\ \mathrm{pW/Hz^{1/2}}$.

In previous tests of GBRs, a major limiting factor in the application of these devices as THz devices is the power loss caused by impedance mismatch. As such, there is considerable potential for improvement by any technique to reduce device input resistance. By combining GBRs into arrays, the conductances of individual devices are added together, although the tests performed here show that the output voltage of the array is not simply given by the sum of each device. Although the intrinsic responsivity of an array of 3 GBRs is 0.55x that of a single device, the reduction in input resistance means that when taking into account impedance mismatch with a $50\ \Omega$ source the overall responsivity is still improved from $19.7\ \mathrm{V/W}$ to $32.5\ \mathrm{V/W}$. GBRs fabricated using CVD-grown graphene showed

surprisingly good results considering the lower mobility, with a single GBR having a responsivity of $10{,}000\ \mathrm{V/W}$. An array of five such devices, however, showed drastically reduced responsivity, even when impedance mismatches were taken into account. Nevertheless the extrinsic responsivities of these devices with a 50Ω source is still good, at $1500\ \mathrm{V/W}$ for the single device and $990\ \mathrm{V/W}$ for the array. Overall, results show that while combining GBRs into arrays reduces input impedance, this is sometimes offset by the large reduction in performance of each device individually, and hence the worse performance of the array.

Combining GSSD arrays into a bridge rectifier structure was shown to be a viable method for constructing a rectifier with the same input/output layout as the GBR. Encapsulated devices showed decent room temperature responsivities in the $\mathrm{kV/W}$ range, and if thermal noise is assumed to dominate the output they would have NEP in the low $\mathrm{pW/Hz^{1/2}}$. However, devices constructed from CVD graphene far outperformed them at low measurement frequencies, demonstrating responsivity of 101,500 V/W due to the high output voltage. The cause of this however is uncertain, making this result somewhat dubious; further testing is essential to confirm or disprove this performance, as well as to test how well it holds up at higher frequencies.

The noise measurements performed in Sections 4.6 and 5.5 used devices fabricated on the same substrate, using a single sample of CVD graphene. Therefore, a very direct comparison can be made between those measurements of these two structures. Despite the complexity of the 15-GBR array measured in Figure 45, it demonstrated far lower spectral noise than the GSSD bridge rectifier measured in Figure 63. It is theorised that the large noise of the CVD-grown GSSD bridge rectifier is due to the extremely long and narrow ($1\ \mu\mathrm{m} \times \sim 100\ \mathrm{nm}$) SSD channels, which mean that edge states play a much larger role in conduction. Charging and discharging of trap states such as these is likely to generate a significant amount of voltage noise [158, 159], causing the measured output noise of the GSSD bridge rectifier to be large. This observation of large noise from the GSSD bridge rectifier structure

does not bode well for the use of these devices as THz detectors. Even taking into account the large measured responsivity of the device in Section 5.4, the minimum NEP at a frequency of $190\ \mathrm{Hz}$ is estimated to be $11.7\ \mathrm{nW/Hz^{1/2}}$, well above what is observed for a GBR [50] or indeed for almost any other room-temperature THz detector [35].

Due to the high measured noise in the CVD GSSD bridge rectifiers shown here, they are less suitable for use in THz detection than GBRs. The theoretical optimised GBRs in Section 4.3 predict a NEP of 0.51 pW/Hz$^{1/2}$. This, as well as previous measurements [50], puts them on par with some of the best reported cooled THz detectors such as bolometers, and far outperforms the best conventional room-temperature detectors [35]. Combined with a suitable antenna, GBRs optimised using the theory outlined here are likely to perform extremely competitively as THz detectors.

The final chapter detailed simulations performed of THz graphene dipole and bowtie antennas, with a range of graphene properties. Graphene antennas are desirable for combining with these graphene-based rectifiers; as well as the higher impedance producing much better matching with high-impedance rectifiers, this also eliminates graphene-metal contact resistance and simplifies fabrication. Due to the need for large-scale manufacturing, and the large areas naturally required for antennas, CVD-grown graphene is by far the most likely candidate for these antennas. However, it has been shown that the antenna properties depend strongly on graphene quality. In lower quality graphene, the lower carrier mobility and shorter carrier relaxation time [37] means that no antenna resonant points exist; drastically worsening performance compared to better-quality graphene. With a $1\ \mathrm{k\Omega}$ source, the S_{11} minimum is only $-12\ \mathrm{dB}$ when simulated with parameters realistic for CVD graphene, compared to well under $-30\ \mathrm{dB}$ for longer relaxation times. While this certainly does not preclude CVD graphene antennas from usefulness, there is significant room for improvement with the development of better quality large-scale graphene production. This may include new techniques, further refinement of CVD growth, or perhaps new methods of treating or encapsulating grown graphene.

7.2. Future Work

There is significant potential for further work in several areas. Further testing of larger GBR arrays would be interesting, to test the limits of how much the input resistance can be lowered and potentially eliminate the problem of impedance mismatching altogether. However, care must be taken that these arrays do not degrade in performance (compared to a single device) so much as to become unusable. There is a lot of potential benefit to be gained from more testing of both GBRs and GSSDs constructed from CVD graphene. Measurement of these devices at higher frequencies and into the THz region will test whether their surprisingly good performance at low frequencies can be maintained as frequency increases.

Following on directly from this work, the next step is to combine the rectifiers presented in chapters 4 and 5 with the antennas simulated in chapter 6. These 'all-in-one' THz graphene rectennas could be fabricated from CVD graphene, because rectifiers and antennas have been demonstrated to function well when constructed from commercial-quality CVD graphene. While it is certainly possible to exfoliate and encapsulate graphene flakes large enough to test these rectennas, it does not help solve the problem of upscaling device fabrication. Improvement to the quality of large-scale graphene will give great improvements to antenna quality, and will likely improve the reproducibility and performance of CVD GSSDs and GBRs. Alternatively, it has been shown that even CVD-grown graphene can have mobilities similar to exfoliated graphene, when encapsulated with hexagonal boron nitride [169]. The development of a good method to upscale this would truly allow large-scale production of excellent performance graphene nanodevices, coupled to graphene antennas with strong resonance in the THz and good impedance matching.

References

[1] K. S. Novoselov, A. K. Geim, S. V. Morozov, D. Jiang, Y. Zhang, S. V. Dubonos, I. V. Grigorieva, and A. A. Firsov, “Electric Field Effect in Atomically Thin Carbon Films,” *Science*, vol. 306, no. 5696, pp. 666–669, Oct. 2004. DOI: 10.1126/science.1102896.

[2] J. Lee, L. Tao, K. N. Parrish, Y. Hao, R. S. Ruoff, and D. Akinwande, “Multi-finger flexible graphene field effect transistors with high bendability,” *Appl. Phys. Lett.*, vol. 101, no. 25, pp. 1–5, 2012. DOI: 10.1063/1.4772541.

[3] F. Torrisi, T. Hasan, W. Wu, Z. Sun, A. Lombardo, T. S. Kulmala, G.-W. Hsieh, S. Jung, F. Bonaccorso, P. J. Paul, D. Chu, and A. C. Ferrari, “Inkjet-Printed Graphene Electronics,” *ACS Nano*, vol. 6, no. 4, pp. 2992–3006, Apr. 2012. DOI: 10.1021/nn2044609.

[4] U. Khan, T. H. Kim, H. Ryu, W. Seung, and S. W. Kim, “Graphene Tribotronics for Electronic Skin and Touch Screen Applications,” *Adv. Mater.*, vol. 29, no. 1, pp. 2–8, 2017. DOI: 10.1002/adma.201603544.

[5] B. G. Choi, M. Yang, W. H. Hong, J. W. Choi, and Y. S. Huh, “3D macroporous graphene frameworks for supercapacitors with high energy and power densities,” *ACS Nano*, vol. 6, no. 5, pp. 4020–4028, May 2012. DOI: 10.1021/nn3003345.

[6] Q. Ke and J. Wang, “Graphene-based materials for supercapacitor electrodes – A review,” *J. Mater.*, vol. 2, no. 1, pp. 37–54, Mar. 2016. DOI: 10.1016/j.jmat.2016.01.001.

[7] J. M. Marmolejo-Tejada and J. Velasco-Medina, “Review on graphene nanoribbon devices for logic applications,” *Microelectronics J.*, vol. 48, pp. 18–38, Feb. 2016. DOI: 10.1016/j.mejo.2015.11.006.

[8] J. Phiri, P. Gane, and T. C. Maloney, “General overview of graphene: Production, properties and application in polymer composites,” *Materials Science and Engineering B: Solid-State Materials for Advanced Technology*. 2017. DOI: 10.1016/j.mseb.2016.10.004.

[9] V. B. Mohan, K. tak Lau, D. Hui, and D. Bhattacharyya, “Graphene-based materials and their composites: A review on production, applications and product limitations,” *Composites Part B: Engineering*. 2018. DOI: 10.1016/j.compositesb.2018.01.013.

[10] N. L. Teradal and R. Jelinek, “Carbon Nanomaterials in Biological Studies and Biomedicine,” *Adv. Healthc. Mater.*, vol. 6, no. 17, pp. 1–36, 2017. DOI: 10.1002/adhm.201700574.

[11] M. E. Foo and S. C. B. Gopinath, “Feasibility of graphene in biomedical applications,” *Biomed. Pharmacother.*, vol. 94, pp. 354–361, Oct. 2017. DOI: 10.1016/j.biopha.2017.07.122.

[12] P. R. Wallace, “The Band Theory of Graphite,” *Phys. Rev.*, vol. 71, no. 9, pp. 622–634, May 1947. DOI: 10.1103/PhysRev.71.622.

[13] A. K. Geim and K. S. Novoselov, “The rise of graphene,” *Nat. Mater.*, vol. 6, no. 3, pp. 183–191, Mar. 2007. DOI: 10.1038/nmat1849.

[14] C. Lee, X. Wei, J. W. Kysar, and J. Hone, “Measurement of the Elastic Properties and Intrinsic Strength of Monolayer Graphene,” *Science*, vol. 321, no. 5887, pp. 385–388, Jul. 2008. DOI: 10.1126/science.1157996.

[15] G. López-Polín, C. Gómez-Navarro, V. Parente, F. Guinea, M. I. Katsnelson, F. Pérez-Murano, and J. Gómez-Herrero, “Increasing the elastic modulus of graphene by controlled defect creation,” *Nat. Phys.*, vol. 11, no. 1, pp. 26–31, 2015. DOI: 10.1038/nphys3183.

[16] Y. Zhu, S. Murali, W. Cai, X. Li, J. W. Suk, J. R. Potts, and R. S. Ruoff, “Graphene and graphene oxide: Synthesis, properties, and applications,” *Adv. Mater.*, vol. 22, no. 35, pp. 3906–3924,

2010. DOI: 10.1002/adma.201001068.

[17] K. Kim, W. Regan, B. Geng, B. Alemán, B. M. Kessler, F. Wang, M. F. Crommie, and A. Zettl, "High-temperature stability of suspended single-layer graphene," *Phys. Status Solidi - Rapid Res. Lett.*, vol. 4, no. 11, pp. 302–304, 2010. DOI: 10.1002/pssr.201000244.

[18] E. B. Secor, P. L. Prabhumirashi, K. Puntambekar, M. L. Geier, and M. C. Hersam, "Inkjet printing of high conductivity, flexible graphene patterns," *J. Phys. Chem. Lett.*, vol. 4, no. 8, pp. 1347–1351, 2013. DOI: 10.1021/jz400644c.

[19] K. I. Bolotin, K. J. Sikes, Z. Jiang, M. Klima, G. Fudenberg, J. Hone, P. Kim, and H. L. Stormer, "Ultrahigh electron mobility in suspended graphene," *Solid State Commun.*, vol. 146, no. 9–10, pp. 351–355, 2008. DOI: 10.1016/j.ssc.2008.02.024.

[20] A. H. Castro Neto, F. Guinea, N. M. R. Peres, K. S. Novoselov, and A. K. Geim, "The electronic properties of graphene," *Rev. Mod. Phys.*, vol. 81, no. 1, pp. 109–162, 2009. DOI: 10.1103/RevModPhys.81.109.

[21] G. P. Williams, "Filling the THz gap—high power sources and applications," *Reports Prog. Phys.*, vol. 69, no. 2, pp. 301–326, Feb. 2006. DOI: 10.1088/0034-4885/69/2/R01.

[22] S. S. Dhillon, M. S. Vitiello, E. H. Linfield, A. G. Davies, M. C. Hoffmann, J. Booske, C. Paoloni, M. Gensch, P. Weightman, G. P. Williams, E. Castro-Camus, D. R. S. Cumming, F. Simoens, I. Escorcia-Carranza, J. Grant, S. Lucyszyn, M. Kuwata-Gonokami, K. Konishi, M. Koch, *et al.*, "The 2017 terahertz science and technology roadmap," *J. Phys. D. Appl. Phys.*, vol. 50, no. 4, p. 043001, Feb. 2017. DOI: 10.1088/1361-6463/50/4/043001.

[23] M. Tonouchi, "Cutting-edge terahertz technology," *Nat. Photonics*, vol. 1, no. 2, pp. 97–105, 2007. DOI: 10.1038/nphoton.2007.3.

[24] J. F. Federici, B. Schulkin, F. Huang, D. Gary, R. Barat, F. Oliveira, and D. Zimdars, “THz imaging and sensing for security applications - Explosives, weapons and drugs,” *Semicond. Sci. Technol.*, vol. 20, no. 7, 2005. DOI: 10.1088/0268-1242/20/7/018.

[25] H. A. Hafez, X. Chai, A. Ibrahim, S. Mondal, D. Fï¿½rachou, X. Ropagnol, and T. Ozaki, “Intense terahertz radiation and their applications,” *J. Opt. (United Kingdom)*, vol. 18, no. 9, 2016. DOI: 10.1088/2040-8978/18/9/093004.

[26] P. Knobloch, C. Schildknecht, T. Kleine-Ostmann, M. Koch, S. Hoffmann, M. Hofmann, E. Rehberg, M. Sperling, K. Donhuijsen, G. Hein, and K. Pierz, “Medical THz imaging: an investigation of histo-pathological samples,” *Phys. Med. Biol.*, vol. 47, no. 21, pp. 3875–3884, Nov. 2002. DOI: 10.1088/0031-9155/47/21/327.

[27] P. U. Jepsen, D. G. Cooke, and M. Koch, “Terahertz spectroscopy and imaging - Modern techniques and applications,” *Laser Photonics Rev.*, vol. 5, no. 1, pp. 124–166, 2011. DOI: 10.1002/lpor.201000011.

[28] R. Köhler, A. Tredicucci, F. Beltram, H. E. Beere, E. H. Linfield, A. G. Davies, D. A. Ritchie, R. C. Iotti, and F. Rossi, “Terahertz semiconductor-heterostructure laser,” *Nature*, vol. 417, no. 6885, pp. 156–159, May 2002. DOI: 10.1038/417156a.

[29] S. Chakraborty, O. Marshall, C. W. Hsin, M. Khairuzzaman, H. Beere, and D. Ritchie, “Discrete mode tuning in terahertz quantum cascade lasers.,” *Opt. Express*, vol. 20, no. 26, pp. B306-14, 2012. DOI: 10.1364/OE.20.00B306.

[30] T. G. Folland, “Graphene Controlled THz Quantum Cascade Lasers,” University of Manchester, 2014.

[31] G. P. Williams, P. Weightman, A. Doria, Y. Shen, D. M. Mittleman, M. Towrie, and H. Roskos, “High-power terahertz synchrotron sources,” *Philos. Trans. R. Soc. A Math. Phys. Eng. Sci.*, vol.

362, no. 1815, pp. 403–414, 2004. DOI: 10.1098/rsta.2003.1325.

[32] T. Idehara, T. Saito, I. Ogawa, S. Mitsudo, Y. Tatematsu, La Agusu, H. Mori, and S. Kobayashi, "Development of Terahertz FU CW Gyrotron Series for DNP," *Appl. Magn. Reson.*, vol. 34, no. 3–4, pp. 265–275, Aug. 2008. DOI: 10.1007/s00723-008-0132-6.

[33] S. V. Benson, "Free-Electron Lasers Push Into New Frontiers," *Opt. Photonics News*, vol. 14, no. 5, p. 20, May 2003. DOI: 10.1364/OPN.14.5.000020.

[34] M. A. Dem'yanenko, D. G. Esaev, B. A. Knyazev, G. N. Kulipanov, and N. A. Vinokurov, "Imaging with a 90frames⁄s microbolometer focal plane array and high-power terahertz free electron laser," *Appl. Phys. Lett.*, vol. 92, no. 13, p. 131116, Mar. 2008. DOI: 10.1063/1.2898138.

[35] R. A. Lewis, "A review of terahertz detectors," *J. Phys. D. Appl. Phys.*, vol. 52, no. 43, p. 433001, Oct. 2019. DOI: 10.1088/1361-6463/ab31d5.

[36] D. Correas-Serrano and J. S. Gomez-Diaz, "Graphene-based Antennas for Terahertz Systems: A Review," *Plasmonics*, vol. 15, no. 2, pp. 417–426, Apr. 2017.

[37] T. Low and P. Avouris, "Graphene plasmonics for terahertz to mid-infrared applications," *ACS Nano*, vol. 8, no. 2, pp. 1086–1101, 2014. DOI: 10.1021/nn406627u.

[38] F. Schwierz, "Graphene transistors," *Nat. Nanotechnol.*, vol. 5, no. 7, pp. 487–496, Jul. 2010. DOI: 10.1038/nnano.2010.89.

[39] L. Britnell, R. V. Gorbachev, A. K. Geim, L. A. Ponomarenko, A. Mishchenko, M. T. Greenaway, T. M. Fromhold, K. S. Novoselov, and L. Eaves, "Resonant tunnelling and negative differential conductance in graphene transistors," *Nat. Commun.*, vol. 4, pp. 2–6, 2013. DOI: 10.1038/ncomms2817.

[40] V. Ryzhii, T. Otsuji, M. Ryzhii, and M. S. Shur, "Double graphene-layer plasma resonances

terahertz detector," *J. Phys. D. Appl. Phys.*, vol. 45, no. 30, 2012. DOI: 10.1088/0022-3727/45/30/302001.

[41] X. Wang, Y. Ouyang, X. Li, H. Wang, J. Guo, and H. Dai, "Room-Temperature All-Semiconducting Sub-10-nm Graphene Nanoribbon Field-Effect Transistors," *Phys. Rev. Lett.*, vol. 100, no. 20, p. 206803, May 2008. DOI: 10.1103/PhysRevLett.100.206803.

[42] A. M. Song, A. Lorke, A. Kriele, J. P. Kotthaus, W. Wegscheider, and M. Bichler, "Nonlinear Electron Transport in an Asymmetric Microjunction: A Ballistic Rectifier," *Phys. Rev. Lett.*, vol. 80, no. 17, pp. 3831–3834, 1998. DOI: 10.1103/PhysRevLett.80.3831.

[43] A. M. Song, M. Missous, P. Omling, A. R. Peaker, L. Samuelson, and W. Seifert, "Unidirectional electron flow in a nanometer-scale semiconductor channel: A self-switching device," *Appl. Phys. Lett.*, vol. 83, no. 9, pp. 1881–1883, Sep. 2003. DOI: 10.1063/1.1606881.

[44] K. S. Champlin and G. Eisenstein, "Cutoff Frequency of Submillimeter Schottky-Barrier Diodes," *IEEE Trans. Microw. Theory Tech.*, vol. 26, no. 1, pp. 31–34, Jan. 1978. DOI: 10.1109/TMTT.1978.1129302.

[45] A. M. Song, P. Omling, L. Samuelson, W. Seifert, I. Shorubalko, and H. Zirath, "Operation of InGaAs/InP-based ballistic rectifiers at room temperature and frequencies up to 50 GHz," *Jpn. J. Appl. Phys.*, vol. 40, no. Part 2, No. 9A/B, pp. L909–L911, 2001. DOI: 10.1143/JJAP.40.L909.

[46] S. R. Kasjoo and A. M. Song, "Terahertz detection using nanorectifiers," *IEEE Electron Device Lett.*, vol. 34, no. 12, pp. 1554–1556, 2013. DOI: 10.1109/LED.2013.2285162.

[47] G. Auton, D. B. But, J. Zhang, E. Hill, D. Coquillat, C. Consejo, P. Nouvel, W. Knap, L. Varani, F. Teppe, J. Torres, and A. Song, "Terahertz Detection and Imaging Using Graphene Ballistic Rectifiers," *Nano Lett.*, vol. 17, no. 11, pp. 7015–7020, Nov. 2017. DOI: 10.1021/acs.nanolett.7b03625.

[48] A. K. Singh, S. R. Kasjoo, and A. M. Song, "Low-frequency noise of a ballistic rectifier," *IEEE Trans. Nanotechnol.*, vol. 13, no. 3, pp. 527–531, 2014. DOI: 10.1109/TNANO.2014.2308593.

[49] A. K. Singh, G. Auton, E. Hill, and A. Song, "Graphene based ballistic rectifiers," *Carbon*, vol. 84, no. 1, pp. 124–129, Apr. 2015. DOI: 10.1016/j.carbon.2014.11.064.

[50] G. Auton, J. Zhang, R. K. Kumar, H. Wang, X. Zhang, Q. Wang, E. Hill, and A. Song, "Graphene ballistic nano-rectifier with very high responsivity," *Nat. Commun.*, vol. 7, no. 1, p. 11670, Sep. 2016. DOI: 10.1038/ncomms11670.

[51] A. Westlund, M. Winters, I. G. Ivanov, J. Hassan, P.-Å. Nilsson, E. Janzén, N. Rorsman, and J. Grahn, "Graphene self-switching diodes as zero-bias microwave detectors," *Appl. Phys. Lett.*, vol. 106, no. 9, p. 093116, Mar. 2015. DOI: 10.1063/1.4914356.

[52] L. Wang, I. Meric, P. Y. Huang, Q. Gao, Y. Gao, H. Tran, T. Taniguchi, K. Watanabe, L. M. Campos, D. A. Muller, J. Guo, P. Kim, J. Hone, K. L. Shepard, and C. R. Dean, "One-dimensional electrical contact to a two-dimensional material," *Science*, vol. 342, no. 6158, pp. 614–617, 2013. DOI: 10.1126/science.1244358.

[53] A. S. Mayorov, R. V Gorbachev, S. V Morozov, L. Britnell, R. Jalil, L. A. Ponomarenko, K. S. Novoselov, K. Watanabe, T. Taniguchi, and A. K. Geim, "Micrometer-Scale Ballistic Transport in Encapsulated Graphene at Room Temperature," *Nano Lett.*, vol. 11, pp. 2396–2399, 2011. DOI: 10.1021/nl200758b.

[54] C. R. Dean, A. F. Young, I. Meric, C. Lee, L. Wang, S. Sorgenfrei, K. Watanabe, T. Taniguchi, P. Kim, K. L. Shepard, and J. Hone, "Boron nitride substrates for high-quality graphene electronics," *Nat. Nanotechnol.*, vol. 5, no. 10, pp. 722–726, 2010. DOI: 10.1038/nnano.2010.172.

[55] C. R. Dean, A. F. Young, P. Cadden-Zimansky, L. Wang, H. Ren, K. Watanabe, T. Taniguchi, P. Kim, J. Hone, and K. L. Shepard, "Multicomponent fractional quantum Hall effect in graphene," *Nat.

Phys., vol. 7, no. 9, pp. 693–696, Sep. 2011. DOI: 10.1038/nphys2007.

[56] K. S. Novoselov, A. K. Geim, S. V. Morozov, D. Jiang, M. I. Katsnelson, I. V. Grigorieva, S. V. Dubonos, and A. A. Firsov, “Two-dimensional gas of massless Dirac fermions in graphene,” *Nature*, vol. 438, no. 7065, pp. 197–200, Nov. 2005. DOI: 10.1038/nature04233.

[57] V. E. Dorgan, M. H. Bae, and E. Pop, “Mobility and saturation velocity in graphene on SiO2,” *Appl. Phys. Lett.*, vol. 97, no. 8, pp. 5–8, 2010. DOI: 10.1063/1.3483130.

[58] D. Delagebeaudeuf and N. T. Linh, “Metal-(n) AlGaAs-GaAs two-dimensional electron gas FET,” *IEEE Trans. Electron Devices*, vol. 29, no. 6, pp. 955–960, Jun. 1982. DOI: 10.1109/T-ED.1982.20813.

[59] E. H. Hwang and S. Das Sarma, “Limit to two-dimensional mobility in modulation-doped GaAs quantum structures: How to achieve a mobility of 100 million,” *Phys. Rev. B - Condens. Matter Mater. Phys.*, vol. 77, no. 23, 2008. DOI: 10.1103/PhysRevB.77.235437.

[60] J. P. Llinas, A. Fairbrother, G. Borin Barin, W. Shi, K. Lee, S. Wu, B. Yong Choi, R. Braganza, J. Lear, N. Kau, W. Choi, C. Chen, Z. Pedramrazi, T. Dumslaff, A. Narita, X. Feng, K. Müllen, F. Fischer, A. Zettl, *et al.*, “Short-channel field-effect transistors with 9-atom and 13-atom wide graphene nanoribbons,” *Nat. Commun.*, vol. 8, no. 1, p. 633, Dec. 2017. DOI: 10.1038/s41467-017-00734-x.

[61] G. Kucinskis, G. Bajars, and J. Kleperis, “Graphene in lithium ion battery cathode materials: A review,” *J. Power Sources*, vol. 240, pp. 66–79, Oct. 2013. DOI: 10.1016/j.jpowsour.2013.03.160.

[62] Z. Yang, J. Tian, Z. Yin, C. Cui, W. Qian, and F. Wei, “Carbon nanotube- and graphene-based nanomaterials and applications in high-voltage supercapacitor: A review,” *Carbon*, vol. 141, pp. 467–480, Jan. 2019. DOI: 10.1016/j.carbon.2018.10.010.

[63] H. Kim, K.-Y. Park, J. Hong, and K. Kang, “All-graphene-battery: bridging the gap between supercapacitors and lithium ion batteries,” *Sci. Rep.*, vol. 4, no. 1, p. 5278, May 2015. DOI: 10.1038/srep05278.

[64] H. Jang, Y. J. Park, X. Chen, T. Das, M. S. Kim, and J. H. Ahn, “Graphene-Based Flexible and Stretchable Electronics,” *Adv. Mater.*, vol. 28, no. 22, pp. 4184–4202, 2016. DOI: 10.1002/adma.201504245.

[65] “Ponor,” “Graphene - sigma and pi bonds.” [Online]. Available: https://commons.wikimedia.org/wiki/File:Graphene_-_sigma_and_pi_bonds.svg.

[66] J.-N. Fuchs, “Dirac fermions in graphene and analogues: magnetic field and topological properties,” UPMC, Paris; Université Paris-Sud, Orsay, 2013.

[67] R. R. Nair, P. Blake, A. N. Grigorenko, K. S. Novoselov, T. J. Booth, T. Stauber, N. M. R. Peres, and A. K. Geim, “Fine structure constant defines visual transparency of graphene,” *Science*, vol. 320, no. 5881, p. 1308, 2008. DOI: 10.1126/science.1156965.

[68] G. I. Ayzenshtat, V. G. Bozhkov, and A. Y. Yushchenko, “Measurement of the electron saturation velocity in an AlGaAs/InGaAs quantum well,” *Russ. Phys. J.*, vol. 53, no. 9, pp. 914–919, Feb. 2011. DOI: 10.1007/s11182-011-9510-x.

[69] J. Brownless, J. Zhang, and A. Song, “Graphene ballistic rectifiers: Theory and geometry dependence,” *Carbon*, vol. 168, pp. 201–208, Oct. 2020. DOI: 10.1016/j.carbon.2020.06.058.

[70] J. Martin, N. Akerman, G. Ulbricht, T. Lohmann, J. H. Smet, K. von Klitzing, and A. Yacoby, “Observation of electron–hole puddles in graphene using a scanning single-electron transistor,” *Nat. Phys.*, vol. 4, no. 2, pp. 144–148, Feb. 2008. DOI: 10.1038/nphys781.

[71] H. Wang, X. Zhang, and H. Takamatsu, “Ultraclean suspended monolayer graphene achieved

insitu current annealing," *Nanotechnology*, vol. 28, no. 4, 2017. DOI: 10.1088/1361-6528/28/4/045706.

[72] A. M. Song, S. Manus, M. Streibl, A. Lorke, and J. P. Kotthaus, "A nonlinear transport device with no intrinsic threshold," *Superlattices Microstruct.*, vol. 25, no. 1, pp. 269–272, 1999.

[73] L. Banszerus, M. Schmitz, S. Engels, M. Goldsche, K. Watanabe, T. Taniguchi, B. Beschoten, and C. Stampfer, "Ballistic Transport Exceeding 28 μm in CVD Grown Graphene," *Nano Lett.*, vol. 16, no. 2, pp. 1387–1391, 2016. DOI: 10.1021/acs.nanolett.5b04840.

[74] T. Taychatanapat, K. Watanabe, T. Taniguchi, and P. Jarillo-Herrero, "Electrically tunable transverse magnetic focusing in graphene," *Nat. Phys.*, vol. 9, no. 4, pp. 225–229, 2013. DOI: 10.1038/nphys2549.

[75] S. Masubuchi, K. Iguchi, T. Yamaguchi, M. Onuki, M. Arai, K. Watanabe, T. Taniguchi, and T. Machida, "Boundary scattering in ballistic graphene," *Phys. Rev. Lett.*, vol. 109, no. 3, pp. 1–5, 2012. DOI: 10.1103/PhysRevLett.109.036601.

[76] M. Y. Han, J. C. Brant, and P. Kim, "Electron transport in disordered graphene nanoribbons," *Phys. Rev. Lett.*, vol. 104, no. 5, pp. 2–5, 2010. DOI: 10.1103/PhysRevLett.104.056801.

[77] L. A. Ponomarenko, F. Schedin, M. I. Katsnelson, R. Yang, E. W. Hill, K. S. Novoselov, and A. K. Geim, "Chaotic Dirac Billiard in Graphene Quantum Dots," *Science*, vol. 320, no. 5874, pp. 356–358, Apr. 2008. DOI: 10.1126/science.1154663.

[78] G. W. Hanson, "Dyadic Green's functions and guided surface waves for a surface conductivity model of graphene," *J. Appl. Phys.*, vol. 103, no. 6, 2008. DOI: 10.1063/1.2891452.

[79] R. Landauer and M. Büttiker, "Resistance of Small Metallic Loops," *Phys. Rev. Lett.*, vol. 54, no. 18, pp. 2049–2052, May 1985. DOI: 10.1103/PhysRevLett.54.2049.

[80] M. Dashti and J. D. Carey, “Graphene Microstrip Patch Ultrawide Band Antennas for THz Communications,” *Adv. Funct. Mater.*, vol. 28, no. 11, p. 1705925, Mar. 2018. DOI: 10.1002/adfm.201705925.

[81] I. Llatser, C. Kremers, A. Cabellos-Aparicio, J. M. Jornet, E. Alarcón, and D. N. Chigrin, “Graphene-based nano-patch antenna for terahertz radiation,” *Photonics Nanostructures - Fundam. Appl.*, vol. 10, no. 4, pp. 353–358, Oct. 2012. DOI: 10.1016/j.photonics.2012.05.011.

[82] D. K. Gramotnev and S. I. Bozhevolnyi, “Plasmonics beyond the diffraction limit,” *Nat. Photonics*, vol. 4, no. 2, pp. 83–91, 2010. DOI: 10.1038/nphoton.2009.282.

[83] A. N. Grigorenko, M. Polini, and K. S. Novoselov, “Graphene plasmonics,” *Nat. Photonics*, vol. 6, no. 11, pp. 749–758, Nov. 2012. DOI: 10.1038/nphoton.2012.262.

[84] M. Jablan, H. Buljan, and M. Soljačić, “Plasmonics in graphene at infrared frequencies,” *Phys. Rev. B - Condens. Matter Mater. Phys.*, vol. 80, no. 24, pp. 1–8, 2009. DOI: 10.1103/PhysRevB.80.245435.

[85] F. H. L. Koppens, D. E. Chang, and F. J. García de Abajo, “Graphene Plasmonics: A Platform for Strong Light–Matter Interactions,” *Nano Lett.*, vol. 11, no. 8, pp. 3370–3377, Aug. 2011. DOI: 10.1021/nl201771h.

[86] F. Stern, “Polarizability of a Two-Dimensional Electron Gas,” *Phys. Rev. Lett.*, vol. 18, no. 14, pp. 546–548, Apr. 1967. DOI: 10.1103/PhysRevLett.18.546.

[87] V. P. Wallace, A. J. Fitzgerald, S. Shankar, N. Flanagan, R. Pye, J. Cluff, and D. D. Arnone, “Terahertz pulsed imaging of basal cell carcinoma ex vivo and in vivo,” *Br. J. Dermatol.*, vol. 151, no. 2, pp. 424–432, Aug. 2004. DOI: 10.1111/j.1365-2133.2004.06129.x.

[88] D. D. Arnone, C. M. Ciesla, A. Corchia, S. Egusa, M. Pepper, J. M. Chamberlain, C. Bezant, E. H.

Linfield, R. Clothier, and N. Khammo, “Applications of terahertz (THz) technology to medical imaging,” *Terahertz Spectrosc. Appl. II*, vol. 3828, no. September 1999, p. 209, 1999. DOI: 10.1117/12.361037.

[89] S. Sy, S. Huang, Y. X. J. Wang, J. Yu, A. T. Ahuja, Y. T. Zhang, and E. Pickwell-MacPherson, “Terahertz spectroscopy of liver cirrhosis: Investigating the origin of contrast,” *Phys. Med. Biol.*, vol. 55, no. 24, pp. 7587–7596, 2010. DOI: 10.1088/0031-9155/55/24/013.

[90] E. Heinz, T. May, D. Born, G. Zieger, S. Anders, V. Zakosarenko, H. G. Meyer, and C. Schäffel, “Passive 350 GHz Video Imaging Systems for Security Applications,” *J. Infrared, Millimeter, Terahertz Waves*, vol. 36, no. 10, pp. 879–895, 2015. DOI: 10.1007/s10762-015-0170-8.

[91] T. Nagatsuma, G. Ducournau, and C. C. Renaud, “Advances in terahertz communications accelerated by photonics,” *Nat. Photonics*, vol. 10, no. 6, pp. 371–379, Jun. 2016. DOI: 10.1038/nphoton.2016.65.

[92] Y. Yang, A. Shutler, and D. Grischkowsky, “Measurement of the transmission of the atmosphere from 0.2 to 2 THz,” *Opt. Express*, vol. 19, no. 9, p. 8830, Apr. 2011. DOI: 10.1364/OE.19.008830.

[93] M. C. Wiedner, I. Mehdi, A. Baryshev, V. Belitsky, V. Desmaris, A. M. Digiorgio, J. D. Gallego, M. Gerin, P. Goldsmith, F. Helmich, W. Jellema, A. Laurens, C. Risacher, A. Cooray, and M. Meixner, “A Proposed Heterodyne Receiver for the Origins Space Telescope,” *IEEE Trans. Terahertz Sci. Technol.*, vol. 8, no. 6, pp. 558–571, 2018. DOI: 10.1109/TTHZ.2018.2876093.

[94] S. Chatterjee, T. Grunwald, D. Köhler, K. Pierz, D. Golde, M. Kira, and S. W. Koch, “THz measurements of the optical response in a two-dimensional electron gas,” *Phys. Status Solidi Curr. Top. Solid State Phys.*, vol. 6, no. 2, pp. 453–456, 2009. DOI: 10.1002/pssc.200880337.

[95] D. Pashnev, V. V. Korotyeyev, J. Jorudas, T. Kaplas, V. Janonis, A. Urbanowicz, and I. Kašalynas, “Experimental evidence of temperature dependent effective mass in AlGaN/GaN

heterostructures observed via THz spectroscopy of 2D plasmons," *Appl. Phys. Lett.*, vol. 117, no. 16, 2020. DOI: 10.1063/5.0022600.

[96] O. P. Cherkasova, M. M. Nazarov, M. Konnikova, and A. P. Shkurinov, "THz Spectroscopy of Bound Water in Glucose: Direct Measurements from Crystalline to Dissolved State," *J. Infrared, Millimeter, Terahertz Waves*, vol. 41, no. 9, pp. 1057–1068, 2020. DOI: 10.1007/s10762-020-00684-4.

[97] R. A. Lewis, "A review of terahertz sources," *J. Phys. D. Appl. Phys.*, vol. 47, no. 37, 2014. DOI: 10.1088/0022-3727/47/37/374001.

[98] K. A. McIntosh, E. R. Brown, K. B. Nichols, O. B. McMahon, W. F. DiNatale, and T. M. Lyszczarz, "Terahertz photomixing with diode lasers in low-temperature-grown GaAs," *Appl. Phys. Lett.*, vol. 67, no. 26, pp. 3844–3846, Dec. 1995. DOI: 10.1063/1.115292.

[99] G. Dodel, "On the history of far-infrared (FIR) gas lasers: Thirty-five years of research and application," *Infrared Phys. Technol.*, vol. 40, no. 3, pp. 127–139, Jun. 1999. DOI: 10.1016/S1350-4495(99)00005-5.

[100] B. S. Williams, "Terahertz quantum-cascade lasers," *Nat. Photonics*, vol. 1, no. 9, pp. 517–525, Sep. 2007. DOI: 10.1038/nphoton.2007.166.

[101] N. Kumar, U. Singh, A. Bera, and A. K. Sinha, "A review on the sub-THz/THz gyrotrons," *Infrared Phys. Technol.*, vol. 76, pp. 38–51, May 2016. DOI: 10.1016/j.infrared.2016.01.015.

[102] G. R. Neil, "Accelerator Sources for THz Science: A Review," *J. Infrared, Millimeter, Terahertz Waves*, vol. 35, no. 1, pp. 5–16, Jan. 2014. DOI: 10.1007/s10762-013-9999-x.

[103] N. M. Burford and M. O. El-Shenawee, "Review of terahertz photoconductive antenna technology," *Opt. Eng.*, vol. 56, no. 1, p. 010901, 2017. DOI: 10.1117/1.oe.56.1.010901.

[104] A. Kosarev, S. Rumyantsev, M. Moreno, A. Torres, S. Boubanga, and W. Knap, “SixGey:H-based micro-bolometers studied in the terahertz frequency range,” *Solid. State. Electron.*, vol. 54, no. 4, pp. 417–419, Apr. 2010. DOI: 10.1016/j.sse.2009.12.032.

[105] “i2S.” [Online]. Available: https://www.i2s.fr/en.

[106] “NEC Corporation.” [Online]. Available: https://www.nec.com/.

[107] F. Rettich, N. Vieweg, O. Cojocari, and A. Deninger, “Field Intensity Detection of Individual Terahertz Pulses at 80 MHz Repetition Rate,” *J. Infrared, Millimeter, Terahertz Waves*, vol. 36, no. 7, pp. 607–612, Jul. 2015. DOI: 10.1007/s10762-015-0162-8.

[108] J. Neu and C. A. Schmuttenmaer, “Tutorial: An introduction to terahertz time domain spectroscopy (THz-TDS),” *J. Appl. Phys.*, vol. 124, no. 23, 2018. DOI: 10.1063/1.5047659.

[109] D. M. Pozar, *Microwave Engineering*, 4th ed. Wiley, 2011.

[110] M. Tooley, *Electronic Circuits: Fundamentals and Applications*. Taylor & Francis, 2012.

[111] S. Keyrouz and H. Visser, “Efficient direct-matching rectenna design for RF power transfer applications,” *J. Phys. Conf. Ser.*, vol. 476, no. 1, 2013. DOI: 10.1088/1742-6596/476/1/012093.

[112] J.-S. Rieh, S. Jeon, and M. Kim, “An overview of integrated THz electronics for communication applications,” in *2011 IEEE 54th International Midwest Symposium on Circuits and Systems (MWSCAS)*, 2011, pp. 1–4. DOI: 10.1109/MWSCAS.2011.6026592.

[113] J. D. Albrecht, M. J. Rosker, H. B. Wallace, and T.-H. Chang, “THz electronics projects at DARPA: Transistors, TMICs, and amplifiers,” in *2010 IEEE MTT-S International Microwave Symposium*, 2010, pp. 1118–1121. DOI: 10.1109/MWSYM.2010.5517258.

[114] Z. Zhu, S. Joshi, S. Grover, and G. Moddel, “Graphene geometric diodes for terahertz rectennas,” *J. Phys. D. Appl. Phys.*, vol. 46, no. 18, 2013. DOI: 10.1088/0022-3727/46/18/185101.

[115] L. Vicarelli, M. S. Vitiello, D. Coquillat, A. Lombardo, A. C. Ferrari, W. Knap, M. Polini, V. Pellegrini, and A. Tredicucci, “Graphene field-effect transistors as room-temperature terahertz detectors,” *Nat. Mater.*, vol. 11, no. 10, pp. 865–871, Oct. 2012. DOI: 10.1038/nmat3417.

[116] M. N. Gadalla, M. Abdel-Rahman, and A. Shamim, “Design, Optimization and Fabrication of a 28.3 THz Nano-Rectenna for Infrared Detection and Rectification,” *Sci. Rep.*, vol. 4, pp. 1–9, 2014. DOI: 10.1038/srep04270.

[117] Y. Wu, Y. Lin, A. A. Bol, K. A. Jenkins, F. Xia, D. B. Farmer, Y. Zhu, and P. Avouris, “High-frequency, scaled graphene transistors on diamond-like carbon,” *Nature*, vol. 427, pp. 74–78, 2011. DOI: 10.1038/nature09979.

[118] Y. Lin, K. Jenkins, D. Farmer, A. Valdes-Garcia, P. Avouris, C. Sung, H. Chiu, and B. Ek, “Development of graphene FETs for high frequency electronics,” in *2009 IEEE International Electron Devices Meeting (IEDM)*, 2009, pp. 1–4. DOI: 10.1109/IEDM.2009.5424378.

[119] D. Dragoman and M. Dragoman, “Geometrically induced rectification in two-dimensional ballistic nanodevices,” *J. Phys. D. Appl. Phys.*, vol. 46, no. 5, 2013. DOI: 10.1088/0022-3727/46/5/055306.

[120] G. Moddel, Z. Zhu, S. Grover, and S. Joshi, “Ultrahigh speed graphene diode with reversible polarity,” *Solid State Commun.*, vol. 152, no. 19, pp. 1842–1845, 2012. DOI: 10.1016/j.ssc.2012.06.013.

[121] M. Dragoman, M. Aldrigo, A. Dinescu, D. Dragoman, and A. Costanzo, “Towards a terahertz direct receiver based on graphene up to 10 THz,” *J. Appl. Phys.*, vol. 115, no. 4, 2014. DOI: 10.1063/1.4863305.

[122] A. Garg, N. Jain, and A. K. Singh, “Modeling and simulation of a graphene-based three-terminal junction rectifier,” *J. Comput. Electron.*, vol. 17, no. 2, pp. 562–570, 2018. DOI: 10.1007/s10825-

017-1123-3.

[123] J. Zhang, J. Brownless, and A. Song, “Graphene bridge rectifier based on self-switching diode arrays,” *Nanotechnology*, vol. 30, no. 36, p. 364004, Sep. 2019. DOI: 10.1088/1361-6528/ab25fd.

[124] M. Yasir, M. Aldrigo, M. Dragoman, A. Dinescu, M. Bozzi, S. Iordanescu, and D. Vasilache, “Integration of Antenna Array and Self-Switching Graphene Diode for Detection at 28 GHz,” *IEEE Electron Device Lett.*, vol. 40, no. 4, pp. 628–631, 2019. DOI: 10.1109/LED.2019.2899028.

[125] G. Auton, R. K. Kumar, E. Hill, and A. Song, “Graphene Triangular Ballistic Rectifier: Fabrication and Characterisation,” *J. Electron. Mater.*, vol. 46, no. 7, pp. 3942–3948, Jul. 2017. DOI: 10.1007/s11664-016-4938-y.

[126] C. W. J. Beenakker and H. van Houten, “Billiard model of a ballistic multiprobe conductor,” *Phys. Rev. Lett.*, vol. 63, no. 17, pp. 1857–1860, Oct. 1989. DOI: 10.1103/PhysRevLett.63.1857.

[127] A. M. Song, “Formalism of nonlinear transport in mesoscopic conductors,” *Phys. Rev. B*, vol. 59, no. 15, pp. 9806–9809, Apr. 1999. DOI: 10.1103/PhysRevB.59.9806.

[128] M. Buttiker, “Four-Terminal Phase-Coherent Conductance M.,” *Linear Algebra Appl.*, vol. 57, no. 14, pp. 1761–1764, 1986. DOI: 10.1016/0024-3795(85)90068-0.

[129] R. Landauer, “Spatial Variation of Currents and Fields Due to Localized Scatterers in Metallic Conduction,” *IBM J. Res. Dev.*, vol. 1, no. 3, pp. 223–231, Jul. 1957. DOI: 10.1147/rd.13.0223.

[130] M. Büttiker, Y. Imry, R. Landauer, and S. Pinhas, “Generalized many-channel conductance formula with application to small rings,” *Phys. Rev. B*, vol. 31, no. 10, pp. 6207–6215, May 1985. DOI: 10.1103/PhysRevB.31.6207.

[131] A. . Song, I. Maximov, M. Missous, and W. Seifert, “Diode-like characteristics of nanometer-scale

semiconductor channels with a broken symmetry," *Phys. E Low-dimensional Syst. Nanostructures*, vol. 21, no. 2–4, pp. 1116–1120, Mar. 2004. DOI: 10.1016/j.physe.2003.11.190.

[132] A. K. Singh, G. Auton, E. Hill, and A. Song, "Estimation of intrinsic and extrinsic capacitances of graphene self-switching diode using conformal mapping technique," *2D Mater.*, vol. 5, no. 3, p. 035023, 2018. DOI: 10.1088/2053-1583/aac133.

[133] H. Shichman and D. A. Hodges, "Modeling and Simulation of Insulated-Gate Field-Effect Transistor Switching Circuits," *IEEE J. Solid-State Circuits*, vol. 3, no. 3, pp. 285–289, 1968. DOI: 10.1109/JSSC.1968.1049902.

[134] J. Mateos, A. M. Song, B. G. Vasallo, D. Pardo, and T. Gonzalez, "THz operation of self-switching nano-diodes and nano-transistors," in *Nanotechnology II*, 2005, vol. 5838, p. 145. DOI: 10.1117/12.609126.

[135] C. Balocco, S. R. Kasjoo, X. F. Lu, L. Q. Zhang, Y. Alimi, S. Winnerl, and A. M. Song, "Room-temperature operation of a unipolar nanodiode at terahertz frequencies," *Appl. Phys. Lett.*, vol. 98, p. 223501, 2011. DOI: 10.1063/1.3595414.

[136] C. Daher, J. Torres, I. Iñiguez-de-la-Torre, P. Nouvel, L. Varani, P. Sangaré, G. Ducournau, C. Gaquière, J. Mateos, and T. González, "Room temperature direct and heterodyne detection of 0.28-0.69-THz Waves Based on GaN 2-DEG unipolar nanochannels," *IEEE Trans. Electron Devices*, vol. 63, no. 1, pp. 353–359, 2016. DOI: 10.1109/TED.2015.2503987.

[137] M. Inoue, S. Kasai, T. Maemoto, Y. Kimura, Y. Sun, and S. Sasa, "Rectification Effects of ZnO-Based Transparent Nanodiodes on Glass and Flexible Plastic Substrates," *Jpn. J. Appl. Phys.*, vol. 52, no. 6S, p. 06GE09, 2013. DOI: 10.7567/jjap.52.06ge09.

[138] L. A. Majewski and A. M. Song, "20 Megahertz Operation of Organic Nanodiodes," *Phys. Status Solidi Basic Res.*, vol. 253, no. 8, pp. 1507–1510, 2016. DOI: 10.1002/pssb.201600050.

[139] F. Al-Dirini, E. Skafidas, and A. Nirmalathas, “Graphene Self Switching Diodes with high rectification ratios,” *Proc. IEEE Conf. Nanotechnol.*, pp. 698–701, 2013. DOI: 10.1109/NANO.2013.6720877.

[140] F. Al-Dirini, F. M. Hossain, A. Nirmalathas, and E. Skafidas, “All-Graphene Planar Self-Switching MISFEDs, Metal-Insulator-Semiconductor Field-Effect Diodes,” *Sci. Rep.*, vol. 4, no. 1, p. 3983, May 2015. DOI: 10.1038/srep03983.

[141] V. R. Manfrinato, A. Stein, L. Zhang, C. Y. Nam, K. G. Yager, E. A. Stach, and C. T. Black, “Aberration-Corrected Electron Beam Lithography at the One Nanometer Length Scale,” *Nano Lett.*, vol. 17, no. 8, pp. 4562–4567, 2017. DOI: 10.1021/acs.nanolett.7b00514.

[142] M. Winters, M. Thorsell, W. Strupiński, and N. Rorsman, “High frequency electromagnetic detection by nonlinear conduction modulation in graphene nanowire diodes,” *Appl. Phys. Lett.*, vol. 107, no. 14, 2015. DOI: 10.1063/1.4932970.

[143] J. B. Johnson, “Thermal Agitation of Electricity in Conductors,” *Phys. Rev.*, vol. 32, no. 1, pp. 97–109, Jul. 1928. DOI: 10.1103/PhysRev.32.97.

[144] F. N. Hooge, “1/f noise,” *Phys. B+C*, vol. 83, no. 1, pp. 14–23, May 1976. DOI: 10.1016/0378-4363(76)90089-9.

[145] G. Ghibaudo, O. Roux, C. Nguyen-Duc, F. Balestra, and J. Brini, “Improved Analysis of Low Frequency Noise in Field-Effect MOS Transistors,” *Phys. Status Solidi*, vol. 124, no. 2, pp. 571–581, Apr. 1991. DOI: 10.1002/pssa.2211240225.

[146] A. A. Balandin, “Noise and fluctuations control in electronic devices: generation- recombination noise in semiconductors,” American Scientific Publishers, 2002.

[147] A. Castellanos-Gomez, M. Buscema, R. Molenaar, V. Singh, L. Janssen, H. S. J. van der Zant, and

G. A. Steele, “Deterministic transfer of two-dimensional materials by all-dry viscoelastic stamping,” *2D Mater.*, vol. 1, no. 1, p. 011002, Apr. 2014. DOI: 10.1088/2053-1583/1/1/011002.

[148] “Graphenea.” [Online]. Available: https://eu.graphenea.com/. [Accessed: 23-Mar-2021].

[149] J. Fan, J. M. Michalik, L. Casado, S. Roddaro, M. R. Ibarra, and J. M. De Teresa, “Investigation of the influence on graphene by using electron-beam and photo-lithography,” *Solid State Commun.*, vol. 151, no. 21, pp. 1574–1578, Nov. 2011. DOI: 10.1016/j.ssc.2011.07.028.

[150] National Instruments, “Labview.” [Online]. Available: https://www.ni.com/en-gb/shop/labview.html. [Accessed: 23-Mar-2021].

[151] OriginLab, “Origin.” [Online]. Available: https://www.originlab.com/. [Accessed: 23-Mar-2021].

[152] MathWorks, “MATLAB.” [Online]. Available: https://uk.mathworks.com/products/matlab.html. [Accessed: 23-Mar-2021].

[153] M. Sampietro, L. Fasoli, and G. Ferrari, “Spectrum analyzer with noise reduction by cross-correlation technique on two channels,” *Rev. Sci. Instrum.*, vol. 70, no. 5, pp. 2520–2525, May 1999. DOI: 10.1063/1.1149785.

[154] D. B. Davidson, *Computational Electromagnetics for RF and Microwave Engineering*. Cambridge: Cambridge University Press, 2010. DOI: 10.1017/CBO9780511778117.

[155] 3DS Simulia, “CST Studio Suite.” [Online]. Available: https://www.3ds.com/products-services/simulia/products/cst-studio-suite/. [Accessed: 23-Mar-2021].

[156] C. A. de Moura and C. S. Kubrusly, *The Courant–Friedrichs–Lewy (CFL) Condition*. New York: Springer, 2013. DOI: 10.1007/978-0-8176-8394-8.

[157] P. G. Silvestrov and K. B. Efetov, “Charge accumulation at the boundaries of a graphene strip induced by a gate voltage: Electrostatic approach,” *Phys. Rev. B - Condens. Matter Mater. Phys.*,

vol. 77, no. 15, pp. 1–5, 2008. DOI: 10.1103/PhysRevB.77.155436.

[158] A. N. Pal, A. A. Bol, and A. Ghosh, "Large low-frequency resistance noise in chemical vapor deposited graphene," *Appl. Phys. Lett.*, vol. 97, no. 13, p. 133504, Sep. 2010. DOI: 10.1063/1.3493655.

[159] H. N. Arnold, V. K. Sangwan, S. W. Schmucker, C. D. Cress, K. A. Luck, A. L. Friedman, J. T. Robinson, T. J. Marks, and M. C. Hersam, "Reducing flicker noise in chemical vapor deposition graphene field-effect transistors," *Appl. Phys. Lett.*, vol. 108, no. 7, p. 073108, Feb. 2016. DOI: 10.1063/1.4942468.

[160] M. Tamagnone, J. S. Gómez-Díaz, J. R. Mosig, and J. Perruisseau-Carrier, "Reconfigurable terahertz plasmonic antenna concept using a graphene stack," *Appl. Phys. Lett.*, vol. 101, no. 21, p. 214102, Nov. 2012. DOI: 10.1063/1.4767338.

[161] M. Tamagnone, J. S. Gómez-Díaz, J. R. Mosig, and J. Perruisseau-Carrier, "Analysis and design of terahertz antennas based on plasmonic resonant graphene sheets," *J. Appl. Phys.*, vol. 112, no. 11, p. 114915, Dec. 2012. DOI: 10.1063/1.4768840.

[162] M. Tamagnone, J. S. G. Diaz, J. Mosig, and J. Perruisseau-Carrier, "Hybrid graphene-metal reconfigurable terahertz antenna," *IEEE MTT-S Int. Microw. Symp. Dig.*, pp. 9–11, 2013. DOI: 10.1109/MWSYM.2013.6697756.

[163] A. H. Kazemi and A. Mokhtari, "Graphene-based patch antenna tunable in the three atmospheric windows," *Optik (Stuttg).*, vol. 142, pp. 475–482, 2017. DOI: 10.1016/j.ijleo.2017.05.113.

[164] J. M. Jornet and I. F. Akyildiz, "Graphene-based nano-antennas for electromagnetic nanocommunications in the terahertz band," in *Proceedings of the Fourth European Conference on Antennas and Propagation*, 2010.

[165] R. Goyal and D. K. Vishwakarma, “Design of a graphene-based patch antenna on glass substrate for high-speed terahertz communications,” *Microw. Opt. Technol. Lett.*, vol. 60, no. 7, pp. 1594–1600, 2018. DOI: 10.1002/mop.31216.

[166] M. Jafari Chashmi, P. Rezaei, and N. Kiani, “Polarization Controlling of Multi Resonant Graphene-Based Microstrip Antenna,” *Plasmonics*, vol. 15, no. 2, pp. 417–426, 2020. DOI: 10.1007/s11468-019-01044-2.

[167] X. Li, W. Cai, J. An, S. Kim, J. Nah, D. Yang, R. Piner, A. Velamakanni, I. Jung, E. Tutuc, S. K. Banerjee, L. Colombo, and R. S. Ruoff, “Large-Area Synthesis of High-Quality and Uniform Graphene Films on Copper Foils,” *Science*, vol. 324, no. 5932, pp. 1312–1314, Jun. 2009. DOI: 10.1126/science.1171245.

[168] T. J. Lyon, J. Sichau, A. Dorn, A. Zurutuza, A. Pesquera, A. Centeno, and R. H. Blick, “Upscaling high-quality CVD graphene devices to 100 micron-scale and beyond,” *Appl. Phys. Lett.*, vol. 110, no. 11, p. 113502, Mar. 2017. DOI: 10.1063/1.4978643.

[169] S. Pezzini, V. Mišeikis, S. Pace, F. Rossella, K. Watanabe, T. Taniguchi, and C. Coletti, “High-quality electrical transport using scalable CVD graphene,” *2D Mater.*, vol. 7, no. 4, p. 041003, Aug. 2020. DOI: 10.1088/2053-1583/aba645.